From strongly-interacting Bose-Fermi mixtures to ultracold molecules

by

Zoe Z. Yan
B.S., Stanford University (2014)

Submitted to the Department of Physics
in partial fulfillment of the requirements for the degree of

Doctor of Philosophy

at the

MASSACHUSETTS INSTITUTE OF TECHNOLOGY

June 2020

Author .....
Department of Physics
May 15, 2020

Certified by .....
Martin W. Zwierlein
Thomas A. Frank (1977) Professor of Physics
Thesis Supervisor

Accepted by .....
Nergis Mavalvala
Associate Department Head of Physics

From strongly-interacting Bose-Fermi mixtures to ultracold molecules

by

Zoe Z. Yan

Submitted to the Department of Physics
on May 15, 2020, in partial fulfillment of the
requirements for the degree of
Doctor of Philosophy

Abstract

This thesis describes experiments on ultracold quantum gases. First, I discuss quantum simulation involving mixtures of bosonic and fermionic atoms. Second, I present work on creating and controlling ultracold dipolar molecules of ^{23}Na^{40}K.

The rich phase diagram of Bose-Fermi mixtures was studied with our system of bosonic ^{23}Na and fermionic ^{40}K atoms. When the fermions were immersed as a minority species within a Bose-Einstein condensate, the system realized the canonical *Bose polaron* quasiparticle, which is an important paradigm in condensed matter physics. We investigated the strongly-coupled Bose polaron as it approached the quantum critical regime of the Bose-Fermi mixture. Using radiofrequency spectroscopy, we probed the binding energy and decay rate as a function of temperature. In particular, the decay rate was found to scale linearly with temperature near the Planckian rate $k_{\mathrm{B}}T/\hbar$ in the unitarity-limited regime, a hallmark of quantum critical behavior.

Bose-Fermi mixtures host a complex spectrum of collective excitations, which can shed light on their properties such as collisional relaxation rates, equilibrium equations of state, and kinetic coefficients. We probed the low-lying collective modes of a Bose-Fermi mixture across different interaction strengths and temperatures. The spin-polarized fermions were observed to transition from ballistic to hydrodynamic flow induced by interactions with the bosonic excitations. Our measurements establish Bose-Fermi mixtures as a fruitful arena to understand hydrodynamics of fermions, with important connections to electron hydrodynamics in strongly-correlated 2D materials.

The second part of this thesis describes the creation and manipulation of ultracold molecules in their ground state. Molecules have more tunable degrees of freedom compared to atoms, paving the way for studies of quantum state-controlled chemistry, quantum information, and exotic phases of matter. We created loosely-bound Feshbach molecules from ultracold atoms, then transferred those molecules to their absolute electronic, vibrational, rotational, and hyperfine ground state by stimulated Raman adiabatic passage. The rotational level structure, sample lifetimes, and coherence properties were studied, culminating in a demonstration of second-scale nuclear

spin coherence times in an ensemble of NaK.

Controlling the intermolecular interactions – which can be tunable, anisotropic, and long range – is an outstanding challenge for our field. We induced strong dipolar interactions via the technique of microwave dressing, an alternative to using static electric fields to polarize the molecules. The origin of these dipolar collisions was the resonant alignment of the approaching molecules' dipoles along their intermolecular axis, resulting in strong attraction. Our observations were explained by a conceptually simple two-state picture based on the Condon approximation.

Thesis Supervisor: Martin W. Zwierlein
Title: Thomas A. Frank (1977) Professor of Physics

Acknowledgments

First of all, I'd like to thank my advisor, Martin Zwierlein, for guiding me throughout my graduate studies. Martin's passion for physics, technical acumen, and determination to deeply understand the underlying science continually inspired me. As a mentor, he always took the time to answer my questions and motivate our team to perform, even when circumstances were demotivating. He also gave me the freedom to pursue topics I found interesting.

Physics at MIT was certainly a team effort, and I'm extremely thankful for the opportunity to work with the brilliant people of Fermi 1. I entered the lab just when Peter Park, the senior grad student, and Sebastian Will, the postdoc, were pioneering the creation of ultracold NaK in its absolute ground state. I can still remember the heady excitement of those days. Peter and Sebastian showed me the ropes around the lab. From them, I learned the basics of the Fermi 1 apparatus, including the fun parts – building ultrahigh vacuum chambers, tweaking optics – and the not-so-fun parts – changing the laser dye. Huanqian Loh entered as our next postdoc. Not only did I learn a lot of experimental physics by working side-by-side with her in the lab, but I also gained insight into basic atomic, quantum, and chemical physics, a testament to her mentorship capabilities. Aside from her formidable scientific skills, Huanqian is a genuinely nice and fun person to be around. The next "generation" of Fermi 1 includes Yiqi Ni, Carsten Robens, and Alex Chuang, a fun and effective group that I'm sad to leave. Carsten, the current postdoc, has incredible technical, computational, and organization skills, not to mention great enthusiasm for science fiction, a trait we share. Both Fermi 1 and my PhD experience have definitely been upgraded due to his ceaseless efforts. Yiqi and Alex are the talented newer grad student members – I'm excited to see what new results come out of this team!

Additionally, I am thankful for other current and former members of Martin's research group. Both in and out of the lab, I've enjoyed their company and learned a lot from them. We group members would have daily lunches and coffee breaks together, as well as outings to Walden Pond, the White Mountains for hiking and skiing, Six

Flags, and paintball. In particular I'd like to thank Biswaroop Mukherjee, Parth Patel, Zhenjie Yan, Cedric Wilson, Airlia Shaffer, Richard Fletcher, Tom Hartke, Matt Nichols, Lawrence Cheuk, Melih Okan, and Katherine Lawrence.

Elsewhere at MIT, Wolfgang Ketterle, Dave Pritchard, and my academic advisor, Vladan Vuletic, deserve thanks for teaching me physics and invaluable career advice. Wolfgang was a member of my thesis committee along with Martin and Ibrahim Cisse; I'm grateful for the committee's comments and feedback. Elisa Soave and Joris Verstraten were two productive visiting students in our group who contributed a lot to Fermi 1. I'm also grateful to Graduate Women in Physics for comraderie and travel support. I'd also like to thank the physics department, CUA, and RLE staff. Cathy Modica, Sydney Miller, Joanna Welch, Paula Sack, and Al McGurl made the research and education experience very smooth. The list of physicists I've interacted with is too long to name, but I'd like to specially thank Tijs Karman, Eugene Demler, Fabian Grusdt, Kushal Seetharam, and Robert Field for valuable discussions.

Outside of the lab, I've been blessed to know a huge group of fun, supportive people. I'd like to thank my housemates: Katherine Lawrence (pastry-master), Claire Boine (chef of elevated French cuisine), Andrew Turner (puzzle-master), Zak Vendeiro (grill-master), and Stan Weisser (Ironman). Cycling trips and outdoor adventures with Biswaroop Mukherjee, Lee Liu, Parth Patel, and Katherine Lawrence were highlights. Additionally, I'm grateful for the friendship of Ivana Chen, Sally Crouch, Angela Ma, Judy Romea, Adele Xu, Sergio Cantu, and Sid Narayanan.

My family has been my bedrock throughout this process. My parents, Dalai and Luhong, are the first scientists I knew, and they inspired me to go into science with their curiosity and love of knowledge. My sister, Eileen, has been a huge support and sender of valued cat photos. Finally, I'm grateful to my husband, Lyubo, who has shared my journey from college to grad school and beyond.

To my family

Contents

List of Figures

List of Tables

Chapter 1

Introduction

One of the main challenges of modern physics is understanding the behavior of strongly-correlated matter. Current knowledge of such systems is limited on multiple fronts: experimentally, these materials are often difficult to create or control in laboratory settings, and numerical simulations quickly become intractable as the number of particles increases. In the spirit of Feynman, physicists can seek to emulate diverse behavior, from high-temperature superconductivity to the hydrodynamics of the quark-gluon plasma, using analog quantum simulation [97]. This approach, combined with powerful concept of universality, allows the modelling of complex phenomena with tractable, tailored systems, which may differ in their microscopic Hamiltonians but reflect the same physics across all energy scales.

In atomic, molecular, and optical (AMO) physics, researchers exercise quantum control over pristine systems made of atoms, molecules, and electromagnetic fields. When atoms are cooled to a millionth of a degree above absolute zero, their motion, internal degrees of freedom, and interatomic interaction strength can be precisely controlled. By providing a "bottom-up" approach to building many-body systems, tabletop cold atom experiments have explored superfluidity, impurity physics, disordered systems, and quantum criticality, all outstanding questions within the field of condensed matter [25, 97].

A key feature of the ultracold atom platform lies in its tunability and versatility. Experiments can control many relevant parameters to high degrees of precision, in-

cluding both external degrees of freedom – density, temperature, and entropy – and internal – the quantum state [25]. Crucially, interparticle interactions can often be continuously tuned by external fields. This allows the study of many-body systems across a huge range of parameter space.

The ability to manipulate and trap atoms with lasers deserves special attention. Lasers within certain wavelength ranges can form trapping (or anti-trapping) potentials for ultracold atoms, which must be confined and levitated against gravity for the duration of most experiments. These "optical dipole traps" are workhorses of ultracold experiments. Moreover, confined with a periodic potential generated by laser light, atoms can form synthetic crystals with tunable geometry and interaction strengths. This technology of "optical lattices" has led to seminal observations, such as the superfluid-to-Mott insulator transition [104].

Despite the successes of atom-based quantum simulation, many key phenomena in condensed matter physics remain out of reach for state-of-the-art cold atom systems that rely on atoms' short-range, isotropic interactions. For example, magnetic correlations in electronic materials are predicted to relate to unconventional superconductivity [146] and topological phases of matter that are beyond the conventional paradigm of symmetry breaking [55]. Nonlocal spin-spin interactions are difficult to be simulated by atoms that experience only contact interactions (or, in certain species, relatively weak magnetic dipole interactions). Quantum simulation will benefit from controlling particles that experience strong, anisotropic, long-range interactions.

These novel features can be accessed by adding tunable degrees of freedom at the cost of experimental complexity. Molecules have rich internal structures compared to atoms, possessing vibrational and rotational modes from their nuclei. This imparts an electric dipole moment in heteronuclear diatomic molecules, which can experience dipole-dipole interactions. Molecules therefore form excellent quantum building blocks, with dense internal structure and the capability for tunable, long-range, anisotropic interactions. The internal and external degrees of freedom offer a powerful playground for precision measurement, quantum information, state-resolved chemistry, and quantum simulation [47]. For these reasons, ultracold molecules lie at

the frontier of AMO physics.

1.1 Thesis overview

This thesis describes my experimental work involving ultracold quantum gases of atoms and molecules, as well as theory background to contextualize the work. The contents can be split into two major themes: systems of interacting bosons and fermions, and ultracold dipolar molecules.

Ch. 2 presents some relevant theory background for ultracold gases and two-body scattering. It does not aim to be comprehensive, only to cover relevant physics results that will be used in Ch. 3-6. Ch. 3 details our group's study of the Bose polaron, a quasiparticle formed by immersing fermionic ^{40}K impurities into a ^{23}Na Bose-Einstein condensate. The low-lying collective dynamics of this Bose-Fermi mixture are covered in Ch. 4. From mixtures of bosons and fermions, we turn our attention to forming ground state molecules of NaK in Ch. 5, which discusses the molecule's creation, low-lying level structure, lifetime, and coherence properties. Ch. 6 presents results on molecule-molecule interactions induced by the technique of microwave dressing. Finally, promising future avenues of research will be discussed in Ch. 7.

Chapter 2

A quantum toolkit of interacting atoms and molecules

In this chapter I present background to contextualize the experimental work described in the following chapters. The building blocks of our quantum toolkit are ultracold bosons and fermions. I highlight key aspects of weakly interacting Bose-Einstein condensates and Fermi gases, both of which play a part in our atomic mixture experiments. From single species physics, I turn to interspecies interactions, which can be continuously tuned in cold atom experiments via *magnetic Feshbach resonances*. Finally, bound molecular states, created with these resonances, are discussed.

2.1 Bose-Einstein condensates

Bosonic atoms were the first to be brought into the ultracold regime. These neutral atoms can be cooled into their lowest energy state, forming a coherent, macroscopic population of atoms occupying the same quantum state – a *Bose-Einstein condensate* (BEC) [189].

Degenerate quantum gases have properties quite different from previously-studied quantum liquids such as ^{4}He and ^{3}He [20]. The history behind atomic BECs is rich, starting in 1995 with experimental realizations by groups in MIT [67] and JILA [3]. Atoms were confined in magnetic traps and cooled to microkelvin and even nanokelvin

temperatures, ultimately condensing into the BEC phase below the critical temperature. The critical temperature is given by the criterion, $n\lambda_{\mathrm{dB}}^3 \sim 1$, where n is the density, $\lambda_{\mathrm{dB}} = \sqrt{2\pi\hbar^2/mk_{\mathrm{B}}T}$ is the thermal de Broglie wavelength at temperature T, and m is the mass.

Here we present basic features of non-interacting and weakly-interacting Bose gases relevant for our experiments. We focus especially on the case where atoms live in a harmonic potential, a commonly used configuration in cold atom experiments [189]. The harmonic trap represents the potential created by optical lasers or magnetic gradients. Many results will be quoted without proof; detailed derivations can be found in Refs. [62, 189]. Condensate dynamics and low-lying collective excitations will be discussed in further detail in Ch. 4.2.2.

First, we consider an ideal Bose gas with no interparticle interactions. The particles of mass m are either existing in a homogeneous external potential $V_{\mathrm{external}} = 0$ of linear dimension L or a harmonic potential $V_{\mathrm{external}}(\vec{r}) = \frac{1}{2}m\sum_{x,y,z}\omega_i^2 r_i^2$. Non-interacting bosons in thermal equilibrium have a mean occupation number

$$f(\epsilon) = \frac{1}{e^{(\epsilon-\mu)/k_{\mathrm{B}}T} - 1} \tag{2.1}$$

for a given energy ϵ of a single-particle state, temperature T, and chemical potential μ. At high temperatures, the occupation recovers the classical Maxwell-Boltzmann distribution $f(\epsilon) = \exp\left[-(\epsilon-\mu)/k_{\mathrm{B}}T\right]$, and the mean occupation of any state is much less than unity. The chemical potential at high T is below zero. As the temperature falls, the chemical potential increases, and the mean occupation per state rises. Yet the chemical potential cannot exceed zero, otherwise the distribution for the lowest energy state (Eq. 2.1) would be negative and therefore unphysical. Thus, the mean occupation of any excited state is limited to $(e^{\epsilon/k_{\mathrm{B}}T} - 1)^{-1}$. (Here, we took the lowest energy state to have energy $\epsilon_0 = 0$.) At the critical temperature T_{c}, the excited states have been saturated to their maximum capacity, causing the lowest energy state to experience a dramatic increase in mean occupation number, N_0. This is the BEC phenomenon.

BEC property	
Critical temperature, harmonic gas	$k_{\rm B}T_{\rm c} = \hbar\bar{\omega}(N/\zeta(3))^{1/3}$
Reduced temperature, harmonic gas	$T/T_{\rm c} = \frac{k_{\rm B}T}{\hbar\bar{\omega}}(\zeta(3)/N)^{1/3}$
Critical temperature, homogenous gas	$k_{\rm B}T_{\rm c} = \frac{2\pi\hbar^2 n^{2/3}}{\zeta(3/2)^{2/3}m}$
Condensate fraction, homogeneous gas	$N_{\rm c}/N = 1 - (T/T_{\rm c})^{3/2}$
Condensate fraction, harmonic gas	$N_{\rm c}/N = 1 - (T/T_{\rm c})^{3}$

Table 2.1: Ideal BEC properties, with ζ the Riemann-zeta function and $\bar{\omega}$ the geometric mean trapping frequency.

To determine this transition temperature, consider the number of excited state particles $N_{ex} = \int_0^\infty d\epsilon\ g(\epsilon)f(\epsilon)$. The density of states $g(\epsilon)$ is the number of states between ϵ and $\epsilon+d\epsilon$ and will depend on the external confining potential. $T_{\rm c}$ is given by setting the total particle number equal to the integral equation at $T = T_{\rm c}$ and $\mu = 0$. Values are given for both the homogeneous and harmonic conditions in Tab. 2.1. Likewise, the fraction of condensed particles N_0/N is given there. Finally, the ground state density $n(\vec{r})$ in a harmonic potential without interparticle interactions is given by

$$\begin{aligned} n(\vec{r}) &= N|\phi_0(\vec{r})|^2 \\ &= \frac{N}{\pi^{3/2}R_xR_yR_z}e^{-x^2/R_x^2-y^2/R_y^2-z^2/R_z^2} \end{aligned} \tag{2.2}$$

where the widths are given by $R_i^2 = 2k_{\rm B}T/m\omega_i^2$.

Next, results for weakly-interacting BECs at zero temperature will be presented. We consider atomic interactions, which are crucial both for evaporative cooling to the degenerate regime as well as determining properties of the ground state. Interactions between ultracold bosons are characterized by the scattering length a_{bb}, giving the low-energy scattering cross section of $8\pi a_{bb}^2$ for identical bosons. (This holds true for two bosons with different momenta, interacting with direct and exchange scattering. However, two condensate bosons with the same zero momentum will only have a cross-section $4\pi a_{bb}^2$ due to the absence of the exchange term.) Scattering at the microscopic level will be considered in Sec. 2.3.1, but now we merely take the result and apply it to the ground state energy of the BEC, providing the basis for the

BEC property	
Thomas-Fermi distribution, harmonic	$\frac{15N}{8\pi x_0 y_0 z_0}\max\left(1-\sum_{i=x,y,z} r^2/r_i^2, 0\right)$
Thomas-Fermi radius	$r_i = \sqrt{2\mu/m\omega^2}$
Chemical potential	$\mu = 4\pi\hbar^2 a n(\vec{r}=0)/m = m\omega^2 r_0^2/2$
Condensate number	$N_{\rm c} = \frac{(2\mu)^{5/2}}{15\hbar^2 m^{1/2}\bar{\omega}^3 a_{bb}}$
Healing length	$\xi = (8\pi a_{bb} n)^{-1/2}$
Mean-field energy	$U_{\rm mf} = \frac{4\pi\hbar^2 a_{bb} n}{m}$
Speed of sound	$c = \sqrt{4\pi\hbar^2 a_{bb} n/m^2}$

Table 2.2: Weakly-interacting BEC properties

mean-field description. This leads to the Gross-Pitaevskii equation, which captures relevant BEC phenomena such as collective excitations, interference, and appearance of vortices. The GP equation can be derived using a variational approach [189], leading to

$$i\hbar\frac{d\psi}{dt} = \left(-\frac{\hbar^2}{2m}\nabla^2 + V + \frac{4\pi\hbar^2 a_{bb}}{m}|\psi|^2\right)\psi \tag{2.3}$$

For large, harmonically-trapped clouds, the kinetic energy term in the GP equation can be neglected if it is much smaller than the interaction energy (requiring $\hbar\omega < 4\pi\hbar^2 a_{\rm bb} n/m$.) This Thomas-Fermi approximation is used to obtain the ground-state distribution, leading to the (time-independent) form $(V(\vec{r}) + \frac{4\pi\hbar^2 a_{bb}}{m} n(\vec{r}))\psi(\vec{r}) = \mu\psi(\vec{r})$. This has the solution $n(\vec{r}) = m(\mu - V(\vec{r}))/4\pi\hbar^2 a_{bb}$. Then, the distribution, chemical potential, and condensate number have the form given in Tab. 2.2.

In the previous section we considered a condensate distribution in a potential that varies smoothly in space. How does the density change when the external potential is not smooth, or if the BEC is subjected to a local perturbation? In reality, there is a finite length scale over which density changes. The *healing length* ξ of a BEC represents the distance over which the wavefunction grows from zero to its finite value. ξ is obtained by equating the kinetic energy $\hbar^2/2m\xi^2$ to the mean-field energy.

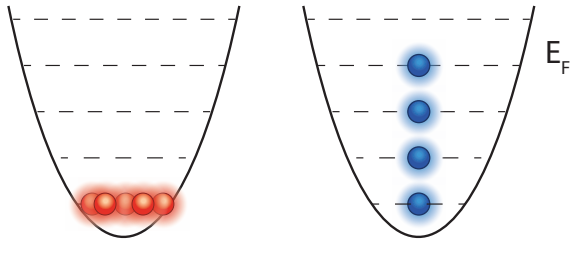

Figure 2-1: Cartoon of how ultracold bosons (left) and ultracold fermions with Fermi energy E_F (right) occupy energy levels.

..

2.2 Ultracold degenerate Fermi gases

The majority of massive elementary particles obey fermionic rather than bosonic statistics, in which two particles must be antisymmetric under exchange. As a consequence of the antisymmetrization requirement, two identical fermions cannot occupy the same quantum state. See Fig. 2-1 for an illustration. In cold atom experiments, laser-cooling works equally well for bosons and fermions, but spin-polarized fermions cannot be evaporatively cooled, as their scattering cross-section vanishes at low energies [see Sec. 2.3.1]. To reach quantum degeneracy, the vast majority of experiments have relied on evaporative cooling involving rethermalizing collisions between particles. Therefore fermions must be evaporatively cooled by using a two-species mixture, either of two different internal states of the same fermion isotope, or by using another atomic species.

In this section we review the equilibrium properties of non-interacting fermions, focusing on the case of homogeneous and harmonically-trapped gases. The Fermi distribution is

$$f = \frac{1}{e^{(\epsilon-\mu)/k_{\mathrm{B}}T}+1} \tag{2.4}$$

A consequence of the Pauli exclusion principle is that each state can only accommodate one fermion. Therefore, N fermions fill up the allowed energy states up to the chemical potential μ. At $T = 0$, $\mu = \epsilon_F$, where ϵ_F is the Fermi energy. A good approximation for the density distribution of a harmonically trapped cloud of fermions is the Thomas–Fermi approximation, which we previously applied to bosons. The properties of the gas at a point $\vec{r}$ are assumed to be those of a uniform gas having a chemical potential equal to the local chemical potential $\mu_{\mathrm{loc}}(\vec{r}) = \mu(0) - V(\vec{r})$. The resulting distribution is given in Tab. 2.3.

Fermi gas property	
Local Fermi temperature	$k_{\mathrm{B}}T_F = \hbar(6\pi^2 n(\vec{r}))^{1/3}$
Fermi temperature, harmonic	$k_{\mathrm{B}}T_F = (6N)^{1/3}\hbar\bar{\omega}$
Thomas-Fermi distribution, harmonic	$\frac{1}{6\pi^2}\left(\frac{2m}{\hbar^2}(\mu - V(\vec{r}))\right)^{3/2}$

Table 2.3: Degenerate Fermi gas properties

2.3 Interactions between atoms

In the previous sections we introduced two key building blocks for our quantum matter toolbox: ultracold bosons and fermions. But it is the the capability to tune interactions between particles that gives ultracold gas experiments incredible versatility. This section provides an overview for a workhorse of cold atom experiments, magnetic Feshbach resonances, which can be used to continuously tune interparticle interactions from attractive to repulsive. Most of the work in this thesis relied on the capability to tune Na-K interactions with such a tool, and details related to these two species can be found in Appendix A. A comprehensive review of general Feshbach resonances can be found in [54]. We begin by reviewing basic concepts in quantum scattering.

2.3.1 Ultracold scattering

In this section we develop the theoretical tools to understand ultracold two-particle collisions. "Ultracold" defines a temperature regime in which scattering must be treated quantum-mechanically. This section will be general for all low-energy quantum scattering unless specified otherwise. A more comprehensive overview can be found in basic quantum mechanics textbooks such as [205].

The basic problem in scattering entails calculating the scattering wavefunction $\psi(\vec{r})$ for a particle approaching some scattering potential $V(\vec{r})$. This requires knowing both the internal and external contributions to the two-body Hamiltonian. For two

alkali atoms A and B, this is

$$\begin{aligned}\mathcal{H} &= \mathcal{H}_{\text{internal}} + \mathcal{H}_{\text{rel}} \\ &= \mathcal{H}_{\text{internal, A}} + \mathcal{H}_{\text{internal, B}} - \frac{\hbar^2}{2\mu}\nabla^2 + V(\vec{r})\end{aligned} \tag{2.5}$$

where r is the relative coordinate, $\mu = m_1 m_2/(m_1 + m_2)$ is the two-particle reduced mass, and V is the two-body effective interaction.

Internal Hamiltonian for two S-alkali atoms

Often, cold atom experiments make use of interactions between two ground state alkali atoms. The single-atom internal Hamiltonian, for an alkali atom A in the ground electronic S state, is the sum of the hyperfine interaction and the Zeeman interaction.

$$\mathcal{H}_{\text{internal, A}} = A^{hf}\mathbf{I_A}\cdot\mathbf{S_A} + \frac{\mu_B}{\hbar}(g_s\mathbf{S_A} + g_I\mathbf{I_A})\cdot\mathbf{B} \tag{2.6}$$

where μ_B is the Bohr magneton, $\mathbf{S_A}, \mathbf{I_A}$ are the electron and nuclear spin operators with respective m_S, m_I projection quantum numbers, $\mathbf{B}$ is the magnetic field, g_S, g_I are the electron spin and nuclear spin g-factors, and A^{hf} is the magnetic dipole constant. Here we have neglected higher order hyperfine terms such as the electric quadrupole term.

The internal Hamiltonian in regards to low-energy molecule-molecule scattering will be discussed in Ch. 6, as molecules have more complex internal structure compared to atoms.

External Hamiltonian

It is useful to separate out the external degrees of freedom from the internal ones. The relative motion can be recast into the Schrödinger picture for two particles undergoing a scattering event in the center of mass frame. The Schrödinger equation is

$$\left(-\frac{\hbar^2}{2\mu}\nabla^2 + V(\vec{r})\right)\psi(\vec{r}) = E\psi(\vec{r}) \tag{2.7}$$

where E is the energy.

Often, the goal of the scattering problem is to calculate a differential cross section that relates the initial approach to the outgoing scattering:

$$\frac{d\sigma}{d\Omega_{\vec{k}'}}(\vec{k},\vec{k}') = |f(\vec{k},\vec{k}')|^2 \tag{2.8}$$

where $\vec{k},\vec{k}'$ are the initial and outgoing wave vectors, respectively, Ω is the solid angle, and f is the scattering amplitude. The differential cross section corresponds to the number of scattered particles detected at a given solid angle $d\Omega$, per number of injected particles per area. The observables in a typical ultracold experiment are related to the scattering amplitude or total scattering cross-section,

$$\sigma(\vec{k}) = \int d\Omega_{\vec{k}'} \frac{d\sigma}{d\Omega_{\vec{k}'}} \tag{2.9}$$

Bosonic and fermionic symmetries place additional constraints on the scattering amplitude:

$$f_{B,F}(\vec{k},\vec{k}') = \frac{1}{\sqrt{2}}\left(f(\vec{k},\vec{k}') \pm f(\vec{k},-\vec{k}')\right) \tag{2.10}$$

How are these quantities calculated for an arbitrary scattering potential $V(\vec{r})$? Assume the potential is short-ranged around $\vec{r}=0$ and falls off to zero some finite distance. Let the free particle operator be defined as $H_0 = -\hbar^2\nabla^2/2\mu$. Then, the solution to the Schrödinger equation at long range is just the free-particle solution, with plane wave eigenfunctions $|\phi\rangle = |\hbar\vec{k}\rangle \propto e^{i\vec{k}\vec{r}}$ and energies $\hbar^2k^2/2\mu$. We can use a normalization convention such that the real space representation of the plane wave is $\langle\vec{x}|\,\phi\rangle = (2\pi\hbar)^{-3/2}e^{i\vec{k}\cdot\vec{x}}$.

For the full solution, we can try a trial wavefunction for the Schrödinger equation, $(E-H_0)\,|\psi\rangle = V\,|\psi\rangle$, of the form

$$|\psi\rangle = |\phi\rangle + \frac{1}{E-H_0+i\epsilon}V\,|\psi\rangle \tag{2.11}$$

This is the famous *Lippmann-Schwinger* equation. The additional imaginary term in

the denominator is included to avoid the pole at $E = H_0$, and is resolved by taking the limit $\epsilon \to 0$ at the end of the calculation. Its sign is positive rather than negative for the problem to obey causality.

The position representation of this equation is more illuminating. Take the inner product with $\langle \vec{x}|$ and insert a complete set of position-basis states to find

$$\langle \vec{x}| \psi \rangle = \langle \vec{x}| \phi \rangle + \int d^3x' \langle \vec{x}| \frac{1}{E - H_0 + i\epsilon} |\vec{x}'\rangle \langle \vec{x}| V |\phi\rangle \tag{2.12}$$

$$= (2\pi\hbar)^{-3/2} e^{i\vec{k}\cdot\vec{x}} - \frac{2\mu}{\hbar^2} \int d^3x' \frac{e^{ik|\vec{x}-\vec{x}'|}}{4\pi|\vec{x}-\vec{x}'|} V(\vec{x}') \langle \vec{x}'| \psi\rangle \tag{2.13}$$

where the last line is obtained by insertion of a complete set of momentum states and contour integration in the complex momentum plane. The interpretation is simple: the first (plane wave) term is an incident particle with fixed momentum, while the second term is the modification from the scattering potential. Furthermore, for the condition $|\vec{x}| \gg |\vec{x}'|$, *i.e.,* far away from the potential's range, the solution simplifies even further

$$\psi(\vec{x}) = \frac{1}{(2\pi\hbar)^{3/2}} \left(e^{i\vec{k}\cdot\vec{x}} + f(\vec{k}, \vec{k}') \frac{e^{ikr}}{r} \right) \tag{2.14}$$

$$f(\vec{k}, \vec{k}') = -\frac{2\mu(2\pi\hbar)^3}{4\pi\hbar^2} \langle \hbar\vec{k}'| V |\psi\rangle \tag{2.15}$$

This approximation is appropriate when the potential is finite-ranged and the observation point is far outside the scattering region.

Isotropic potentials

In special cases, the scattering potential is isotropic and the scattering cross-section is only a function of $|\vec{k} - \vec{k}'|$ and not of the relative angle. For example, this occurs for scattering between ground-state non-magnetic atoms or molecules in the absence of external fields. A drastic simplification of the scattering amplitude is then possible using the partial-wave expansion with the spherical wave basis of angular momentum l, as angular momentum is conserved and we can solve the scattering problem for each partial wave separately. (The partial wave basis is also useful for certain non-isotropic

potentials).

Choose k to be aligned with the z-axis, without loss of generality. The plane wave term and scattering amplitude of Eq. 2.14 can be decomposed into a sum over partial waves: $e^{ikz} = \sum_{l=0}^{\infty}(2l+1)i^l j_l(kr)P_l(\cos(\theta))$ and $f(\vec{k},\vec{k'}) = f(k,\theta) = \sum_{l=0}^{\infty}(2l+1)P_l(\cos(\theta)f_l$. Here, P_l is the Legendre polynomial, j_l is the spherical Bessel function, and all the scattering properties are contained in the complex numbers f_l. For asymptotic behavior at long distances, f_l can be computed by insertion of the wavefunction into the Lippmann-Schwinger equation, or via the optical theorem [205]. The scattering amplitude has the form

$$f(k,\theta) = \sum_{l=0}^{\infty}(2l+1)P_l(\cos(\theta))\frac{e^{i\delta_l}\sin\delta_l}{k} \tag{2.16}$$

Here, $2\delta_l$ is the phase shift of the outgoing wave relative to the incoming and θ is the angle between $\vec{k},\vec{k'}$. The l-th partial wave component of the radial wavefunction behaves as $\sim e^{2i\delta_l}e^{ikr}/r - (-1)^l e^{-ikr}/r$, comprising a scattered portion with the additional phase factor and the incoming wave with phase factor $(-1)^l$. In terms of the phase shifts, the cross section has the form

$$\sigma = \frac{4\pi}{k^2}\sum_l (2l+1)\sin^2(\delta_l) \tag{2.17}$$

Actual calculations of the phase shift stem from solving the radial Schrödinger equation for each partial wave and taking the asymptotic limit $r \to \infty$.

In the above simplification of the scattering amplitude, we have made use of the *unitarity* relation: probability with respect to flux is conserved, and there is no source or sink of particles. This holds for each partial wave separately because of angular momentum conservation. So the s-wave scattering cross section is maximally

$$4\pi\sin^2\delta_0/k^2 \to 4\pi/k^2 \tag{2.18}$$

and so on for higher l: this upper boundary is termed *the unitarity limit*. Eq. 2.17 holds for distinguishable particles, but for identical bosons (fermions), only even (odd)

partial waves contribute, and the total cross section in Eq. 2.17 must also be multiplied by two to preserve unit probabilities.

Low-energy scattering produces additional simplifications – when the de Broglie wavelength is comparable to or larger than the potential's range, partial waves for higher l become unimportant. Conceptually, low energy colliders cannot penetrate the centrifugal barrier for high l, whose height goes as $\sim l(l+1)/r^2$. Indeed, the phase shift goes to zero as $\delta_l \sim k^{2l+1}$ for small k. This so-called *threshold* behavior indicates that the s-wave cross section of Eq. 2.17 is constant for small k.

Relative potential for two S-alkali atoms

Cold atom experiments often need to consider collisions between two electronic ground state atoms. Two alkali atoms in their ground S states can have their collision decomposed into a singlet $\mathbf{S} = \mathbf{0}$ and triplet $\mathbf{S} = \mathbf{1}$ portion, depending on whether their valence electron spins are anti-aligned or aligned.

$$V(r) = \sum_S |S\rangle\, V_S(r)\, \langle S| \tag{2.19}$$

where $V_S(r)$ is the potential for total electron spin quantum number $\mathbf{S} = \mathbf{S_A} + \mathbf{S_B}$.

Both the singlet V_s and triplet V_t potentials have associated s-wave scattering lengths that dominate at low temperatures,

$$a_{s,t} = -\lim_{k\to 0} \frac{\tan(\delta_{s,t})}{k} \tag{2.20}$$

where $\delta_{s/t}$ are the s-wave phase shifts for scattering off of $V_{s/t}$.

When two atoms are separated by a large distance, the asymptotic $r \to \infty$ limit of the potential reduces to its famous van der Waals form, which is usually written in terms of a C_6 coefficient as $V_{\mathrm{vdW}} = -C_6/r^6$. This potential has a range $r_0 = (2\mu C_6/\hbar^2)^{1/4}/2$. This range represents the distance below which the van der Waals energy magnitude becomes large compared to the collision energy (for low-energy collisions), and where the wavefunction of any partial wave starts to oscillate rapidly in space. In contrast, for distances far above r_0, the wavefunction oscillates with a

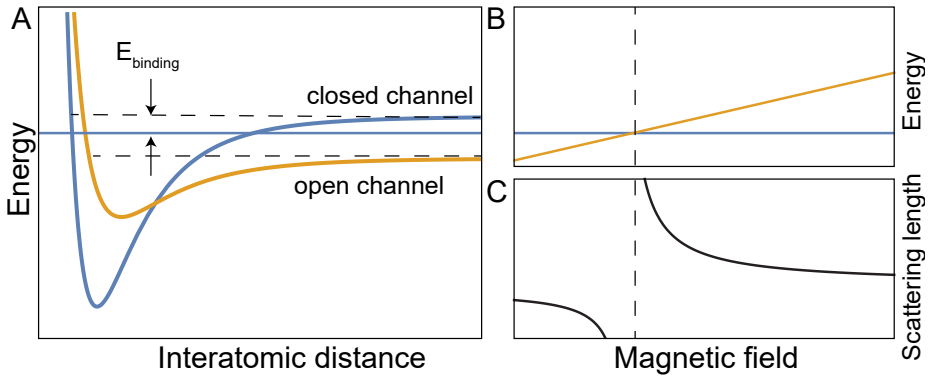

Figure 2-2: Schematic of a Feshbach resonance showing how **(A)** entering scatterers in the open channel are coupled to a bound molecular state that is energetically closed at $r \to \infty$. The bound state has a binding energy E_{binding}. **(B)** The relative energy of the two channels is tuned by an external magnetic field. **(C)** At the Feshbach resonance (vertical dashed line), the scattering length reaches its maximum absolute value.

longer period determined by the relative de Broglie wavelength.

2.3.2 Magnetic Feshbach resonances

We have established notations and basic concepts for two alkali atoms scattering at low energies. The properties of the internal states and $V_{s,t}(r)$ determine the s-wave scattering length a. Specifically, the presence of a bound molecular state within $V_{s,t}$ can affect the value of a if its energy is close to $E = 0$, the threshold of the continuum of free states. The bound state is a *closed channel* since it cannot be populated at $r \to \infty$ by energy conservation. This closed channel may have a different internal structure than the open (entrance) channel, allowing an external field to tune the two channels' relative energy. At a special magnetic field B_0, the closed channel is tuned on resonance with the open channel – the Feshbach resonance. The channels are illustrated in Fig. 2-2.

Phenomenological model for a

Here we discuss the scattering length in the special case of resonance scattering involving a single open channel and a single closed channel. Far away from any Feshbach resonances, the open channel scattering length is a_{bg}. Approaching the resonance at

B_0, we define the magnetic moment difference $\Delta\mu$ between the entrance and closed channels as $-\partial(E' - E)/\partial B$. The s-wave scattering length near the resonance is

$$a = a_{bg}\left(1 - \frac{\Delta B}{B - B_0}\right) = a_{bg} - \frac{a_{bg}}{B - B_0}\frac{C}{\Delta\mu} \tag{2.21}$$

Here, $C = \Delta\mu\Delta B$ has units of energy, and corresponds to the coupling strength between the open and closed channels. The results of the model can be derived by considering two coupled spherical well potentials or by coupling a single bound state to a continuum of plane wave states [54].

An important point is the *zero crossing* of the s-wave scattering length, occurring at $B{=}B_0 + \Delta B$. There, the two scatterers have no s-wave contribution to their interactions.

The energy of the bound molecular state, with respect to the threshold of two free atoms at zero kinetic energy, is

$$E_b = \frac{\hbar^2}{2\mu a^2} \tag{2.22}$$

for large positive values of a near resonance. In this limit, E_b depends quadratically on the magnetic detuning $B - B_0$. Here the state can be described in terms of a single effective molecular potential having scattering length a, and the wavefunction extends to a size on the order of a. *Broad Feshbach resonances* are characterized by having molecular binding energies that obey Eq. 2.22 for a large portion of their width ΔB. They occur when the bound state has the spin character of the open channel (*e.g.*, both incoming electron spins aligned to a triplet state, scattering off a bound triplet electronic molecular state) for much of the width ΔB, and they are often termed *open channel dominated*.

By contrast, *narrow Feshbach resonances* are *closed channel dominated*, where the bound state quickly has a different spin character away from B_0, and the universal binding energy formula of Eq. 2.22 only applies for a tiny fraction of the width near the resonance. These resonances need to be treated with a coupled channels description [54].

To summarize, magnetic Feshbach resonances allow the tuning of two-body inter-

atomic interactions in ultracold systems. At MIT, we use this important feature to simulate interesting problems in condensed matter physics with mixtures of bosonic ^{23}Na and fermionic ^{40}K. The realization of the Bose polaron problem is discussed in Ch. 3. There, interspecies interactions were tuned so that a background BEC of ^{23}Na atoms dressed a ^{40}K impurity into a quasiparticle, which has a distinct energy, mass, and lifetime compared to a bare ^{40}K impurity. Furthermore, we studied the low-lying collective excitations of the Bose-Fermi mixture as a function of interaction strength in Ch. 4. All work presented in this thesis relates in some way to Feshbach resonances.

2.4 From mixtures to molecules

Not only can Feshbach resonances tune interactions in quantum mixtures, but they can also be used to coherently form molecules. Cold molecules offer new opportunities for quantum simulation of many-body physics, precision measurements, chemistry, and quantum computation. Thus far, the coldest attainable molecules and the largest phase-space density of molecules have been created by Feshbach association of ultracold atoms [174, 65, 224, 167, 183, 113, 202, 210, 249, 72]. These so-called *Feshbach molecules* are formed by leveraging the Feshbach resonances discussed in the previous section.

There are several methods to create Feshbach molecules, reviewed in [54]. Ramping an external magnetic field across a resonance takes advantage of the coupling between the free atoms state and the bound state to adiabatically convert two atoms into a dimer. Alternatively, modulation of the magnetic field near a resonance induces a stimulated transition from two scattering atoms and the dimer. Another method involves a radio-frequency transition, taking an initial hyperfine spin channel of one atomic state into another spin channel that couples to a molecular state bound to the other species (in our case, Na). We use this method of "rf association" most commonly for our molecule studies.

Directly using Feshbach molecules for physics applications is often limited by

their short lifetimes. Vibrational relaxation typically limits the lifetimes to 10's of ms or much lower, depending on densities [54]. Feshbach states are highly-excited vibrational states, and a collision between a Feshbach molecule and an unpaired atom or another molecule has a huge number of open channels to scatter into, leading to high inelastic collision rates. For this and other reasons, the ultracold molecules community has developed methods to work with more stable molecular states. At MIT, we coherently transfer Feshbach molecules of ^{23}Na^{40}K into the absolute ground state; this will be discussed further in Ch. 5. Interactions between these molecules can be tuned, not (yet) by Feshbach resonances, but by turning on the long-range, anisotropic dipole-dipole interaction, as we will see in Ch. 6. Quantum control over ultracold molecules represents an exciting addition to the ultracold quantum toolbox that our community uses.

Chapter 3

Impurities interacting with a Bose-Einstein condensate

In this chapter I discuss a paradigmatic problem in strongly-correlated systems: the Bose polaron quasiparticle. In quantum many-body physics, strongly interacting systems can often be described by a collection of weakly interacting quasiparticles [180]. A famous example of such a quasiparticle is an electron propagating through an ionic crystal [143]. The electron "impurity" becomes dressed by lattice distortions – the bosonic bath of phonons – forming a quasiparticle, which Pekar named the polaron [187, 188].

First, I present some historical background on the polaron concept, starting from Landau and Pekar's insight into self-trapping of an electron in an ionic crystal. I discuss Fröhlich's Hamiltonian [90], applicable to weak-coupling systems, and sketch its derivation. A more recent theoretical framework, quantum criticality, will be presented along with its implications on the existence of quasiparticles in general [203] and for Bose polarons in particular.

Secondly, I present modern experimental techniques and results to realize the Bose polaron using impurities in ultracold systems, focusing on rf spectroscopy. I describe how our MIT experiment realizes Bose polarons with bosonic ^{23}Na and fermionic ^{40}K, measuring the energy, quasiparticle lifetime, and contact using rf ejection spectroscopy. Our research on the equilibrium polaron properties is contrasted with two

previous studies on strong-coupling Bose polarons [123, 128], which used a different spectroscopy method to determine excited polaron properties. Finally, I interpret our finding of the quasiparticle decay rate, which was observed to scale linearly with temperature $\sim k_{\mathrm{B}}T/\hbar$ at strong-coupling, in the framework of quantum criticality. The research described in this chapter has resulted in the following publication:

Zoe Z. Yan, Yiqi Ni, Carsten Robens, Martin Zwierlein, *Bose polarons near quantum criticality,* Science **368**, 190 (2020).

3.1 Bose polarons in condensed matter

Here I present some theoretical framework of the Bose polaron as it was historically developed to apply in condensed matter, starting from the idea's conception [143], to the commonly-used Fröhlich Hamiltonian [90]. The polaron's history, beginning in 1933 with a seminal paper by Landau [143], reflects the development of quantum field theory. Today, the Bose polaron problem continues to play a crucial role in diverse areas of physics, including in colossal magnetoresistance, semiconductor quantum dots, high-temperature superconductors, and ^{3}He impurities in ^{4}He superfluids [1]. As this thesis does not claim to comprehensively cover polaron physics, a more detailed review can be found in Ref. [1].

Self-trapping of an electron

In the solid state, polarons can be formed by electrons dressed by a cloud of phonons. The polaron was the first example of propagating self-localized excitations in a quantum field theory, and many theorists throughout history were inspired by and significantly contributed to its theory [1].

As anticipated by Landau [143], Pekar found that an electron in a solid can create its own bound state by polarizing its environment [187, 188]. Under the *continuum* assumption, where the polaron's spatial extent is larger than the lattice constant and its associated kinetic energy is low, ionic deformations smoothly follow the polaron's motion. This is the continuum or large polaron limit [1]. Then, the system's ground

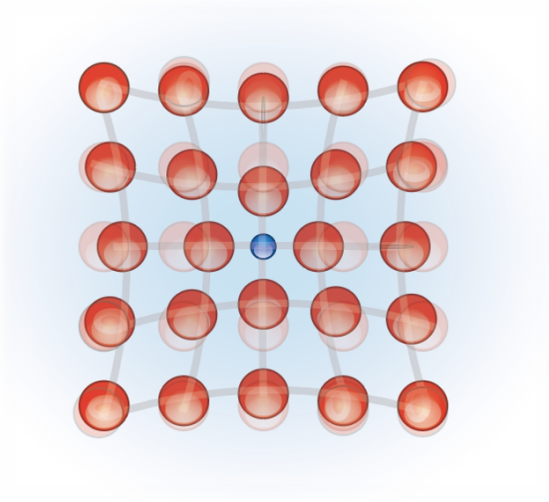

Figure 3-1: Cartoon of a polaron in the solid state: an electron impurity (blue) in a crystal lattice of ions (red) causes lattice distortions, or phonons, due to electron-phonon coupling.

state is an electron, localized to and dressed by a phononic bath, with a negative energy compared to the continuum energy– a bound "polaron" state.

Here I highlight the key points of Pekar's derivation of the polaron binding energy [188]. Assume the electron possesses a stationary charge distribution $\rho(\mathbf{r}) = e|\phi|^2$, with the electron charge e and wavefunction ϕ, inducing a polarization in its surrounding dielectric medium. Then the electron experiences a field of potential

$$V = -e^2 \frac{\epsilon - 1}{\epsilon} \int d\mathbf{r}' \frac{|\phi(\mathbf{r}')|^2}{|\mathbf{r} - \mathbf{r}'|} \tag{3.1}$$

where ϵ is the medium's dielectric constant. The electron is assumed to be localized, experiencing a potential well V, and the energy thus obeys the corresponding Schrödinger equation. Writing the Lagrangian action as a functional $S[\phi] = \int dt \left(\hbar^2(\nabla\phi)^2/2m + V\phi^2/2\right)$ and minimizing, Pekar determined that the ground state Bose polaron energy was

$$E_p = -0.164 \left(\frac{\epsilon - 1}{\epsilon}\right)^2 \frac{me^4}{\hbar^2} \tag{3.2}$$

The Pekar solution is valid only in the strong-coupling limit in which the dielectric medium's polarization is static, not dynamic. Electric charge must rearrange itself quickly enough compared to the phonon timescale, requiring the electron kinetic energy to exceed the phonon energy: $\hbar^2/m\lambda_{\mathrm{dB}}^2 > \hbar\omega_{\mathrm{phonon}}$, where λ_{dB} and m are

the electron de Broglie wavelength and mass, respectively [90]. Most materials do not meet this requirement, and the interaction parameter is typically less than half the value necessary for Eq. 3.2 to hold [90]. Thus, although Landau's and Pekar's formulation of the polaron was an important conceptual step, in reality it did not directly apply to many materials in the solid state. A useful *dynamical* approach was applied to the polaron problem by Fröhlich.

Fröhlich model for the weak-coupling polaron

The Fröhlich Hamiltonian [90] is one of the most commonly used models of the electron-phonon impurity problem. Generically, it describes a large class of problems involving a single mobile impurity interacting with a reservoir of bosons. It can be applied to the interaction between an impurity atom and Bogoliubov modes of a BEC when quantum depletion of the BEC is small and finite-momentum phonon scattering is neglected (see [108] for a review).

In this section, the Hamiltonian is discussed for the case of an impurity within a weakly-interacting BEC. First, the BEC is described with standard Bogoliubov theory, in which the relevant particles are the excitations of the Bose gas. Let the boson field operator be $\phi_{\mathrm{B}} = L^{-3/2}\sum_{\mathbf{k}} e^{i\mathbf{k}\cdot\mathbf{r}}\hat{b}_{\mathbf{k}}$, where $L \to \infty$ is the system length and the boson operators obey $[\hat{b}_{\mathbf{k}}, \hat{b}^{\dagger}_{\mathbf{k}'}] = \delta_{\mathbf{k},\mathbf{k}'}$. The operators $\hat{a}_{\mathbf{k}}, \hat{a}^{\dagger}_{\mathbf{k}}$ respectively annihilate and create Bogoliubov excitations with wave number $\vec{k}$. The boson operators and excitation operators are related by the Bogoliubov transformation $\hat{b}_{\mathbf{k}} = \cosh\theta_{\mathbf{k}}\hat{a}_{\mathbf{k}} - \sinh\theta_{\mathbf{k}}\hat{a}^{\dagger}_{-\mathbf{k}}$. Here the parameters obey $\cosh\theta_k = \sqrt{\frac{\hbar^2k^2/2m_{\mathrm{B}}+g_{\mathrm{BB}}n_0+\hbar\omega_k}{2\omega_k}}$ and $\sinh\theta_k = \sqrt{\frac{\hbar^2k^2/2m_{\mathrm{B}}+g_{\mathrm{BB}}n_0-\hbar\omega_k}{2\omega_k}}$, where $g_{\mathrm{BB}} = 4\pi\hbar^2 a_{\mathrm{BB}}/m_{\mathrm{B}}$, m_{B} is the boson mass, a_{BB} is the Bose-Bose scattering length, and n_0 is the BEC density.

The boson portion of the Hamiltonian expressed in terms of the Bogoliubov phonons is $\mathcal{H}_{\mathrm{B}} = \sum_{\mathbf{k}} \hbar\omega_k \hat{a}^{\dagger}_{\mathbf{k}}\hat{a}_{\mathbf{k}'}$, where $\omega_k = ck\sqrt{1+\xi^2k^2/2}$, ξ is the BEC healing length, and c is the speed of sound.

Secondly, an important portion of the Hamiltonian is the impurity-boson interac-

tion term, with $\phi_{\rm I}$ the impurity wavefunction.

$$\mathcal{H}_{IB} = g_{\rm IB} \int \frac{d^3\mathbf{r}}{L^3} \phi_{\rm I}^\dagger(\mathbf{r}) \phi_{\rm I}(\mathbf{r}) \sum_{\mathbf{k},\mathbf{k}'} e^{i(\mathbf{k}-\mathbf{k}')\cdot\mathbf{r}}\, \hat{b}_{\mathbf{k}}^\dagger \hat{b}_{\mathbf{k}'} \tag{3.3}$$

Here, $g_{\rm IB}$ is the effective impurity-boson interaction strength. The state at $\mathbf{k} = \mathbf{0}$ is special: it represents the macroscopic BEC occupation with atom number N_0 and can be taken out of the sum over k, k' states. Then, the impurity-boson Hamiltonian is

$$\mathcal{H}_{IB} = g_{\rm IB} \int \frac{d^3\mathbf{r}}{L^3} \phi_{\rm I}^\dagger(\mathbf{r}) \phi_{\rm I}(\mathbf{r}) \left(N_0 + \sum_{\mathbf{k}\neq\mathbf{0}} \sqrt{N_0} e^{i\mathbf{k}\cdot\mathbf{r}}\, \hat{b}_{\mathbf{k}}^\dagger + \text{h.c.} + \sum_{\mathbf{k},\mathbf{k}'\neq\mathbf{0}} e^{i(\mathbf{k}-\mathbf{k}')\cdot\mathbf{r}}\, \hat{b}_{\mathbf{k}}^\dagger \hat{b}_{\mathbf{k}'} \right) \tag{3.4}$$

In Fröhlich's approximation the last term is neglected, keeping only the lowest order in the bosonic operator; this is valid at low temperatures where the BEC density far outweighs the density of excitations, $n_0 \gg n_{ex}$. Additionally, the boson operators may be rewritten in terms of excitation operators.

The final portion of the Hamiltonian is the impurity kinetic energy term. Then, adding the bosonic, impurity, and Bose-impurity portions, and taking the continuum limit, the Fröhlich Hamiltonian can be written [227, 108]

$$\begin{aligned} \mathcal{H}_{\rm F} = g_{\rm IB} n_0 &+ \int d^3\mathbf{k} \left(\hbar\omega_k \hat{a}_{\mathbf{k}}^\dagger \hat{a}_{\mathbf{k}} + \int d^3\mathbf{r}\, \phi_{\rm I}^\dagger(\mathbf{r}) \phi_{\rm I}(\mathbf{r})\, V_{\mathbf{k}} e^{i\mathbf{k}\mathbf{r}} (\hat{a}_{\mathbf{k}} + \hat{a}_{-\mathbf{k}}^\dagger) \right) \\ &- \int d^3\mathbf{r} \phi_{\rm I}^\dagger(\mathbf{r}) \frac{\hbar^2\nabla^2}{2m_{\rm I}} \phi_{\rm I}(\mathbf{r}) \end{aligned} \tag{3.5}$$

where $V_{\mathbf{k}} = \sqrt{n_0} \frac{g_{\rm IB}}{(2\pi)^{3/2}} \left(\frac{\xi^2 k^2}{2+\xi^2 k^2} \right)^{1/4}$ and $m_{\rm I}$ is the impurity mass.

The applicability of the Fröhlich model to Bose polarons comes under question at strong interactions because of the relevance of multiphonon terms, but it is nevertheless a popular starting point for theoretical investigations [108].

Looking beyond the Fröhlich paradigm, the theoretical literature on Bose polarons is vast. A comprehensive list of various approaches to the problem is beyond the scope of this thesis and can be found in other reviews [1, 108]. However, we highlight

historical efforts by Lee, Low, and Pines [147] using a canonical transformation to solve the variational problem based on Pekar, and Feynman's path-integral-based approach improving on Fröhlich's solution [86]. More recent theoretical works have studied the polaron ground state (at zero-temperature) in the context of impurities in a BEC (see Sec. 3.3 for a short review).

3.2 Quasiparticles near quantum criticality

The polaron is one example of a quasiparticle – an emergent excitation of a many-body system that has properties similar to those of a real particle. I now discuss in brief the quasiparticle description of weakly-interacting matter, and its breakdown in certain strongly-interacting systems.

Properties of the quasiparticle

Quasiparticles are particle-like excitations in condensed matter with well-defined properties such as energy, momentum, and mass. Their existence allows the use of powerful methods like mean-field theories to describe the system. Quasiparticles were first formulated in the 1940's and 1950's, most famously in the context of Landau Fermi liquid theory [190, 20], in which a nearly degenerate Fermi gas hosts weakly-interacting, long-lived quasiparticle excitations in the form of holes and electrons near the Fermi surface.

Formally, quasiparticles are identified as the poles of the single particle Green's function G [95] in the complex frequency plane. In quantum many-body theory, Green's functions are correlation functions, describing how a wavefunction at position and time $(\mathbf{r}, t)$ evolves into another wavefunction at $(\mathbf{r}', t')$. Knowing the Green's function enables the extraction of the density of states, relaxation times, and response functions of the system under study. Functionally, they are solutions to the inhomogeneous Schrödinger equation,

$$\left(\frac{i\hbar\partial}{\partial t} + \frac{\hbar^2}{2m_I}\nabla^2\right) G(\mathbf{r}, \mathbf{r}', t, t') = \delta(\mathbf{r} - \mathbf{r}', t - t') \tag{3.6}$$

whereas the retarded G^R is non-zero only for $t > t'$, such that we can calculate the response of the system after it has been perturbed. Using Dyson's formula, the impurity Green's function in the complex frequency plane $G^R(\omega, \mathbf{p})$ can be written

$$G_I^R(\omega, \mathbf{p}) = \frac{1}{\hbar\omega - p^2/2m_{\mathrm{I}} - \Sigma(\omega, \mathbf{p}) + i0^+} \tag{3.7}$$

where Σ is the impurity self-energy [95]. A detailed description of Green's functions can be found for general many-body systems [95] and specifically for the Bose polaron problem [198].

The impurity Green's function encapsulates four properties that, together, characterize the quasiparticle.

1. The **binding energy** E_p is defined by the recursive dispersion $E_p(p) = \frac{p^2}{2m_{\mathrm{I}}} + \mathrm{Re}\,\Sigma[E_p(p), p]$ [198]. The frequency $\omega = E_p/\hbar$ corresponds to a pole so long as Σ has no imaginary portion.

2. The **residue** $Z(p) = \lim_{\omega \to E_p/\hbar}(1 - \partial \mathrm{Re}\Sigma[E_p(p), p]/\partial\omega)^{-1}$ represents the quasiparticle spectral weight.

3. The **decay rate** of the quasiparticle corresponds to the imaginary component of the self-energy, $\gamma(p) = -Z(p)\mathrm{Im}\,\Sigma[E_p(p), p]$.

4. The **effective mass** is given by the inverse slope of the dispersion relation, $\frac{1}{m^*} = \frac{1}{p}\frac{\partial E}{\partial p}$, and reduces to the bare impurity mass m_{I} in the absence of impurity-bath coupling. This value can be lower or higher than m_{I}.

Quasiparticles are well-defined as long as the decay rate is very low, or mathematically, as long as the poles of the Green's function in the complex ω plane are close to the real axis. The quasiparticle description is an essential foundation of condensed matter, effectively describing thermodynamic and transport properties across many metals and in liquid helium [20].

Quasiparticle breakdown near quantum criticality

The quasiparticle description of matter breaks down in certain strongly-interacting systems, including in *quantum-critical* regions. Understanding many-body physics

that is not amenable to the quasiparticle paradigm remains an outstanding challenge for many-body quantum physics.

Many such systems are predicted to fall within the framework of *quantum criticality*. Here, the properties of matter are controlled by a so-called *quantum critical point* (QCP), a $T = 0$ quantum phase transition separating two or more phases [203] (see Fig. 3-2A). A quantum phase transition leads to a qualitative change in the ground state wavefunction upon tuning some parameter in the system's Hamiltonian (*e.g.,* magnetic field, doping). It is distinct from a classical phase transition, which is thermally driven (*e.g.,* steam to liquid water). Commonly, quantum phase transitions are second-order, meaning the transition is continuous in the tuning parameter but its derivative is not continuous. In these cases, the length scale below which the wavefunction 'knows' about the transition (typically an effective correlation length) diverges as we approach the QCP [203]. Though the QCP lives at absolute zero temperature, its influence extends over a wide region of finite, experimentally-accesible temperatures: the quantum critical regime.

A hallmark of quantum criticality lies in the scaling of the system's thermal equilibration time [203]

$$\tau_e = C_e \frac{\hbar}{k_{\mathrm{B}} T} \tag{3.8}$$

where C_e is a dimensionless universal number independent of the Hamiltonian's microscopic form. Quantum critical systems have been described as "nearly perfect fluids" because the equilibration time is as short as quantum mechanics allows [203]. When only one relaxation timescale is left, experiments that probe response functions as a function of frequency ω and temperature T can thus universally describe those responses by the dimensionless $\hbar\omega/k_{\mathrm{B}}T$, so long as they remain in the quantum-critical regime.

It is illustrative to consider a few examples. A simple realization of quantum criticality in ultracold gases is found in the non-interacting Fermi gas [177, 203]. The quantum critical point separates the vacuum of fermions from the Fermi liquid phase. More precisely, the vacuum phase has zero fermion density ($n_{\mathrm{F}} = 0$) at negative

chemical potential $\mu_F < 0$, while the Fermi liquid phase supports positive density, $n_F \sim \mu_F^{3/2}$ at $\mu_F > 0$. The density in the region at non-zero temperature above this quantum critical point, $n_F \sim 1/\lambda_{dB}^3$, corresponds to an interparticle distance on the order of the de Broglie wavelength λ_{dB}, showing that quantum and thermal effects are equally important [203].

As another example, the weakly interacting Bose gas can be discussed from the viewpoint of quantum criticality [203]. Here, the quantum critical point at $T = 0$ separates the boson vacuum ($n_B = 0$ at $\mu_B < 0$) from the gas at finite density ($n_B = \mu_B/g_{BB}$). The classical second-order phase transition of Bose-Einstein condensation is a line in the T-μ_B plane terminating at the $T = 0$ quantum critical point (see the phase diagram of Fig. 3-2B).

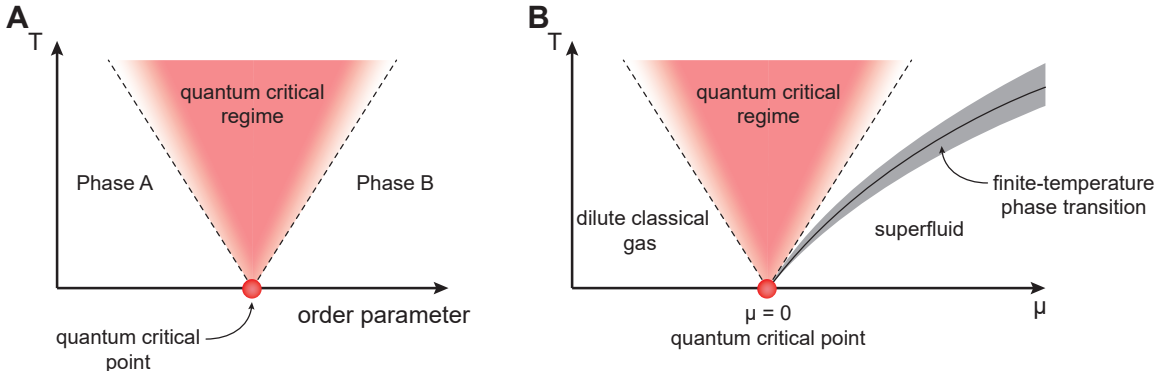

Figure 3-2: **(A)** Phase diagram of a system with two quantum phases separated by a zero-temperature QCP. A quantum-critical regime lies above the QCP at finite temperatures. **(B)** Phase diagram of a dilute Bose gas with chemical potential μ. The solid line is the classical phase transition where the superfluid order disappears [203].

As a final example, a Bose-Fermi mixture contains several quantum (multi-)critical points at zero temperature, leading to a complex quantum critical regime above zero temperature. Most relevant to our experiment at MIT is the quantum phase transition from having a BEC but no impurities to having a BEC in the presence of impurities. Ludwig et al. examined the phases of the Bose-Fermi mixture across different densities, chemical potentials, and Bose-Fermi interactions [157]. There, they demonstrated the existence of this quantum phase transition and showed that it separates two distinct phases. The Bose-Fermi phase diagram for the fermion minority limit is reproduced in Fig. 3-3.

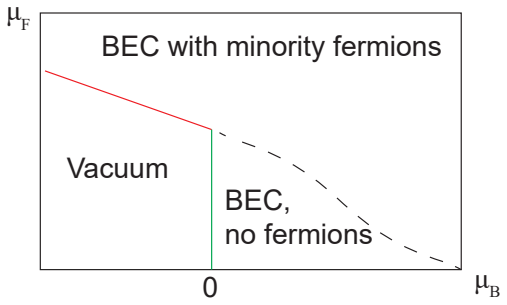

Figure 3-3: Phase diagram of a Bose-Fermi mixture, adapted from [157]. There are three different regimes of a Bose-Fermi mixture at $T = 0$ as a function of fermion (boson) chemical potential $\mu_{\mathrm{F(B)}}$ in the fermion minority limit. See [157] for a quantitative description.

Here we point out that though the viewpoint of criticality relies on the thermodynamic limit (high N particle number), critical phenomena can still manifest in impurity-bath problem, even down to the limit of a single impurity. We are interested in the class of quantum phase transitions where only the degrees of freedom of a subsystem become critical. Impurity quantum phase transitions require the thermodynamic limit in the bath system, but are independent of possible bulk phase transitions in the bath. An example includes the coupled Bose-Fermi mixture deep in the Fermi impurity limit [157], which was discussed previously. Other examples include the dissipative spin-boson model and the anisotropic Kondo models [234].

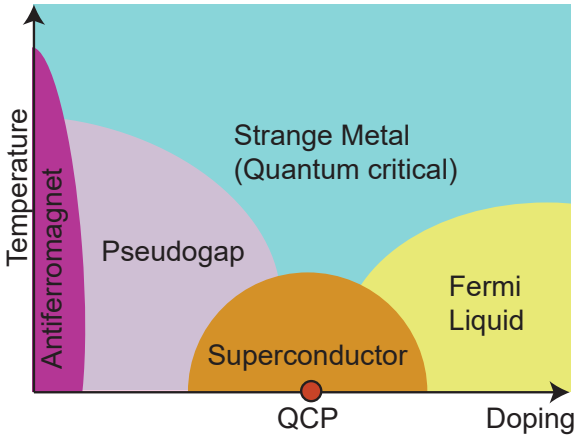

Figure 3-4: Hypothesized phase diagram of the hole-doped cuprate superconductors, with the underlying quantum critical point (QCP) giving rise to the strange metal phase. See [146] for a review.

The cold atom platform is well positioned to study quantum critical systems, as species composition, densities, interaction strengths, and confining geometries can be precisely controlled [25]. Furthermore, these platforms could give insight to complex phenomena in solids where quantum criticality might play a role. Famously, *strange metal* behavior has been found in strongly correlated-electron materials, notably in high-temperature cuprate superconductors [66, 146]. Strange metals demonstrate

electrical resistivity proportional to T and not T^2 as predicted by Fermi liquid theory. The T-linear behavior has become associated to the quantum critical regime of the critical hole doping point (see Fig. 3-4). Already, cold atom experiments studying transport in the Hubbard regime have discovered T-linear behavior reminiscent of these strange metals [34]. To the best of our knowledge, however, no one thus far has undertaken a quantum simulation of the impurity problem with the cold atom platform and demonstrated the signatures of quantum criticality therein. We will now focus on the problem of an impurity in a bosonic bath, examining where the quasiparticle picture breaks down.

3.3 Impurities in ultracold atoms

This section highlights the efforts of cold atom experiments to study the quantum impurity problem, focusing on the polaron context.

The dressing of resonant impurities into quasiparticles in a cold atom environment was first considered theoretically in the case of the Fermi polaron [53, 192, 161, 208] – an atomic impurity embedded in a Fermi sea. This system was experimentally probed in [207, 171, 138, 137, 51, 206, 245]. As a result, the understanding of the imbalanced Fermi gas phase diagram and Fermi polaron ground state has been significantly enriched. However, Bose polarons are more analogous to the generic solid-state impurity problem, since the surrounding media of both systems share the same quantum statistics (phonons or bosonic atoms), with both phonons and weakly-interacting BEC's having linear low-energy dispersion relations. In contrast to the Fermi case, the bosonic bath does not suppress interactions beyond the two-body regime, giving rise to a vast array of interesting phenomena but also rendering the theoretical description challenging.

The Bose polaron in cold atoms has been a subject of extensive theoretical research. Impurities dressed by a Bose-Einstein condensate have been posited to form the paradigmatic Bose polarons in a series of proposals [131, 61]. Predicting the Bose polaron's energy, residue, lifetime, and effective mass upon entering the regime of

strong impurity-boson interactions has proven a challenge even at zero temperature. Impurity self-localization was studied using mean-field approximations [131, 61, 35]. Within the paradigm of the Fröhlich Hamiltonian (see Sec. 3.1), the impurity-BEC problem was approached using Feynman's path-integral method [227], a diagrammatic Monte Carlo calculation [233], a renormalization group approach [107, 109], and a variational method based on Gaussian wavefunctions [213]. Beyond the Fröhlich approximation, efforts to solve the impurity-BEC problem include a diagrammatic method with contributions from the lowest-order T-matrix [198], an equivalent variational method [152] generalizing the Chevy ansatz [53], a quantum Monte Carlo approach [7, 8], a coherent-state-based ansatz [214], a renormalization group approach for strong-couplings [106, 110], and an extended Fröhlich model treating multiple impurities with the Lee-Low-Pines approximation [232].

These approaches, however, did not include three-body Efimov correlations. These correlations were accounted for by a perturbative expansion in a [56], and within a variational approach that includes up to two Bogoliubov excitations [149]. Effects of the closed-channel molecular dimer mediating the impurity-boson interaction were considered in [215, 254]. Beyond treating a single impurity, two impurities have been predicted to form a bound bipolaron state in a BEC [48, 42].

The complexity of describing the strongly-coupled Bose polaron increases further at non-zero temperatures [150, 111, 80, 87]. Even for weak interactions, the decay rate of polarons has been predicted to be strongly enhanced with increasing temperature, achieving its maximal value near the BEC transition temperature of the host gas [150]. Near resonance, in the quantum critical regime of the boson-impurity mixture, the very existence of a well-defined quasiparticle is in question [203, 157, 23].

On the experimental side, evidence of Bose polaronic phenomena was observed in the expansion [184] and trapping [76] of fermions immersed in a BEC. In 1D, the dynamics of impurities immersed in a BEC were studied, leading to measurements of the effective mass [50]. In 3D, an analog to the hydrogen Lamb shift from impurity-BEC coupling was investigated via motional Ramsey spectroscopy, where the BEC induced a "phononic Lamb shift" on the impurity [200]. The continuum of excited

states of impurities was probed spectroscopically on Bose-Fermi mixtures [242, 123] and in a two-state mixture of bosons [128], yielding evidence for polaronic energy shifts of such excitations. Specifically, in the works of [128, 123], Bose polaron energies were quantified across different impurity-BEC interaction strengths via a technique called rf injection spectroscopy, as we explain in the following section. However, many open questions remained regarding the polaron properties at strong-coupling and the dependency on BEC temperature.

3.3.1 Radiofrequency spectroscopy on polarons

In cold atom platforms, a common probe of many-body systems is radiofrequency (rf) spectroscopy [114]. This technique typically uses rf waves to measure the energy difference between two hyperfine states in an atom. Because the hyperfine splitting is well-known in the absence of interparticle interactions (to a degree that a hyperfine transition defines the SI unit of time, the second), deviations from the bare splitting can be attributed to external effects, such as electric and magnetic fields or interparticle collisions.

Our many-body system of interest is an impurity atom interacting with host bosons. Microscopically, interactions stem from collisions. A well-controlled rf spectroscopy experiment can map out the spectral response of the impurity-bath system and detect deviations from the bare impurity spectral response due to impurity-bath coupling. The spectral response encodes many quantities of interest – energy, relaxation times, correlators – and gives rise to macroscopic properties such as transport coefficients.

Two variants of rf spectroscopy are commonly used in cold atom platforms: *ejection (direct)* and *injection (indirect)* spectroscopy. The former involves preparing the system initially in an interacting state, the polaronic many-body state of interest. Then an rf pulse transfers the impurity into a hyperfine state that does not interact with the majority atoms (meaning the impurity-bath collision rate is negligible; see Fig. 3-5). For injection spectroscopy, the scenario is reversed, with the initial state noninteracting and the final state the polaronic state. More generally than the in-

jection or ejection method, both initial and final states can interact with the bath. However, in that case the absence of a clear baseline makes interpretation of the spectral response difficult.

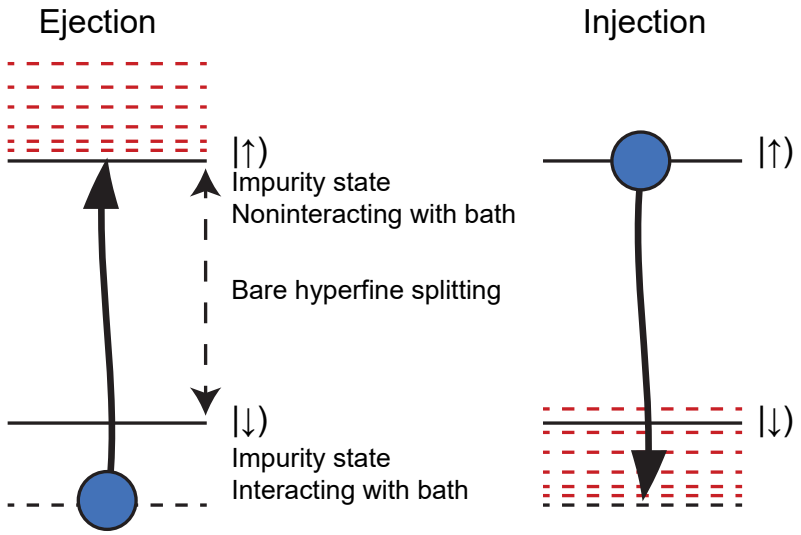

Figure 3-5: Schematic comparison of rf ejection and injection spectroscopy protocols. Ejection starts with the initial many-body state, which is offset from the bare spin state $|\downarrow\rangle$ by interactions, and transfers the system to a noninteracting final state $|\uparrow\rangle$. The injection method transfers the initial noninteracting state ($|\uparrow\rangle$) into a continuum of excited polaronic states (red dashed lines, not to scale), not solely to the equilibrium state (black dashed line).

Experimentalists detect a signal proportion to the rf absorption cross section – typically a change in atom number. An rf pulse changes its target's internal state without changing the momentum p. The rf transition rate of impurities can be computed using the spectral function $A(\omega, \mathbf{p})$, the energy-dependent density distribution of the many-body environment $n(E)$, and the noninteracting impurity energy $\epsilon_p = p^2/2m_I$. The rate is expressed [212],

$$\Gamma(\omega_{\mathrm{rf}}) = \sum_{\mathbf{p}} \int dE\, A(E/\hbar, \mathbf{p}) n(E) \delta(E - \hbar\omega_{\mathrm{rf}} - \epsilon_p) \tag{3.9}$$

The spectral function A has a direct relationship to the retarded Green's function (see, for example, Refs. [198, 212]):

$$A(\omega, \mathbf{p}) = -2\mathrm{Im}\, G_I^R(\omega, \mathbf{p}) \tag{3.10}$$

Rf spectroscopy can therefore reveal the characteristic properties of the quasiparticle, as described in Sec. 3.2. The binding energy can be assigned as the rf frequency at which the spectrum has its maximal response, corresponding to a pole in the Green's function. The decay rate is empirically determined as the spectral width.

With these features in mind, we can now examine the results of two pioneering injection spectroscopy studies of the Bose polaron across different interaction strengths [123, 128]. Both experiments varied the impurity-bath coupling by tuning the s-wave scattering length a; the interaction parameter is normalized by $k_n = (6\pi^2 n_{\text{bath}})^{1/3}$. By leveraging a Feshbach resonance, both attractive and repulsive interactions were studied. Two distinct peaked features were seen, one at positive and one at negative energies (see Fig. 3-6). The lowest-energy feature was interpreted as an attractive polaron for $a < 0$, where the impurity enhances the local density of bosons around it. Its signal crossed into a molecular branch that begins at $1/a = 0$, corresponding to the pairing of an impurity and a host atom. However, whether the attractive polaron evolves smoothly into the two-body molecular dimer or undergoes a phase transition is still an open question. The upper energy branch at $a > 0$ was interpreted as the repulsive branch, where the impurity repels neighboring bosons. This is only a metastable state, as the attractive polaron and molecular branches lie at lower energies. The sharpness of the spectrum diminished approaching unitary scattering, $1/a = 0$, indicating a decrease in quasiparticle lifetime. Together, these experiments were the first to observe signatures of the attractive and repulsive Bose polaron by measuring the energy through rf injection spectroscopy.

However, the rf injection protocol cannot directly measure the binding energy by assigning the peak of the spectra as E_p. Because this procedure does not resolve momentum, injection into a final interacting state can populate states with finite momentum (and thus costing a different amount of rf energy $\hbar\omega_{\text{rf}}$) at a higher rate than the true ground state with $p = 0$. Therefore, the binding energy can only be assigned to the *onset* of the injection spectrum, a more empirically difficult determination; see Sec. 3.4.2 for details. For clearer understanding of equilibrium Bose polaron properties, ejection spectroscopy is employed in our experiment at MIT.

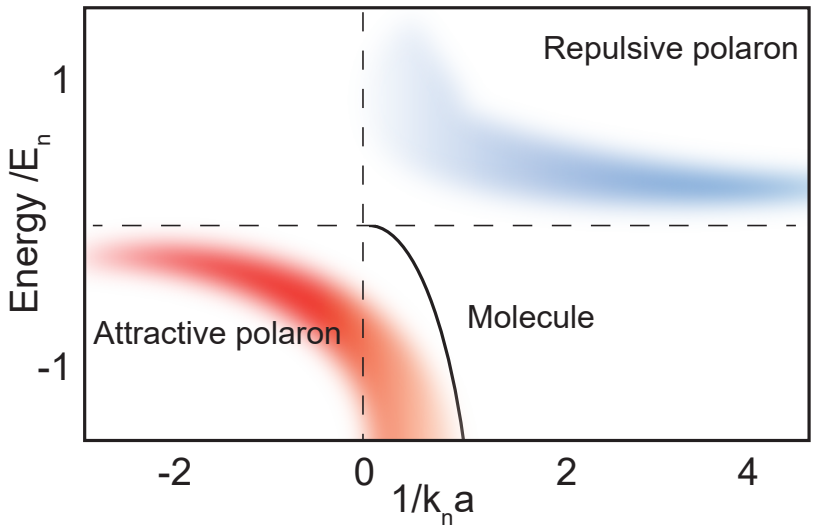

Figure 3-6: **Spectral response of the excited Bose polaron continuum measured by rf injection spectroscopy**, reproduced as a cartoon following the results of [123, 128]. The maximum spectral response is shown versus the interaction parameter, $1/k_n a$. The attractive branch was measured to have negative energies. The deeply bound attractive branch extends to $a > 0$, where the molecular branch appears. The metastable upper repulsive branch was measured to have positive energies [123, 128].

3.4 Realizing Bose polarons with ultracold bosonic ^{23}Na and fermionic ^{40}K

The following section details our experimental realization of the Bose polaron system using ultracold K atoms immersed in a BEC of Na. Details involving sample preparation and rf ejection spectroscopy are discussed.

3.4.1 Preparing high phase-space-density mixtures

To realize the Bose polaron system with ultracold Na and K atoms, we follow a similar prescription as detailed in [241, 181]; we will only highlight any significant differences in the following paragraphs.

We create a mixture of K impurities in a BEC of Na through a combination of laser-cooling and evaporative cooling. After the Na and K magneto-optical traps (MOTs) are sequentially loaded and pumping is completed, a triple-stage evaporation sequence is commenced, starting with magnetic evaporation. Na and K atoms are respectively

in their $|F = 2, m_F = 2\rangle$ and $|9/2, 9/2\rangle$ states. The MOT and magnetic gradient traps share the same field coils in an anti-Helmholtz configuration, but the power supplies are two independent units (both Lambda ES 30-500), to enable precharging and fast current rampup of the latter trap. The atomic mixture collides for 8 s in a magnetic quadrupole trap with vertical gradient $B'_z \approx 200\,\mathrm{G/cm}$.

To commence evaporative cooling, a microwave field is applied from an antenna within the vacuum chamber, changing the Na spin state. The microwave frequency is swept from 1860 MHz to 1804 MHz in 4 s, then to 1780 MHz in the final 4s. Then, when three-body inelastic collisions start to dominate, the gradient is relaxed to 13% its peak value over 200 ms. A second stage of evaporation occurs with the microwave sweeping from 1774 MHz to 1773.2 MHz over 1 s. Halfway through this magnetic evaporation stage, the optical dipole trap (ODT) at 1064 nm is linearly ramped up from zero. The final decompression occurs over 200 ms, after which approximately 80% of atoms are transferred into the ODT.

The ODT is generated by two crossed lasers in the x-y plane (Nufern NuAmp 40W and IPG YLR-300-LP). The Nufern is seeded by 95 mW of light provided by a Mephisto S. Optical trapping enables us to change both atomic species into a lower-energy, high-field seeking state that would be antitrapped by the magnetic quadrupole. When the ODT reaches its maximum intensity, we apply a 60 Hz retrigger to synchronize all hardware. Then we adiabatically spinflip the Na from the $|F = 2, m_F = 2\rangle \rightarrow |1, 1\rangle$ state over 20 ms using the Landau-Zener approach, by applying a stationary microwave pulse at 1781.14 MHz and ramping an x bias field through the resonance. A short optical pulse removes leftover $|2, 2\rangle$ atoms. Immediately thereafter, we spinflip the K from $|9/2, 9/2\rangle \rightarrow |9/2, -9/2\rangle$ using a programmable waveform generator to ouput a linear sweep from 1.56 - 1.36 MHz over 50 ms. The two resultant spin states are the lowest states in their respective hyperfine manifolds, and at microkelvin temperatures, a two-body collision is energetically forbidden to populate any other final state, thus ensuring favorable evaporation given adequate collision rates.

Both ODT intensities are decreased over 8 s in the final evaporation. We found

that exponential ramps (with decay time constant of 1.5 s) empirically gave the highest phase space density after evaporation.

The Bose polaron experiment starts with an ultracold gas of fermionic ^{40}K atoms immersed in a BEC of ^{23}Na [184] at a temperature of $T \approx 130\,\mathrm{nK}$. Both species are trapped in an optical dipole trap as ellipsoidal atom clouds in their respective hyperfine ground states ($|F=1, m_F=1\rangle$ for ^{23}Na and $|9/2, -9/2\rangle \equiv |\downarrow\rangle$ for ^{40}K). Peak boson and fermion densities are $n_{\mathrm{Na}} = 6 \times 10^{13}\,\mathrm{cm}^{-3}$ and $n_{\mathrm{K}} = 2 \times 10^{11}\,\mathrm{cm}^{-3}$, corresponding to an impurity concentration of 0.3%. The BEC is weakly interacting, with an interboson scattering length of $a_{\mathrm{BB}} = 52\,a_0$ [230].

To create strongly-coupled Bose polarons in their attractive ground state, we ramp the magnetic field close to an interspecies Feshbach resonance [184] (see Appendix A), where impurities in the $|\downarrow\rangle$ state are strongly attracted to the sodium atoms with a peak interaction strength of $(k_n a)^{-1} = -0.3$. Here, $k_n = (6\pi^2 n_{\mathrm{Na}})^{1/3} = (1300\,a_0)^{-1}$ is the inverse interboson distance, a is the interspecies scattering length, and a_0 is the Bohr radius. For these near-resonant interactions, the thermal equilibration time set by two-body collisions is near its unitarity-limited value of $\hbar/E_n \approx 4\,\mu\mathrm{s}$, three orders of magnitude faster than the lifetime of the gas mixture in this regime, limited by three-body losses to about 4 ms. Here, $E_n = \hbar^2 k_n^2 / 4m_{\mathrm{r}}$ is the degeneracy energy scale, and $m_{\mathrm{r}} = m_{\mathrm{K}} m_{\mathrm{Na}}/(m_{\mathrm{K}} + m_{\mathrm{Na}})$ is the reduced mass of the impurity-boson scattering problem. By preparing the strongly interacting system within 2 ms, we can study Bose polarons in equilibrium before losses become significant. Fig. 3-8A depicts the experimental setup.

3.4.2 Rf ejection spectroscopy on Bose polaron impurities

At the chosen magnetic field, impurities in the $|\downarrow\rangle$ state are strongly interacting with the condensate, whereas they are non-interacting in the hyperfine state $|\uparrow\rangle$. This provides us with the ideal conditions to perform rf ejection spectroscopy, whereby an rf pulse transfers impurities from the interacting $|\downarrow\rangle$ state into the non-interacting $|\uparrow\rangle$ state. We employ an rf pulse of Gaussian envelope (see Fig. 3-7) with a full-width-half-maximum resolution of 6 kHz and measure the fraction of impurities $I(\omega)$

transferred into the $|\uparrow\rangle$ state.

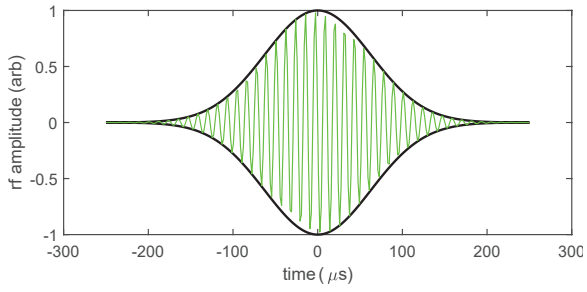

Figure 3-7: Illustration of rf pulse applied for ejection spectroscopy. Rf is applied near 24.5 MHz (not shown to scale in the green trace). The pulse has a Gaussian envelope giving a peak Rabi frequency of Ω_P ($=11.0$ kHz on the bare impurities at 93.2 G) with a standard deviation σ of 62.5μs: $\Omega_R(t) = \Omega_P e^{-t^2/2\sigma^2}$. The pulse is truncated to 500 μs total duration.

Figure 3-8 displays the locally-resolved rf spectrum of strongly-coupled Bose polarons. As shown in Figure 3-8D, the rf transfer $I(\omega)$ is strongly spatially dependent, and its maximum is shifted furthest from the bare atomic resonance for impurities deep inside the BEC (Fig. 3-8B). Here, the rf photon must supply a significant additional amount of energy to transfer the bound impurity into the non-interacting state. The central peak shift in Fig. 3-8C corresponds to an energy shift of $h{\cdot}32\,\mathrm{kHz} = 0.82\,E_n$, indicating an impurity energy that is unitarity-limited, given by the degeneracy energy scale E_n. For comparison, the mean-field energy experienced by bosons in the BEC is only $\approx h{\times}0.8\,\mathrm{kHz}$. In addition to the strong shift, we also observe long tails at higher frequencies in the rf transfer, a tell-tale sign of contact interactions [21, 194, 31]. Quantifying these contact interactions will be discussed in Sec. 3.6.1.

Comparison to *injection* spectroscopy

We benchmark our rf ejection spectra with the injection technique. As we will demonstrate in the following, the two techniques lead to different spectral responses: the former method excites the impurity into a continuum of states while the latter probes the impurity's ground state.

We compare the two methods at an interaction strength of $-3900\,a_0$, as shown in Fig. 3-9. The ejection spectrum, in blue, is identical to the spectrum shown in Figure 3-8(D), taking only the contribution from the central axial position. The injection method is performed with all other parameters (*i.e.* density, rf pulse profile)

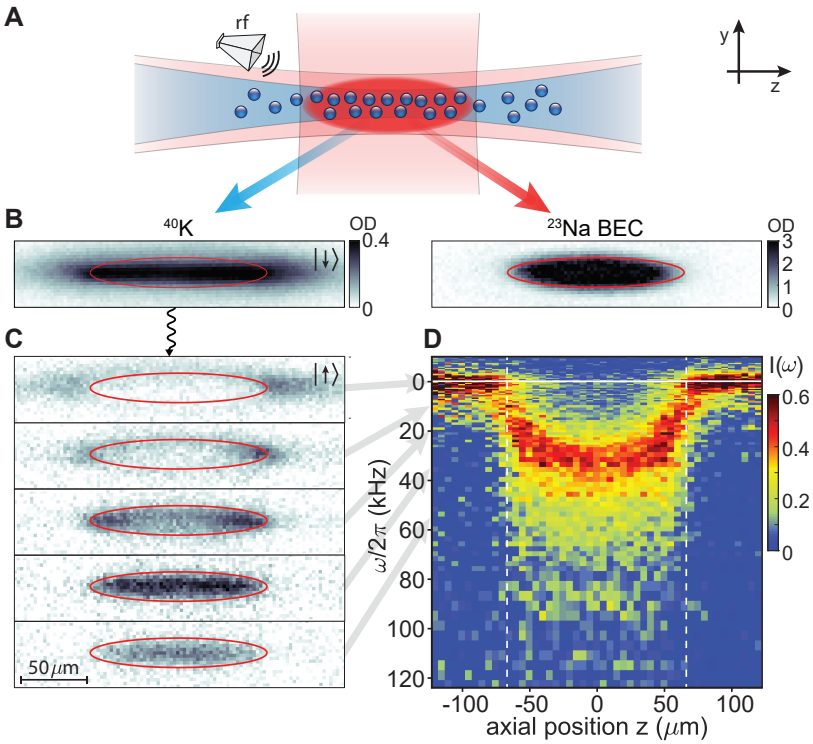

Figure 3-8: **Locally-resolved radiofrequency (rf) ejection spectroscopy of strongly-coupled Bose polarons**. Shown are the data for a peak interaction strength of $(k_n a)^{-1} = -0.3$. **(A)** Illustration of impurities (blue) immersed in a Bose-Einstein condensate (red), both trapped in a dual-color optical dipole trap. **(B)** *In-situ* column densities of ^{40}K impurities in the strongly-interacting spin state $|\downarrow\rangle$ (left) immersed in a ^{23}Na BEC (right), where the red ellipses mark the BEC's Thomas-Fermi boundary. **(C)** Impurities transferred into the non-interacting $|\uparrow\rangle$ state at various rf frequencies, as indicated by the arrows. **(D)** Local rf transfer $I(\omega)$ of the impurity column density as a function of axial position. The dashed vertical lines mark the condensate's axial Thomas-Fermi radius and the solid horizontal line at $\omega/2\pi = 0\,$kHz denotes the bare atomic transition. Figure reproduced from [247].

held constant compared to the ejection scenario. As shown in Fig. 3-9(B), in the injection protocol, the maximum transfer of population occurs at a normalized energy of $0.2\,E_n$, much lower compared to the measured energy shift of $0.8\,E_n$ obtained from ejection spectroscopy. Thus, assigning the spectral peak of $0.2\,E_n$ as the polaron binding energy would be a significant under-prediction. It is the onset and not the peak of the injection spectrum that encodes any meaning for the ground state polaron energy E_p [246, 9]. Moreover, only the ejection method can recover additional equilibrium quantities of the Bose polaron, including its lifetime and short-range correlations, as the injection spectrum convolves the spectral response of a continuum

of excited polaron states [9].

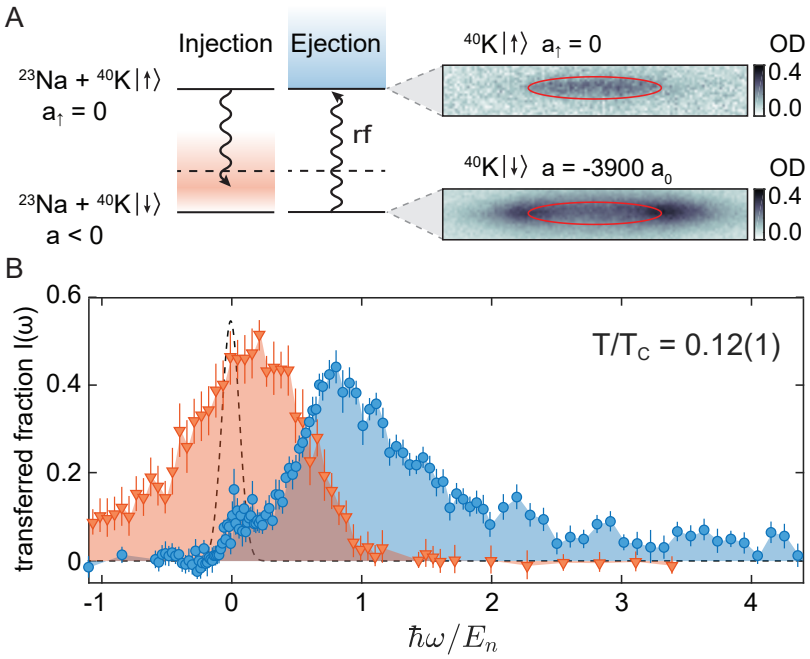

Figure 3-9: **Spectral response of ^{40}K impurities using ejection and injection spectroscopy. (A)** The energy levels of the many-body system (left). The dashed lines denote the impurity's hyperfine energies and the solid lines denote the ground state polaron energies. In the ejection technique, the polaron ground state is prepared and ejected out (pictured on the bottom right as an absorption image of K in $|\downarrow\rangle$) via an rf drive to the non-interacting state $|\uparrow\rangle$ (pictured on the top right.) The BEC's Thomas-Fermi radius is marked by the red line. **(B)** A comparison of the injection and ejection lineshapes at $a = -3900\ a_0$, in red and blue respectively, with peak interaction strength $(k_n a)^{-1} = -0.3$. The transfer from the initial to the final spin state is shown as a function of normalized rf frequency. The dotted black line shows the Gaussian response of the bare impurity state. Figure reproduced from [247].

3.4.3 Local analysis of boson density and reduced temperature

The following section details how the local boson density and T/T_c were derived from images of the condensate. We interpret the spatially-resolved spectrum under the assumption of the local density approximation (LDA) [133], giving access to the rf spectrum of the impurity as a function of the condensate's local chemical potential $\mu(z) = \mu_0 - V_{\mathrm{Na}}(z)$ (see Sec. 3.4.3). Here, $\mu_0 = 4\pi\hbar^2 a_{\mathrm{BB}} n_{\mathrm{Na}}/m_{\mathrm{Na}}$ is the condensate's

chemical potential at its peak density, and $V_{\mathrm{Na}}(z)$ is the radially-centered trapping potential along the axial direction. The *in-situ* local boson density $n_{\mathrm{Na}}(\mathbf{r})$ – the sum of the condensate density $n_c(\mathbf{r})$ and the thermal density $n_t(\mathbf{r})$ – has the following form under LDA and the Thomas-Fermi limit [170]:

$$n_c(\mathbf{r}) = \frac{15N_c}{8\pi R_x R_y R_z} \max\left(1 - \frac{x^2}{R_x^2} - \frac{y^2}{R_y^2} - \frac{z^2}{R_z^2}, 0\right) \tag{3.11}$$

$$n_t(\mathbf{r}) = \frac{1}{\lambda_{\mathrm{dB}}^3} g_{3/2}\left(\exp\big(-\beta\big|\mu_0 - \frac{1}{2}m_{\mathrm{Na}} \sum_{i=x,y,z} \omega_i^2 r_i^2\big|\big)\right) \tag{3.12}$$

where $\lambda_{\mathrm{dB}} = \sqrt{2\pi\hbar^2/m_{\mathrm{Na}}k_{\mathrm{B}}T}$ is the thermal de Broglie wavelength, g the Polylogarithm function, $\beta \equiv 1/k_{\mathrm{B}}T$, and μ_0 the peak boson chemical potential. R_i is the Thomas-Fermi radius along the ith coordinate, defined by $\mu_0 = m\omega_i^2 R_i^2/2$. The condensate number is $N_c = \frac{8\pi}{15g_{\mathrm{BB}}}\mu_0 R_x R_y R_z$, where $g_{\mathrm{BB}} = 4\pi\hbar^2 a_{\mathrm{BB}}/m_{\mathrm{Na}}$ is the boson-boson coupling constant. The condensate is assumed to only experience mean-field repulsion, while the thermal atoms are an ideal gas confined in the external harmonic trap and the mean-field repulsion of the condensate [170]. Experimental values of μ_0 are derived from the speed of the BEC's hydrodynamic expansion after releasing the cloud in time-of-flight [62]. Temperature is also measured in time-of-flight by fitting the outer wings to the thermal density distribution. From the local density, we compute the local critical temperature T_{C}, where

$$k_{\mathrm{B}}T_{\mathrm{C}}(\mathbf{r}) = \frac{3.31\hbar^2}{m_{\mathrm{Na}}} n_{\mathrm{Na}}(\mathbf{r})^{2/3}\,. \tag{3.13}$$

3.5 Measurements of energy and quasiparticle lifetime

We now analyze the main results of the rf spectroscopy study: the Bose polaron's energy and inverse lifetime.

Fig.3-10A shows the rf spectrum as a function of $\beta\mu(z)$, the chemical potential

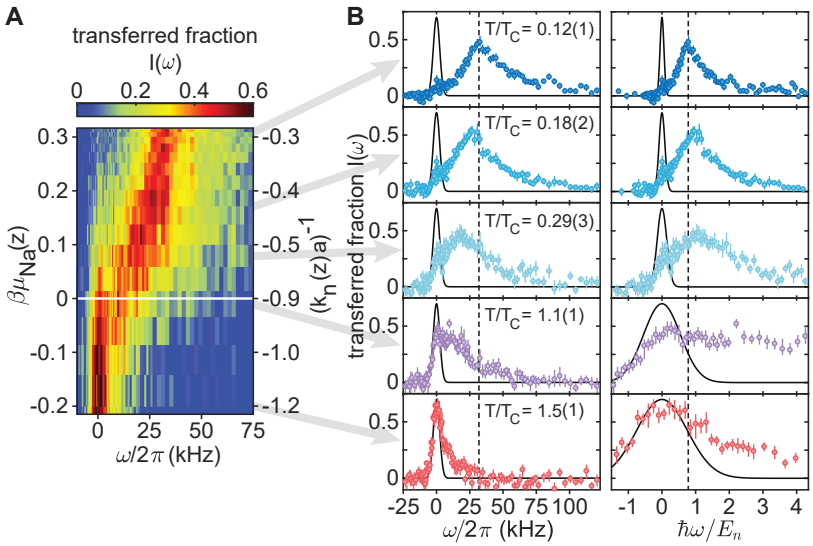

Figure 3-10: **Rf ejection spectra of Bose polarons at various reduced temperatures** T/T_{C}. The peak interaction strength is $(k_n a)^{-1} = -0.3$. **(A)** Color density map of the rf transfer $I(\omega)$ as a function of the normalized local chemical potential $\beta\mu(z)$ and the local interaction strength $(k_n a)^{-1}$. The solid white line marks the BEC phase transition at $\beta\mu = 0$. **(B)** Fraction of impurities transferred into the non-interacting state $|\uparrow\rangle$ as a function of rf frequency (left) and of normalized frequency, $\hbar\omega/E_n$ (right). The dashed black line marks the peak transfer location of the impurities at the lowest T/T_{C}. The solid black lines show the rf spectrum of bare ^{40}K atoms, indicating the spectral resolution. Error bars reflect 1σ statistical uncertainty. Figure reproduced from [247].

normalized by $\beta = 1/k_{\mathrm{B}}T$. The interaction parameter $(k_n a)^{-1}$ also varies with the local density $n_{\mathrm{Na}}(z)$ as indicated. A strong shift of the rf transfer for positive chemical potentials is clearly visible. Fig.3-10B shows a selection of spectra, indicating the temperature T normalized by the local critical temperature $T_{\mathrm{C}}(z)$ for a homogeneous gas. The absolute frequency of the spectral peak continuously decreases with higher reduced temperatures (left panel). However, when normalized by the degeneracy energy scale E_n, the spectral peak frequency in fact increases with temperature, indicating a more strongly-bound impurity with increasing temperatures up to the critical temperature T_{C} (right panel).

To ensure that our polaron peak and width assignations were not affected by the possible nonlinear response of $I(\omega)$, we measured the spectra at $a = -3900\ a_0$ with varying pulse powers, shown in Fig. 3-11 as color density plots of local impurity transfer. Under the LDA, the spectra at the lowest reduced temperatures were extracted

and their lineshapes were compared to one another in Fig. 3-12. There, the heights of the two lower-power spectra have been scaled by constant factors. Neither the peak position nor the width was affected beyond the experimental signal-to-noise limitations, giving us confidence that the extracted energy and linewidth were not affected by the nonlinear response.

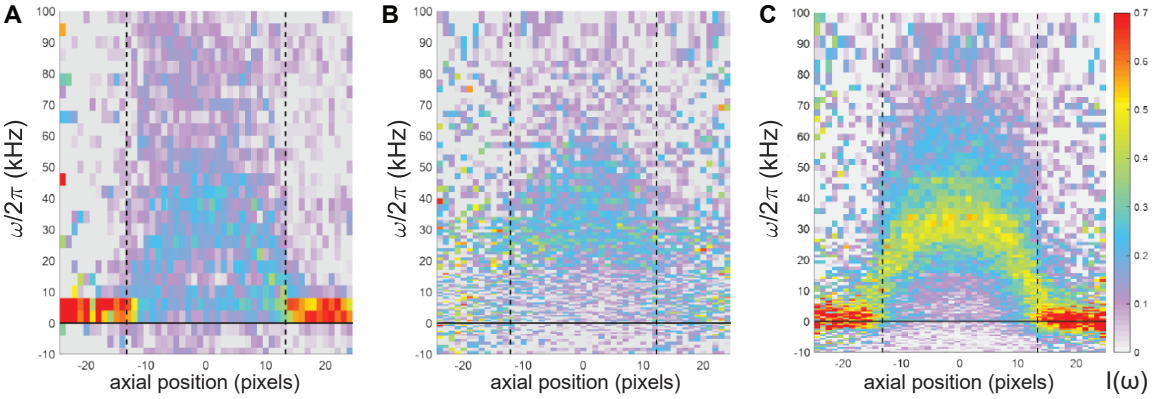

Figure 3-11: Ejection spectra at $a = -3900\,a_0$ obtained with Gaussian pulses of varying peak powers, corresponding to (**A**) π, (**B**) 2π, and (**C**) 3π transfer of the bare impurities from the $|\downarrow\rangle$ to the $|\uparrow\rangle$ state. Vertical dashed lines indicate the BEC Thomas-Fermi boundary.

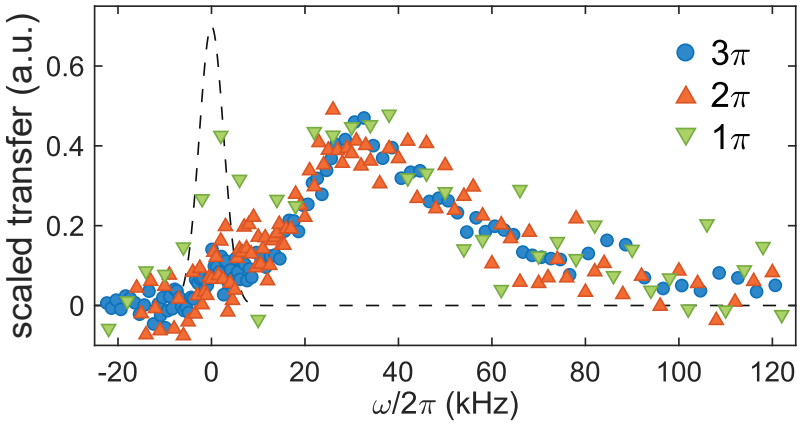

Figure 3-12: Lineshape versus rf power, testing the effect of possible nonlinear response in our spectra. Rf spectra at $a = -3900\,a_0$ and $T/T_C \approx 0.1$ are shown, obtained from considering the central six pixels of the axial positions shown in Fig. 3-11. The three powers are represented by green downward-facing triangles, red upward-facing triangles, and blue circles, respectively. The heights of the π- and 2π- spectra have been scaled by constant factors to compare to the 3π lineshape. Figure reproduced from [247].

Bose polaron binding energy

The extracted quantities E_p are summarized in Fig.3-13A, in which the peak frequency shift ω_p is interpreted as the ground-state energy $E_p = -\hbar\omega_p$ of the Bose polaron. We observe a decrease of E_p as a function of reduced temperature for the strong-coupling impurity, for temperatures up to the BEC critical temperature. Stronger binding of the impurity to the bosonic bath with increasing temperature has been predicted [111]. Additionally, a broadening of the spectral function underlying the rf spectrum may contribute to the observed shift [245].

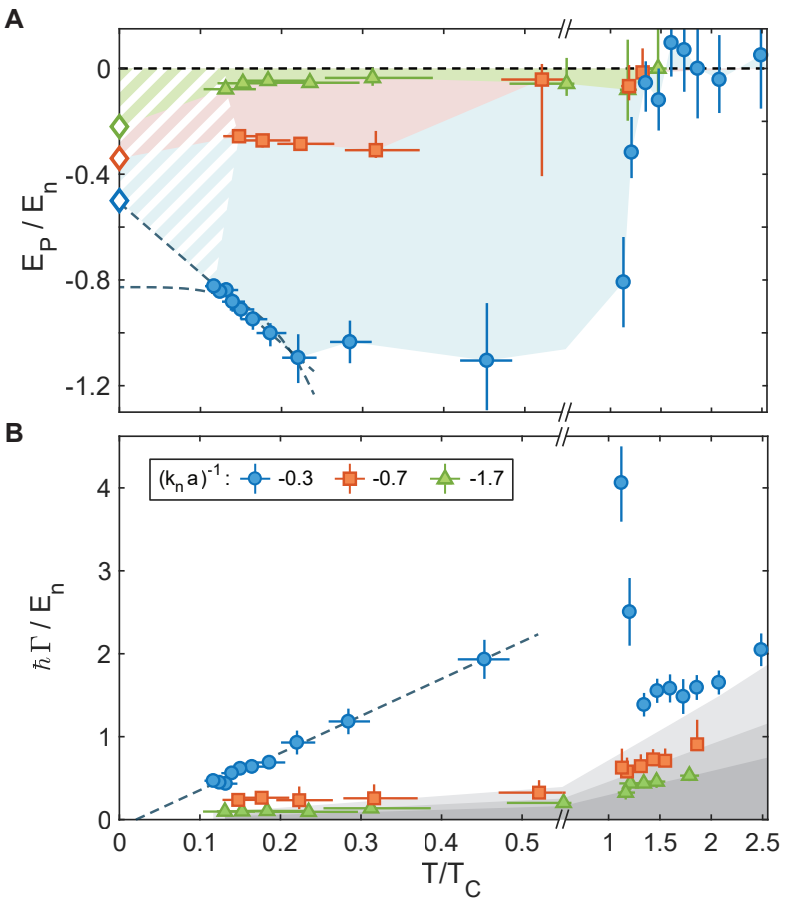

Figure 3-13: **Evolution of the Bose polaron as a function of the local reduced temperature** T/T_{C}. Shown are the data for various peak interaction strengths $(k_n a)^{-1}$. **(A)** Energy of the Bose polaron. The shaded areas are a guide to the eye and the blue dashed lines represent linear and quartic extrapolations to zero temperature. The prediction of the lowest-order T-matrix calculation is represented by open diamonds at $T = 0$. **(B)** The inverse lifetime of the Bose polaron, represented by the half-width at half-maximum (Γ) of the local rf spectra. The grey shaded areas indicate the spectral resolutions of the corresponding rf pulses. The dashed line is a linear fit to the data below T_{C}. Figure reproduced from [247].

Above T_{C} the peak energy shift suddenly jumps to zero, despite the near-unitarity-limited interactions. This behavior is expected when the temperature exceeds the energy difference between the attractive and repulsive branches of the resonantly interacting impurity, which occurs near the onset of quantum degeneracy [120, 88]. A similar jump in binding energy was recently observed for an impurity resonantly interacting with a nearly degenerate Fermi gas [245]. At weaker attractive interaction, we observe that the Bose polaron is less strongly bound to the bath, as expected [198,

152] (see Fig.3-13A).

In the strongly interacting regime where $|k_n a| \gg 1$, our measurements probe a regime where the binding energy is much larger than the condensate's local mean-field energy. In this regime, a universal description for the Bose polaron at low temperatures emerges from a lowest order T-matrix and an equivalent variational approach [198, 152]. See Appendix D for a detailed calculation. Here, the impurity acquires an energy shift that is the sum of the individual and uncorrelated shifts from each host boson:

$$E_p \equiv -\frac{\hbar^2 \kappa^2}{2m_r} = -\frac{2\pi\hbar^2 n_{\mathrm{Na}}}{m_r} f(i\kappa) \tag{3.14}$$

where $f(i\kappa) = -\frac{a}{1-\kappa a}$ is the two-body scattering amplitude evaluated at imaginary momentum $i\kappa$, as appropriate for a bound state. The equation implicitly gives E_p, whose natural energy scale is confirmed as the degeneracy energy scale E_n for an effective particle of reduced mass m_r and density n_{Na}. In this scenario, E_p/E_n is a universal function of $(k_n a)^{-1}$ only. For weak attractive impurity-boson interactions ($(k_n a)^{-1} \ll -1$) one finds the mean-field result $E_p = 2\pi\hbar^2 n_{\mathrm{Na}} a/m_r$, whereas on the molecular side of the Feshbach resonance in the limit $(k_n a)^{-1} \gg 1$, the polaron energy becomes equal to the energy of a two-body molecule of size a, $E_p = -\frac{\hbar^2}{2m_r a^2}$. On resonance, the approach yields $E_p/E_n = -0.71$, which is similar to the result for the unitary Fermi polaron, $E_p/E_n = -0.61$ [53, 58]. The Bose polaron is more strongly bound than its fermionic counterpart owing to the lack of constraints imposed by Pauli exclusion (see Appendix D). The polaron energies according to the T-matrix approach for $T = 0$ are indicated as open diamonds in Fig. 3-13A. A linear extrapolation to zero temperature of our strong-coupling binding energy data appears to agree well with this theory. Alternatively, assuming the increase in binding strength with temperature results from coupling to the BEC's finite temperature phonon bath, one may attempt a T^4 fit to the data [150]. However, this quartic scaling is only predicted to hold at much lower temperatures and weaker interactions than our observed strong-coupling results. Both the linear and quartic extrapolations exclude a simple mean-field prediction that yields $E_p/E_n = -1.4$ for $(k_n a)^{-1} = -0.3$.

Quasiparticle lifetime

The binding energy alone does not reveal whether the impurities in the bosonic bath form well-defined quasiparticles. This requires knowledge of the impurities' spectral width, a measure of the quasiparticle's decay rate [207, 245, 256, 209]. Generally, the width of an rf spectrum corresponds to the rate at which the coherent evolution of an atomic spin is interrupted during the rf pulse. For quasiparticles, it is momentum-changing collisions with host bosons that cause such decoherence, the same process that limits the quasiparticle's lifetime. The rf spectral width thus directly measures the inverse lifetime of the quasiparticles [207, 245, 256, 209].

Fig. 3-13B shows that the strong-coupling impurity's spectral width follows a linear dependence with temperature, and strikingly at the Planckian scale: $\Gamma = 8.1(5)\, k_{\mathrm{B}}T/\hbar$. Observing decay rates at this scale is consistent with quantum critical behavior [203]. The observed linear trend suggests a well-defined quasiparticle with vanishing spectral width in the limit of zero temperature. However, near T_{C}, the rf spectral width increases significantly beyond the measured binding energy E_p, signaling a breakdown of the quasiparticle picture.

We attribute both the linear temperature dependence at the Planck scale $k_{\mathrm{B}}T/\hbar$ and the quasiparticle breakdown to the proximity of the Bose-Fermi mixture's quantum multi-critical points [157]: the impurity gas is close to the quantum phase transition between the vacuum of impurities, $n_K = 0$, and the phase at non-zero impurity density, $n_K > 0$; interactions are tuned near the resonant point $(k_n a)^{-1} \to 0$; and the host boson gas traverses its own quantum critical regime near the onset of quantum degeneracy at $\mu_{\mathrm{B}} \to 0$. Here, only one relevant energy scale remains $(k_{\mathrm{B}}T \approx k_{\mathrm{B}}T_{\mathrm{C}} \approx 0.55\, E_n)$, because Efimov trimers are not expected to enter in the description of our system at quantum criticality, as their size is predicted to be orders of magnitude larger than the interparticle spacing at our densities. Thus, the spectral width also scales as $E_n/\hbar$ and no quasiparticles are predicted to persist [177, 203].

In this regime, the impurities have the shortest mean-free path possible with contact interactions, *i.e.*, one interboson distance. For all temperatures $T < T_{\mathrm{C}}$, the scattering rate at the Planckian scale naturally emerges, assuming polarons scatter

with thermal excitations of the saturated Bose gas, at density $n_{\rm th} \sim 1/\lambda_{\rm B}^3$. Given a unitarity-limited scattering cross section $\sigma_{\rm coll} \sim \lambda_{\rm rel}^2$ and the most probable relative scattering speed $v_{\rm rel} \propto \sqrt{\frac{k_{\rm B}T}{m_r}}$, we derive a rate

$$\Gamma = n_{\rm th}\, \sigma_{\rm coll}\, v_{\rm rel} \sim (m_{\rm B}/m_r)^{3/2}\, k_{\rm B}T/\hbar \tag{3.15}$$

Here, $\lambda_{B/\rm rel}$ are the thermal de Broglie wavelengths at the boson and the reduced mass, respectively. At weaker interaction strengths where $\sigma_{\rm coll} \sim a^2$, the above relation for Γ yields a non-universal rate $\Gamma \propto a^2T^2$ [150]. Experimentally, the spectral width drops rapidly for the weaker interaction strengths probed here, down to our resolution limit, prohibiting us from discerning the scaling with temperature (see Fig. 3-13B).

To conclude this section, we have performed the first measurement of the equilibrium Bose polaron's binding energy and decay rate. Below the superfluid critical temperature, the inverse lifetimes increase linearly with temperature at the so-called *Planckian* scale, consistent with quantum critical behavior. Close to the T_c, the spectral width exceeds the impurity's binding energy, indicating the failure of the quasiparticle picture.

3.6 Short-range correlations of the Bose polaron

The following section discusses the Bose polaron's *contact*, which quantifies the short-range correlations of the system. We derive the relation between impurity transfer and contact, and we present our experimental measurements of Bose polaron contact.

3.6.1 Contact

The behavior of two distinguishable particles that interact with an s-wave scattering length is set by universal relations that are general to any state of the system. These relations are quantified by a parameter called the *contact*, which controls the thermodynamics of the system as well as large-momentum, high-frequency portions

of correlation functions [225, 226, 30, 29]. In the impurity limit, the physical picture of contact tells us the density enhancement of bath atoms around a single impurity.

The extensive contact obeys the universal relation

$$C = \lim_{k\to\infty} n(k)k^4 \tag{3.16}$$

where k is the wavevector.

We first note the relation between extensive C and intensive contact $C(\mathbf{R})$, where $\mathbf{R}$ is the interparticle separation.

$$C = \int d^3\mathbf{R} C(\mathbf{R}) \tag{3.17}$$

Tan showed that the intensive contact is related to the pairwise density correlator between a two-component Fermi gas with scattering length a [225]. The result also holds for a Bose-Fermi mixture with scattering length a and densities $n_\mathrm{B}, n_\mathrm{F}$. For any small distance r, the correlation between the two states' number densities diverges as $1/r^2$ with a coefficient proportional to the contact:

$$\langle n_\mathrm{B}(\mathbf{R}+\mathbf{r}/2)\, n_\mathrm{F}(\mathbf{R}-\mathbf{r}/2)\rangle = \frac{C(\mathbf{R})}{16\pi^2}\left(\frac{1}{r^2} - \frac{2}{ar}\right) \tag{3.18}$$

For a single fermion impurity, replace n_F with a Dirac Delta function. Then, integrate both sides of equation 3.18 over all space. The right-hand-side intensive contact becomes the extensive contact.

$$\langle \int d^3\mathbf{R}\, n_\mathrm{B}(\mathbf{R}+\mathbf{r}/2)\delta(\mathbf{R}-\mathbf{r}/2)\rangle = \frac{C}{16\pi^2}\left(\frac{1}{r^2} - \frac{2}{ar}\right) \tag{3.19}$$

Upon changing variables $\mathbf{R} \to \mathbf{R} - \mathbf{r}/2$, we have

$$\langle n_\mathrm{B}(\mathbf{r})\rangle = \frac{C}{16\pi^2}\left(\frac{1}{r^2} - \frac{2}{ar}\right) \tag{3.20}$$

This is the expected boson density in a shell of distance r away from the impurity. To find the expected number of bosons within a distance b around the impurity,

integrate again.

$$\int_0^b 4\pi r^2 dr \, \langle n_{\mathrm{B}}(r) \rangle = \frac{C}{4\pi}(b - b^2/a) \tag{3.21}$$

At unitarity-limited scattering, the second term on the right-hand side drops out, leaving only $Cb/4\pi$.

Through the Hellmann-Feynman theorem, the contact is also equal to the change in energy with the inverse impurity-bath scattering length: $\frac{C}{k_n} = 2\pi \frac{d}{d(k_n a)^{-1}} \left(\frac{-E_p}{E_n} \right)$ [21, 194, 225, 257].

Relation to spectral response

Spectra obtained via rf ejection spectroscopy encode the wavefunction overlap between a interacting, dressed impurity and a non-interacting state. As such, they not only contain information about the binding energy and lifetime of the impurity, but also about the short-range correlations between the impurity and the surrounding medium. Indeed, the final state of an ejection spectrum at high rf frequencies is a free impurity with large momentum $\hbar k$. Hence, high frequencies in ejection spectroscopy probe the initial wavefunction at short distances [21, 194, 30, 257]. This leads to characteristic tails $\propto \omega^{-3/2}$ of the rf spectra, reflecting the two-body nature of the wavefunction at short distances, as we will now derive.

The extensive contact for the Bose polaron can be obtained from the spectral transfer ratio, $I = \frac{N_\uparrow}{N_\downarrow + N_\uparrow}$. The transfer rate in the limit of high frequencies is derived from Fermi's Golden Rule and Equation 3.16. We assume the rf drives the particle from the initial many-body state into a noninteracting final state $|\uparrow \mathbf{k}\rangle$ with wavevector $\mathbf{k}$. The driving operator is $\hat{V}(t) = \frac{\hbar}{2}\Omega_R(t) \sum_{\mathbf{k}} d^\dagger_{\mathbf{k}} c_{\mathbf{k}} + \text{c.c.}$, where $d^\dagger_{\mathbf{k}}$ creates an impurity in the noninteracting state and $c_{\mathbf{k}}$ annihilates the impurity in the initial, many-body state. We assume a sinusoidal drive whose amplitude (and thus Rabi freq) varies with time and make the rotating wave approximation. This drive transfers population out of the initial state $|\Psi_{MB}\rangle$ into a final state of two free particles

with kinetic energies $\epsilon_{k1}, \epsilon_{k2}$. Fermi's Golden Rule predicts the rate

$$\begin{aligned}
\lim_{\omega\to\infty}\Gamma(\omega,t) &= \lim_{\omega\to\infty}\frac{2\pi}{\hbar}\sum_{\mathbf{k}}|\langle\uparrow\mathbf{k}|\hat{V}|\Psi_{MB}\rangle|^2\delta(\hbar\omega-\epsilon_{k1}-\epsilon_{k2}) \\
&= \lim_{\omega\to\infty}\frac{2\pi}{\hbar}\left(\frac{\hbar\Omega_R(t)}{2}\right)^2\int\frac{dk^3}{(2\pi)^3}\,n(k)\delta(\hbar\omega-\epsilon_{k1}-\epsilon_{k2}) \\
&= \frac{\pi\hbar\Omega_R(t)^2}{2}\int\frac{4\pi k^2dk}{(2\pi)^3}\,\frac{C}{k^4}\delta(\hbar\omega-\hbar^2k^2/(2m_r)) \\
&= \frac{\Omega_R(t)^2}{8\pi}\sqrt{\frac{\hbar}{2m_r}}\frac{C}{\omega^{3/2}}
\end{aligned}$$

Here, m_r is reduced mass and C has units of inverse length and is the extensive contact from Section 3.6.1.

To derive rf lineshape in dimensionless units of transfer I, we assume linear response. To take an explicit example, our pulse has a Gaussian envelope with peak Rabi frequency of $\Omega_P = 11.0$ kHz and $T = 500\,\mu$s total duration with a standard deviation of 62.5μs: $\Omega_R(t) = \Omega_P e^{-t^2/2\sigma^2}$. We integrate $\Gamma(\omega,t)$ from $-T/2$ to $T/2$ to obtain the population transfer.

$$\begin{aligned}
I(\omega) &= \int_{-T/2}^{T/2}dt\,\frac{\Omega_R(t)^2}{8\pi}\sqrt{\frac{\hbar}{2m_r}}\frac{C}{\omega^{3/2}} \\
&= \frac{\Omega_P^2}{8\pi}\sqrt{\frac{\hbar}{2m_r}}\frac{C}{\omega^{3/2}}\int_{-T/2}^{T/2}dt\;e^{-t^2/\sigma^2} \\
&\approx \frac{\Omega_P^2}{8\pi}\sqrt{\frac{\hbar}{2m_r}}\frac{C}{\omega^{3/2}}\sqrt{\pi}\sigma
\end{aligned}$$

In the last step of the previous equation, we have approximated the integration limits to go to infinite time, which is a good approximation given our duration of 500μs compared to $\sigma = 62.5\mu$s (see Fig. 3-7 for an illustration of the applied rf pulse).

If we extract the contact prefactor, fitting I with a $\omega^{-3/2}$ slope, we will derive the

a constant A with units of $\mathrm{kHz}^{3/2}$.

$$I = \frac{\Omega_P^2}{8\pi}\sqrt{\frac{\hbar}{2m_r}}\frac{C}{(2\pi\nu)^{3/2}}\sqrt{\pi}\sigma = A\nu^{-3/2} \tag{3.22}$$

Therefore, when using only SI units, C can be obtained in units of inverse meters,

$$C = \frac{8\pi A(2\pi 1000)^{3/2}\sqrt{2m_r}}{\sqrt{\pi}\sigma\Omega_P^2\sqrt{\hbar}} \tag{3.23}$$

The contact can be normalized into the dimensionless quantity C/k_n.

In the case that the final state interaction is not zero, the transfer rate must be amended to include both the final state interaction a_f with the majority species, as well as the initial state interaction a_i [30].

$$\Gamma(\omega) = \frac{\Omega_R^2\sqrt{\hbar}(a_i^{-1} - a_f^{-1})^2}{8\pi\sqrt{2m_r}\omega^{3/2}(a_f^{-2} + 2m_r\omega/\hbar)}C \tag{3.24}$$

3.6.2 Linear response of the experiment

To obtain the contact from our observed spectral lineshape, we require the rf transfer to be in the linear response regime. Furthermore, the contact's relation to the spectral response (Eq. 3.22) is expected to only hold for the high momentum wings of the cloud, $\hbar\omega \gg E_n$. We extract the contact by fitting the high frequency tail of the ejection spectra where the transfer is well within the linear response regime (below 0.2) and the spectral response follows a $\omega^{-3/2}$ dependence within our signal to noise, as demonstrated in the main text. To confirm the that the response is within the linear response regime, we measure the transfer as a function of the rf pulse duration. We verify this linear behavior for various interaction strengths and Rabi frequencies and show one example in Fig. 3-14.

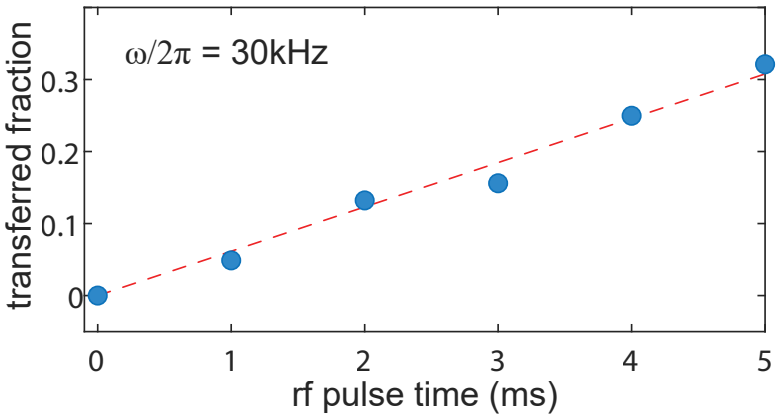

Figure 3-14: Time-resolved rf response of the impurity located at the trap center, a test of linear response for the contact measurements. The interaction strength is $a = -840\,a_0$, and a rf pulse with constant power is employed with varying duration at a detuning of $2\pi\times 30\,\mathrm{kHz}$ above the atomic resonance. The dashed line is a linear fit through the data. Figure reproduced from [247].

3.6.3 Experimental results

Here we present the experimental results of the Bose polaron's contact. As derived in Sec. 3.6.1 and Ref. [30], the high-frequency tail of the rf transfer $I(\omega)$ can be written:

$$I(\omega) \underset{\omega\to\infty}{=} \frac{\Omega_P^2\sigma}{8}\sqrt{\frac{\hbar}{2\pi m_\mathrm{r}}}\frac{C}{\omega^{3/2}} \tag{3.25}$$

where σ is the Gaussian $e^{-1/2}$ width of the rf pulse's duration and Ω_P the peak Rabi frequency. Our spectra follow this behavior closely: when multiplied by $\omega^{3/2}$, they asymptote to plateaus that yield the contact's value, shown for $(k_n a)^{-1} = -1$ in Fig. 3-15A and $(k_n a)^{-1} = -0.3$ in Fig. 3-15B, respectively. Fig. 3-15 C summarizes our measurements of the contact, normalized by k_n, as a function of T/T_C for various interaction strengths. From weak to strong attractive interactions, the contact increases monotonically. For the strongest interaction strength the normalized contact remains approximately constant for all values $T/T_\mathrm{C} < 1$. An abrupt drop of the normalized contact is seen above the BEC transition temperature, though it remains non-zero. This is expected for a Boltzmann gas with unitarity-limited interactions that has a non-zero contact given by the inverse mean-free path, $n\sigma_\mathrm{coll} \propto 1/T$, where σ_coll is the

two-body cross section. Therefore C/k_n decreases as T_{C}/T in the non-degenerate regime [88, 245].

The low-temperature value of the normalized contact is close to what one finds for the unitary Fermi polaron ($C/k_n = 4.3$ [245]), the balanced unitary Fermi gas [153, 168, 46], and the near-unitary BEC [238]. Using the variational ansatz for the Bose polaron's energy (see Eq. 3.14), we obtain an expression for the normalized contact:

$$\frac{C}{k_n} = \pi^2 \frac{E_p/E_n}{E_n/E_p - \frac{\pi}{4}\frac{1}{k_n a}} \tag{3.26}$$

which yields $\frac{C}{k_n} = \pi^2 \left(\frac{E_p}{E_n}\right)^2 = 5.0$ on resonance. The contact can also be interpreted in an intuitive picture [225]: it gives the number of bosons $n_{\mathrm{B}}(s)$ within a sphere of radius s around the impurity: $n_{\mathrm{B}}(s) = Cs/4\pi$ for $s \ll n_{\mathrm{Na}}^{-1/3}$ and $s \ll |a|$, as derived in Sec. 3.6.1. The measured near-unity value of $C/4\pi$ in units of the interboson spacing thus indicates that even for near-unitarity-limited interactions – on average – only about one extra boson is in close proximity to the impurity. In this respect, the resonant Bose polaron shares traits with a molecular dimer of a size given by the interboson distance. Within the variational description, the localized part of the polaron's wavefunction is of identical form to that of a molecule, and away from resonance where $a > 0$, the polaron smoothly evolves into a molecule of size a [198, 152].

3.7 Summary and outlook

In conclusion, we have created Bose polarons near quantum criticality by immersing atomic impurities in a Bose-Einstein condensate with near-resonant interactions. Using locally-resolved radiofrequency spectroscopy, we probed the energy, spectral width, and short-range correlations of the impurities as a function of temperature. We found that the impurities formed well-defined quasiparticles with low decay rates far below the BEC critical temperature. However, their inverse lifetime, given by their spectral width, increased linearly with temperature at the Planckian scale $k_{\mathrm{B}}T/\hbar$, a

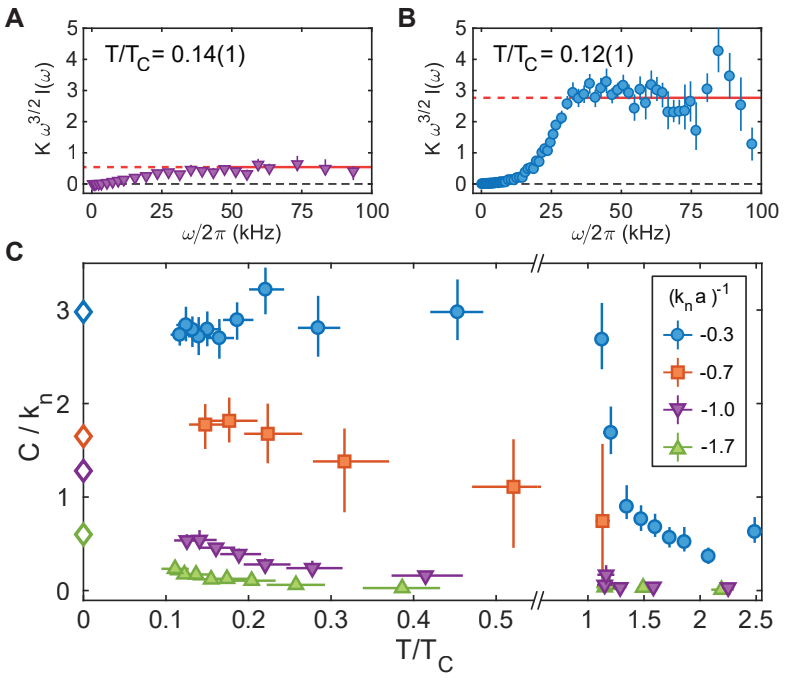

Figure 3-15: **Contact of the Bose polaron.** The low temperature rf transfer for **(A)** $(k_n a)^{-1} = -1$ and **(B)** $(k_n a)^{-1} = -0.3$ multiplied by $K\omega^{3/2}$, with $K = \frac{8\sqrt{2\pi m_r}}{\Omega_P^2 \sigma \sqrt{\hbar}} \frac{1}{k_n}$, displays a plateau that yields the normalized contact C/k_n. The contact is obtained from fits in the frequency region indicated by the solid red line. **(C)** The contact, normalized by k_n, as a function of the reduced temperature at various interaction strengths. The open diamonds at $T = 0$ are the T-matrix predictions from Eq. 3.26. Figure reproduced from [247].

hallmark of quantum critical behavior. Close to the BEC critical temperature, the spectral width exceeded the binding energy of the impurities, signaling a breakdown of the quasiparticle picture. This is in striking analogy to the strange metal phase of the cuprate superconductors [146].

For future studies, it will be interesting to probe transport properties of the impurities and specifically investigate whether their resistivity scales linearly with temperature, in even closer analogy to findings in the strange metal phase. Furthermore, increasing the impurity concentration might allow the formation of bipolarons [42] and the observation of phonon-induced superfluidity [81, 134].

Chapter 4

Collective excitations of a Bose-Fermi mixture

This chapter will discuss the observation of hydrodynamic flow of ultracold, spin-polarized fermions induced by interactions with a Bose-Einstein condensate. The theory of hydrodynamics has successfully described the collective behavior of diverse fluids, from classical liquids to strongly-interacting quantum matter. Its central premise is the notion of local equilibrium, whereby frequent interparticle collisions allow a macroscopic description of collective behavior, on a scale far above typical interparticle distances. By contrast, collisionless or ballistic flow occurs when interparticle scattering is too infrequent to establish local equilibrium. The precise control over interactions in ultracold quantum gases make these systems an ideal test environment to study the transition between the collisionless to hydrodynamic regime, which has been theorized to play an important role for electron transport in strongly-interacting systems [219, 116, 5].

First, I will define the two opposing regimes that define collective motion in many-body systems. I provide background on realizations of both collisionless and hydrodynamic flow, in solid state and cold atom systems.

Focusing on ultracold atomic systems, I will introduce a commonly-used probe to study excitations: collective oscillations. Collective oscillations reveal the low-lying excitations of the ground state, extracting properties such as the equilibrium equation

of state, collisional relaxation rates, and transport coefficients. Oscillation frequencies are measured after perturbations of the trapping potential. These frequencies depend on the interparticle interactions, and for a single-species gas with contact interactions, have known analytical forms in the limit of small perturbations. These solutions will be discussed for the collisionless and hydrodynamic regimes. The spectrum of a weakly-interacting BEC will be derived for the trapping geometry used in our MIT experiment, as a crucial background to interpreting our fermionic oscillation measurements.

As the main result of this chapter, I describe how we implemented and detected hydrodynamic flow in spin-polarized ultracold fermionic ^{40}K. By themselves, the fermions are collisionless. Immersed in a ^{23}Na BEC background, these fermions cross over to the hydrodynamic regime when Bose-Fermi interactions are raised, giving the fermions the chance to scatter frequently with the bosons. They then inherit the modes of the BEC, which obeys superfluid hydrodynamics.

As an outlook, in Section 4.4, I discuss the observation of a novel nonlinear excitation in a Bose-Fermi mixture: Faraday resonances.

The research described in this chapter is the result of unpublished work by Zoe Z. Yan, Yiqi Ni, Alex Chuang, Carsten Robens, and Martin Zwierlein.

4.1 Hydrodynamic versus collisionless regimes

The framework of hydrodynamic flow constitutes one of the most successful descriptions of interacting materials. A fluid's collective motion can be described in this framework as long as the microscopic degrees of freedom remain in local thermal equilibrium through frequent interparticle collisions. Ultracold atomic gases obey hydrodynamics if the two-particle collision rate exceeds the frequency at which excitations propagate in the system. The mean free path quantifies the effect of collisions as the average distance a moving particle travels before colliding with another particle:

$$l_{\mathrm{mf}} = \frac{1}{n\sigma} \tag{4.1}$$

where n is the particle density and σ is the total scattering cross section. When l_{mf} is much shorter than the system size, local thermal equilibrium is established. The hydrodynamic condition also requires the collisional relaxation timescale $\tau \sim 1/n\sigma\bar{v}$ to be significantly shorter than the inverse excitation frequency $1/\omega_{\mathrm{ex}}$, where $\bar{v}$ is the average relative velocity.

In contrast to hydrodynamic flow, if $\omega_{\mathrm{ex}}\tau \gg 1$, the atoms remain in the so-called collisionless regime, in which they follow ballistic motion. Here, the motion of one particle does not affect another particle, and locally the ensemble cannot equilibrate.

Collective modes in the extreme collisionless or extreme hydrodynamic limit can be studied, often with analytic results, using a variety of methods (see Sec. 4.2). However, most realistic systems fall somewhere between the two regimes. For example, a zero-temperature BEC obeys superfluid hydrodynamics [189], but at finite temperatures the non-condensed portion of a bosonic gas can cause its motion to deviate from pure hydrodynamic behavior. A key aspect of understanding a many-body system is determining its position on the collisionless-hydrodynamic spectrum.

In the solid state, hydrodynamic flow is emerging as a paradigm of electron transport that holds when simple Fermi liquid descriptions break down [116, 5, 156, 117]. Electron transport in metals is conventionally described as classical "billiard balls" that propagate through the bulk and scatter with impurities, edges, or phonons. Such scattering typically relaxes momentum in the electron gas. However, this semiclassical picture of ballistic electrons does not apply for ultraclean materials with few defects, in which electron-electron collisions provide the shortest scattering length. In such cases, electrons resemble a classical fluid. Recent experiments in two-dimensional materials have detected phenomena consistent with hydrodynamic electron flow, including in negative vicinity resistance [14, 15, 32], superballistic transport [141], a size-dependent electrical resistance [69, 166], violation of the Wiedemann-Franz law [60, 99], signatures of Hall viscosity [115, 22], and a spatial Poiseuille flow profile [222]. For hydrodynamic flow demonstrated in the Fermi liquids, such as in the Fermi liquid regime of graphene [14], conventional kinetic theory (and its hydrodynamic limit) is sufficient to describe experiments [69, 117].

Beyond electron fluidity, phonons have been shown to obey hydrodynamics in liquid and solid helium via measurements of second sound, a mode that only exists in the superfluid hydrodynamic regime [20]. Electrons (near the Fermi surface) and phonons are the two quasiparticle species that form the bedrock of convential transport in condensed matter. A recent experiment has observed thermoelectric signatures of electron-phonon fluidity, in which strongly-coupled electrons and phonons have a total momentum that is long-lived [91]. There, the electron gas itself was not hydrodynamic, but the electrons and phonons collectively obeyed hydrodynamics when their fast collision rate dominated all timescales.

Interest in electron-phonon hydrodynamics has been stimulated by recent theoretical works suggesting that hydrodynamic effects explain transport of unconventional metals such as the high-T_c cuprates in their strange metal phase [68, 117]. Unlike in Fermi liquids, the onset of hydrodynamics cannot be explained by a quasiparticle model with conventional kinetic theory in quantum-critical systems where quasiparticles do not persist, such as the strange metal regime [63, 116, 156, 117]. Future experiments are needed to shed light on the nature of hydrodynamic flow in electron and phonon subsystems. Mixtures of ultracold fermions and bosons, which are defect-free, have continuously tunable interactions, and can realize quantum-critical systems [247], are thus primed to study the transition between collisionless to hydrodynamic flow that can be challenging for condensed matter theory.

4.2 Collective excitations in ultracold gases

This section will establish theory framework governing ultracold gases in the collisionless and hydrodynamic regimes. Analytic solutions for low-energy excitations are derived using a scaling formalism for the collisionless regime (with Boltzmann-Vlasov equations) and for the hydrodynamic regime (using Gross-Pitaevskii equations). Past experimental work using ultracold fermions and bosons confirming these theories will be highlighted.

4.2.1 Trapped gases in the collisionless regime

Many experiments of interest involve harmonically-trapped gases within the collisionless regime, which will now be examined for two cases: a strictly non-interacting gas, as well as a gas that experiences weak, mean-field interactions with a bath.

Ideal gases in harmonic traps

We start by deriving the equations describing the collective evolution of an ideal gas [38]: for example, a single-component gas of ultracold fermionic atoms. The particles experience a harmonic potential, $V^{\text{ho}} = \frac{m}{2}\sum_i \omega_i^2 r_i^2$, with i signifying the dimensions. Let us consider the response of this trapped gas to a modulation of the potential.

Newton's laws are given by $m\ddot{r}_i = -m\omega_i(t)^2 r_i$. This time evolution can be approached using a scaling transformation, $u_i = \gamma_i(t)v_i - \frac{d\gamma_i(t)}{dt}r_i$ and $\gamma_i(t) = r_i(t)/r_i(0)$. Here, u is the scaled velocity, $v_i = \dot{r}_i$, and γ_i is the scaling parameter. Then, Newton's laws require that the scaling parameters satisfy the equations,

$$\ddot{\gamma}_i(t) + \omega_i^2(t)\gamma_i(t) - \frac{\omega_i(0)^2}{\gamma_i(t)^3} = 0 \tag{4.2}$$

With sinusoidal modulation of the trapping potential, certain modulation frequencies will *resonantly* drive the cloud, causing a dramatic response in the scaling parameters. Take the case of a spherically symmetric harmonic trap $\omega_i(0) = \omega_0$ for simplicity. For low-energy oscillations and weak perturbations about the equilibrium distribution $\gamma_i = 1$, one finds a resonance frequency at $2\omega_0$. Here, "resonant" means that the amplitude of the size oscillations will diverge in time for arbitrarily small periodic drives. This resonance is also often called the "parametric" resonance in the literature. Intuitively, if one "squeezes" the cloud twice per every cycle by modulating at twice the natural frequency, the gas particles will undergo resonant excitation, much like a child on a swing being pushed toward the center every time she reaches a local maximal height. Strictly speaking, this resonance at 2ω is not considered a true collective mode of the system, as it results from every particle performing its own

motion [189]. In 3D, a parametric resonance from modulating one dimension would not couple to the other axes. See Fig. 4-1a for a cartoon of driving the parametric resonance in an ideal, collisionless gas.

Two-component gases in harmonic traps

Beyond ideal gases, I now consider weak interactions in the collisionless regime. Here, kinetic theory is often employed to describe collective dynamics. Introduced by Boltzmann to describe a classical gas, the Boltzmann equation relates macroscopic long-time Brownian motion of particles to microscopic two-body collisions.

$$\left(\frac{\partial}{\partial t} + \vec{v}\cdot\nabla_{\vec{r}} + \frac{\vec{K}}{m}\cdot\nabla_{\vec{v}}\right) f(\vec{r},\vec{v},t) = \left(\frac{\partial f}{\partial t}\right)_{\text{coll}} \tag{4.3}$$

The gas distribution f has been spatially coarse-grained, parametrized by position $\vec{r}$, velocity $\vec{v}$, and time t, and subjected to an external force $\vec{K}$. The right-hand-side is the so-called collision integral representing binary collisions.

In its quantum formulation [20], the equation can be applied to particles or quasi-particles so long as focus is restricted to regions of space larger than relevant length-scales, i.e. the de Broglie wavelength or interparticle spacing. The collision cross-section can be computed using Fermi's golden rule, but is set to zero in the collisionless gas case.

I consider the case of a trapped, collisionless gas immersed in a bath of another species. The first species of atoms with mass m and distribution function f is subjected to a force from an external harmonic trapping potential. Additionally, it feels a mean-field potential from the other species with distribution f'. The interspecies interaction, arising from s-wave scattering, has coupling strength $g = 2\pi\hbar^2 a/\mu$, where $\mu \equiv mm'/(m+m')$ is the reduced mass. The dynamics are captured by the Boltzmann-Landau-Vlasov kinetic equation [162]

$$\frac{\partial f}{\partial t} + \vec{v}\cdot\nabla_{\vec{r}} f - \frac{1}{m}\nabla_{\vec{r}} V^{\text{ho}}\cdot\nabla_{\vec{v}} f - \frac{g}{m}\nabla_{\vec{r}} n'\cdot\nabla_{\vec{v}} f = 0 \tag{4.4}$$

where $n'(\vec{r},t) = \int f' d\vec{v}$ is the atomic density of the second species.

Eq. 4.4 admits a scaling solution [162, 154] for the distribution f and velocity v_i

$$f(\vec{r},\vec{v},t) = f_0\left(r_i/\gamma_i(t), \vec{u}(\vec{r},t)\right)$$
$$u_i(\vec{r},t) = \gamma_i(t)v_i - \frac{d\gamma_i(t)}{dt}r_i \tag{4.5}$$

where f_0 is the equilibrium distribution. By assuming equal density distributions of the two species and substitution of the scaling ansatz into Eq. 4.4, one obtains the differential equation for the time-evolution of the gas's scaling parameters [162]:

$$\ddot{\gamma}_i(t) + \omega_i^2(t)\gamma_i(t) - \frac{\omega_i(0)^2}{\gamma_i(t)^3} + \frac{3}{2}\chi\omega_i^2\left(\frac{1}{\gamma_i^3} - \frac{1}{\gamma_i\prod_j\gamma_j}\right) = 0 \tag{4.6}$$

where $\chi = \frac{g}{4}\int d^3r\, n^2(\vec{r})/(\int d^3r\, V^{\rm ho}(\vec{r})n(\vec{r}))$ is the ratio between the interaction energy and the oscillator energy. This result, which reduces to the ideal gas situation in the absence of interspecies interaction, determines the evolution of atomic density and is independent of the particles' quantum statistics.

4.2.2 Hydrodynamic theory

In the opposite limit to the collisionless case, gases can behave as liquids in the hydrodynamic regime. This arises when all particles have reached local thermal equilibrium. Fundamentally, hydrodynamic flow is governed by conservation laws such as conservation of momentum, charge, and energy. Moreover, particle densities are assumed to be spatially continuous (described by fields) rather than discrete.

Both normal fluids and superfluids can exhibit hydrodynamic behavior [189]. Normal fluids obey collisional hydrodynamic flow when the mean free path is small compared to the cloud size, $l_{\rm mf}/R \ll 1$. For example, in a harmonically trapped thermal Bose gas, this is equivalent to the condition $\frac{8\pi m_{\rm B}\omega_0(N^{1/3}a)^2T_c}{\hbar T} \gg 1$, where N is the atom number, $m_{\rm B}$ is the boson mass, and T_c is the critical temperature (see Ch. 11 of Ref. [189]). For typical experiments with thermal bosons (far from any interboson scattering resonances), atom numbers need to be over $\sim 10^6$ to satisfy the hydrodynamic condition.

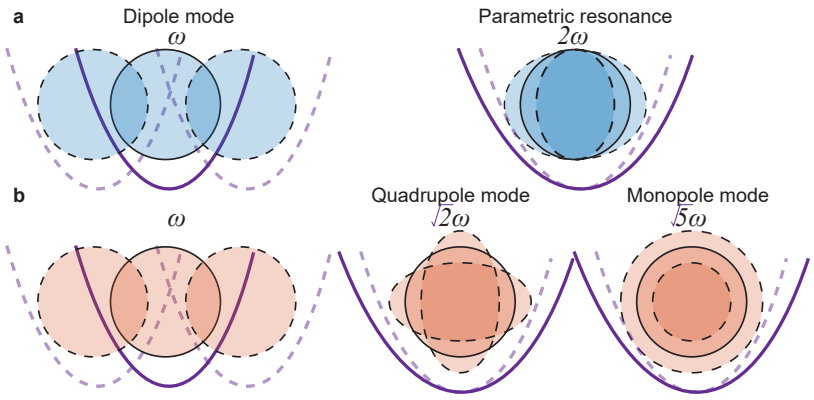

Figure 4-1: The low-lying collective modes of a gas in a spherical harmonic trap of frequency ω (purple lines), in the **(a)** collisionless and **(b)** hydrodynamic limits. The dipole center-of-mass mode corresponds to a slosh along a trap axis without deformation of the cloud shape, and is always at ω regardless of interparticle interactions. It can be efficiently excited by shifting the trap position. The mode at 2ω can be excited via parametric excitation: modulating the trap intensity at 2ω. For the hydrodynamic gas with repulsive interactions, the quadrupole mode is an out-of-phase oscillation at $\sqrt{2}\,\omega$ corresponding to a superposition of right- and left-going surface waves. The monopole mode (breathing/compression mode) is excited at $\sqrt{5}\,\omega$ for an in-phase oscillation; see Sec. 4.2.2 for a derivation. The particles move in the radial direction and have local velocities proportional to the distance from the origin.

Let us now focus on the low-lying collective excitations of non-relativistic superfluids in the Thomas-Fermi limit. For weak oscillations of a BEC in a harmonic trap, Ref. [221] derived a set of dispersion relations for the resonant energies based on hydrodynamic relations and a sum rule approach. Motion is governed by the time-dependent Gross-Pitaevskii equation, which was previously introduced in Ch 2:

$$i\hbar\frac{\partial}{\partial t}\phi = \left(-\frac{\hbar^2\nabla^2}{2m} + V^{\rm ho}(\vec{r}) + g_{\rm BB}|\phi|^2\right)\phi \tag{4.7}$$

where $g_{\rm BB} = 4\pi\hbar^2 a_{\rm BB}^2/m_{\rm B}$ is the Bose-Bose coupling.

The low-energy dynamics are determined by the hydrodynamic equations for the density $n_B \equiv |\phi|^2$, which arise from the GP equation [221]:

$$\frac{\partial n_B}{\partial t} + \nabla\cdot(\mathbf{v_B} n_B) = 0 \tag{4.8}$$

$$m_{\rm B}\frac{\partial \mathbf{v}_B}{\partial t} + \nabla\left(V^{\rm ho} - \mu + g_{\rm BB}n_B + m_{\rm B}v_B^2/2\right) = \mathbf{0} \tag{4.9}$$

where $\mathbf{v_B}$ is the velocity field and μ is the chemical potential. These equations govern the superfluid hydrodynamics of the BEC. Respectively, they are the continuity equation for particles and the Euler equation for irrotational fluids [189]. Because zero-temperature BECs are inviscid, there is no need to add viscosity terms (that are present in, for example, the more general Navier-Stokes equations). I have dropped the quantum pressure contribution to the energy ($-\frac{\hbar^2\nabla^2\phi}{2m}$) in Eq. 4.9, which is typically much smaller than external and interparticle energies.

The ground state density for the GP equation is the known Thomas-Fermi form when quantum pressure is neglected, $n_B(\vec{r}) = \max\left(\frac{m_\mathrm{B}}{4\pi\hbar^2 a_\mathrm{BB}}(\mu - V(\vec{r})), 0\right)$. Assume an isotropic trap, $V^\mathrm{ho}(\mathbf{r}) = \frac{1}{2}m_\mathrm{B}r^2\omega_0^2$. Substituting the ground state solution into Eq. 4.8 and 4.9, the hydrodynamic equations of motion simplify into [221]

$$\omega^2\delta n_B = -\frac{1}{2}\omega_0^2\nabla(R^2 - r^2)\nabla\delta n_B \tag{4.10}$$

where $R = \sqrt{2\mu/m\omega_0^2}$ is the Thomas-Fermi radius and $\delta n_B(\vec{r})e^{-i\omega t} = n_B(\vec{r},t) - n_B^0(\vec{r})$.

Stringari showed the solutions give the dispersion relation of the system's normal modes [221]

$$\omega(n,l) = \omega_0(2n^2 + 2nl + 3n + l)^{1/2} \tag{4.11}$$

Here, (n,l) are the principal and angular momentum quantum numbers, respectively. To compare to experimental results, the effect of quantum pressure can be "added back" through a sum rule approach. The quadrupole mode ($n = 0, l = 2$) becomes $\omega_Q = \sqrt{2}\omega_0(1 + E_k/E_{ho})^{1/2}$, with E_k/E_{ho} the ratio between kinetic and harmonic potential energy expectation values. Thus the quadrupole mode has energy $\approx \sqrt{2}\omega_0$ for the Thomas-Fermi limit. In the same manner, the monopole ($n = 1, l = 0$) breathing or compression mode is $\omega_M = \omega_0(5 - E_k/E_{ho})^{1/2} \approx \sqrt{5}\omega_0$. See Fig. 4-1b for illustrations of these modes in a isotropic harmonic trap.

For a time-varying trap, the spatial BEC distribution can be computed using a scaling ansatz. Here I follow Ref. [49] to derive analytical results for the dilation of a BEC in a time-dependent harmonic potential. This approach is used to analyze our experimental results on the collective excitation of a BEC, explained in Sec. 4.3.3.

Atoms are trapped by an anisotropic time-dependent harmonic potential $V^{\rm ho}(\mathbf{r},t) = \frac{1}{2}m_{\rm B}(\omega_x(t)^2x^2 + \omega_y(t)^2y^2 + \omega_z(t)^2z^2)$, with ω_i the trapping frequencies. As before, start with the time-dependent GP equation. First take the equilibrium Thomas-Fermi condensate distribution for a static trap at $\omega(t=0)$. Introduce a force on each particle $\vec{F}(\vec{r},t) = -\nabla(V^{\rm ho}(\vec{r},t) + g_{\rm BB}n_B(\vec{r},t))$. Next, apply a scaling ansatz to the BEC size, corresponding to dilating the equilibrium distribution n_B^0 by dimensionless scaling parameters b_i:

$$n_B(\mathbf{r},t) = \frac{1}{b_xb_yb_z}n_B^0(r_i/b_i) \tag{4.12}$$

$$v_{bi}(\mathbf{r},t) = \frac{1}{b_i}\frac{db_i}{dt}r_i \tag{4.13}$$

Let us explicitly solve the hydrodynamic equations in the z-component using the above ansatz. This is identical to applying Newton's law to the particle trajectories.

$$\begin{aligned} m_{\rm B}\frac{dv_z}{dt} + \frac{d}{dz}(V^{\rm ho} + g_{\rm BB}n_B + m_{\rm B}(v_x^2+v_y^2+v_z^2)/2) &= 0 \\ m_{\rm B}\frac{d}{dt}\left(\frac{\dot{b}_z z}{b_z}\right) + \frac{d}{dz}\left(m_{\rm B}\omega_z^2z^2/2 + \frac{g_{\rm BB}n_B^0}{b_xb_yb_z} + m_{\rm B}(v_x^2+v_y^2+v_z^2)/2\right) &= 0 \\ \left(-\frac{\dot{b}_z^2}{b_z^2} + \frac{\ddot{b}_z}{b_z}\right)z + \left(\omega_z^2 z + \frac{g_{\rm BB}}{m_{\rm B}b_xb_yb_z}\frac{dn_B^0}{dz} + \frac{d}{dz}\left(\frac{z^2}{2b_z^2}\left(\frac{db_z}{dz}\right)^2\right)\right) &= 0 \end{aligned} \tag{4.14}$$

The first and last terms on the left-hand side in Eq. 4.14 cancel. I now take the spatial derivative of Thomas-Fermi equilibrium distribution,

$$\frac{dn_B^0}{dz} = n_B^0(\vec{0})\frac{d}{dz}(1 - z^2/z_{TF}^2) = n_B^0(\vec{0})(-2z/z_{TF}^2) \tag{4.15}$$

where z_{TF} is the condensate Thomas-Fermi radius in the z-direction. Substitution into Eq. 4.14 gives

$$\ddot{b}_z + \omega_z^2 b_z + \frac{g_{\rm BB}(-2n_B^0(\vec{0}))}{m_{\rm B}b_xb_yz_{TF}^2} = 0 \tag{4.16}$$

Next, rewrite the equilibrium condensate density as $n_B^0(\vec{0}) = \frac{\mu}{g_{\rm BB}} = \frac{m_{\rm B}\omega_z^2z_{TF}^2/2}{g_{\rm BB}}$ and

substitute to derive a simple form for the z-scaling parameter:

$$\ddot{b}_z + \omega_z(t)^2 b_z - \frac{\omega_z(0)^2}{b_z \prod_{i=x,y,z} b_i} = 0 \tag{4.17}$$

Naturally, this equation also holds for the x- and y-scaling parameters with appropriate substitutions. The initial conditions are $b_i(0) = 1$ and $\dot{b}_i(0) = 0$ if the gas is at rest.

In conclusion, I have derived Castin's and Dum's analytic solution (Eq. 4.17) to the BEC size in a time-varying potential. This result is used in our experiment to analyze experimental BEC collective modes, rather than solving a time-dependent nonlinear Schrödinger equation for the BEC wavefunction.

4.2.3 Models for multi-component gases

A single-component gas can fall in the collisionless, hydrodynamic, or crossover regime. What about the collective modes of a gas containing two or more components? For a two-component Bose-Fermi mixture with contact interactions, there are two interaction parameters to consider: a_{BB}, a_{BF}. The Bose-Bose scattering length a_{BB} can lead to hydrodynamic behavior of the bosons, as described in Sec. 4.2.2. However, fermion intraspecies scattering is suppressed by Pauli blocking. Fermions must scatter in p- or higher odd partial waves, which are suppressed by the centrifugal barriers that far exceed the thermal energy scales $k_{\mathrm{B}}T$ for $\sim$100 nK temperatures. Thus, at low temperatures the fermions by themselves are collisionless.

What of the Bose-Fermi interactions? If $a_{\mathrm{BF}} = 0$, the fermions trivially remain collisionless, but a high $|a_{\mathrm{BF}}|$ may force the species into local thermal equilibrium with the bosons (see Fig. 4-2). Strong interspecies scattering also can change the equilibrium density distribution; for example, repulsive interactions can cause phase separation between the species. The density of particles also plays a role. A single fermionic impurity may scatter with bosons down to $T = 0$ (see Ch. 3 for a detailed discussion), but for a Fermi sea at ultracold temperatures, Bose-Fermi scattering is suppressed by Pauli blocking of the fermions, favoring the collisionless regime regard-

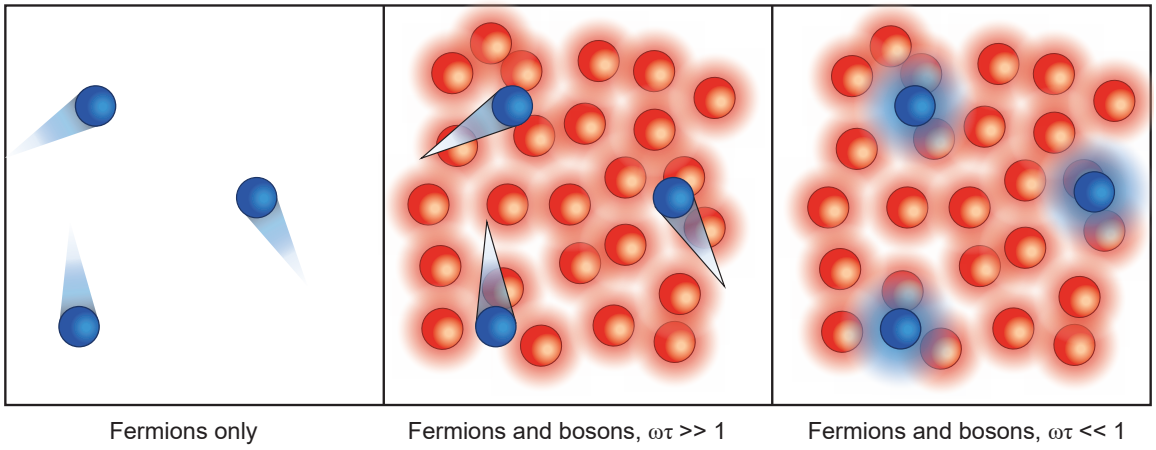

Figure 4-2: **Distinguishing different regimes in a Bose-Fermi mixture**. (Left) Spin-polarized ultracold fermions move independently without scattering off each other. (Middle) Immersed in a BEC (red atoms), the fermions are still collisionless if $\omega_{\rm ex}\tau \gg 1$, despite the bosons being hydrodynamic. (Right) When $|a|$ is sufficiently high to establish local equilibrium between bosons and fermions, and $\omega_{\rm ex}\tau \ll 1$, the fermions cross over to the hydrodynamic regime.

ing interspecies interactions. The interplay of temperature, densities, and quantum statistics makes the collective modes of Bose-Fermi mixtures very rich.

I now review various theoretical efforts to calculate the excitation spectrum of Bose-Fermi mixtures. Theoretically, collective modes can be studied within the random phase approximation (RPA) or its approximations– the sum-rule or scaling approach. The sum-rule approach was taken by [165, 16] for collective oscillations across different Bose-Fermi interaction strengths. The principle is the same as the approach in [221], presented in Sec. 4.2.2, and does not require knowledge of eigenstates beside the ground state. To summarize the sum-rule approach, the oscillation frequencies may be estimated by the ratio between certain energy-weighted moments of the dynamic structure factor [165, 16].

However, the sum-rule approach provides information only on a weighted average of multipole excitations, revealing nothing about specific eigenstates. Thus, the random phase approximation (RPA) method was utilized by [253, 44, 217, 45] for Bose-Fermi mixtures, giving access to wavefunction-dependent observables such as the dynamic structure factor. In essence, the Landau picture of quasiparticles applies

here, where quasiparticle excitations are responsible for low-lying collective modes. Small collective oscillations are the coherent superpositions of these particle-hole excitations. The RPA equation is derived using equations of motion for particle-hole excitation operators and solved numerically.

These methods apply only in the collisionless Bose-Fermi regime. A different approach was taken by [154] for both collisionless and hydrodynamic behavior, employing a scaling ansatz similar to the one presented in Sec. 4.2.2 and developed by [49] for bosons. [160] also applied a scaling method, applied to Bose-Fermi mixtures in deformed traps.

Finally, another approach to solve for collective modes is to search directly for solutions of coupled Boltzmann equations, linearized about equilibrium distributions obtained within the mean-field approximation [11, 10]. The case has been exactly solved in 1D systems [126].

4.2.4 Past experimental work in cold atoms

Low-lying collective excitations are excellent probes of interacting systems of ultracold fermions and bosons. The high accuracy and precision of excitation frequency measurements make them a well-established technique to determine collisional relaxation rates, equilibrium equations of state, and kinetic coefficients. Thus far, single species experiments have found bosonic superfluids [127, 158, 220] to obey hydrodynamic flow using motional excitation measurements. Harmonic trap potentials were modulated, causing resonant shape oscillations in the BECs at certain frequencies. These experiments were done in anisotropic magnetic traps, and their results agreed with the mean-field results of Sec. 4.2.2. Additionally, thermal bosons can be tuned from collisionless to the collisional hydrodynamic regime upon changing interaction strength [89]. In contrast, spin-polarized fermions have vanishingly few collisions at ultracold temperatures. Ref. [71] studied the suppression of collisions at low temperatures in ^{40}K fermions. There, a spin-polarized sample interacting only through p-waves exhibited a scattering cross-section $\propto T^2$ in accordance with expected threshold behavior. Therefore, spin-polarized ultracold fermions obey collisionless dynamics, as

described in Sec. 4.2.1.

Excitations in two-component atomic gases are characterized by the interspecies and intraspecies interactions. Interspecies interactions can bring both components into thermal equilibrium, becoming hydrodynamic with respect to cross-component collisions. For example, normal-state fermionic spin mixtures were found to obey collisional hydrodynamics when in the strongly-interacting regime, through observation of anisotropic expansion [178, 199, 28] or frequency shifting of collective modes [96, 2, 228]. Measurements of superfluid fermion hydrodynamics have also been made, probing viscosity [43, 129], spin transport [218], first sound [186, 142], and second sound [216].

Two-component Bose-Fermi mixtures have also been studied. Collisional hydrodynamic interactions between a spin-polarized Fermi gas and thermal bosons were observed using center-of-mass oscillations [83]. Excitation experiments involving degenerate Bose-Fermi mixtures have probed the dipole [75], quadrupole [92], and breathing modes [124]. Bose and Fermi superfluid mixtures have been realized, involving a BEC and two-component fermionic spin mixtures, and dipole oscillations were found to depend on the Bose-Fermi and Fermi-Fermi couplings [85, 70, 201, 243]. These studies have all reported signatures of Bose-Fermi interactions on collective excitations.

4.3 Fermionic crossover from collisionless to hydrodynamic flow induced by bosons

In the MIT experiment, we studied the low-lying collective modes of fermionic ^{40}K atoms immersed in a Bose-Einstein condensate of ^{23}Na atoms, by perturbation of the atoms' common trapping geometry. We observed the first experimental indication of *hydrodynamic* flow of a spin-polarized Fermi gas, induced by collisions with a Bose superfluid.

We measured this change by driving the dipole, quadrupole, and breathing oscillations in the mixture. The dipole or "sloshing" mode involve the center-of-mass

oscillating at the trapping frequency. Collective excitations such as the quadrupole and breathing modes are oscillations of the cloud's shape. The energies and damping rates of these modes were determined across different Bose-Fermi interaction strengths. We found clear evidence of the fermions' crossover from the collisionless to hydrodynamic regime upon inducing strong interactions, as the fermions inherit the superfluid hydrodynamic modes of the bosons.

The experiment starts with an ultracold gas of fermionic ^{40}K atoms immersed in a BEC of ^{23}Na at a temperature of $T \approx 80\,\mathrm{nK}$. Both species are trapped in a 1064 nm optical dipole trap in their respective hyperfine ground states ($|F=1, m_\mathrm{F}=1\rangle$ for ^{23}Na and $|9/2, -9/2\rangle$ for ^{40}K). Differential gravitational sag was cancelled between the two species using a magnetic gradient (see Appendix C). The optical potential is approximately cylindrically symmetric with trap frequencies of $\omega^\mathrm{B}_{x,y,z}/2\pi = [103(3), 94(2), 12.2(0.3)]\,\mathrm{Hz}$ and $\omega^\mathrm{F}_{x,y,z}/2\pi = [125(2), 114(2), 15(1)]\,\mathrm{Hz}$ for bosons and fermions. We define the transverse (x-y) trapping frequency as $\omega^\mathrm{B}_\perp = (\omega^\mathrm{B}_x \omega^\mathrm{B}_y)^{1/2}$. See Fig. 4-3a for a schematic of the trapping potential.

The typical peak number density ratio of fermions to bosons is $\frac{n_\mathrm{F}}{n_\mathrm{B}} \approx 0.003\text{–}0.02$, and the fermions are nearly degenerate with T/T_F ranging from 0.6 to 2, where T_F is the Fermi temperature. The BEC is weakly interacting with a Bose-Bose scattering length of $a_\mathrm{BB} = 52\,a_0$, where a_0 is the Bohr radius. Our lowest temperatures are $T/T_\mathrm{c} \approx 0.3$ with respect to the BEC critical temperature T_c.

To create an interacting Bose-Fermi mixture, we ramp the magnetic field in between two interspecies Feshbach resonances (see Appendix A), allowing us to continuously tune the interspecies interaction strength a from zero to near the unitarity limit. (We sometimes normalize the scattering length a by $k_n = (6\pi^2 n_\mathrm{B})^{1/3}$, the inverse interboson distance.) Equivalently, this tunes the mean free path of the impurity fermions, $l_\mathrm{mf} = (4\pi a^2 n_\mathrm{B})^{-1}$ compared to the system size L, approximated by the BEC Thomas-Fermi radius. Approximating the cross-section as $4\pi a^2$ is valid as long as the interaction strength is below the regime of unitarity-limited scattering, $|k_n a| < 1$.

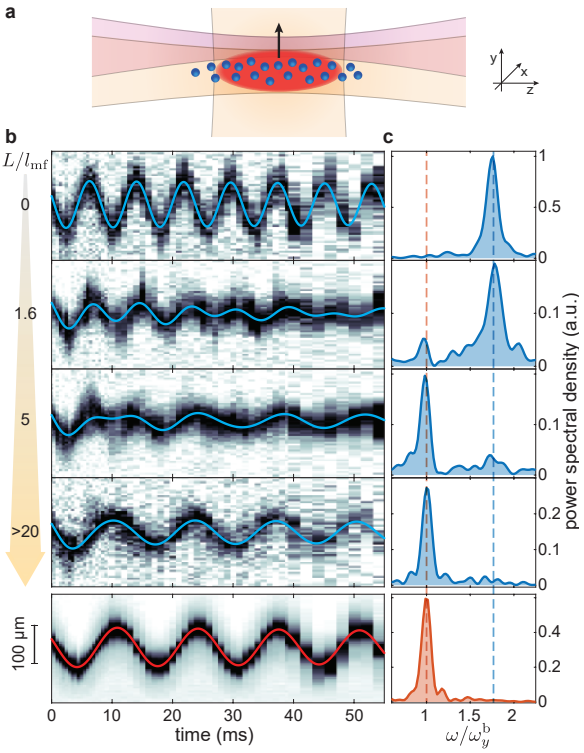

Figure 4-3: **Dipole oscillations showing the transition from collisionless to hydrodynamic flow. (a)** Illustration of a Fermi gas (blue circles) immersed in a Bose-Einstein condensate (red ellipse), both trapped in an optical potential. Dipole oscillations are induced upon the simultaneous switching on of a 850 nm trap (purple) and turning off of the z-directional 1064 nm trap (orange). **(b)** Oscillations of the fermion y-center-of-mass at various interaction strengths a with the bosons, equivalent to changing L/l_{mf}. Corresponding power spectra are shown in **c**. At the strongest interactions, the fermions are "locked" to the BEC motion. The bottom trace shows a typical BEC oscillation. Blue (red) lines fit the fermion (BEC) oscillations, as described in the text.

4.3.1 Dipole modes of fermionic impurities interacting with a BEC

We first study dipole modes of the Bose-Fermi mixture as a function of interaction strength. We induce a center-of-mass motion on both species by changing the optical trapping potential, causing a global shift of the atoms in the y-direction (see Fig. 4-3(a)). We adiabatically turn on a z-directional 850 nm beam that is displaced in the y-axis, let the distributions equilibrate, then suddenly turn off the parallel arm of the crossed 1064 nm trap. The final trapping frequencies along the motional direction are 78 (130) Hz for the bosons (fermions). The system evolves for a variable evolution time. Absorption images are then taken along the transverse x-direction of the cloud.

In the absence of interspecies interactions, the bosons and fermions are observed to oscillate independently of each other at $\omega_y^{\mathrm{B}} = 78$ Hz and $\omega_y^{\mathrm{F}} = 130$ Hz, respectively. This motion is shown as the top trace in Fig. 4-3(b). As interactions are progressively increased, the bosons are unaffected whereas the fermion oscillations change behavior, first showing significant damping, then changing their frequency of oscil-

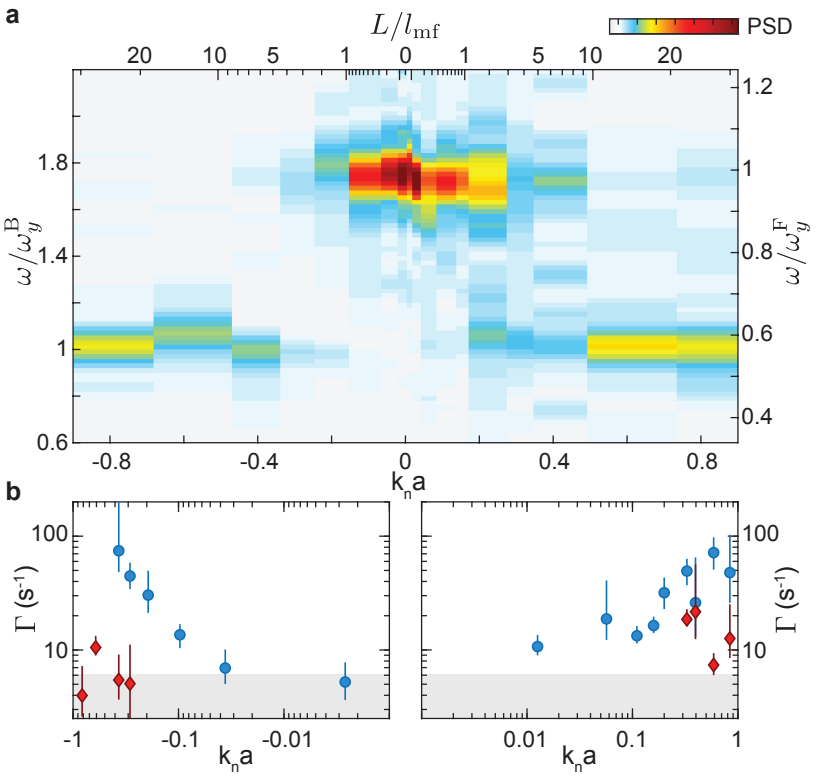

Figure 4-4: **Frequencies and damping of the fermionic dipole mode versus interaction. (a)** The power spectral density of the dipole oscillation frequencies as a function of $k_n a$ (bottom) and the system size normalized by mean free path (top). At weak interactions, the fermions oscillate at the collisionless dipole mode $\omega_y^{\rm F}$, but at strong interactions their motion "locks" onto that of the boson center-of-mass mode at $\omega_y^{\rm B}$. **(b)** The dampening of the collisionless fermion mode versus interaction. The circles (diamonds) show the fermion decay coefficients $\Gamma_{1(2)}$ for the higher (lower) frequency component. The shading indicates the typical range of decay rates Γ_b ($\pm 1\sigma$) for the boson oscillations.

lation (see bottom three traces of Fig. 4-3(b)). For $L/l_{\rm mf} > \approx 1$, the fermion dipole oscillation dramatically slows to $\omega_y^{\rm B}$. The measured fermion dipole mode frequencies are summarized as a frequency spectrum in Fig. 4-3(a), which is reconstructed from a least-squares spectral analysis of the center-of-mass time evolutions. Specifically, we use the Lomb-Scargle periodogram, an estimate of the power spectral density of data that are unevenly sampled in the time domain.

Coupled harmonic oscillator model

To extract the frequencies and decay rates of the dipole oscillations, we use an empirical model of the boson and fermion centers-of-mass as two coupled harmonic

oscillators [84, 83]:

$$\begin{aligned}\ddot{y}_{\mathrm{B}}(t) &= -(\omega_y^{\mathrm{B}})^2 y_{\mathrm{B}} - \frac{N_B m_{\mathrm{F}}}{N(m_{\mathrm{F}}+m_{\mathrm{B}})} K(\dot{y}_{\mathrm{B}} - \dot{y}_{\mathrm{F}}) \\ \ddot{y}_{\mathrm{F}}(t) &= -(\omega_y^{\mathrm{F}})^2 y_{\mathrm{F}} + \frac{N_B m_{\mathrm{B}}}{N(m_{\mathrm{F}}+m_{\mathrm{B}})} K(\dot{y}_{\mathrm{B}} - \dot{y}_{\mathrm{F}}) \end{aligned} \tag{4.18}$$

Here N is total particle number, $N_{\mathrm{B(F)}}$ is the number of bosons (fermions), K is a phenomenological Bose-Fermi coupling constant proportional to Γ_c, the drag coefficient,

$$\Gamma_c = \bar{n}\sigma v_{rel} \tag{4.19}$$

Here, $\bar{n}$ is the mean overlap density, $v_{\mathrm{rel}} = \sqrt{8k_B T/\pi\mu}$ the average relative thermal velocity between the species, and the cross-section is $\sigma = 4\pi a^2$. For perfect spatial overlap between the two clouds, K=4/3 [84].

For our data, appropriate for the limit of $n_{\mathrm{B}} \gg n_{\mathrm{F}}$, the boson center-of-mass is fitted to a sinusoid with an exponentially-decaying envelope, with frequency ω_{B} and decay rate Γ_{B} as free parameters. Γ_{B} is observed to be independent of a (see the shaded area of Fig. 4-4(b)). The fermion center-of-mass is fitted to $y_{\mathrm{F}}(t) = A_1 e^{-\Gamma_1 t}\sin(\omega_1 t + \phi_1) + A_2 e^{-\Gamma_2 t}\sin(\omega_{\mathrm{B}} t + \phi_2)$. The oscillation has a higher frequency component (ω_1) and lower frequency component (fixed at ω_{B}), each with a corresponding amplitude $A_{1/2}$ and decay $\Gamma_{1/2}$, and phase offset $\phi_{1/2}$. All fermion parameters are extracted by least-squares fitting to the fermion center-of-mass, except ω_{B}.

The evolution of the fermion dipole oscillations is consistent with hydrodynamic flow induced by interactions with bosons. The boson oscillations are observed to have frequencies and decay rates that are independent of a; their typical decay rate is shown as the shaded area of Fig. 4-4(b). As the interaction $|a|$ increases, the mean free path l_{mf} grows larger compared to the system size L (the BEC's Thomas-Fermi radius in the y-direction). Then, the fermion response at the ω_y^{F} frequency diminishes, reflected by both a decreasing amplitude $A_{\mathrm{f,1}}$ and increasing damping Γ (see Fig. 4-4(b)). A separate frequency component arises around ω_y^{B}, becoming the only steady-state response of the system. To within experimental error, the attractive

and repulsive sides are indistinguishable in their frequency and decay responses.

We attribute this "locking" of the fermion dipole mode with the bare bosonic dipole mode to interspecies collisions, forcing the fermions to be in local equilibrium with the bosons and to inherit the bosonic collective modes. We do not observe a mean-field shift at low interaction strengths. Such a shift would occur due to the additional attractive or repulsive potential from the BEC. However, the average overlap of the Fermi gas and BEC is low at weak interactions, preventing the observation of mean-field shifts in the fermion dipole mode. What we observe is much more abrupt: above a threshold interaction strength, the fermions stop oscillating at their collisionless dipole mode resonance ω_y^{F} and instead oscillate at the boson's dipole mode ω_y^{B}, suggesting that Bose-Fermi interactions have brought the fermions out of the collisionless regime and into the hydrodynamic regime.

4.3.2 Dipole modes of fermions interacting with thermal bosons

In the previous section we reported on the fermion dipole mode's crossover to hydrodynamic behavior induced by coupling to a BEC. We repeat the dipole oscillation experiment with thermal bosons and fermions. As in the case of the BEC, in the absence of interactions, the fermions oscillate at their bare trapping frequency ω_y^{F}, as shown in Fig. 4-5. Above a certain interaction strength, they are observed to lock to the boson's trapping frequency ω_y^{B}. Regardless of whether the bosons are thermal or superfluid, this crossover of the fermions to the hydrodynamic regime occurs when the mean free path is roughly the system size.

4.3.3 Transverse quadrupole and breathing modes

Although the fermions' dipole mode locks to the bosons' dipole mode at strong coupling, the dipole oscillation does not distinguish whether the interactions originate from the superfluid (condensed) or the thermal bosons. The dipole mode for both bosonic components is independent of the Bose-Bose collision properties, a consequence of Kohn's Theorem [77]. Therefore, both the superfluid portion, which is

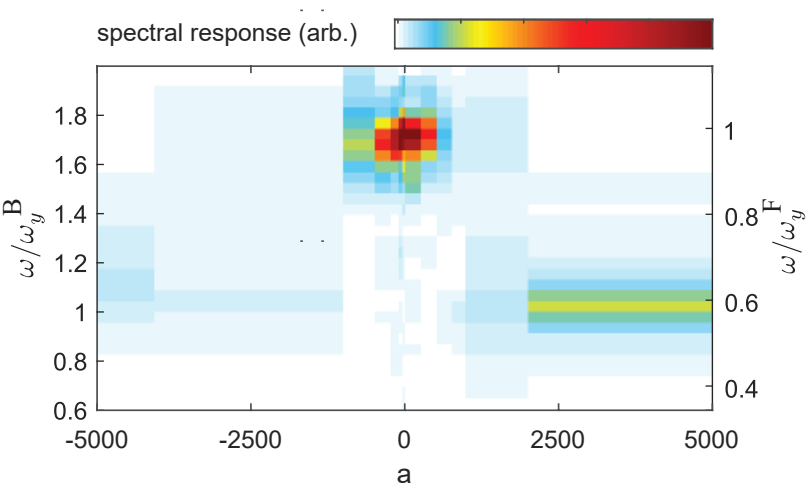

Figure 4-5: Dipole oscillation frequency spectogram of the fermions immersed in a thermal Bose gas, as a function of interaction strength a. Peak boson densities are $2 \times 10^{12}/\mathrm{cm}^{-3}$ for the attractive side and $8 \times 10^{12}/\mathrm{cm}^{-3}$ for the repulsive side. The crossover from the collisionless regime, where fermions oscillate at their natural trap frequency, to the hydrodynamic regime, where fermions are locked to the boson dipole mode, is seen for both attractive and repulsive interactions.

hydrodynamic, and the thermal portion, which is collisionless at the given a_{BB}, have dipole resonances at the same frequency: ω_y^{B}. In contrast to the dipole mode, collective modes that couple to local density can distinguish the superfluid from the normal component.

To further explore the origin of hydrodynamic flow in the Fermi gas, we parametrically excite low-lying quadrupolar and breathing modes as a function of interaction strength and temperature. In a hydrodynamic gas, density fluctuations along one axis couple to another, much like how squeezing a balloon along its equator causes expansion along the orthogonal axis. The transverse quadrupole mode corresponds to the two transverse axes compressing and expanding in an out-of-phase manner, while the transverse breathing mode sees the two axes compressing in phase (see Fig. 4-6(a)). For a hydrodynamic BEC with $a_{\mathrm{BB}} > 0$, repulsive interboson interactions cause the quadrupolar mode to cost less energy than the breathing mode, resulting in two resonances at $\sqrt{2}\omega^{\perp}$ and $2\omega^{\perp}$ in the limit $\omega^{\perp} \gg \omega_z$ [221]. However, for a collisionless gas, motions along different axes are decoupled, and resonances for transverse modes occur at $2\omega_x$ and $2\omega_y$. Therefore, in our system where $\sqrt{2}\omega^{\perp} < \omega_y < \omega_{\perp} < \omega_x$, colli-

sionless and hydrodynamic behavior can be discriminated by the measured resonance frequencies.

Collective excitations are initiated by parametrically modulating the trapping potential in the transverse direction at a variable frequency. A sinusoidal intensity perturbation on the z-axis 1064 nm trap beam is applied with a modulation amplitude of 20% and a variable drive frequency for 15 cycles. This method primarily excites the transverse breathing mode. (The 850 nm optical trap is not used in these collective excitation studies.) When a transverse collective resonance is excited, the cloud expands in size along the y-direction.

Fig. 4-6(b) shows the spectrograms of the boson and fermion cloud sizes as a function of drive frequency, for a selection of interactions.

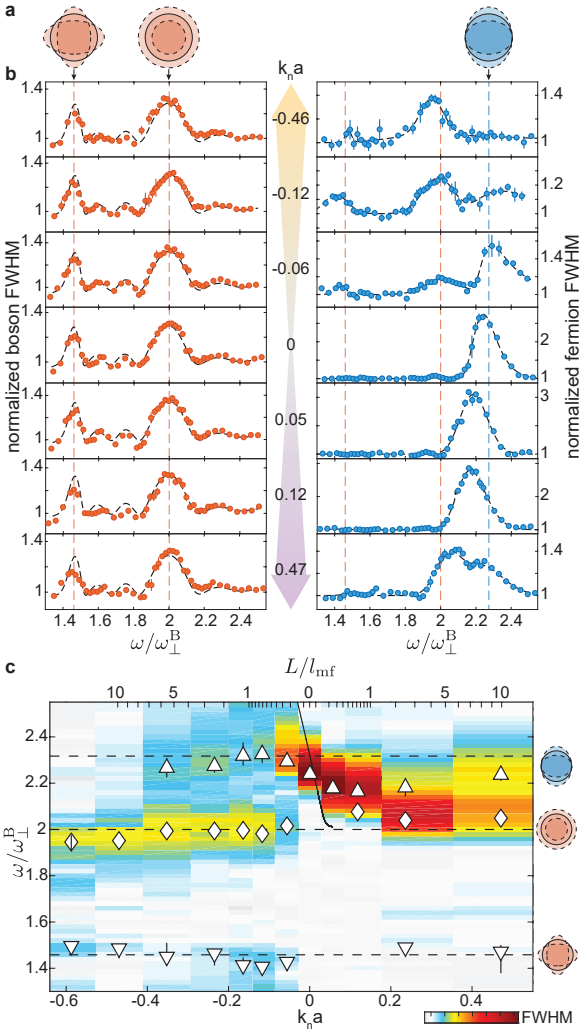

Figure 4-6: **Collisionless to hydrodynamic flow in the transverse quadrupole and breathing modes.** **(a)** Cartoons depicting the oscillations of the cloud's transverse (x-y) cross-section. The boson quadrupole and breathing modes lie at $\sqrt{2}\omega_\perp^{\mathrm{B}}$ and $2\omega_\perp^{\mathrm{B}}$, respectively, while the fermion collisionless mode lies at $2\omega_y^{\mathrm{F}}$. **(b)** Spectrograms of boson and fermion y-widths versus $k_n a$, showing cloud width (circles) for varying modulation frequency. The boson dashed lines fit the power spectra using the scaling ansatz [49], and the dashed lines on the fermion traces fit the data using a multiple Gaussian peak function. **(c)** Color density plot summarizing the fermions' spectral response with peak positions plotted as points. For weak interactions, the resonance positions are linear in $|a|$ and qualitatively agree with a mean-field prediction (solid line). Horizontal dashed lines indicate the bosons' quadrupole, breathing, and the bare fermion modes.

BEC collective modes

First, we aim to understand the excitations in the boson spectra. The BEC is the majority host component of the fermions, and because of the large density imbalance, their spectra in Fig. 4-6(b) show no dependence on $k_n a$. The two peaks correspond to the hydrodynamic bosons' transverse quadrupolar and breathing modes, which are illustrated as red cartoons in Fig. 4-6(a). Our observations can be numerically simulated as a function of driving frequency ω using the scaling ansatz of [49] (see Sec. 4.2.2). The BEC size scaling parameters obey

$$\begin{aligned}
\ddot{b}_x(t) &= \frac{\omega_x^2}{b_x b_x b_y b_z} - \omega_x^2\big(1 + \frac{\alpha_1}{2}\sin(\omega t + \phi) + \frac{\alpha_2}{2}\sin(\omega t)\big) b_z \\
\ddot{b}_y(t) &= \frac{\omega_j^2(0)}{b_j b_x b_y b_z} - \omega_y^2(t)\big(1 + \alpha_2 \sin(\omega t)\big) b_j \\
\ddot{b}_z(t) &= \frac{\omega_j^2(0)}{b_j b_x b_y b_z} - \omega_z^2(t)\big(1 + \alpha_1 \sin(\omega t + \phi)\big)
\end{aligned} \tag{4.20}$$

with initial conditions $b_i(0) = 1,\ \dot{b}_i(0) = 0$. Here, α_1, α_2 are the modulation intensities of the y- and z- directional ODT's, respectively, and ϕ is the relative phase difference between the two beams' drives. Solving these coupled equations using our experimental parameters results in the spectrogram shown in Fig. 4-7(top figure) and as the dashed lines of the boson traces in Fig. 4-6(b). These simulations reproduce our observations quantitatively.

Fermion collective modes

Having understood the response of the majority bosons, we now turn to the fermion collective modes. Fig. 4-6(b) shows spectrograms of the fermion cloud sizes as a function of drive frequency, for a selection of interactions. The red dashed lines indicate the position of the hydrodynamic bosons' transverse quadrupolar and breathing modes (see Sec. 4.3.3 for details). The dashed blue line denotes the collisionless fermions' transverse mode at $2\omega_y^{\mathrm{F}}$. Fermion collective oscillations are summarized in Fig. 4-6(c), a color map representing the spectral responses of the widths, with white

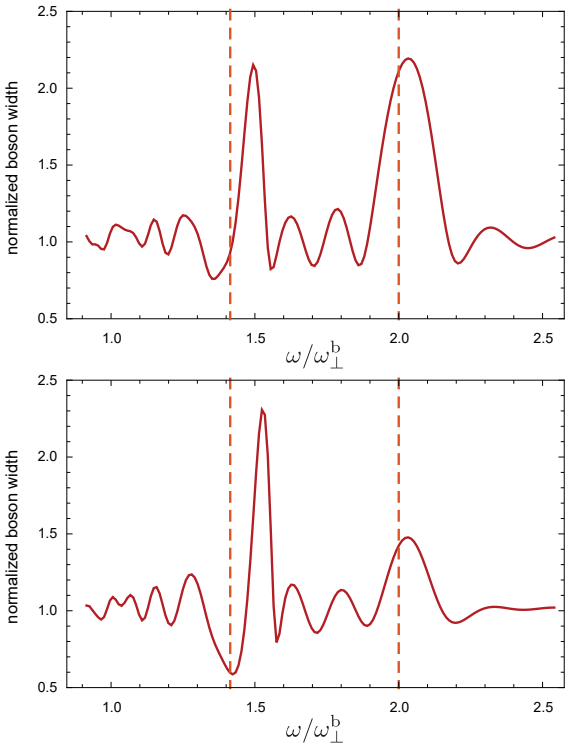

Figure 4-7: **Calculated spectrograms of boson widths in the hydrodynamic regime** with trap parameters specified in Sec. 4.3.3, modeled by the scaling ansatz [49] detailed in Sec. 4.2.2. (Top) Single-axis drive with 20% modulation. (Bottom) Both axes driven 180° out-of-phase with 15% modulation. Lower and higher frequency dashed lines indicate the linear-response transverse quadrupole and breathing frequencies, respectively. Deviations from the peak spectral response are due to strong driving and Fourier broadening.

points indicating peak positions.

Strikingly, the fermion collective oscillations greatly depend on the interaction strength. The Fermi gas responds at its collisionless mode $2\omega_y^{\mathrm{F}}$ only around zero interaction. At weak attraction, *e.g.*, $k_n a = -0.05$, the fermion mode shifts to higher frequencies, while at weak repulsion it downshifts. In Fig. 4-6(c) we compare the fermion peak positions (upward-facing triangles) to a prediction from a collisionless kinetic model that assumes mean-field interaction between the bosons and fermions [154]. In the impurity limit, this predicts a shift of the fermion collective resonance,

$$\omega_y^{\mathrm{F}'} = 2\omega_y^{\mathrm{F}} \sqrt{1 - \frac{g_{\mathrm{BF}}\alpha_B}{g_{\mathrm{BB}}\alpha_{\mathrm{F}}}} \tag{4.21}$$

where $g_{\mathrm{BF}} = 2\pi\hbar^2 a/\mu$, $g_{\mathrm{BB}} = 4\pi\hbar^2 a_{\mathrm{BB}}/m_{\mathrm{Na}}$, and $\alpha_{\mathrm{B(F)}}$ is the boson (fermion) ac polarizability. The result, shown as the solid line, predicts the direction of the fermion collective mode shift for weak interaction strengths but overpredicts the shift value. We hypothesize that the lack of quantitative agreement owes to the non-perfect spatial overlap of the two species. The model fails to capture the trend of the mode locking

to the BEC mode as L/l_{mf} increases beyond ≈ 1.

We find compelling proof that hydrodynamic flow in the Fermi gas arises from coupling to the superfluid bosons at the strongest interactions $|k_n a| \geq 0.2$. There, a new mode appears in the fermion spectrograms at $2\omega_{\perp}^{\mathrm{B}}$, the superfluid boson breathing mode, both for attractive and repulsive interactions. These peak positions are plotted as diamonds in Fig. 4-6(c). We attribute this mode to strong interactions between the two species, forcing the fermions into local equilibrium with the BEC. Furthermore, the imprint of the BEC quadrupole mode can be seen (downward-facing triangles) on the fermions at $\sqrt{2}\omega_{\perp}^{\mathrm{B}}$. While collisionless thermal bosons will exhibit oscillations at $2\omega_y^{\mathrm{B}}$ ($\approx 2\omega_{\perp}^{\mathrm{B}}$), *only* hydrodynamic bosons feature a resonance at $\sqrt{2}\omega_{\perp}^{\mathrm{B}}$. No collisionless mode lies in its vicinity. The appearance of the boson quadrupole mode in the fermion spectrogram signifies hydrodynamic flow in the Fermi gas induced by the BEC.

4.3.4 Temperature dependence of collective modes

Having established the existence of hydrodynamic collective modes in our Fermi gas, we now study the evolution of the excitation spectra as a function of temperature. The temperature dependence is of interest because the fermion impurities can serve as a sensor of quantum behavior of the host Bose gas, which is not well understood at finite temperatures [189]. Furthermore, when an impurity is dressed by bosons to form a quasiparticle called the *Bose polaron*, the quasiparticle lifetime is thought to be limited by incoherent scattering from the bosons [247]. However, whether the normal or superfluid component dominates the scattering as T varies is unknown. If scattering from the normal component dominates and a_{BB} can be neglected, increasing temperatures for $T \ll T_{\mathrm{c}}$ should lead to more Bose-Fermi collisions, as the collision rate is proportional to a^2T^2 for weak interactions. For unitarity-limited scattering ($|k_n a| > 1$), the collision rate is predicted to increase linearly in T up to T_{c} [247]. Studying the excitations of fermions immersed in a BEC as the bosons gradually approaches T_{c} could elucidate the finite-temperature behavior of the Bose polaron.

To study the collective excitation spectra versus temperature, we vary the evap-

oration efficiency of the bosons, resulting in T/T_c ranging from 0.2 to 1.0. As before, we parametrically excite the gas by modulating the trap intensity sinusoidally, with varying frequency. The interspecies scattering length is fixed at $-400a_0$. In this case, the z- and y-directional 1064 nm beams are both intensity-modulated 180° out of phase, to better couple into the transverse quadrupole mode. The modulation depths are both 15%. As before, we excite for 15 cycles. For increasing T/T_c, the fraction of dilute thermal bosons grows relative to the dense condensate, causing a decrease in the peak boson density. The resulting spectrograms for both species are shown in Fig. 4-8(a), with peak frequencies summarized in Fig. 4-8(b).

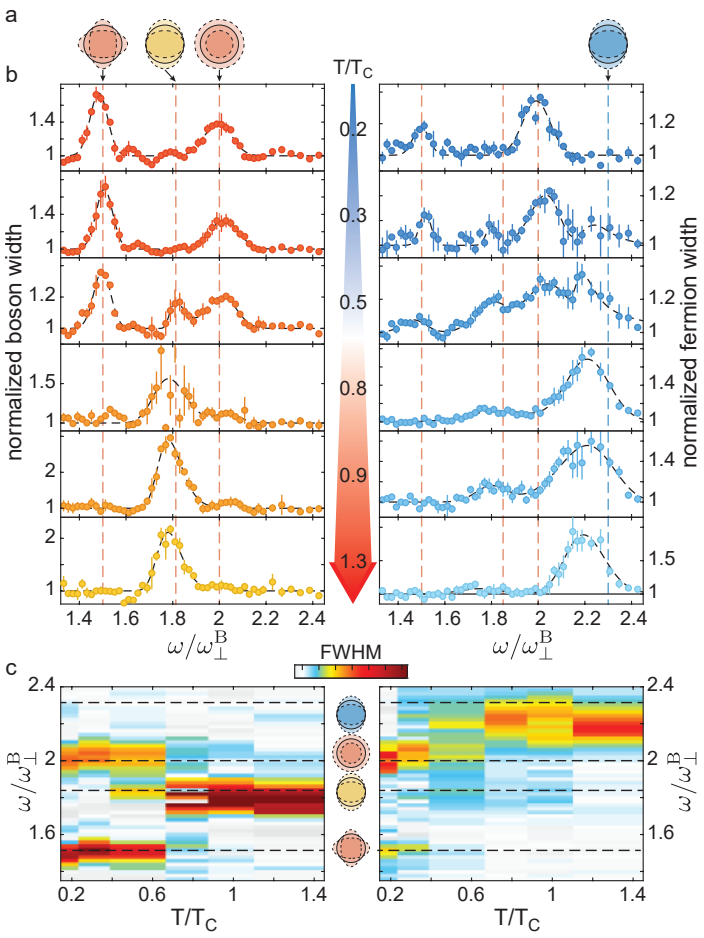

Figure 4-8: **Temperature dependence of the boson and fermion collective modes at $a = -400a_0$.** **(a)** Illustration of the boson hydrodynamic quadrupole, collisionless parametric, and hydrodynamic breathing modes (red) and the fermion collisionless mode (blue). **(b)** Spectrograms of the boson (left) and fermion (right) widths, as a function of the bosons' reduced temperature T/T_c. The red and blue dashed lines mark the modes illustrated in (a) for the bosons and fermions, respectively. Interaction strengths corresponding to the increasing T/T_c are $k_n a = -(0.38, 0.35, 0.34, 0.27, 0.25, 0.08)$. The fermion spectrograms indicate hydrodynamic response at the bosons' quadrupole and breathing mode frequencies for the lowest temperatures. At $T/T_c > 0.5$, the bosons become collisionless, exhibiting a resonance at $2\omega_y^B$. The fermions respond primarily at their collisionless resonance of $2\omega_y^F$, but collisions with the thermal bosons cause a resonance at $2\omega_y^B$. **(c)** Summary of the extracted peak frequencies for bosons (left) and fermions (right), with color indicating spectral response. Fermion frequencies match the observed boson modes for both the superfluid-dominated ($\leq 0.5T_c$) and thermal-dominated responses ($> 0.5T_c$).

The boson spectra for low temperatures match the hydrodynamic predictions from the scaling ansatz (see Fig. 4-7, top figure).

The fermion excitation spectra are observed to probe the complex crossover of modes in the Bose gas itself. At the coldest temperatures, both species respond at the bosons' transverse hydrodynamic modes, $\sqrt{2}\omega_\perp^{\mathrm{B}}$ and $2\omega_\perp^{\mathrm{B}}$. The fermions remain "locked" to the boson hydrodynamic modes. However, as the temperature is increased beyond $T/T_{\mathrm{c}} > 0.5$, the bosons begin to respond at the collisionless mode $2\omega_y^{\mathrm{B}}$ (marked by the middle dashed red line in Fig. 4-8(a)) and the hydrodynamic modes dramatically diminish or disappear. We attribute the peaks at $2\omega_y^{\mathrm{B}}$ to the thermal bosons. These bosons are in the collisionless regime, being over an order of magnitude less dense compared to the condensate bosons. Analogously, the fermions begin to respond near their own collisionless frequency $2\omega_y^{\mathrm{F}}$ at $T/T_{\mathrm{c}} > 0.3$. We note the relative frequency decrease of the fermion response for $T/T_{\mathrm{c}} > 0.3$ compared to $2\omega_y^{\mathrm{F}}$, shown as the blue dashed line in Fig. 4-8(b), and attribute the deviation to the anharmonicities of the trap. (The same effect of anharmonicities can be seen in the decrease of the boson mode frequencies near $2\omega_y^{\mathrm{B}} \approx 1.8\omega_\perp^{\mathrm{B}}$.) Despite the evidence of collisionless fermionic behavior for $T/T_{\mathrm{c}} > 0.3$, there, the fermions still exhibit a slight response at the boson frequency $2\omega_y^{\mathrm{B}}$ that is absent in the case without interparticle interactions. Even though the bosons are themselves collisionless above $T/T_{\mathrm{c}} > 0.3$, enough collisions occur between the species that the fermions still demonstrate hydrodynamic behavior with respect to the Bose gas.

We conclude that hydrodynamic flow can originate from fermion collisions with both the normal and superfluid bosons. A detailed microscopic model would ideally show how bosonic excitations couple to the impurities. The observation of boson-induced hydrodynamic flow across a large range of temperatures below and at T_{c} highlights the rich interplay between interaction strength, collision rates, and degeneracy within a Bose-Fermi mixture.

4.4 Faraday modes of a Bose-Fermi mixture

The Bose-Fermi system introduced in Ch. 3 and this chapter has been studied by our group using radiofrequency and spatial density excitations. Perhaps the most

visually striking observation is the appearance of Faraday waves in the system, and this section presents some preliminary results.

Pattern formation in driven systems has been the object of intense study in diverse fields ranging from nonlinear optics to biological media. In a seminal 1831 fluid mechanics experiment, Michael Faraday demonstrated how certain fluids form standing waves on their surfaces when driven in a transverse direction at a particular frequency. These waves, termed *Faraday waves*, arise from the parametric excitation of collective modes in the fluid.

In the context of atomic gases, Faraday waves have been observed in elongated BEC's [82, 105, 173]. These experiments modulated weakly-interacting BECs along the radial direction, inducing striated density patterns along the longitudinal direction. For a radial modulation around one or two times the trapping frequency, the cloud density and thus speed of sound changes, leading to a parametric excitation of "soundlike" modes in the longitudinal axis.

We observed the emergence of Faraday waves on an elongated Fermi gas, induced by strong interactions with the background BEC. The system of spin-polarized ^{40}K minority fermions in a majority ^{23}Na BEC is as described in Ch. 4.3. We modulate the radial trapping potential at varying frequencies, for various Bose-Fermi interaction strengths $k_n a$, where $k_n = (6\pi^2 n_{\mathrm{B}})^{1/3}$ is the inverse interboson distance, and a is the interspecies scattering length. The BEC exhibits a Faraday resonance regardless of the Fermi gas's presence when we drive around 8 cycles at $2\omega_r^B$, or twice the boson radial trap frequency. When interspecies interactions are weak, the fermions are not excited by this drive, as it is off-resonant to any of its modes (see Sec. 4.2.1 for a detailed overview of collisionless Fermi modes). However, when interactions are tuned to the repulsive side, we begin to see the imprint of the boson density on the fermions. Fig. 4-9 shows an example of an image of the overlapped Bose and Fermi gases at $a = 500a_0$. To our knowledge, this is the first observation of spatial patterns analogous to Faraday modes in an ultracold Fermi gas.

Further work is necessary to characterize the onset of these patterns as a function of interaction strength, relative species density, and temperature. Local analysis of

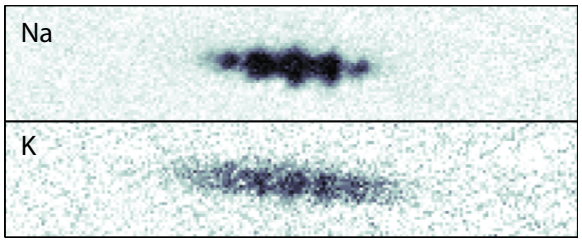

Figure 4-9: Faraday waves in a Bose-Fermi mixture (*in-situ*), showing the longitudinal density pattern in the BEC, with axial Thomas-Fermi radius of $\sim$70 μm (top), and fermions (bottom) at an interspecies interaction of $500a_0$. Bose-Fermi interactions cause the BEC density striation to be imprinted on the fermions.

the wave periodicity should reveal the local speed of sound in the condensate. It will be interesting to compare those results to predictions from Bogoliubov theory, and to study whether any deviations arise due to Bose-Fermi coupling. Furthermore, these nonlinear excitations may shed light on the properties of the Bose polaron quasiparticle (see Ch. 3 and Ref. [247]) and the relative contributions of the normal and superfluid components to the collisions that limit the quasiparticle lifetime.

4.5 Summary and outlook

In conclusion, we have explored the transition from collisionless to hydrodynamic flow in a spin-polarized Fermi gas. The onset of hydrodynamics was induced by strong interaction with both the normal and superfluid components of the bosons. Cold atom systems with tunable fluidity can thus shed light on the origin of hydrodynamics in electron fluids. Furthermore, we investigated nonlinear Faraday oscillations within the interacting Bose-Fermi mixture. As an outlook, induced fermion-fermion interactions could arise within the hydrodynamic Bose-Fermi mixture due to phonon-mediated interactions. This requires colder temperatures and higher fermion densities. Such a system is promising for studies of p-wave superfluidity of fermions mediated by bosons [134].

Chapter 5

Creation and control of ultracold ^{23}Na^{40}K

While ultracold atomic gases have led to groundbreaking results in quantum simulation and metrology, extending such control to molecules has opened up new avenues of exploration. This chapter motivates why full quantum control over ultracold molecules is desirable, highlighting recent experimental progress toward this goal. I will describe our team's creation of ultracold fermionic ^{23}Na^{40}K, starting with taming the degrees of freedom at the single-molecule level. Details on molecular creation are discussed in depth in Jee Woo Park's thesis [181] and will not be repeated here unless necessary. Spectroscopy on NaK's low-lying rotational and hyperfine structure is described. Additionally, molecular lifetimes and coherence properties are discussed.

The research described in this chapter has resulted in the following publications:

Sebastian Will, Jee Woo Park, Zoe Z. Yan, Huanqian Loh, Martin W. Zwierlein, *Coherent Microwave Control of Ultracold $^{23}Na^{40}K$ Molecules,* Phys. Rev. Lett. **116**, 225306 (2016).

Jee Woo Park, Zoe Z. Yan, Huanqian Loh, Sebastian Will, Martin W. Zwierlein, *Second-scale nuclear spin coherence time of ultracold $^{23}Na^{40}K$ molecules,* Science **357**, 372 (2017).

5.1 Advantages of molecules

Molecule-based quantum simulation is primed to advance our understanding of many-body physics. Despite the successes of atom-based quantum simulation, many key phenomena in condensed matter remain out of reach for state-of-the-art cold atom systems that rely on atoms' short-range, isotropic interactions. Indeed, several proposals for realizing novel paired superfluid phases [18, 59, 191], dipolar crystals [39, 195], quantum magnets [19, 101], and interacting spin systems [163] utilize particles with long-ranged dipolar interactions. Polar diatomic molecules serve as an excellent potential platform for these studies.

Moreover, atoms' internal states are simplistic compared to those of molecules. Ultracold polar molecules realize a quantum element that combines the long-range, anisotropic dipole-dipole interaction with a vast array of internal states that span convenient frequencies (*e.g.* radiofrequency, microwave, infrared, visible, and ultraviolet wavelengths). Beyond quantum simulation of many-body physics, molecules are expected to add richness to schemes for quantum computation, quantum state-controlled chemistry, and probes of fundamental physics [26, 204, 6, 135]. I now examine the justification for looking beyond cold atoms for these various applications.

5.1.1 Expanding the quantum toolbox beyond cold atoms

Novel phenomena can be accessed by adding degrees of freedom at the cost of experimental complexity. Molecules have a rich internal structure due to vibrational and rotational modes from their nuclei. This imparts an electric dipole moment in heteronuclear diatomic molecules, which experience dipole-dipole interactions:

$$V_{\mathrm{DDI}}(\vec{d_1}, \vec{d_2}, \vec{R}) = \frac{\vec{d_1} \cdot \vec{d_2} - 3(\vec{d_1} \cdot \hat{R})(\vec{d_2} \cdot \hat{R})}{R^3} \tag{5.1}$$

where $\vec{d_i}$ is the dipole moment of molecule i, both molecules have body-frame electric dipole moments of magnitude $|d_0|$, and they are separated by a relative coordinate $\vec{R}$ (see Fig. 5-1).

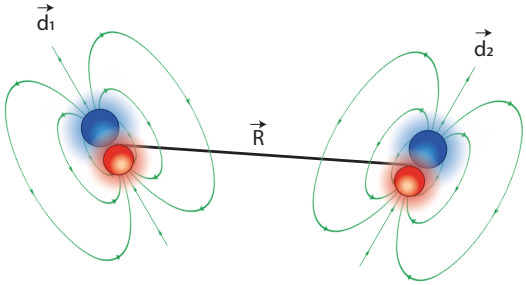

Figure 5-1: Schematic of the electric dipole-dipole interaction between two molecules with dipolar orientations $\vec{d_1}, \vec{d_2}$ and relative coordinate $\vec{R}$. Green lines represent the local electric field generated by each molecule.

..

Three defining characteristics make this interaction useful: one, it is anisotropic, ranging from attractive to repulsive depending on orientation; two, it is long-ranged, scaling with distance as R^{-3} compared to R^{-6} for ground state atoms at long distances; three, the laboratory-frame dipole moment can be tuned, from zero in the absence of any symmetry-breaking external fields, to the "fully-polarized" value of d_0 in large electric fields. These features make molecules an attractive quantum resource.

A basic primer on diatomic molecules

A full introduction of even the "simple" diatomic molecules is out of the scope of this thesis; readers are referred to Refs. [119, 33] for details. I only highlight the basic level structure of molecules essential for understanding experiments described in the following chapters.

Diatomic molecules have the ability to vibrate and rotate, in addition to the degrees of freedom that atoms possess. The wavefunction is a combination of electronic, vibrational, rotational, and nuclear spin degrees of freedom. Under the Born-Oppenheimer approximation, the electrons' and nuclei's motions can be separated, with the wavefunction written as a product of the electronic and nuclear portions, $|\psi_{\text{mol}}\rangle = |\psi_{\text{el}}\rangle\,|\psi_{\text{nuc}}\rangle$. The cross-terms $\langle\psi_{\text{el}}|\,\mathcal{H}\,|\psi_{\text{nuc}}\rangle$ are neglected, a good approximation for most molecules given the large separation of energy, time, and mass scales between the electron and nucleus.

First, the Schrödinger equation can be solved for the electrons with the internuclear separation $\vec{r}$ as a parameter. *Ab initio* calculations are impossible for all but the simplest dimers, so typically these potentials are semi-empirical, taking measured energy differences from molecular spectroscopy experiments to produce the most accu-

rate electronic potential energy surfaces. The electronic energy solutions as a function of $\vec{r}$ are shown for NaK in Fig. 5-2. For each electronic state, the potential energy is minimized at some equilibrium distance on the order of a few a_0, where a_0 is the Bohr radius. The potential is approximately harmonic near the equilibrium, and falls to zero at large internuclear separation as r^{-6} due to van der Waals interaction (when magnetic dipolar interactions are absent). At short range there exists a steep repulsive wall, physically representing where the electron cores of the two atoms start to overlap. The typical energy associated to electronic excitations is a few eV, given by $\sim e^2/a_0$, where e is the electron charge.

To label electronic states, one must consider the symmetry of a molecule. An atom with a single nucleus does not break the spherical symmetry for its electrons, so electronic orbital angular momentum L is a constant of motion (neglecting spin-orbit couplings). However, in a diatomic molecule, the symmetry of the field is reduced due to the two nuclei, and consequentially, only the *component* of electronic orbital angular momentum about the internuclear axis is a constant of the motion. Greek letters label this projection onto the internuclear axis: $\Sigma, \Pi, \Delta...$ representing the quantum number $\Lambda = 0, 1, 2....$

For Σ states, the superscript $+(-)$ denotes that the wavefunction is symmetric (antisymmetric) with respect to reflection about any plane containing the internuclear axis. As in atoms, S denotes the total spin quantum number. Ω is the projection of the total angular momentum along $\vec{r}$. A molecular state has the general form

$$^{2S+1}\Lambda_{\Omega}^{(+/-)} \tag{5.2}$$

By convention, the ground state of a molecule is labelled X; the state $^1X^+$ is identical to $^1\Sigma^+$ in NaK.

Molecules' nuclei provide additional degrees of freedom beyond the electronic. Once the electronic potentials are established, these can be used as effective potentials to solve the nuclear Schrödinger equation, involving the vibration, rotation, and nuclear spin of the nuclei. The relative vibration of the nuclei is quantized, with the

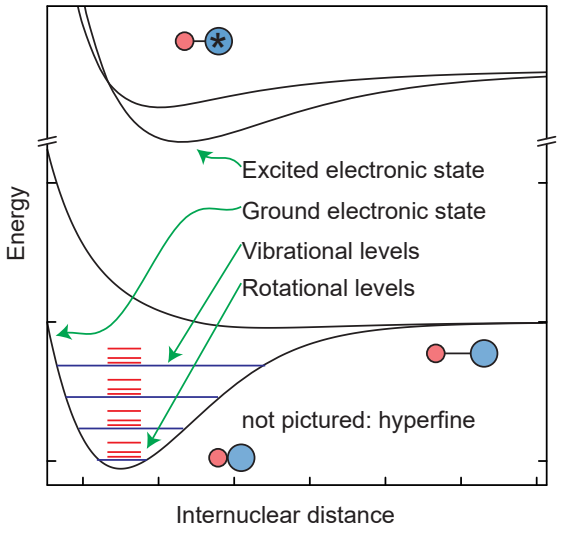

Figure 5-2: Potential energy landscape of a diatomic molecule as a function of the separation between the two constituents' nuclei. Electronic energies (black lines) form the largest scale, followed by vibrational and rotational energies (blue and red lines, respectively, not pictured to scale). Hyperfine energies are even smaller.

..

lowest-lying vibrational energy spacings in each electronic potential scaling as $\sqrt{\frac{m_e}{m_r}}\frac{e^2}{a_0}$, where m_e is the electron mass and m_r is the two atoms' reduced mass.

Next, the hierarchy of energy scales decreases to rotational excitations. Any given vibrational state can rotate about the center of mass, and the quantum number R represents the rotational angular momentum. For a rigid rotor molecule with no electronic spin or orbital angular momentum, such as the singlet ground state of NaK, the total electronic angular momentum J is equivalent to R [33]. Rotational energies scale as $\frac{m_e e^2}{m_r a_0}$, corresponding to splittings of order GHz. Finally, the smallest energy scales are due to hyperfine splittings (if nuclear spin $I \neq 0$).

Many previous efforts toward ultracold molecules

Due to their complex internal structures, molecules are far more difficult to cool than atoms. Only in the last decade have these molecules entered the ultracold regime [93], defined as the temperature at which collisions must be treated quantum-mechanically.

Around the world, fewer than ten dipolar molecular species have been created in their ground state in the ultracold regime. The vast majority use a "bottom-up" approach of laser-cooling two atomic species, following the pioneering work done at JILA [174] and Innsbruck [64]. Here, ultracold atoms are magnetically associated into a loosely-bound dimer. Then, the dimer is coherently transferred into a longer-lived ground molecular state using lasers [174, 65, 224, 167, 183, 113, 202, 210, 249]. The list

of ultracold ground state molecules is likely to grow as experiments on heteronuclear mixtures progress. This approach of making molecules, utilized by our MIT team, thus far has created the highest phase-space densities of all molecular experiments [72], but is limited to creating molecules out of species that are laser-coolable (with optical cycling transitions).

Another approach is "top-down," directly cooling molecules to cold temperatures. Buffer-gas cooling, Stark deceleration, Zeeman deceleration, magneto-optical trapping with laser-cooling, and molasses-based approaches fall under this category (see Ref. [93] for a detailed description and references therein). Current available methods for direct cooling have thus far not achieved phase space densities close to degeneracy, but the field is progressing rapidly.

5.1.2 Myriad applications of ultracold molecules

In this section we highlight a few specific applications of dipolar molecules. For recent comprehensive reviews, refer to [93, 26, 135].

Realization of lattice spin models

Dipolar molecules in optical lattices are the ideal candidate to implement spin models that underlie diverse condensed matter systems [19, 163, 39, 235, 237, 231, 101, 17, 159, 223, 250]. For example, the t-J model is an important limit of the Hubbard model that represents hard-core electrons hopping on a lattice with tunneling amplitude t and nearest-neighbor Heisenberg interaction J. Thought to be a minimal model for high-T_c superconductivity [146], an extended t-J model can be realized with dipolar molecules occupying a single band of a 2D lattice [101], where two molecular states act as pseudospins:

$$\mathcal{H} = \mathcal{H}_0 + t \sum_{i<j,m}^{N} (c_{im}^\dagger c_{jm} + \text{h.c.}) + \frac{1}{2} \sum_{i \neq j}^{N} R_{ij}^{-3} \left(J_z \hat{S}_i^z \hat{S}_j^z + \frac{J_\perp}{2} (\hat{S}_i^+ \hat{S}_j^- + \hat{S}_i^- \hat{S}_j^+) \right) \quad (5.3)$$

Here, $\mathcal{H}_0$ is the single-molecule Hamiltonian, t is the intersite tunneling rate, $c_{im}^\dagger$ creates a molecule at site i, $m \in (\uparrow, \downarrow)$ labels the spin, $\hat{S}_i$ denotes the usual spin-1/2

operator, and $J_{\perp,z}$ are the coupling constants. The experimentalist's arsenal includes electric fields, choice of internal states (rotational/hyperfine levels), and microwaves to couple those states, leading to full and independent tunability of t, J_z, and $J_\perp$ [101]. This tunability within the ultracold molecule platform is compelling in comparison to competing platforms such as cold atoms, superconducting qubits, or trapped ions.

To be concrete, let us consider how this Hamiltonian acts on spins represented by the two lowest rotational states in a molecule, with tunneling turned off ($t = 0$, *i.e.,* by high optical lattice intensities). Then, Eq. 5.3 represents the XXZ model for quantum magnetism. Two spins in the same rotational state (with the same parity) experience zero dipole-dipole interaction, due to selection rules. Two spins of opposite parity, i.e., states $|\downarrow\rangle$ and $|\uparrow\rangle$, experience a strong dipole-dipole interaction whose sign and magnitude depend on the exact choice of the rotationally excited state $|\uparrow\rangle$: $|J, m_J\rangle = |1, -1\rangle, |1, 0\rangle$, or $|1, 1\rangle$, where m_J is the projection of the rotational quantum number J on the quantization axis. $J_\perp$ and J_z are typically different because of the anisotropy of the dipolar interaction; the strength of an electric field perpendicular to the lattice plane will smoothly tune the ratio between the coupling terms. Their magnitudes, for dipolar molecules with typical lattice spacing, gives an exchange coupling frequency of $\sim 1-10\,\mathrm{kHz}$, very high compared to other relevant energy scales of the system (temperature, spin decoherence) when the entropy per particle is low. Compared to atom-based quantum simulation, where nearest-neighbor interactions must be mediated by superexchange based on intersite tunneling, dipolar molecules interact two to three orders of magnitude more strongly. Furthermore, superexchange mediated by tunneling limits interactions to nearest-neighbor sites, but the dipolar interaction extends beyond nearest neighbors, allowing long-range coherent spin dynamics to propagate. Thus, molecules are a better-suited platform to study quantum magnetism under the anisotropic, tunable XXZ model.

Allowing molecules to tunnel would open the door to even richer phases. Unlike in cold atoms, where the coupling depends on tunneling via superexchange ($J \sim t^2$), a dipolar-molecule-based simulator can independently vary the J, t terms. The thermodynamic phase diagram of the 2D t-J model is not resolved with classical com-

puters, making quantum simulation an attractive option. Moreover, dynamical properties are even harder to compute numerically, compared to equilibrium properties, and have been studied in recent years on cold atom platforms, revealing measurements of spin and charge diffusion, optical conductivity, hole dynamics, and resistivity [176, 34, 4, 136]. With dipolar molecules, a greater array of strongly-correlated phenomena should emerge, free of the limitations posed by atoms' weak and isotropic interactions.

Quantum information processing

Ultracold molecules have been proposed as a platform for quantum computation [73, 145, 252]. A quantum computer is theorized to be much faster at solving certain tasks compared to classical computers. The quantum advantage lies in the *qubit*, consisting of a superposition of two quantum states $|\uparrow\rangle, |\downarrow\rangle$, which do not merely have to take on values of 0 and 1 as a classical bit does. To implement operations in a quantum computer, one needs a high-fidelity two-qubit operation whereby one qubit coherently changes its state depending on its interaction with another qubit and that qubit's state. Several physical systems have been proposed as possible platforms for quantum computing, including superconducting circuits, trapped ions, neutral atoms, and quantum dots, among others.

Proposals involving dipolar molecules [73, 145, 252] would have qubit states be opposite-parity states, *i.e.*, states coupled by considerable electric dipole matrix elements. Individual molecules would be held in some array (for instance, an optical lattice). Electric field gradients, optical tweezers, and ac fields would allow individual spectroscopic targeting of each site. Bits are coupled via the dipole-dipole interaction, allowing gate operations ($\sim$ kHz) much faster than typical decoherence timescales.

Quantum state-controlled chemistry

A new paradigm of quantum state-controlled chemistry is emerging with the ability to bring molecules to the cold and ultracold regimes [139, 47, 197, 12]. Each step of a complex chemical reaction, in principle, can be monitored when molecules' external

degrees of freedom and internal quantum states are controlled. Compared to atoms, molecules have more "tuning knobs" for their external degrees of freedom; an electric field changes how polar molecules collide. Internally, the array of quantum states is vast, opening up more channels for chemistry to occur. In ultracold reactions that only involve a few scattering partial waves, the rules of quantum mechanics govern the entire process. First-principles understanding of fundamental reaction processes in molecules would shed light on potential landscapes, intermediate states, and internal/external energy distributions – possibilities that are coming within reach for experiments [26].

One may expect chemical reactions to freeze out at ultracold temperatures, but several theory works and experiments show that this is not the case. At high temperatures, reaction rate constants Γ usually slow with decreasing temperature T, governed by the empirical Arrhenius equation: $\Gamma \propto \exp(-E_a/k_B T)$, where E_a is the reaction's activation energy. However, at sufficiently low temperatures, the de Broglie wavelength of relative motion exceeds the interaction range, rendering rate constants independent of energy and described instead by the Wigner threshold law [26]. The seminal theoretical work of Ref. [13] showed that at zero temperature, a chemical reaction ($F+H_2 \rightarrow FH+H$) proceeds rapidly with a constant value below 0.2 K, due to a near-threshold van der Waals resonance causing tunneling through the reaction barrier.

Experimentally, ultracold state-controlled chemistry can be studied by manipulating the incoming reactants (both internal state and relative motion) and measuring intermediate complexes or reaction products. Effects of quantum statistics on reaction rates were detected [179] in ultracold fermionic KRb molecules. Recent work has directly observed intermediates and products of the KRb+KRb$\rightarrow$ K_2+Rb_2 reaction via ionization spectroscopy [122, 155]. External fields can manipulate the internal state of the reactants as well as how they approach each other. An electric field applied on polar molecules was seen to accelerate dipolar collisions [175, 112]. Magnetically tunable Feshbach resonances between K atoms and NaK molecules were observed in [249]. Broadly, ultracold chemistry opens new doors for controlling the pathways

and outcomes of reactions. Future goals may include the design or manipulation of molecular reactions with targeted, applicable products [26].

5.1.3 Advantages of $^{23}Na^{40}K$

Of the almost infinite molecules out there, why do we work with $^{23}Na^{40}K$? To create the highest phase-space density of ultracold molecules, it is favorable to choose two species that are amenable to laser cooling, then associate two ultracold atoms together, a process pioneered by the JILA [174] and Innsbruck [64] teams. This technique, thus far, is the only successful method of obtaining quantum degenerate ground state molecules [72]. NaK combines two alkali species with convenient laser-cooling transitions, and reaching quantum degeneracy should be feasible in this case, as well. Prospects for this will be discussed in the final chapter of this thesis.

Moreover, NaK has a strong body-frame electric dipole moment of $d_0 = 2.72$ Debye. Of the bi-alkali diatomic molecules, only NaRb, LiK, LiRb, and LiCs have greater dipole moments [93]. NaK is the fermionic bi-alkali with the largest dipole moment that is chemically stable against two-body collisions in its absolute ground state, in the absence of trapping light that can cause photochemistry [57].

The electric dipolar interaction strength can be compared to other relevant energy scales like the Fermi energy E_F. The two become equal for a fully polarized molecule when

$$E_{DDI} = \frac{d_0^2}{4\pi\epsilon_0 R^3} \approx E_F = \frac{\hbar^2}{2m_{\mathrm{NaK}}} \left(\frac{6\pi^2}{R^3}\right)^{2/3} \tag{5.4}$$

This condition is fulfilled in NaK when R, the intermolecular spacing, is approximately $1\,\mu$m and the density is $\sim 10^{12}/\mathrm{cm}^3$. This density is realistic for both bulk and lattice experiments (where typical optical lattice spacings are $\sim$0.5 µm.) Thus, it is realistic to be in a regime where dipolar interaction dominates the many-body physics.

To conclude this section, I have discussed the advantages of polar molecules and provided basic background on diatomic level structure and the dipole-dipole interaction, focusing on the molecule we create and control: NaK.

5.2 Taming ^{23}Na^{40}K in the laboratory

This section will describe our team's efforts to develop quantum control over ultracold ^{23}Na^{40}K. Physics described here can mostly be understood at the single-particle level; effects involving engineered molecular interactions will be deferred to Chapter 6. First, the low-lying level structure is described, based on microwave spectroscopy. Then, the ability to coherently control the quantum state is discussed. Finally, I will describe our observation of long nuclear spin coherence times of two hyperfine states, and its implications for molecules in quantum simulation and computation.

5.2.1 Creation of ultracold ^{23}Na^{40}K

As this creation of ground state NaK is detailed in Jee Woo Park's thesis [181] and the publications [182, 183], I will only describe the minimum information to understand the following sections.

Molecule creation starts with preparing ultracold atomic mixtures. Following a procedure similar to the one detailed in Chapter 3, we started with a nearly equal population of $\sim 10^5$ Na and K atoms trapped in a crossed 1064 nm trap. The atoms were in the $|F, m_F\rangle = |1, 1\rangle$ and $|9/2, -7/2\rangle$ states, respectively, where m_F is the projection of the total angular momentum F on the quantization axis set by a magnetic field. We created Feshbach molecules at $\sim 6 - 10\,\%$ efficiency by radiofrequency injection of the K into the $|9/2, -9/2\rangle$ state at a magnetic field of 85.6 G. A Landau-Zener rf sweep lasting 1 ms was directed onto the mixture, with the frequency detuning linearly varied over 10 kHz. The rf frequency was centered above the bare hyperfine transition $|9/2, -7/2\rangle \rightarrow |9/2, -9/2\rangle$ by ~ 80 kHz, the magnitude of the dimer binding energy.

Two Raman lasers at 567 nm and 804 nm coherently transferred the Feshbach state into the rovibrational singlet ground state $X^1\Sigma^+, |v = 0, J = 0\rangle$ via an excited state with strong triplet-singlet mixing [182], in a process called STIRAP (Stimulated Raman Adiabatic Passage). The one-way transfer efficiency was $\sim$75%. The process is depicted in Fig. 5-3. Here, v, J are the vibrational and rotational quantum numbers, respectively (recall J is equivalent to the rotational quantum number in the $X^1\Sigma^+$

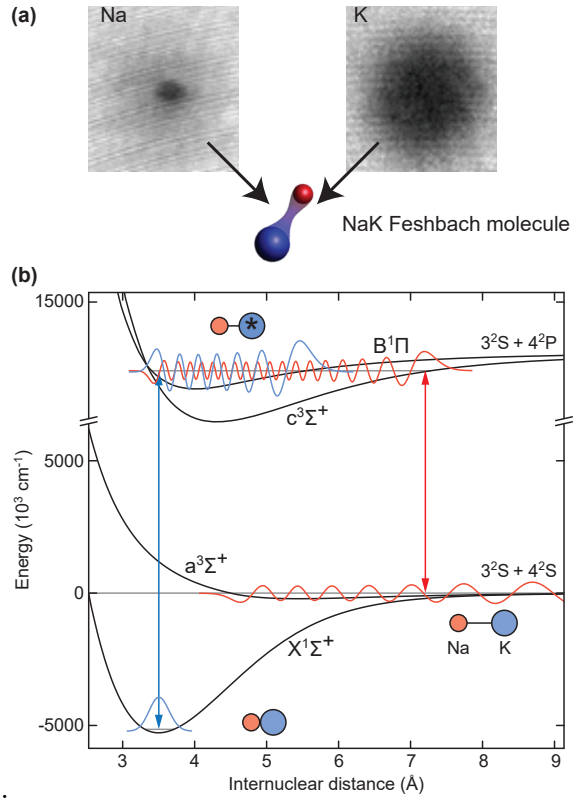

Figure 5-3: Creation of ground state ^{23}Na^{40}K molecules. **(a)** Ultracold mixtures of Na and K are associated into loosely-bound Feshbach molecules, which are then transferred into the absolute ground state via the STIRAP process, depicted in **(b)**. The relevant molecular potentials are shown for the transfer to the rovibrational ground state $|v = 0, J = 0\rangle$ in the $X^1\Sigma^+$ level. The Feshbach molecular occupies the highest vibrational $|v = 19\rangle$ state of the $a^3\Sigma^+$ potential. In the excited states, spin-orbit coupling mixes the $c^3\Sigma^+$ $|v = 35, J = 1\rangle$ and $B^1\Pi$ $|v = 12, J = 1\rangle$ levels with 64% triplet and 36% singlet character [182]. The red and blue curves represent the radial wavefunctions associated to each state. Reproduced from [183].

ground state, see Sec. 5.1.1). The transfer was also hyperfine selective, with $m_{I_{\mathrm{Na}}} = 3/2, m_{I_{\mathrm{K}}} = -4$ the respective components of the nuclear spins of Na and K along the magnetic field. Depending on initial atom preparation, we created 1000-3000 ground state molecules at $T \approx 600\,\mathrm{nK}$.

5.2.2 Low-lying level structure

After creating the molecules, our first experimental step was to understand the low-lying energy levels. In this section I describe the hyperfine and rotational structure of ground vibronic NaK molecules. Then, I discuss our microwave spectroscopy experiment and compare our empirically determined microwave transitions with a theoretical model. Many results from this section can also be found in Ref. [239].

Hyperfine structure in rotational ground state

In the electronic ground (spin-singlet) state, $X^1\Sigma^+$, the hyperfine structure arises solely from the nuclear spins of ^{23}Na and ^{40}K, I_{Na}=3/2 and I_{K}=4, and their interplay

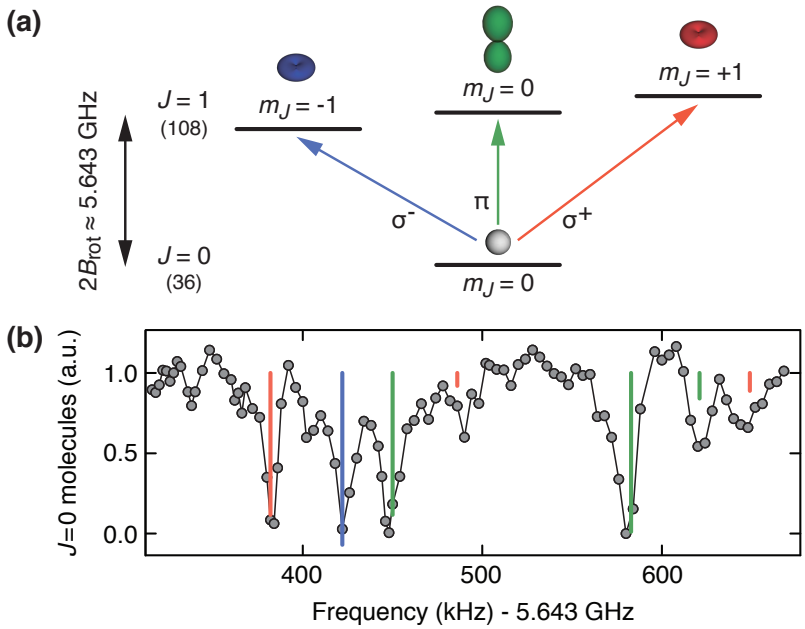

Figure 5-4: **Rotational excitations of ^{23}Na^{40}K molecules from the rovibrational ground state**, reproduced from [239]. J=0 is coupled to the excited J=1 states using microwave radiation with π, $\sigma^{\pm}$ polarization. **(a)** Simplified schematic omitting hyperfine interactions, such that m_J is a good quantum number. **(b)** Spectrum of rotational transitions between the lowest hyperfine state of J=0 and J=1 at B = 216.6 G and E = 0. The position (height) of each vertical bar indicates the transition frequency (strength) according to our theoretical model. The calculated π-transition strength is scaled up by 1.9, accounting for the radiation characteristics of our antenna. During microwave exposure, the optical dipole trap is switched off to avoid differential Stark shifts.

with the rotation of the molecule. This leads to $(2I_{\mathrm{Na}}{+}1)(2I_{\mathrm{K}}{+}1) = 36$ hyperfine states in the rotational ground state J=0, and 108 states in the first rotationally excited state J=1. For B$>$ 2 G and zero electric field, the hyperfine structure of the rotational ground state J=0 is dominated by the Zeeman effect of the ^{23}Na and ^{40}K nuclei; here, the states $\mathrm{X}^1\Sigma^+|v{=}0, J{=}0, m_J{=}0, m_{I_{\mathrm{Na}}}, m_{I_{\mathrm{K}}}\rangle$ form a good basis. The lowest energy hyperfine state is $\mathrm{X}^1\Sigma^+|v{=}0, J{=}0, m_J{=}0, m_{I_{\mathrm{Na}}}{=}3/2, m_{I_{\mathrm{K}}}{=}{-}4\rangle$, abbreviated by $|0, 0, 3/2, -4\rangle$ in the following.

Rotational transitions

The rotational energy of NaK in its vibronic ground state is given by $\hbar^2 J(J+1)/2I$, where I is the moment of inertia. The quantity $\hbar^2/2I$ is quantified by the rotational

constant $B_{\rm rot}$ of v=0. Therefore, the frequencies of rotational transitions from J=0 to J=1 are approximately $2B_{\rm rot} \approx h \times 5.643\,\mathrm{GHz}$.

Neglecting nuclear spins, the J=1 state splits into three sub-levels with m_J=0, ±1, giving rise to three electric dipole-allowed transitions from J=0 to J=1, as schematically shown in Fig. 5-4(a). However, hyperfine interactions strongly couple rotation and nuclear spin, and additional states in the J=1 manifold with different nuclear spin projections becoming accessible. The only quantum number that remains good at all magnetic and electric fields is the projection of the total angular momentum $m_F = m_J + m_{I_{\rm Na}} + m_{I_{\rm K}}$. From the initial state, only those J=1 hyperfine states that satisfy the selection rule Δm_F=0, ±1 can be reached using $\pi, \sigma^{\pm}$ polarization, respectively.

Microwave spectroscopy on $J = 1$ states

This section discusses our microwave spectroscopy experiment to probe low-lying levels in NaK and reconciles our observed transition frequencies with the molecular Hamiltonian, which will be presented in Eq. 5.5.

To resolve the hyperfine structure of the first excited rotational state, we apply a microwave field onto molecules initialized in the absolute ground hyperfine state. This microwave can drive the electric dipole transition to hyperfine states in $J = 1$. The microwave includes all three polarization components, π, σ^+, σ^-, with respect to the quantization axis, which is set by the external magnetic field. We detect loss of $J = 0$ molecule number when microwave frequency addresses an allowed transition. A spectrum is displayed in Fig. 5-4(b), showing the remaining population in the absolute ground state after microwave exposure.

The spectra are described by a theoretical model of the excitations in $v = 0$, $\mathrm{X}^1\Sigma^+$, given by the molecular Hamiltonian

$$H_{\rm mol} = H_{\rm rot} + H_{\rm Z} + H_{\rm S} + H_{\rm hf} \tag{5.5}$$

Here, $H_{\rm rot} = B_{\rm rot} J(J+1)$ is the rotational contribution discussed previously. The

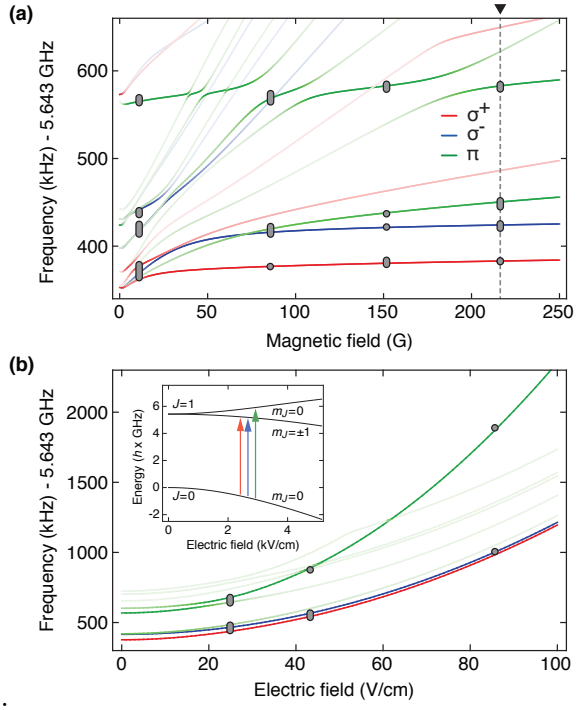

Figure 5-5: **Rotational spectroscopy in magnetic and electric fields**, reproduced from [239]. **(a)** Spectra versus B-field with no electric field. Gray markers indicate the observed transition frequencies; colored lines show the calculated transition frequencies for σ^- (blue), π (green), and σ^+ (red) transitions using best-fit parameters. The vertical dashed line indicates the spectrum of Fig. 5-4(b). **(b)** Spectra versus E-field, with gray markers showing observed transition frequencies. A magnetic field of 85.6 G was applied in the same direction as the electric field. The observed Stark shift is used to calibrate the electric field assuming a dipole moment of $d_0 = 2.72\,\mathrm{D}$. The inset shows the expected Stark shift up to 5 kV/cm.

Zeeman term $H_\mathrm{Z} = -\mu_\mathrm{N}(g_\mathrm{rot} m_J + g_\mathrm{Na} m_{I_\mathrm{Na}} + g_\mathrm{K} m_{I_\mathrm{K}})B$ captures the effect caused of the nuclear magnetic moments of ^{23}Na and ^{40}K and the weak rotational magnetic moment $g_\mathrm{rot}\mu_\mathrm{N}$, with μ_N the nuclear magneton. The dc Stark effect is $H_\mathrm{S} = -\vec{d}_0 \cdot \vec{E}$, where $\vec{E}$ is the external electric field.

Hyperfine interactions cause H_mol to have non-diagonal components our basis. Two relevant hyperfine contributions are $H_\mathrm{eq} = -\sum_{i=\mathrm{Na,K}} e(\nabla\mathbf{E})_i \cdot \mathbf{Q}_i$ and $H_\mathrm{ss} = c_4 \vec{I}_\mathrm{Na} \cdot \vec{I}_\mathrm{K}$. H_eq describes the interaction of the intramolecular electric field gradient $(\nabla\mathbf{E})_i$ at nucleus i with the respective nuclear electric quadrupole moment $e\mathbf{Q}_i$, where e is the electron charge. H_eq vanishes for J=0 but dominates for J=1. Matrix elements of $-e(\nabla\mathbf{E})_i \cdot \mathbf{Q}_i$ are proportional to the quadrupole coupling constant $(eqQ)_i$. H_ss denotes the relatively weak scalar nuclear spin-spin interaction, present both for J=0 and J=1. Matching observations from our spectroscopy experiment with the model Hamiltonian produced tighter estimates for various molecular constants including the B_rot, $(eqQ)_\mathrm{K}$, $(eqQ)_\mathrm{Na}$, and the c_4 coefficients; a summary may be found in Table 1 of Ref. [239].

Additionally, we studied the dependency of energy levels with respect to tuning

external fields. Spectra taken at various magnetic and electric fields show the evolution with respect to the Zeeman and Stark terms in Fig. 5-5. For sufficiently high electric fields $E \sim B_{\mathrm{rot}}/d_0$, only m_J and not J remains as a good quantum number and the spectrum simplifies significantly. This is a result of polarizing the NaK wavefunction so that it aligns with $\vec{E}$.

To conclude this section, we performed microwave spectroscopy on the ground and first excited rotational states of NaK, resulting in spectra that were accurately modeled by the single-molecule Hamiltonian in Eq. 5.5.

5.3 Lifetime

To use molecules as a quantum resource, it is not sufficient to understand their energy spectra. We also require long lifetimes of our molecular ensembles for many purposes, *e.g.,* simulation of many-body dynamics or performing sufficiently many qubit gates for quantum computation. This section discusses measurements of bulk NaK lifetimes in a harmonic optical potential.

The J=0 state lifetime is measured by creating ground state molecules trapped by a 1064 nm laser, waiting for various hold times, reversing the STIRAP procedure, and imaging the remnant atoms. Molecules that transfer into other quantum states (via inelastic collisions and/or photon absorption) or leave the trap for any reason would not be addressed by the reverse STIRAP procedure. Therefore, they would not transfer to the free atom state and thus contribute to the loss signal. The molecule population decays to half its original value in $\sim 3.2\,\mathrm{s}$, as shown in Fig. 5-6(a).

We can also measure the excited rotational state lifetime by transferring the initial population from $J = 0$ to the lowest hyperfine state of $J = 1$ using a microwave π-pulse. After a wait time, the same π-pulse is applied to transfer remaining molecules back to the ground state, where they are imaged as before. We observe collisional lifetimes of 2.3 s, which is comparable to the ground state lifetime; both data sets were taken for an initial peak density of $0.7 \times 10^{11}\,\mathrm{cm}^{-3}$ and a temperature of 400 nK. These data were first presented in Ref. [239].

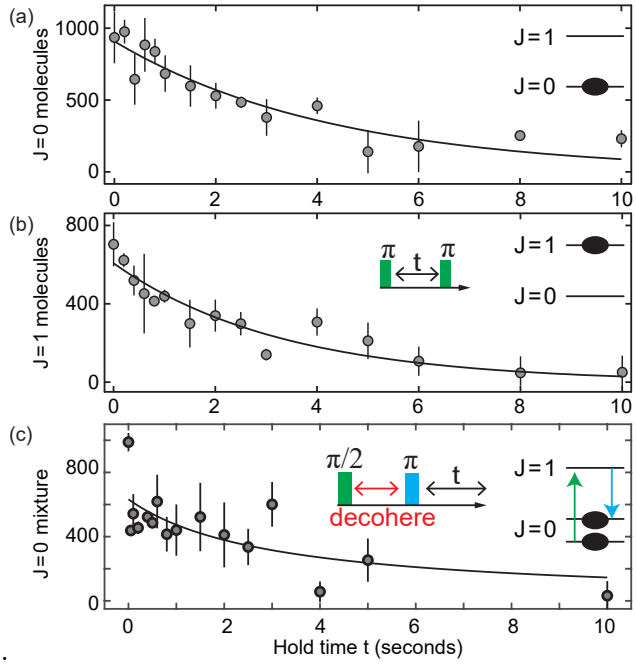

Figure 5-6: **Collisional lifetimes of NaK molecules** in the **(a)** J=0 ground hyperfine state and **(b)** J=1 lowest hyperfine state, adapted from [239]. **(c)** shows the lifetime of a 50:50 mixture of two J=0 hyperfine states. Data points show the average of typically three experimental runs; the error bars denote the standard deviation of the mean. The two-body lifetimes for all three cases are comparable, with half-lives of roughly 3 s.

Intriguingly, a 50:50 mixture of two J=0 rotational states shows a similar lifetime (Fig. 5-6(c)). This was measured by applying a resonant $\pi/2$-pulse on J=0 molecules to create a superposition with the lowest J=1 hyperfine state, and waiting for trap ac Stark shifts to cause global decoherence in the sample for 2 ms (see next section). Next, a downleg microwave π-pulse transfers the J=1 molecules into another hyperfine state in J=0, the $|0,0,3/2,-3\rangle$ state. The population is now a 50:50 decohered mixture of the $|0,0,3/2,-4\rangle$ and $|0,0,3/2,-3\rangle$ states. Collisions then occur for a variable hold time. Imaging and counting of $|0,0,3/2,-4\rangle$ molecules are performed as before. In a decohered mixture with distinguishable particles, s-wave collisions can occur, rather than only p-wave collisions between identical fermions. The strong dependence of lifetime on quantum statistics was previously studied in [179]. However, our mixture of two J=0 states did not show greater inelastic collision rates to within our experimental signal. Perhaps the mixture was not fully decohered at the local (nearest neighbor molecule) level but only globally across the ensemble. Future work is necessary to investigate s- and p-wave collisional lifetimes.

What is the origin of these lifetimes, which are far shorter than the background-gas limited vacuum lifetimes $\gg 10$ s for atoms at equivalent densities? Though NaK is stable against two-body collisions in free space, the trapping light is predicted to

photoexcite two NaK molecules in short range to highly excited complexes, which will be lost with near-unit probability [57]. This light-assisted chemistry has been experimentally detected and characterized in other bialkali species [102, 155]. Assuming that the lifetime is limited by inelastic two-body collisions, we therefore model the number density evolution of molecules as

$$\frac{dn(t)}{dt} = -\beta n(t)^2 \tag{5.6}$$

where n is the NaK density. The solution is $n(t) = n(0)/(1 + \beta n(0)t)$, where β is the rate coefficient. Fitting to our loss curves results in $\beta \approx 2 \times 10^{-11}\,\mathrm{cm}^3/\mathrm{s}$ for typical 1064 nm trapping intensities of $\sim \mathrm{kW/cm}^2$ [183, 239, 248].

The dependence of the $|0, 0, 3/2, -4\rangle$ lifetime versus trap intensity was studied by adiabatically ramping the dipole traps to various values. Results, shown in Fig. 5-7, suggest a monotonic increase of loss rate with intensity. We will later make use of this light-induced loss mechanism to measure dipolar collisions in Ch. 6. Ways to mitigate this loss mechanism will be discussed in Ch. 7.

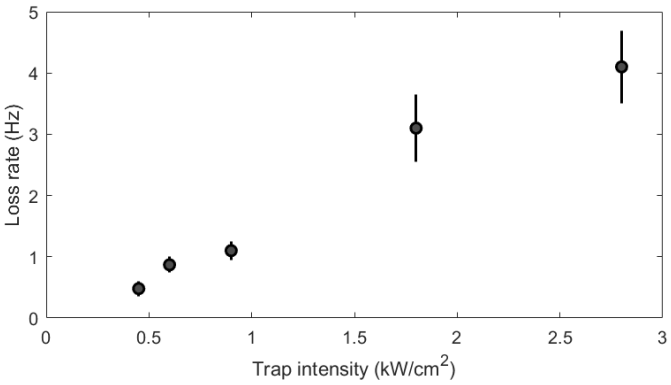

Figure 5-7: **Molecule loss rate versus trap intensity.** The two-body collisional loss rate $\beta n(0)$ of the absolute ground state as a function of the 1064 nm trap intensity. We point out that there is a dependency of the loss rate on initial density and temperature as well as trap intensity.

5.4 Coherence

One prerequisite for using molecules as a quantum resource entails the manipulation of internal states with long coherence times. This allows high-resolution spectroscopy, the ability to perform many gate operations for quantum information purposes, and generally, a separation of timescales between interesting many-body

physics and lossy processes. In this section I examine coherence between rotational states and between hyperfine states through the techniques of Rabi and Ramsey spectroscopy. One limitation of coherence, differential light shifts, will be analyzed.

5.4.1 Rabi oscillations

We can coherently transfer population between the ground and excited rotational states, as demonstrated by the Rabi oscillations depicted in Fig. 5-8. Here, a constant microwave pulse was applied for a varied time, coupling the ground state to the lowest energy hyperfine state of J=1, which is dominated by $|1,1,3/2,-4\rangle$ character. After the pulse, the number of remaining $|0,0,3/2,-4\rangle$ molecules was counted.

We note that the observed Rabi rate of $\sim 4\,\mathrm{KHz}$ is comparable to a typical Rabi rate for an atomic hyperfine (magnetic dipole) transition. Yet the coupling here is electric dipole-allowed and could theoretically be much stronger by the ratio of the electric/magnetic dipole matrix elements, $ea_0c/\frac{e\hbar}{m_e} = 1/\alpha$, where α is the fine structure constant. Constructing a microwave antenna with better impedance matching should allow microwave Rabi rates on the 100 kHz-1 MHz scale.

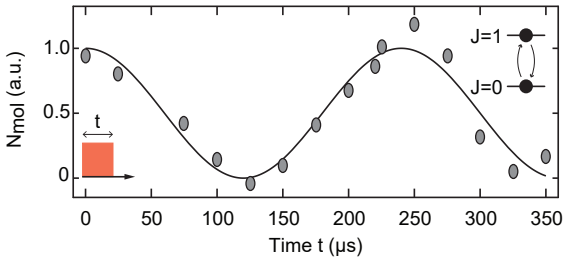

Figure 5-8: **Coherent microwave transfer to the J=1 state**, reproduced from [239]. High-contrast Rabi oscillations between $|0,0,3/2,-4\rangle$ and the lowest energy hyperfine state of J=1 at B=85.6 G and E=0.

..

5.4.2 Ac polarizability of ^{23}Na^{40}K and rotational coherence

In this section, we discuss the effect of light shifts on the level structure and rotational coherence properties of NaK. We study the polarizability of the rotational ground and first excited state due to the 1064 nm trap laser, and its dependence on intensity and relative orientation of the quantization axis and laser polarization. We point out that rotational coherences and anisotropic polarizabilities were studied in KRb [172], CaF [41], and RbCs [24]. Recently, rotational coherence times were

extended to over 10 ms by using a magic dc field and polarization angle of 1550 nm light in NaK by the Munich group [211].

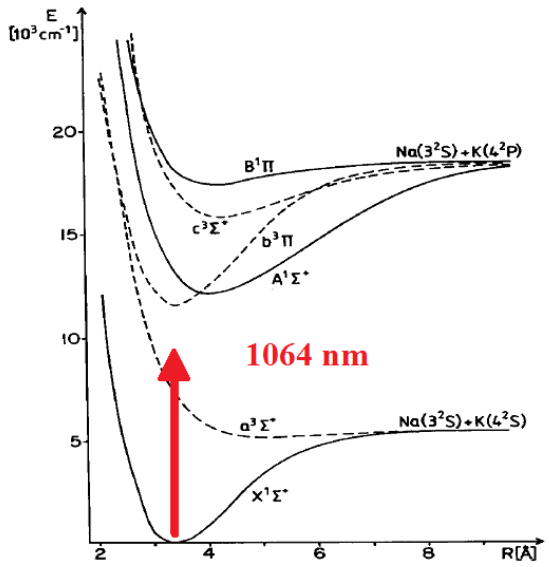

Figure 5-9: **Ac Stark shifts in NaK.** Depiction of trapping light energy (1064 nm / 9398 cm^{-1}) relative to relevant NaK potentials. For trapping of the $X^1\Sigma^+$ state, the excited $^1\Sigma^+$,$^1\Pi$ potentials are most relevant [151].

Any experimentalist, particularly one working with molecules, views the optical trapping laser as both a blessing and curse. Clearly, optical dipole traps are workhorses of AMO experiments, responsible for confining and levitating particles against gravity due to the dipole force from the ac Stark shift. However, light causes unwanted effects – decoherence and uncontrolled shifting of levels – due to intensity gradients (beam inhomogeneity) and differential coupling of light to various molecular states. Light can even cause loss through excitation of a single molecule, described by the imaginary portion of the polarizability, or by aiding an inelastic binary molecular collision [57] (see Sec. 5.3). Light-induced loss of molecules will be further discussed in Chapter 6; for now we restrict our investigation to the real part of the ac polarizability, responsible for trapping and light shifts. Compared to atoms, molecules have a far greater number of electric dipole-allowed optical transitions, increasing the complexity of ac polarizability calculations and rendering light-induced decoherence more problematic.

How does ac polarizability affect rotational coherence times? Consider the microwave transition between $J=0$ and $J=1$. The far-detuned ac Stark shift is proportional to laser intensity by the polarizability α, but the polarizability generally

differs between two rotational states, leading to a difference in trapping potentials $U(r)$(see Fig. 5-10(B)). The microwave resonance between two states in $J=0,1$ will therefore change over the spatial extent of the trap. One microwave field at a fixed frequency is unable to uniformly interrogate the entire sample, leading to decoherence.

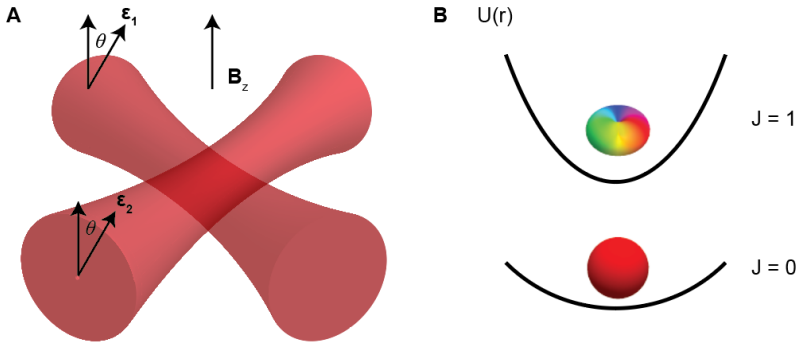

Figure 5-10: **Schematic of the setup to study differential ac polarizability** (**A**), with molecules trapped in a crossed 1064 nm trap in the x-y plane, with quantization defined by a magnetic field in z. The angle θ between the beam polarizations ϵ and z will affect the first order differential ac Stark shift between rotational states, shown in (**B**). Cartoons depict molecule wavefunctions in the $|J=0, m_J=0\rangle$ and $|1, \pm 1\rangle$ states.

We describe this differential ac Stark shift with the Hamiltonian modified from Eq. 5.5,

$$H_{\mathrm{mol}} = H_{\mathrm{rot}} + H_{\mathrm{Z}} + H_{\mathrm{S}} + H_{\mathrm{hf}} + H_{\mathrm{pol}}(I_{\mathrm{trap}}(\vec{r}), \alpha(\nu, \vec{\epsilon})) \tag{5.7}$$

The H_{pol} term of the Hamiltonian captures the ac polarizability as distinct from the dc Stark response in H_{S}. It is a function of trap intensity $I_{\mathrm{trap}}(\vec{r})$, trap wavelength ν, and laser polarization $\vec{\epsilon}$. We introduce the reduced radial electronic polarizabilities $\alpha_{\parallel}, \alpha_{\perp}$, coming from contributions parallel and perpendicular to the intermolecular axis, which capture the average effect from all electronically excited potentials $^1\Sigma^+$,$^1\Pi$ [151]. For NaK, Ref. [151] calculated the values of $\alpha_{\parallel}$=1013.4 a.u. and $\alpha_{\perp}$=361.46 a.u. for a 1064 nm trap, where the atomic unit of polarizability is $(ea_0)^2/E_h$, with e the electron charge and E_h the Hartree energy. (To change to S.I. units of MHz/(W/ cm^2), multiply by 4.68645×10^{-8}.) We will use these values for the remainder of our calculations.

How the molecules experience the ac Stark shift heavily depends on their orientation with respect to the ac field. The $J = 0$ state is spherical and its polarizability for trap wavelength ν has no angular dependence:

$$\alpha_{|J=0,m_J=0\rangle}(\nu) = \frac{1}{3}(\alpha_{\parallel}(\nu) + 2\alpha_{\perp}(\nu)) \tag{5.8}$$

In contrast to the $|0,0\rangle$ state, $J=1$ states have anisotropic wavefunctions. For example, the $|J=1, m_J=0\rangle$ corresponds to a p-orbital aligned along the z-axis, so its polarizability in this hyperfine-free picture is largest when the ac field polarization $\vec{\epsilon}$ is parallel to $\hat{z}$, the quantization axis set by either the magnetic or electric field. Let θ parametrize the angle between $\vec{\epsilon}$ and $\hat{z}$. $J=1$ polarizabilities can be modeled using a 3×3 Hamiltonian in the $|J, m_J\rangle = (|1,0\rangle, |1,-1\rangle, |1,1\rangle)$ basis, neglecting hyperfine couplings,

$$H_{\text{pol, J=1}} = \begin{pmatrix} -\alpha_{11}I_{\text{trap}} + E_1 & -\alpha_{12}I_{\text{trap}} & -\alpha_{13}I_{\text{trap}} \\ -\alpha_{12}I_{\text{trap}} & -\alpha_{22}I_{\text{trap}} + E_2 & -\alpha_{23}I_{\text{trap}} \\ -\alpha_{13}I_{\text{trap}} & -\alpha_{23}I_{\text{trap}} & -\alpha_{33}I_{\text{trap}} + E_3 \end{pmatrix} \tag{5.9}$$

where α_{ij} is a function of $(\alpha_{\parallel}, \alpha_{\perp})$ and is given explicitly in Ref. [172], and E_i is the energy of the state for $I_{\text{trap}}=0$. Using this formalism, the expected $J=0 \rightarrow 1$ transition energies can be estimated, and the three lowest rotational transitions from $|0,0,3/2,-4\rangle$ are shown in Fig. 5-11(A) as a function of θ.

However, adding hyperfine couplings lifts the degeneracies between different nuclear spin states with the same projection m_J. Though $|J, m_J, m_{I_{\text{Na}}}, m_{I_{\text{K}}}\rangle$ are strictly not good quantum numbers for $J=1$, we will still use these labels for a rotationally state $|e\rangle$, where the labels denote the component maximized by $|\langle e\,|J, m_J\, m_{I_{\text{Na}}}, m_{I_{\text{K}}}\rangle|^2$, for the remainder of this section. Including H_{pol} and hyperfine couplings into the 144-basis Hamiltonian of Eq. 5.7 results in the calculated transitions shown in Fig. 5-11(B).

Theory calculations can be confirmed by spectroscopy. Resonances were detected by exposing $|0,0,3/2,-4\rangle$ molecules to a microwave π-pulse at various frequencies

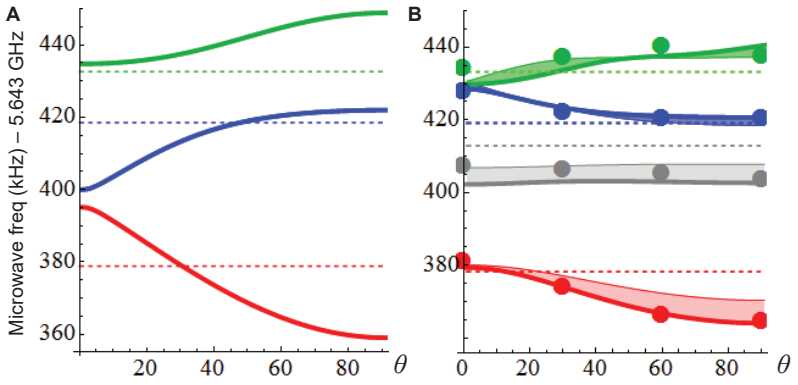

Figure 5-11: **Energy shifts of the $J=0 \rightarrow 1$ transition due to the ac Stark effect**, at $I=4000\,\mathrm{W/cm^2}$ and $\mathrm{B}=130\,\mathrm{G}$. (**A**) Calculated transition energies in the simple 3×3 basis for the σ^- (red), σ^+ (blue), and π (green) transitions as a function of the angle between the quantization axis and laser polarization axis. Dotted lines show the bare transitions absent any trap light. (**B**) Including hyperfine structure, the levels are further shifted and mixed due to nuclear electric quadrupole couplings. Shadings represent additional shifts from intensity variations in the Gaussian trap. Circles show observed transitions. At $\theta = 14°$, the lowest frequency transition to predominantly the $|1,1,3/2,-4\rangle$ state has a magic condition. There, the three higher-lying states predominantly have respective characters of $|1,0,3/2,-2\rangle$, $|1,0,3/2,-4\rangle$, and $|1,0,3/2,-1\rangle$, not corresponding to the naive state-labelling of (A). This demonstrates that the 3×3 model is insufficient to explain the ac polarizability; hyperfine interactions must be included.

near $2B_{\mathrm{rot}}$ and imaging the remainder $J=0$ molecules. Positions were determined by fitting a Gaussian to the center of the absorption feature. Fig. 5-11(B) shows the differential ac Stark shift as a function of the trap polarization angle, which was experimentally varied by rotating a half-wave plate in the 1064 nm trap beam path. Only the full 144-state model and not the naive 3×3 model captures the observed transitions. We observed shifting and mixing of levels as a function of angle, and we noted a "magic" condition for the lowest transition at around 14°. Here, the ground and excited rotational states should feel the same trapping potential.

We measured rotational coherence times as a function of angle with Ramsey spectroscopy to study the effect of the magic polarization angle. Starting with the sample in $J=0$, we applied a $\pi/2$ pulse to create a nearly-equal superposition of the $|0,0,3/2,-4\rangle$, and $|1,1,3/2,-4\rangle$ state. After a varied hold time for field-free Ramsey precession, the pulse was repeated. Ground state molecules were imaged, and

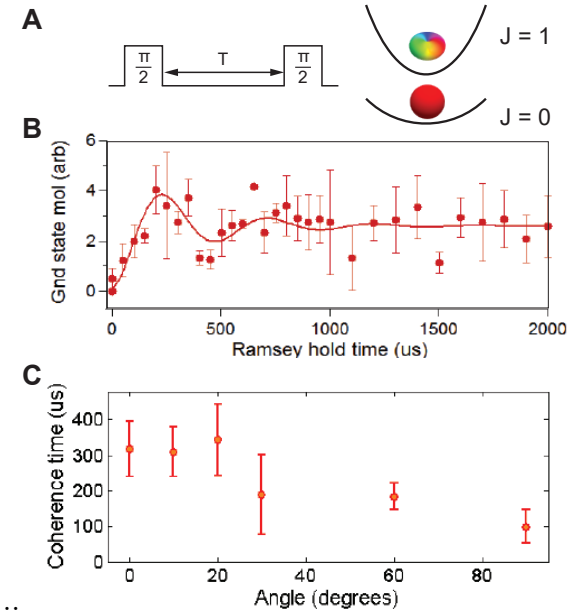

Figure 5-12: **Ramsey spectroscopy between J=0 and J=1 rotational states.** (**A**) Schematic of procedure, with a $\pi/2$ MW pulse transferring the ground state to a superposition state, a varied Ramsey hold time T, and the final readout pulse. (**B**) A sample Ramsey evolution curve taken at θ=20°, with the solid line fitted by Eq. 5.10. (**C**) Coherence times for various angles. At approximately $10-20°$, the differential polarizability vanishes, resulting in a coherence time $\sim$ 3 times longer than the worst-case scenario at 90°.

their number evolution $N(T)$ is shown in Fig. 5-12(B). The coherence times τ_2^* were extracted by a least-squares fit to the form

$$N(T) = N_0 + A\sin(\omega T - \phi_0)\exp(-T/\tau_2^*) \tag{5.10}$$

where N_0, A, and ϕ_0 are free fitting parameters. As expected from the differential polarizability calculation, angles near 14° resulted in longer coherence times, approaching 0.3 ms.

To conclude, we studied how differential light shifts affect the observed energy splittings, and we moderately improved the rotational coherence times of $|0,0\rangle, |1,0\rangle$ by choosing the "most magic" angle. However, further work is required to boost coherence times beyond $\sim$ ms scales, which is needed for schemes involving multiple levels interacting via dipole-dipole interactions. An intriguing prospect that mitigates light-induced decoherence altogether is a repulsive box potential, discussed in Chapter 7.

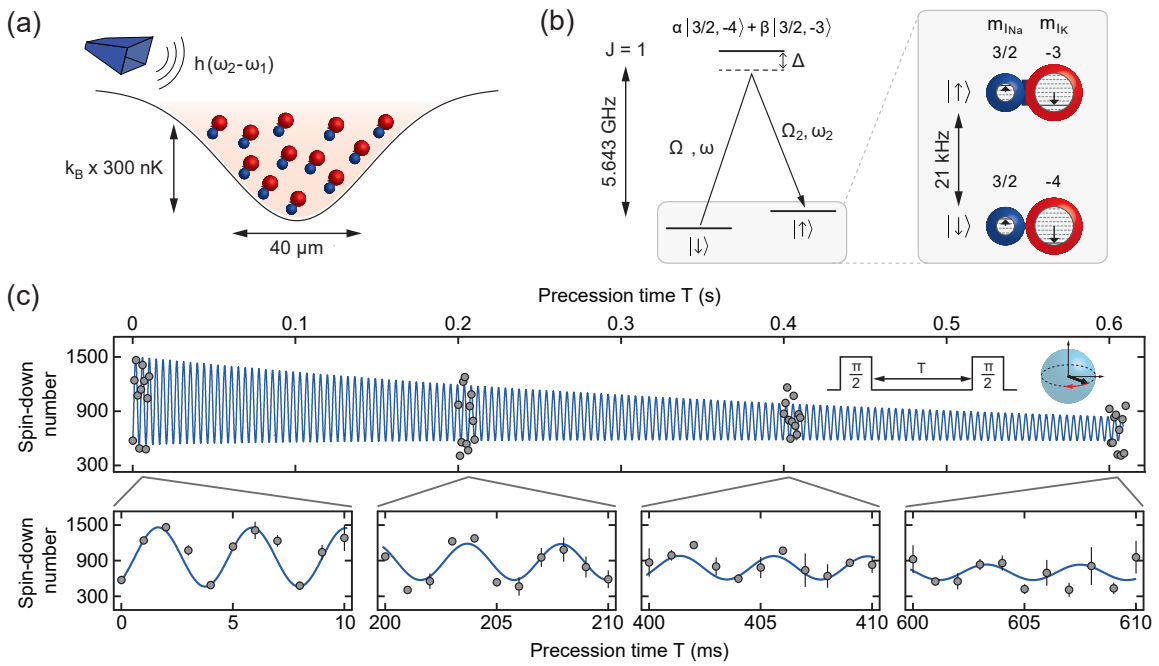

Figure 5-13: **Coherent Ramsey precession of nuclear spin states in ^{23}Na^{40}K.** **(a)** The ensemble was held in a ODT, and microwave fields were applied to coherently couple two nuclear spin states $|\downarrow\rangle$=$|m_{I_{\mathrm{Na}}}$=3/2, $m_{I_{\mathrm{K}}}$= − 4$\rangle$ and $|\uparrow\rangle$=$|3/2,-3\rangle$ in the rotational ground state J=0. **(b)** Level scheme of the two-photon microwave coupling. $\Omega_{1(2)}$ and $\omega_{1(2)}$ correspond to the Rabi coupling and microwave frequency, respectively, of the up-leg (down-leg) rotational transition. The ground and first excited rotational states J=0 and J=1 are separated by $h \times 5.643$ GHz. Δ denotes the single-photon detuning from the intermediate state, typically about $h \times 12$ kHz. The nuclear spins $|\downarrow\rangle$ and $|\uparrow\rangle$ are separated by about $h \times 21$ kHz. **(c)** Evolution showing $|\downarrow\rangle$ number versus precession time, upon applying the Ramsey sequence (see inset). The solid line is a fit of the complete data set with a single oscillation frequency and phase. Figure reproduced from [185].

5.4.3 Second-scale nuclear spin coherence times

This section details our team's measurement of coherence between hyperfine levels of NaK molecules within $J = 0$. Results of this section can also be found in Ref. [185]. Compared to rotational coherences, hyperfine coherences are expected to be longer because these states have no electric dipole transition matrix element. We measured hyperfine coherence times approaching one second, corresponding to sub-Hertz frequency resolution.

We began with absolute ground state molecules at B= 85.6 G and measured the coherence between the initial, lowest hyperfine level $|0, 0, 3/2, -4\rangle$ and the first excited

hyperfine level $|0,0,3/2,-3\rangle$, denoted by $|\downarrow\rangle$ and $|\uparrow\rangle$ in the following. A two-photon microwave pulse was applied to prepare each of the molecules in a superposition of these two levels, as shown in Fig. 5-13(b). For the coherent transfer between $|\downarrow\rangle$ and $|\uparrow\rangle$, a hyperfine level with mixed $m_{I_K} = -4$ and -3 character in the rotationally excited J=1 state was used as an intermediate state.

Ramsey precession was initiated by applying a $\pi/2$-pulse near the microwave two-photon resonance. Subsequently, the superposition state underwent field-free time evolution with respect to the unperturbed resonance frequency ω_{res}. After a hold time T, we applied a second $\pi/2$-pulse and recorded the number of molecules in $|\downarrow\rangle$, as shown in Fig. 5-13(c). By fitting the observed Ramsey precession with a model that incorporates the decay of molecule number and coherence (see supplementary materials of [185]), we extracted the molecule lifetime T_1 and the coherence time T_2^*. At a molecular lifetime of T_1=1.9(5) s, we observed a coherence time of T_2^*=0.7(3) s, a thousand times longer than our rotational coherence times.

The oscillation frequency of the Ramsey precession is given by the difference of the two-photon microwave drive, $\omega_1 - \omega_2$, and the unperturbed resonance frequency, ω_{res}. From this, we extracted the energy difference between $|\downarrow\rangle$ and $|\uparrow\rangle$ to be $\omega_{\text{res}} = 2\pi \times 20.514(10)$ kHz at a magnetic field of 85.6 G, which allowed us to precisely determine the weak nuclear spin-spin coupling constant of ^{23}Na^{40}K as $c_4 = -409(10)$ Hz.

Utilizing the long coherence time between $|\downarrow\rangle$ and $|\uparrow\rangle$, we recorded high-resolution Ramsey fringes in the frequency domain. These fringes can be a sensitive probe to measure small variations in the resonance frequency due to trap ac Stark shifts and molecular density, as shown in Fig. 5-14. The spectrum was measured by varying the microwave drive frequency, $\omega_1 - \omega_2$, while keeping the precession time T between the $\pi/2$-pulses constant. The spacing between the Ramsey fringes is given by $2\pi/T$. By varying trap intensities and monitoring the phase variation of the spectra, we detected differential energy shifts between $|\downarrow\rangle$ and $|\uparrow\rangle$ with Hertz-precision. These differential light shifts were consistent with being the bottleneck for our measured T_2^* time. However, our lack of observable density shifts show that interparticle interactions

do not yet play a role for these densities – perhaps unsurprising given that there is no expected dipole-dipole coupling for these states, which are both in J=0.

Our observation of second-scale coherence times in trapped ^{23}Na^{40}K molecules supports the use of molecules as a versatile quantum resource. Coherence times could be even further enhanced by exploiting "magic" conditions of the trap wavelength, intensity, polarization angle, or electric field that suppress differential light shifts [211].

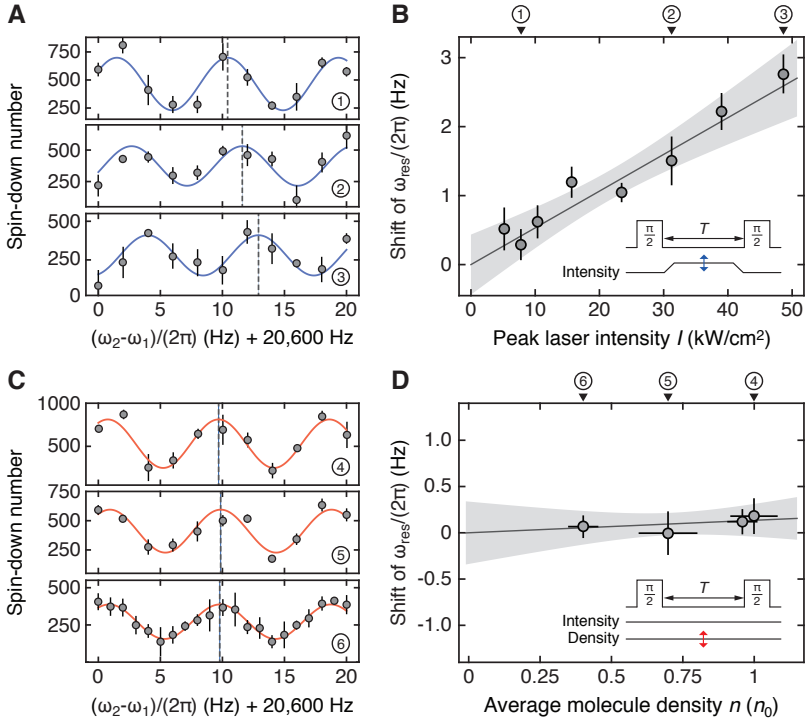

Figure 5-14: **Hertz-level light shifts and absence of density-dependent clock shift.** A shift in the Ramsey fringes corresponds to a change in the resonance frequency between $|\downarrow\rangle$ and $|\uparrow\rangle$. **(A)** Ramsey spectroscopy for various dipole trap laser intensities. The intensity of the trap laser was varied during the free precession time T=112 ms. The solid lines show sine-fits, used to extract the phase of the Ramsey fringes. For the fits, the oscillation frequency was set by the precession time, and only the phase and the amplitude of the oscillations were taken as free parameters. **(B)** Shift of the resonance frequency as a function of dipole trap intensity. A linear fit (solid line) yields a slope of 50(10) mHz/(kW/cm^2); the grey-shaded area reflects the 95% confidence interval of the fit. **(C)** Ramsey spectroscopy for various molecule densities at constant trap laser intensity of 31 kW/cm^2. The average densities were normalized with respect to $n_0 = 2.5 \times 10^{10}$ cm^{-3}. Solid lines show sine-fits. **(D)** Shift of the resonance frequency as a function of molecular density. The grey-shaded area reflects the 95% confidence interval of a linear fit. The fit is consistent with the absence of a collisional shift. Data points in A and C correspond to the average of two experimental runs, with error bars denoting the standard deviation of the mean. Figure reproduced from [185].

5.5 Summary

We created ultracold fermionic molecules of NaK in its absolute ground state. Microwave spectroscopy revealed the structure of the lowest rotational and hyperfine states. We demonstrated coherent control over rotational and spin degrees of freedom using Rabi and Ramsey spectroscopy, culminating in the measurement of second-scale nuclear spin coherence times. NaK molecules have sufficiently long lifetimes and coherence times for many studies, but limiting factors include two-body inelastic collisions and differential ac Stark shifts in the presence of trapping light.

To harness the full potential of ultracold molecules, these effects must be mitigated. Future studies of spin physics can take place in deep optical potentials with no more than one molecule per site, thereby preventing tunneling and photoassisted chemical reactions. Magic wavelength (or electric field) engineering will be required to suppress decoherence between rotational levels. Studies with mobile molecules, such as realizations of t-J models and exotic superfluids, may require electric-field or microwave-shielding that prevents two molecules from entering short-range where chemistry is allowed. Alternatively, molecules may be trapped in repulsive "box" potentials, where species like NaK would not undergo inelastic two-body losses in the absence of light. This prospect will be discussed in Ch. 7.

Above all, we would like to control the anisotropic dipole-dipole interaction between molecules. This current chapter has focused on single molecule physics and interactions in the absence of external fields and laboratory-frame dipole moments. Engineering dipolar interactions will be the subject of Ch. 6.

Chapter 6

Strongly interacting dipolar molecules of ^{23}Na^{40}K

Controlling the strong, long-range dipolar interactions is key to realizing the potential of ultracold molecules. These interactions turn molecules into a promising platform for simulating quantum many-body physics [163, 39, 195, 47, 93], precision measurements of fundamental constants [47, 140, 204], quantum computation [73, 145, 252], and quantum state-resolved chemistry [139, 47, 197, 12]. This chapter will discuss how to engineer such long-range interactions in ensembles of ultracold molecules. I then describe how the technique of microwave dressing was implemented using NaK in the MIT experiment, resulting in observation of resonant dipolar collisions. Work presented here has resulted in the following preprint,

Zoe Z. Yan, Jee Woo Park, Yiqi Ni, Huanqian Loh, Sebastian Will, Tijs Karman, Martin Zwierlein, *Resonant dipolar collisions of ultracold molecules induced by microwave dressing,* ArXiv: 2003.02830.

6.1 Dipolar collisions

This section develops the theoretical tools to understand dipolar collisions. A review of the basic concepts in quantum scattering, focused on isotropic (*e.g.*, contact) interactions, can be found in Ch. 2.3.1. Here I focus on the dipole-dipole interac-

tions, including how to induce a laboratory-frame dipole moment with an external field. Past experimental realizations are highlighted. Finally, I describe theoretical proposals involving microwave-induced dipolar interactions between molecules.

6.1.1 Ultracold dipole-dipole scattering

Consider the general case of two dipoles with respective dipole moments $\vec{d_1}, \vec{d_2}$, separated by a relative coordinate $\vec{R}$. In contrast to contact interactions experienced by alkali atoms and unpolarized molecules, dipole-dipole scattering is anisotropic and falls off as R^{-3}. The potential is given by

$$V_{\mathrm{DDI}}(\vec{d_1}, \vec{d_2}, \vec{R}) = \frac{\vec{d_1} \cdot \vec{d_2} - 3(\vec{d_1} \cdot \hat{R})(\vec{d_2} \cdot \hat{R})}{R^3} \tag{6.1}$$

If both dipoles have the same magnitude and are polarized in the same direction $\hat{z}$, the dipole potential simplifies to

$$V_{\mathrm{DDI}}(\theta, \vec{R}) = \frac{d^2}{R^3}(1 - 3\cos^2\theta) \tag{6.2}$$

where (θ, ϕ) are the polar and azimuthal angles, respectively, between the intermolecular axis and the z-axis. The long-range portion of this interaction is often written in the form $V_{\mathrm{DDI}} = -C_3/R^3$, with the C_3 coefficient dependent on the particular molecular species.

Consider low-energy scattering between two particles in the same internal state. I use the partial wave basis $|L, m_L\rangle$ as introduced in Ch. 2.3.1 to describe the relative collision angular momentum, quantized by L, and its projection on the quantization axis $\hat{z}$, m_L. Internal and external degrees of freedom are treated separately. Then, the first order contribution to the dipolar interaction is

$$\langle \psi_{\mathrm{internal},1}\, \psi_{\mathrm{internal},2} \otimes L, m_L |\, V_{\mathrm{DDI}}\, | \psi_{\mathrm{internal},1}\, \psi_{\mathrm{internal},2} \otimes L', m_L' \rangle \tag{6.3}$$

where the internal quantum numbers of the wavefunctions of both particles are captured in ψ_{internal}. If both dipoles are fully polarized in the $\hat{z}$ direction with magnitude

d_0, *e.g.*, by a strong electric field, then $V_{\rm DDI}$ reduces to its simple form in Eq. 6.2 and is no longer a function of the internal wavefunctions. Then, the interaction simplifies:

$$\begin{aligned}\langle L, m_L | \, V_{\rm DDI} \, | L', m'_L \rangle &= \frac{d_0^2}{R^3} \int d\theta d\phi \;\; \sin\theta \; Y^*_{L,m_L}(\theta,\phi) \left(-4\sqrt{\frac{\pi}{5}} Y_{2,0}(\theta,\phi) \right) Y_{L',m'_L}(\theta,\phi) \\ &= -\frac{2d_0}{R^3}(-1)^{m_L} \sqrt{(2L+1)(2L'+1)} \begin{pmatrix} L & 2 & L' \\ -m_L & 0 & m'_L \end{pmatrix} \begin{pmatrix} L & 2 & L' \\ 0 & 0 & 0 \end{pmatrix}\end{aligned} \tag{6.4}$$

In the first step the dipole-dipole interaction was written in terms of the unit-normalized spherical harmonic Y_{L,m_L}: $1 - 3\cos^2\theta = -4\sqrt{\frac{\pi}{5}} Y_{2,0}$. Secondly, the integral product of three spherical harmonics was reduced in terms of Wigner 3-j symbols (in parentheses), along with the identity $Y^*_{L,m_L} = (-1)^{m_L} Y_{L,-m_L}$. From this equation and the Wigner 3-j selection rules, it is apparent the dipole-dipole interaction couples partial waves with the same parity and identical projections $m_L = m'_L$. Thus, m_L remains a good quantum number but L is not, unlike in the case of an isotropic potential.

In general, for low energy dipolar scattering, only low L are expected to contribute to the cross section. Furthermore, identical bosons (fermions) only scatter in even (odd) partial waves.

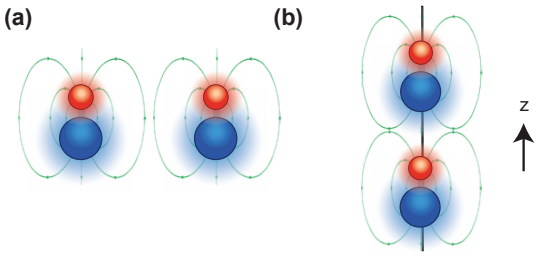

Figure 6-1: Cartoon of the dipole-dipole interaction showing repulsive head-to-head **(a)** and attractive head-to-tail **(b)** collisions of dipoles polarized in $\hat{z}$.

..

To develop a conceptual picture of dipolar scattering, picture two molecules polarized in the z-direction. Exactly how this is achieved will be discussed in Sec. 6.1.2. The dipoles scatter differently than their spherically symmetric counterparts; the centrifugal p-wave barrier (for fermions) becomes anisotropic. When dipoles collide "head-to-head," corresponding to the projection angular momentum $m_L = \pm 1$, they experience repulsion. An $m_L = 0$ collision involves attractive "head-to-tail" scattering

(see Fig. 6-1).

To conclude this section, dipolar collisions were treated in the limit of fully polarized molecules oriented in $\hat{z}$. More generally, the internal states would be coupled by V_{DDI}, necessitating a calculation beyond the first order expression of Eq. 6.4, involving off-diagonal terms in the two-molecule basis. Then, diagonalization of the Hamiltonian would produce the adiabatic potentials. These can be used to calculate scattering amplitudes and cross sections.

The case of dipolar interaction between molecules in electric fields will be considered next.

6.1.2 Using dc or ac fields to polarize molecules

Molecules require an external, symmetry-breaking field to be polarized in the laboratory frame. Though they may possess a permanent dipole moment in the body frame, this time-averages to zero in the laboratory. The following section will discuss ways to polarize molecules, using either static or microwave fields. Molecules are assumed to be in well-defined quantum states within the ground electronic state in all cases. A external electric field (taken to be in $\hat{z}$ for this section), whether static or alternating, can mix opposite-parity states, which are odd and even J rotational states in the $^1\Sigma^+$ level.

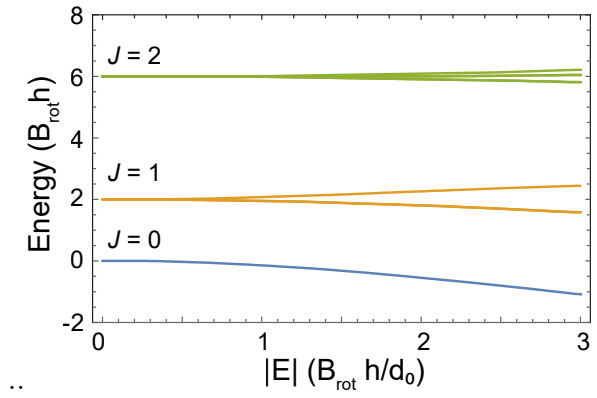

Figure 6-2: Dc Stark shifts of molecular energies from Eq. 6.7 showing the states that adiabatically connect to the J=0, 1, 2 rotational levels, computed with J up to 5.

..

Static electric fields

A common way to induce dipolar interactions in these systems is the application of

static electric fields that align molecules in the laboratory frame. To acquire dipoles on the order of the molecule's body-frame moment d_0 requires fields on the order of $E \sim B_{\rm rot} h/d_0$ where $B_{\rm rot}$ is the rotational constant. These field values are on the order of $\sim 1 - 10$kV/cm for typical bialkali species. To see why this is the case, it is instructive to consider what quantum states have transition dipole moments, and how an electric field mixes states to "construct" a wavefunction that orients in the field direction.

Let us compute the expectation of the dipole operator $\vec{d} = e\vec{r}$ explicitly. The coordinate system will have the normal polar angles ϕ, θ, with the position unit vector $\hat{r} = (\sin\theta\cos\phi,\ \sin\theta\sin\phi, \cos\theta)$. We use the $|J, m_J\rangle$ basis, where J is the rotation quantum number and m_J is its projection on the quantization axis set by the electric field. Then, two states with the same parity cannot have a dipole moment in the laboratory frame, *e.g.*,

$$\langle 00|\,\vec{d}\,|00\rangle = d_0 \int d\Omega\ Y_{00}^*(\theta,\phi)\hat{r}Y_{00}(\theta,\phi) = \vec{0} \tag{6.5}$$

However, opposite parity (odd and even J) states will have a nonzero dipole matrix element, *e.g.*,

$$\langle 00|\,\vec{d}\,|10\rangle = d_0 \int d\Omega\ Y_{00}^*(\theta,\phi)\hat{r}Y_{10}(\theta,\phi) = d_0(0,0,1/\sqrt{3}) \tag{6.6}$$

The effect of an external field is to mix J states with opposite parity such that m_J becomes the only good quantum number in the limit of high fields.

What are the energy levels in an external dc field? Ignoring hyperfine interactions, the Hamiltonian can be written

$$\langle J, m_J|\,\mathcal{H}\,|J', m_J'\rangle = B_{\rm rot}\, J(J+1)\delta_{J,J'}\delta_{m_J,m_J'} - \langle J, m_J|\,\vec{d}\cdot\vec{E}\,|J', m_J'\rangle \tag{6.7}$$

where the diagonal terms come from the rotational energy, and the off-diagonal terms come from the dc Stark effect. If $\vec{E}$ is constant over the molecules and oriented in $\hat{z}$,

the Stark terms can be written

$$\langle J, m_J | \mathcal{H}_s | J', m'_J \rangle = d_0 |E| \sqrt{(2J+1)(2J'+1)} (-1)^{m_J} \begin{pmatrix} J & 1 & J' \\ -m_J & 0 & m'_J \end{pmatrix} \begin{pmatrix} J & 1 & J' \\ 0 & 0 & 0 \end{pmatrix} \tag{6.8}$$

where the terms in parentheses are Wigner 3-j symbols. The Hamiltonian is diagonalized, and resulting energy levels are shown in Fig. 6-2 (with J truncated at 5). Shifts start out quadratic but quickly become linear once the electric field reaches $E \sim B_{\text{rot}} h/d_0$. The induced dipole moment of a particular state is the derivative of the energy with respect to field magnitude, $-\frac{d\text{Energy}}{d|E|}$, and it saturates to the maximum value of d_0 in the linear Stark regime.

Microwave fields

This section demonstrates how dipoles can be induced by ac fields. The presence and strength of static electric fields can be technically inconvenient in experiments due to unwanted electric field gradients and polarization of optics elements. In an alternate scheme, weak microwave electric fields that drive rotational transitions near resonance can lead to dipole moments on the order of the maximum value d_0. For example, dressing between the ground and first excited rotational states of a diatomic molecule yields dipole moments as large as the transition dipole moment for the electric dipole transition, $d_0/\sqrt{3}$, and thus dipolar interactions as large as $1/3$ of the maximum value at a given distance. (This is true in the two-level picture, neglecting all other hyperfine states.)

Let us compute this explicitly by considering the interaction of a molecule and a sinusoidal microwave field of frequency ω. The total energy is described by

$$\mathcal{H} = \mathcal{H}_{\text{rot}} + \mathcal{H}_{\text{mw}} + \mathcal{H}_{\text{mol-mw}} \tag{6.9}$$

$$= B_{\text{rot}} h\, J(J+1) + \hbar\omega(\hat{N} - N_0) - \vec{d} \cdot \vec{E}(t{=}0) \cos(\omega t) \tag{6.10}$$

where $\hat{N}$ is the microwave photon number operator, N_0 is a reference photon number, and $\vec{E}$ is the electric field. The long-wavelength approximation is valid for microwaves

(whose wavelengths $\sim$cm much exceed the ensemble size $\sim$ 100 μm.)

Neglecting hyperfine structure, there are four relevant levels in the $J = 0, 1$ manifolds, pictured in Fig. 6-3(a). Consider when the ac field is π-polarized (electric field parallel to quantization axis) with frequency $2B_{\text{rot}}$. Then it will only resonantly address the $|J = 0, m_J = 0\rangle \Longleftrightarrow |10\rangle$ transition. The only non-diagonal terms of the Hamiltonian involve the $|00\rangle, |10\rangle$ terms, allowing us to consider a simple 2×2 Hamiltonian. In the well-known dressed picture, the dressed state $|00, N_0\rangle$ is the rotational ground state with N_0 photons, and $|10, N_0 - 1\rangle$ is the rotationally excited state with one fewer photon. The dressed eigenstates are $|\pm\rangle = (|00, N_0\rangle \pm |10, N_0 - 1\rangle)/\sqrt{2}$. In the laboratory frame, we consider one of the eigenstates, $|\psi\rangle = (|00\rangle - e^{-i\omega t}|10\rangle)/\sqrt{2}$ and explicitly calculate its expected dipole moment.

$$\langle\psi|\,\vec{d}\,|\psi\rangle = \frac{1}{2}\big(\langle 00|\,\vec{d}\,|00\rangle + \langle 10|\,\vec{d}\,|10\rangle - \langle 00|\,\vec{d}\,|10\rangle\, e^{-i\omega t} - \langle 10|\,\vec{d}\,|00\rangle\, e^{i\omega t}\big) \tag{6.11}$$

$$= \frac{d_0}{\sqrt{3}}(0, 0, -\cos(\omega t)) \tag{6.12}$$

This corresponds to a oscillating dipole in the laboratory frame aligned to the z-axis. A similar calculation can be done for the σ-polarized case, coupling to the $|1, \pm 1\rangle$ states, resulting in a rotating dipole in the xy-plane, again with frequency ω. The time-evolution of these dipoles is pictured in Fig. 6-3(b).

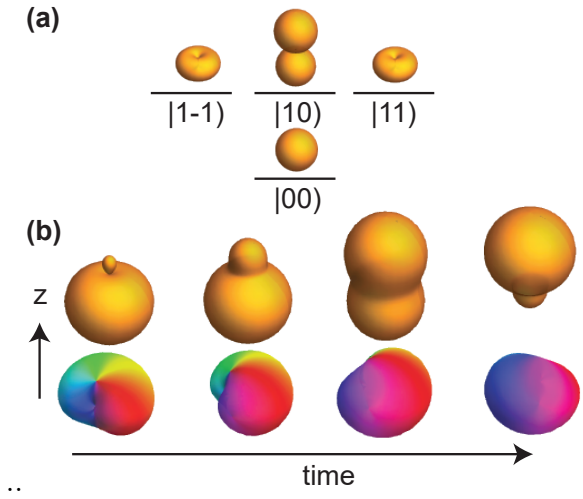

Figure 6-3: Time-evolution of microwave-dressed dipoles. **(a)** The simplified level diagram of the $J = 0, 1$ rotational states with molecular wavefunctions pictured. **(b)** On-resonance dressing for the π (top row) or σ (bottom row) transitions will induce an oscillating or rotating dipole moment, respectively, in the laboratory frame.

As a final exercise, let us compute the first order dipole-dipole interaction for two molecules in the $|i\rangle \equiv (|00\rangle - e^{-i\omega t}|11\rangle)/\sqrt{2}$ superposition. This calculation will

elucidate our experimental work presented in Sec. 6.2. Recall that the interaction term is

$$\langle i_1, i_2 \otimes L, m_L | \, V_{\mathrm{DDI}} \, | i_1, i_2 \otimes L', m_L' \rangle \tag{6.13}$$

In the real-space representation, there are now three sets of angles: $\theta_{1,2}, \phi_{1,2}$ representing the polar and azimuthal angles of each molecule with respect to the quantization axis $|z\rangle$, and the relative coordinates θ, ϕ. First, we compute the DDI expectation for the internal portion of the wavefunctions. We can time-average by integrating out the time-dependence, as no dynamics are fast enough to occur at microwave frequencies of the ac field. Then, the only surviving terms are components in which molecule 1 (in the $|00\rangle$ state) and molecule 2 (in the $|11\rangle$ state) exchange a quantum of rotational excitation, and vice versa. These components are calculated by integration over the two molecules' solid angles,

$$\begin{aligned}\langle i_1, i_2 | \, V_{\mathrm{DDI}} \, | i_1, i_2 \rangle &= \frac{d_0^2}{2R^3} \int\int d\Omega_1 d\Omega_2 \times \\ &\quad Y_{0,0}^*(\theta_1, \phi_1) Y_{11}^*(\theta_2, \phi_2) \left(\hat{r}_1 \cdot \hat{r}_2 - 3(\hat{r}_1 \cdot \hat{r})(\hat{r}_2 \cdot \hat{r})\right) Y_{1,1}(\theta_1, \phi_1) Y_{00}(\theta_2, \phi_2) \\ &= \frac{d_0^2}{R^3}\left(\frac{1}{6} - \frac{\sin^2\theta}{4}\right)\end{aligned} \tag{6.14}$$

To give a conceptual picture of this interaction term, consider this potential as a function of polar angle θ, as plotted in Fig. 6-4. When the relative angle $\theta = 0$, molecules are always meeting in the parallel configuration, with head-to-head orientation; thus V_{DDI} is positive and repulsive. At $\theta = \pi/2$, sometimes they meet head-to-head, sometimes head-to-tail, but on average the potential is attractive (negative).

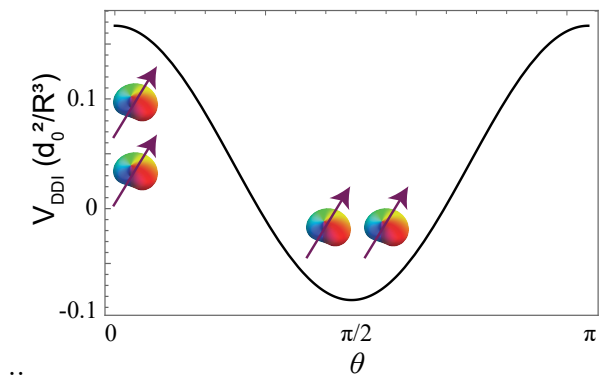

Figure 6-4: The first-order dipole-dipole interaction between two identical molecules in the $|i\rangle = \frac{1}{\sqrt{2}}(|J=0, m_J=0\rangle - e^{-i\omega t}|1,1\rangle)$ state, as calculated in Eq. 6.14. Cartoons show the relative orientation for polar angle θ between the two wavefunctions, with the arrows indicating the dipole orientation.

The final step would be to consider the collisional (external) degree of freedom by "sandwiching" the expression 6.14 between $\langle L, m_L|...|L, m'_L\rangle$,

$$\begin{aligned}\langle L, m_L, i_1, i_2| V_{\mathrm{DDI}} |L', m'_L, i_1, i_2\rangle &= \frac{d_0^2}{R^3}\int d\theta d\phi \sin\theta Y^*_{L,m_L}(\theta,\phi)\times \\ &\sqrt{\frac{\pi}{45}}Y_{2,0}(\theta,\phi)Y_{L',m'_L}(\theta,\phi) \\ &= \frac{d_0}{6R^3}(-1)^{m_L}\sqrt{(2L+1)(2L'+1)}\times \\ &\begin{pmatrix} L & 2 & L' \\ -m_L & 0 & m'_L \end{pmatrix}\begin{pmatrix} L & 2 & L' \\ 0 & 0 & 0 \end{pmatrix} \end{aligned} \tag{6.15}$$

Finally, a sum over partial waves with the appropriate symmetry conditions is needed.

To conclude, I have analyzed dipolar collisions in the cases of dc- and ac-field polarized molecules, deriving explicit expressions for the expectation of dipolar interaction energy for certain cases.

6.1.3 Past work on ultracold molecular collisions

This section reviews the investigations into molecule-molecule collisions, in the cases of unpolarized and polarized molecular ensembles.

Without an external symmetry-breaking field, unpolarized molecules collide with isotropic, short-range interactions. Experimentally, ultracold collisions in unpolarized molecules have been studied in ^{40}K^{87}Rb [174, 179], ^{23}Na^{40}K [183], ^{87}Rb^{133}Cs [224, 103], ^{23}Na^{87}Rb [251], ^{23}Na^{6}Li [202], ^{87}Rb$_2$ [78], and ^{40}Ca^{19}F [52]. These experiments were performed with molecules populating the $^1\Sigma$ ground state, with the exception of metastable $^3\Sigma$ for NaLi and Rb_2 and ground state $^2\Sigma$ for CaF. The proof of collisions came from measured two-body loss rates, β, defined as the number of molecules lost per unit time per initial density. These rates were all found within an order of magnitude predicted by universal loss models [196, 125] in which two molecules have unit probability of loss upon reaching short range.

Several two-body loss mechanisms must be considered, in principle. Molecules in excited states can collide and relax into lower-lying states. Absolute ground state

molecules can also undergo chemical reactions. With molecules formed by atomic constituents A and B, reactions can take one or more of the following forms, depending on (energy, momentum) conservation laws:

$$\begin{aligned} AB + AB &\rightarrow A_2 + B_2 \\ AB + AB &\rightarrow AB_2 + A \text{ or } A_2B + B \\ AB + AB\,(+ \text{ trap light}) &\rightarrow \text{Complex}\,(\text{A}, \text{A}, \text{B}, \text{B}) \end{aligned} \tag{6.16}$$

The two-particle loss is dominated by chemical reactions, possibly aided by the presence of optical trap light [57]. Trap-induced loss was recently characterized in ground state RbCs [102] and KRb [155] in the presence of 1064 nm light.

Collisions between dipolar molecules are especially important in order to make use of molecule's long-range, anisotropic interactions. Dipolar collisions with electrically polarized molecules were first studied in the JILA group [175] by observation of an increase in loss rate of fermionic KRb due to enhanced chemical reaction rates, with a dipole moment of up to ~ 0.2 D induced by an electric field. Using a similar technique, Ref. [112] reported inducing a dipole moment up to 0.7 D in bosonic NaRb and studied the temperature-dependent dipolar loss rates. Dipolar interactions in lattice-trapped KRb molecules were realized in [244, 118] by resonantly coupling rotational states. Another method of allowing dipolar collisions is the preparation of an incoherent mixture of opposite-parity rotational states, realized in Ref. [103] using bosonic RbCs molecules and equivalent to the interaction of two space-fixed dipoles at 0.5 D.

In these experiments, tunability of the dipolar interaction was limited by maximum experimental electric field strength, intrinsically small dipole moments, or the initial state admixture. We extended the study of dipolar collisions to fermionic NaK and demonstrated a highly flexible method to induce a significant fraction of NaK's body frame dipole moment of 2.7 D: *microwave dressing*.

6.1.4 The promise of microwave dressing

As the preceding sections have demonstrated how to induce dipole moments with microwaves, I now review selected theoretical proposals involving such *microwave dressing* schemes. Microwave dressing of molecules is a crucial component of several proposals that require induced long-range dipole-dipole interactions. It can be used to create exotic states of matter in bulk [39, 164, 37, 59, 148] and lattice quantum gases [236, 101]. In addition, standing-wave microwave fields in resonant cavities have been proposed to trap polar molecules [74, 79, 240]. Furthermore, engineering repulsive interactions via microwave dressing can potentially shield molecules from binary collisions [98, 39, 164, 100, 132, 144], which limit the lifetime of bulk molecular gases both in chemically reactive [179, 251] and non-reactive species [224, 239, 185, 112, 103] in the presence of trapping light [57].

6.2 Resonant dipolar collisions of ultracold ^{23}Na^{40}K

In this section, I present the first experimental results of microwave dressing on ultracold molecules and the observation of resonant dipolar collisions with cross sections exceeding three times the s-wave unitarity limit [248]. The origin of these collisions is the resonant alignment of the approaching molecules' dipoles along the intermolecular axis, which leads to strong attraction. Microwave dressing enhances the probability for two molecules to reach short-range, where they can undergo light-assisted chemical reactions in the presence of the trapping laser [57]; while ultimately this photoinduced loss can be eliminated by using repulsive box potentials [94, 169], here the loss is employed as an efficient detector for the two-body collision cross section. We explain our observations with both coupled-channels calculations as well as a conceptually simple two-state picture based on the Condon approximation.

6.2.1 Sample preparation of relevant $J = 0, 1$ states

In the MIT experiment, we observe strong microwave-induced interactions between fermionic ^{23}Na^{40}K molecules. The microwaves address the transition between the ground and the first excited rotational state. To start our experiment, we prepare a molecular gas in the absolute electronic, vibrational, rotational and hyperfine ground state, as described in Ch. 5 and Ref. [183, 182, 239]. In short, ultracold atomic mixtures of ^{23}Na and ^{40}K are confined in an optical trap at 1064 nm and cooled to a temperature of $T = 560(80)$ nK. ^{23}Na^{40}K molecules are coherently associated from this sample and initialized in the lowest vibrational, rotational and hyperfine state of the ground electronic $X^1\Sigma^+$ manifold, with a peak density of $3.2(3) \times 10^{10}$ cm^{-3}.

Without any external electromagnetic fields, the dominant interaction is the background rotational van der Waals (vdW) interaction resulting from second-order dipolar coupling to the first rotationally excited state [183]. A microwave field near the resonance of the transition between the ground and first excited rotational state is applied, thereby inducing a time-varying dipole moment in each molecule as explained in the preceding section. Tuned to the transition between $J = 0$ and $J = 1$, a resonant circularly polarized microwave field induces a dipole moment of $d_0/\sqrt{6} \approx 1.1$ D, rotating with the microwave electric field (see Sec. 6.1.2). We note the microwave antenna produces radiation at all polarizations: π, σ^+, and σ^-.

6.2.2 Observation of Autler-Townes splitting

To demonstrate the presence of microwave dressing, we induce an Autler-Townes splitting of the $J = 0 \rightarrow J = 1$ transition. A microwave field with Rabi frequency $\Omega_R/2\pi$=7 kHz is applied on resonance with the transition between $|g_2\rangle \equiv |0, 0, -3, 3/2\rangle$ and $|f\rangle$, predominantly equal to $|1, 0, -4, 3/2\rangle$, as shown in Fig. 6-5(b). This dressing field induces a splitting of the excited state, which is probed by scanning the frequency of a weaker microwave tuned near the $|g_1\rangle \rightarrow |f\rangle$ transition. We observe an Autler-Townes doublet as shown in Fig. 6-5(c), demonstrating that the $|g_1\rangle$ state is only depleted by the probe field when it is tuned to the dressed resonances. The appearance

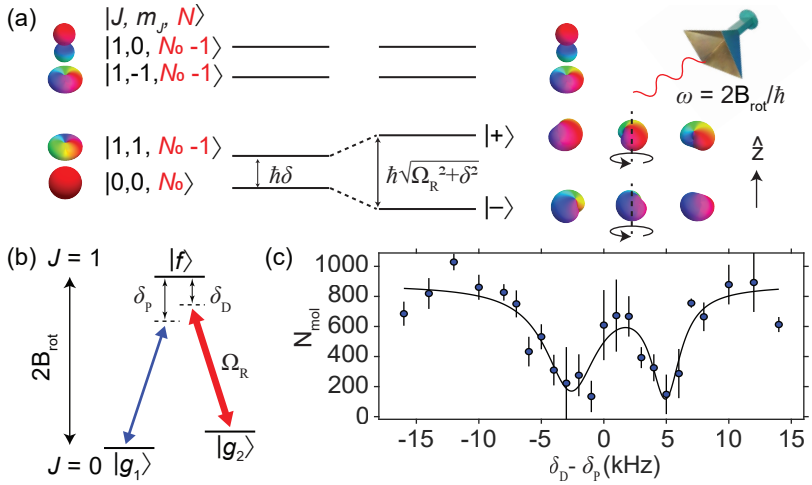

Figure 6-5: Microwave dressing in ^{23}Na^{40}K, reproduced from [248]. **(a)** Schematic energy level diagram, labeled by rotational quantum numbers J, m_J and microwave photon number N. Hyperfine structure is omitted for simplicity. The rotational ground state $|J=0, m_J=0\rangle$ is coupled by a σ^+-polarized microwave field to the lowest energy state in the J=1 manifold, $|1,1\rangle$, resulting in dressed states $|-\rangle, |+\rangle$. Higher-lying "spectator" states (*i.e.*, $|1,0\rangle$ and $|1,-1\rangle$) are not coupled by the microwaves. Molecular wavefunctions are depicted with color encoding the wavefunction's phase. **(b)** Level scheme with the relevant molecular states for Autler-Townes spectroscopy. A microwave field with Rabi frequency $\Omega_R/2\pi = 7$ kHz is used to address the $|g_2\rangle \rightarrow |f\rangle$ transition. The weaker probe microwave field has a frequency detuning δ_P that is scanned around the $|g_1\rangle \rightarrow |f\rangle$ transition. **(c)** An Autler-Townes doublet is observed when scanning the probe microwave. The solid line shows a double Lorentzian fitted to the lineshape.

of the doublet is an unambiguous signature of dressing.

6.2.3 Microwave dressing: 2-body loss rate and collision cross-section

In this section, the methods and main results of the microwave dressing experiment are presented. We found that microwave dressing dramatically enhances molecular interactions. Although ^{23}Na^{40}K should not experience two-body collisional loss in its electronic and vibrational ground state, the trapping laser at 1064 nm leads to photoinduced loss for two molecules at short range [57]. We employ this loss mechanism as a probe for microwave-induced two-body collisions.

To start, the dressing microwave field was first applied with a frequency far below

the lowest rotational resonance, the $|g_1\rangle \rightarrow |f\rangle$ transition. Here, and for the remainder of the chapter, $|f\rangle$ represents the lowest energy $J = 1$ state, which has predominantly $|1, 1, -4, 3/2\rangle$ character. More precisely, at $\mathrm{B} = 129\,\mathrm{G}$, $I_{\mathrm{trap}} = 4000\,\mathrm{W/cm^2}$, and the trap polarization angle $\sim 15^\circ$ from the magnetic field, the state decomposition of $|f\rangle$ is $|f\rangle \approx 0.74\,|1, 1, -4, 3/2\rangle + 0.63\,|1, 0, 3/2, -3\rangle + 0.12\,|1, 0, 3/2, -4\rangle$.

The frequency was then swept adiabatically from the initial detuning $\delta_{\mathrm{initial}}$, where the molecule in the lower dressed eigenstate $|-\rangle$ has predominantly $|g_1\rangle$ character, to a detuning δ_{final} near or on the dressed resonance (see Fig. 6-6(a)). The field was generated using a fixed microwave frequency source (Rohde and Schwarz, SMF100A) at $\omega_{\mathrm{MW}} = 5.573\,379\,\mathrm{GHz}$ and a programmable radio-frequency source (Agilent 33250A function generator) at $\omega_{\mathrm{RF}} \approx 70\,\mathrm{MHz}$. The two signals were mixed (Mini Circuits mixer ZMX-7GHR), and the radio-frequency source was tuned so the higher-frequency sideband $\omega_{\mathrm{MW}} + \omega_{\mathrm{RF}}$ was initially $\delta_{\mathrm{initial}}$ away from the $|g_1\rangle \rightarrow |f\rangle$ resonance, ending at a detuning of δ_{final} after a linear sweep lasting 4 ms. $\delta_{\mathrm{initial}}$ was typically 12 kHz below δ_{final}. The carrier frequency and the lower sideband were more than 70 MHz detuned from any rotational transitions and were not expected to play any role in the dynamics.

The radiation characteristics of the microwave antenna were empirically determined via microwave spectroscopy in a previous experiment [239]. Rotational transitions were driven to multiple hyperfine states in $J = 1$, and the microwave absorption features were scaled to match the line strengths determined by a theoretical model of the single-molecule Hamiltonian [239]. The resulting radiation had an estimated 50% π, 25% σ^+, and 25% σ^- character.

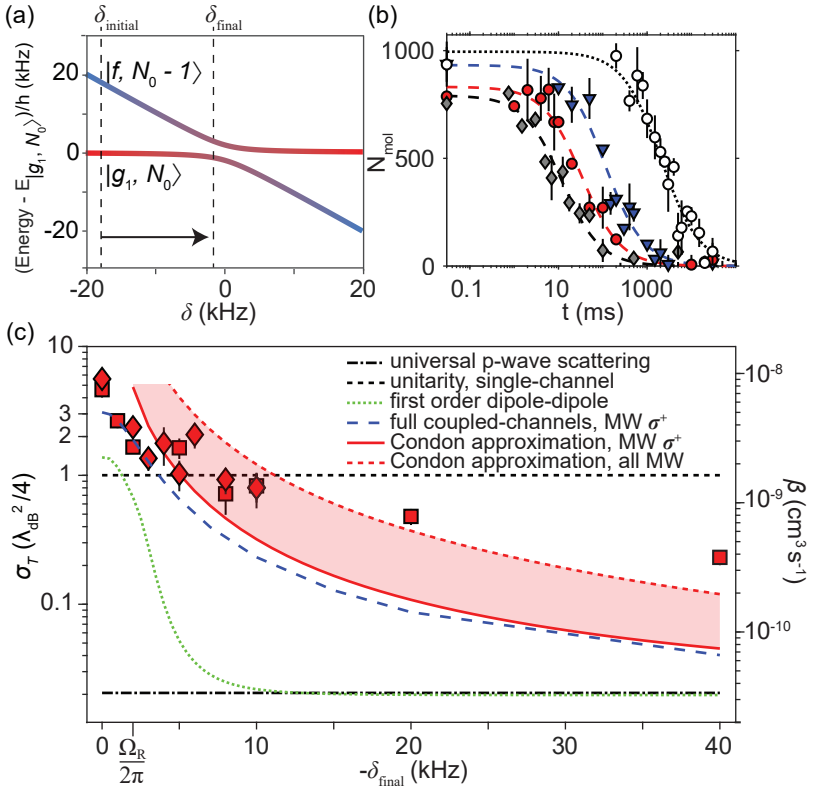

Figure 6-6: Observation of resonant dipolar collisions between dressed molecules, reproduced from [248]. **(a)** Dressed energies as a function of the microwave frequency detuning δ from the $|g_1\rangle \rightarrow |f\rangle$ transition, at 129 G. δ is swept from far-off-resonance (typically 12 kHz below δ_{final}) to a final detuning at a rate of 3 kHz ms^{-1} and held for a varying hold time t. **(b)** Evolution of the molecule number under microwave dressing with $\Omega_R/2\pi = 1.7$ kHz for $\delta_{\text{final}} = -20, -5$, and 0 kHz (in blue triangles, red circles, and grey diamonds). A lifetime curve of $|g_1\rangle$ taken without microwaves is shown as open circles. Dashed lines are two-body decay fits. **(c)** Collision rates (left axis) obtained from loss coefficients (right axis) of dressed molecules as a function of δ_{final} for $\Omega_R/2\pi = 1.7$ kHz (squares) and 2.4 kHz (diamonds). The black dot-dashed line shows the universal p-wave loss at 560 nK [125], the green dotted line includes the additional loss from first-order dipole-dipole interactions. The unitarity limit for the loss rate from a single partial wave is shown as the black dashed line. The blue dashed line shows the coupled-channels prediction, assuming pure σ^+ microwave polarization, and the red line depicts the rate given by the Condon approximation. Including all microwave polarizations, the Condon approximation increases to the red dashed line.

Fig. 6-5(a) depicts the dressed eigenstate $|-\rangle$, a superposition of the states $|g_1\rangle$ and $|f\rangle$. The red-detuned microwaves avoided driving other hyperfine transitions during the sweep (the "spectator" states of Fig. 6-5(a)); the next higher $J = 1$ state

lies 27 kHz above the $|f\rangle$ state. The microwave field was held at its final detuning for a varying amount of time, allowing collisions to occur, before the detuning was swept back to δ_{initial} and the remaining $|g_1\rangle$ molecules were imaged.

We observed the evolution of the molecule number in $|g_1\rangle$ as a function of hold time to extract the loss rate of the ensemble. The loss curves were fit to a two-body decay model, where the Gaussian density $n(t)$ as a function of time obeys

$$n(t) = n_0/(1 + \beta n_0 t) \tag{6.17}$$

Here, n_0 is the initial average molecule density and β is the two-body loss coefficient. This evolution is governed by solving the differential equation, $\frac{dn}{dt} = -\kappa_\gamma n(t)^\gamma$, where κ_γ is the rate constant stemming from γ-body collisions. To verify that two-body loss more appropriately models the data compared to one- and three-body losses, the lifetime curves were also fitted with solutions of the differential equations with $\gamma = 1, 3$. The reduced chi-squared goodness-of-fit for $\gamma = 2$ gave the best performance, as shown in Fig. 6-7 for the case of $\delta_{\text{final}} = 2\,\text{kHz}$.

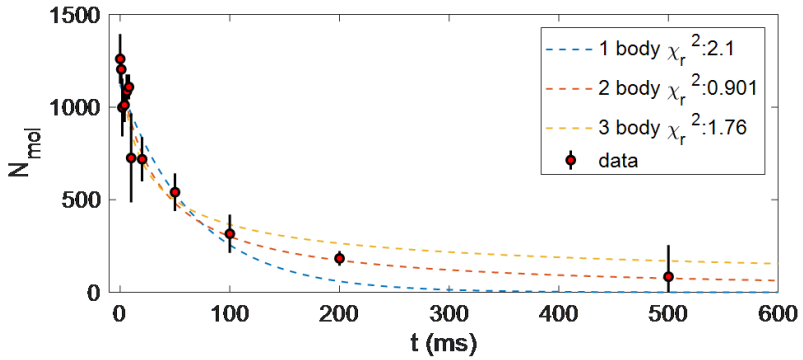

Figure 6-7: Comparison of 1-, 2-, and 3-body decay models for molecular lifetimes during microwave dressing. Circles represent $J = 0$ molecule numbers for $\delta_{\text{final}} = 2\,\text{kHz}$. The decay curves were determined via least-squares fitting with $\gamma = 1, 2, 3$ respectively. The reduced chi-squared is minimized for the two-body decay curve given by Eq. 6.17.

The microwave dressing shortened the sample lifetime by orders of magnitude, compared to the $\sim$3 s lifetime in the absence of microwaves (see [183, 239] and Sec. 5.3). Examples for certain detunings are shown in Fig. 6-6(b). Since both

molecules involved in the collision are lost, the loss rate is related to the two-body scattering cross section σ by $\beta = 2\langle\sigma v\rangle$, where $\langle\dots\rangle$ denotes the ensemble average and v the relative velocity of colliding molecules. We therefore define a thermally averaged scattering cross section $\sigma_{\mathrm{T}} = \beta/2\langle v\rangle$, with $\langle v\rangle = \sqrt{8k_{\mathrm{B}}T/\pi\mu}$ the average relative velocity and $\mu = (m_{\mathrm{Na}} + m_{\mathrm{K}})/2$ the reduced mass.

Figure 6-6(c) shows the measured collision cross section (red data points, left axis) and associated loss rate (right axis) as a function of microwave detuning. The resonant scattering rate is an order of magnitude larger than rates found in previous experiments [175, 112, 103]. Away from resonance, the scattering cross section is reduced but remains orders of magnitude larger than that of both the bare $|g_1\rangle$ and $|f\rangle$ states in the absence of microwaves. The bare states feature loss rates of only $\beta^{(\mathrm{bare})} = 2\times10^{-11}$ cm^{3}s^{-1} [183, 239], close to the universal loss rate of $\beta^{(\mathrm{universal})} = 3\times10^{-11}$ cm^{3}s^{-1} [125], which reflects the loss when the molecules only experience vdW interactions under p-wave collisions.

Comparison of loss rate to the unitarity limit

To emphasize how strongly microwave dressing can modify interactions, the comparison to the s-wave unitarity limit is useful. A single partial wave contributes at most the unitarity limit, $\sigma^{(\mathrm{unitarity})} = \lambda_{\mathrm{dB}}^2/4$, limited by the de Broglie wavelength $\lambda_{\mathrm{dB}} = \sqrt{2\pi\hbar^2/\mu k_{\mathrm{B}}T}$, corresponding to a loss rate $\beta^{(\mathrm{unitarity})} = 2\hbar\lambda_{\mathrm{dB}}/\mu = 1.7\times10^{-9}$ cm^{3}s^{-1}. For ultracold bosons that undergo only s-wave collisions, $\sigma^{(\mathrm{unitarity})}$ and $\beta^{(\mathrm{unitarity})}$ are upper limits to the collisional cross section and loss rate, respectively. For ultracold fermions such as ^{23}Na^{40}K, one might expect the p-wave centrifugal barrier to prevent molecules from reaching short-range and thus reduce losses, but the dipole-dipole interaction suppresses this barrier. For dressing on a σ^+ resonance, the first-order dipole-dipole interaction is attractive for $M_L = \pm1$, where M_L is the projection of the molecules' relative angular momentum, leading to a p-wave loss rate that is at most twice the unitarity limit.

6.2.4 Discussion of resonant collisions

Here, the origins of the dressing-induced collisions are explained. We first consider a simple description where the molecules in the $|-\rangle$ state only experience background vdW interactions and the first-order dipole-dipole interaction, neglecting all "spectator states" and the upper dressed state $|+\rangle$. The first-order interaction was explicitly calculated in Sec. 6.1.2. In this approximation, the molecular dipole moments always align with the rotating electric field. The resulting loss curve, shown as the green dotted line in Fig. 6-6(c), is comparable to the unitarity limit near resonance. Away from resonance where $|\delta_{\text{final}}| \gg \Omega_{\text{R}}/2\pi$, microwave dressing induces a negligible dipole moment and the first order approximation to the collision rate rapidly decreases to the universal limit. This disagrees with the experimental loss rates, which remain an order of magnitude higher than the bare rate without microwave dressing even for detunings greater than Ω_R. Thus, the first order dipole-dipole effect is insufficient to explain the enhanced collision rates.

Next, we also consider contributions from the upper dressed state $|+\rangle$, restricting the two-molecule basis to $|--\rangle$ and $(|+-\rangle + |-+\rangle)/\sqrt{2}$, written as $|-+\rangle$ for convenience in the remainder of the chapter. This approximation is valid at detunings greater than Ω_R, when accounting for only σ^+ microwave polarization and neglecting the presence of "spectator states" $|J=1, m_J=0\rangle$ and $|1,-1\rangle$. Neglecting these spectators, the dipoles can only ever point in the direction of the rotating microwave electric field, *i.e.,* in the x-y plane, as they approach each other at close range. The interactions will thus be repulsive if molecules meet along the z-direction ($M_L = 0$) and attractive if they meet in the x-y plane, i.e. for $M_L = \pm 1$ (see Fig. 6-4). One might therefore expect a maximum p-wave cross section of at most *twice* the unitarity limit corresponding to the two attractive $M_L = \pm 1$ channels for thermal energies far greater than the barrier height.

The potential landscape of two scattering molecules in the approximation of the two-molecule basis is shown in Fig. 6-8(a). For red detunings exceeding the Rabi frequency, the adiabatic potential curves for $L = 1$, $M_L = 1$ display an avoided

crossing between the incoming centrifugal potential $\sim\hbar^2/\mu R^2$, with negligible dipolar interaction, and the attractive potential

$$V \sim -h\delta_{\text{final}} - \frac{d_0^2}{12R^3} + \frac{\hbar^2}{\mu R^2} \tag{6.18}$$

corresponding to the time-averaged dipolar attraction of two classical rotating dipoles of strength $d_0/\sqrt{6}$ approaching in the plane of rotation. The diabatic potentials cross at the Condon point R_{C}, and an effective Rabi coupling leads to a p-wave barrier

$$V_b \sim \frac{\hbar^2}{\mu R_{\text{C}}^2} \propto |\delta_{\text{final}}|^{2/3} \tag{6.19}$$

Intuitively, the closer the microwaves are to resonance, the further down the barrier is pulled compared to the field-free case. Incoming molecules can reach this barrier, entering short range, leading to high scattering rates even for off-resonant dressing.

We have just considered a simplified two-level treatment involving $|-\rangle$ and $|+\rangle$. However, a quantitative comparison to the data requires treating the "spectators" $|J=1, m_J=0\rangle$ and $|1,-1\rangle$, as they are sufficiently close in energy (within 27 kHz). These "spectators" enable the molecules to reorient so that their dipoles point head to tail (see Fig. 6-8(b)), leading to resonant dipole-dipole interactions. This occurs when the dipolar energy overcomes the energy difference between the dressed incoming state and the state of attractively interacting molecules, or classically, when the electric field applied by one molecule on the other exceeds the electric field of the applied microwaves. Then, the relevant excited two-molecule state discussed previously for Fig. 6-8(a) is no longer $|-+\rangle$ in character, but rather $\hat{\mathcal{R}}\,|00,10\rangle$, corresponding to the state with the dipole moments aligned with the intermolecular axis. This state will be discussed in depth in Sec. 6.2.5. The excited and initial states are coupled by the microwave field, leading to the blue adiabatic potential curve in Fig. 6-8(b).

Thus at short range the interaction between two microwave-dressed molecules incoming in the lowest internal state $|--\rangle$ will *always* be attractive regardless along which direction the molecules meet, *i.e.,* for all three M_L components, giving a po-

tential

$$V \sim -h\delta_{\text{final}} - \frac{2d_0^2}{3R^3} \tag{6.20}$$

This resonant dipolar collision leads to p-wave loss as high as *three times* the unitarity limit. (The lowest adiabatic potential curve contains only a small barrier that is well below the thermal kinetic energy of 12 kHz. Hence, M_L=0 collisions can occur essentially without a barrier and add to the total cross section by about one additional unitarity-limited cross section, in contrast to expectations from only first-order dipolar interactions.) Even faster losses require inclusion of higher partial waves, $L > 1$. Compared to the spectator-free case of Fig. 6-8(a), the barrier height is shifted down and the Condon point is moved outwards. In this description, strong losses (beyond the universal p-wave rate) will occur even at detunings much larger than Ω_R – where there is almost no dressing and no admixture of the excited $J = 1$ level in the single-molecule eigenstate.

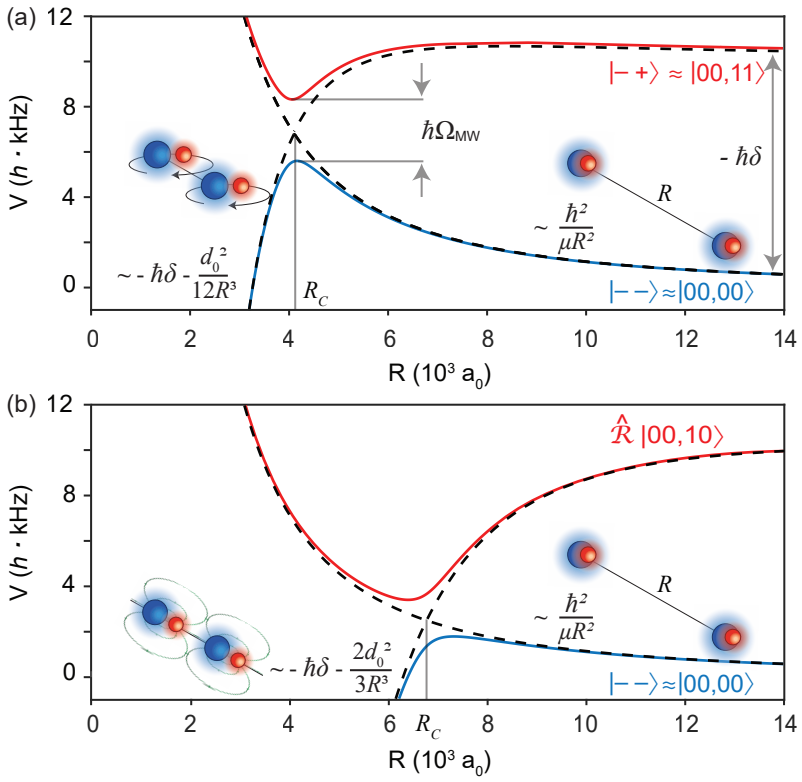

Figure 6-8: Two-state picture of dipolar interactions between microwave-dressed molecules, valid for detunings larger than the Rabi coupling, and shown here for $M_L = 1$. Reproduced from [248]. **(a)** Interaction potentials for molecules in the $|{-}{-}\rangle$ and $|{-}{+}\rangle$ states. An effective microwave Rabi coupling between the branches causes an avoided crossing at R_C. Excluding spectator states, the molecules remain aligned with the microwave field. Ω_{MW} is the effective Rabi frequency between the two states, proportional to Ω_R (see supplement of [248]). **(b)** The same as (a) but including spectator states: the relevant excited potential comes from two molecules in the $\hat{\mathcal{R}}\left(|00\rangle|10\rangle + |10\rangle|00\rangle\right)/\sqrt{2}$ state (see Sec. 6.2.5), which represents the molecules aligning at short range along the intermolecular axis $\hat{R}$. Here, molecules experience strong, resonant dipole-dipole interactions.

Full coupled-channels model of loss rates

For a full model of the observed loss curves we employ coupled-channel (c.c.) calculations (see the dashed blue line of Fig. 6-6(c)). These were computed by Tijs Karman, and a more complete description can be found in the supplement of [248]. The molecules are represented as rigid rotors with hyperfine structure that interact through dipole-dipole interactions and undergo photoinduced loss at short range, modeled by an absorbing boundary condition. S-matrices were calculated for both

the long- and short-range product channels. Two types of lossy collisions were considered: inelastic scattering to other molecular levels (computed from the long-range part), or flux reaching the absorbing boundary condition at $R_{\mathrm{min}} = 50\ a_0$ (computed from the short-range part). Collision cross-sections for both processes were computed for many energies, between 1 nK and 10 μK. Thermal rate coefficients were then calculated by averaging the cross sections over a Maxwell-Boltzmann distribution,

$$\beta = \sqrt{\frac{8k_{\mathrm{B}}T}{\pi\mu}} \frac{1}{(k_{\mathrm{B}}T)^2} \int_0^\infty \sigma(E) \exp\left(-\frac{E}{k_{\mathrm{B}}T}\right) E dE, \tag{6.21}$$

where the temperature is $T = 560$ nK.

The scattering calculations capture both the high loss rate on resonance, exceeding three times the s-wave unitarity limit, and the slow decrease with detuning: even at $|\delta_{\mathrm{final}}| \gg \Omega_{\mathrm{R}}/2\pi \approx 2\,\mathrm{kHz}$, the loss is significantly higher than the universal loss rate, obtained without microwave dressing. However, the experimentally observed loss decreases even more slowly with detuning than for c.c. calculations that include only σ^+ polarization. We attribute this to the π and σ^- components of the microwave field (which together account for about 75% of the radiation amplitude for our antenna). On the σ^+ resonance, these field components address far-detuned hyperfine transitions, and their effect can be neglected. Away from resonance, however, these field components should contribute comparably and hence double the effective Rabi frequency.

To summarize the coupled-channels results, we have shown this calculation accurately reproduces experimental losses, especially for small detunings.

6.2.5 Simplified two-state picture of losses

Without the full coupled-channels machinery, losses can be analytically derived in a conceptually simple two-state picture. This section presents the theoretical basis for using this picture and comparisons to experiment. At short R, where the dipole-dipole interaction becomes larger than $\hbar\Omega$ and $k_{\mathrm{B}}T$, the molecular dipole moments quantize along the intermolecular axis, and the microwaves resonantly drive a transition from

the incoming two-molecule state $|{-}{-}\rangle$ to an excited two-molecule state that is immediately lost. Thus, the calculation of the loss rate reduces to a calculation of the microwave coupling strength between the initial and final lossy state. For detunings exceeding the Rabi frequency $\delta \gg \Omega$, we employ the reflection approximation for the Franck-Condon overlap [130, 40, 27] to estimate loss rates, with results that match experimental observations. In this discussion, we neglect hyperfine interactions. A more concise version of the following discussion can be found in the supplement of [247].

A new basis for the two-molecule wavefunction

First, the two-state picture will be introduced, involving a more convenient basis of eigenstates. Our original basis vectors are the two-molecule states, where a single molecule is labeled by $|J, M\rangle$:

$$|00,00\rangle\,, |00,1{-}1\rangle\,, |00,10\rangle\,, |00,1{+}1\rangle\,, |11,1{-}1\rangle\,, |11,10\rangle\,, |11,1{+}1\rangle \tag{6.22}$$

We consider only the resonant subspace where $J = 0$ molecules have one more microwave photon than $J = 1$ molecules. The microwave polarization is defined in the laboratory frame with respect to the z quantization axis. For the case of σ^+-polarized microwaves, the states $|10,10\rangle\,, |10,1{-}1\rangle$ and $|1{-}1,1{-}1\rangle$ are purely bystanders and do not participate in the dynamics, and thus may be ignored. Furthermore, we implicitly symmetrize the wavefunctions, *i.e.,* $|00,11\rangle$ stands for $(|00,11\rangle + |11,00\rangle)/\sqrt{2}$.

The dipolar interaction only couples the $|00,1M\rangle$ states amongst each other. The diagonal term arising from the dipole-dipole coupling was solved explicitly for the $|00,11\rangle$ case in Sec. 6.1.2. The Hamiltonian is the sum of the dipole-dipole interaction,

rotational energy, and microwave energy:

$$\begin{pmatrix}
0 & 0 & 0 & \frac{\hbar\Omega}{\sqrt{2}} & 0 & 0 & 0 \\
0 & \frac{1}{3}\frac{d_0^2}{R^3}C_{2,0}(\hat{R}) - \hbar\delta & \frac{1}{\sqrt{3}}\frac{d_0^2}{R^3}C_{2,1}(\hat{R}) & \sqrt{\frac{2}{3}}\frac{d_0^2}{R^3}C_{2,2}(\hat{R}) & \frac{\hbar\Omega}{2} & 0 & 0 \\
0 & -\frac{1}{\sqrt{3}}\frac{d_0^2}{R^3}C_{2,-1}(\hat{R}) & -\frac{2}{3}\frac{d_0^2}{R^3}C_{2,0}(\hat{R}) - \hbar\delta & -\frac{1}{\sqrt{3}}\frac{d_0^2}{R^3}C_{2,1}(\hat{R}) & 0 & \frac{\hbar\Omega}{2} & 0 \\
\frac{\hbar\Omega}{\sqrt{2}} & \sqrt{\frac{2}{3}}\frac{d_0^2}{R^3}C_{2,-2}(\hat{R}) & \frac{1}{\sqrt{3}}\frac{d_0^2}{R^3}C_{2,-1}(\hat{R}) & \frac{1}{3}\frac{d_0^2}{R^3}C_{2,0}(\hat{R}) - \hbar\delta & 0 & 0 & \frac{\hbar\Omega}{\sqrt{2}} \\
0 & \frac{\hbar\Omega}{2} & 0 & 0 & -2\hbar\delta & 0 & 0 \\
0 & 0 & \frac{\hbar\Omega}{2} & 0 & 0 & -2\hbar\delta & 0 \\
0 & 0 & 0 & \frac{\hbar\Omega}{\sqrt{2}} & 0 & 0 & -2\hbar\delta
\end{pmatrix} \tag{6.23}$$

with $C_{\ell,m}(\hat{R})$ the Racah-normalized spherical harmonics. Note that $\hat{R} = (\cos\phi\sin\theta, \sin\phi\sin\theta, \cos\theta)$, where θ/ϕ are the polar/azimuthal angles of the intermolecular axis with respect to the lab frame.

The microwave polarization can be reduced to three independent components, $\hat{e}_{\pm}, \hat{e}_0$. In the following we assume the microwave field has only σ^+ polarization along $\hat{e}_+$.

To find a basis that is "more diagonal" in the dipole-dipole interaction, consider linear combinations of the states $|00, 1M\rangle$. For each of these three states, one may define a unit vector that represents the orientation of the transition dipole matrix element shared by the two molecules: $\langle 00|\,\hat{d}\,|1M\rangle \propto \hat{e}_M$. These three unit vectors span 3D space and thus we can construct a two-molecule state $|00, 1\hat{v}\rangle$ whose dipole moment orientation $\hat{v}$ is orthogonal to the internuclear axis $\hat{R}$. This orthogonality condition restricts $\hat{v}$ to lie in a plane. To choose a single $\hat{v}$, consider the subspace spanned by the spectators $\{|00, 1{-}1\rangle, |00, 10\rangle\}$; one such orthogonal vector $\hat{e}_+ \times \hat{R}$, exists in this subspace and is also perpendicular to the microwave polarization.

We rotate the spectator subspace $\{|00, 1{-}1\rangle, |00, 10\rangle\}$ to make one of the resulting basis states $|00, 1\hat{v}\rangle$. What is the effect of this basis rotation on the other original vectors? Each of the original spectator states $|00, 1{-}1\rangle, |00, 10\rangle$ was coupled with equal Rabi rate $(\Omega/2)$ to $|11, 1{-}1\rangle, |11, 10\rangle$, respectively. Thus, when we simultaneously rotate the excited spectator subspace $\{|11, 1{-}1\rangle, |11, 10\rangle\}$, no additional Rabi

couplings are introduced. There naturally arises another vector $\hat{w}$, orthogonal to both $\hat{v}$ and the internuclear axis.

In the new basis $\{|00,00\rangle, |00,1\hat{v}\rangle, |00,1\hat{w}\rangle, |00,1\hat{e}\rangle, |11,1\hat{v}\rangle, |11,1\hat{w}\rangle, |11,1\hat{e}\rangle\}$ the Hamiltonian becomes

$$\begin{pmatrix}
0 & 0 & 0 & \frac{\hbar\Omega}{\sqrt{2}} & 0 & 0 & 0 \\
0 & \frac{d_0^2}{3R^3} - \hbar\delta & 0 & 0 & \frac{\hbar\Omega}{2} & 0 & 0 \\
0 & 0 & -\frac{2d_0^2}{3R^3} + \frac{d_0^2}{2R^3}\sin^2\theta - \hbar\delta & \frac{d_0^2}{2R^3}\sin\theta e^{i\phi}\sqrt{1+\cos^2\theta} & 0 & \frac{\hbar\Omega}{2} & 0 \\
\frac{\hbar\Omega}{\sqrt{2}} & 0 & \frac{d_0^2}{2R^3}\sin\theta e^{-i\phi}\sqrt{1+\cos^2\theta} & \frac{d_0^2}{3R^3} - \frac{d_0^2}{2R^3}\sin^2\theta - \hbar\delta & 0 & 0 & \frac{\hbar\Omega}{\sqrt{2}} \\
0 & \frac{\hbar\Omega}{2} & 0 & 0 & -2\hbar\delta & 0 & 0 \\
0 & 0 & \frac{\hbar\Omega}{2} & 0 & 0 & -2\hbar\delta & 0 \\
0 & 0 & 0 & \frac{\hbar\Omega}{\sqrt{2}} & 0 & 0 & -2\hbar\delta
\end{pmatrix} \tag{6.24}$$

In the limit of $|\delta| \gg \Omega$ and for short distances, the eigenvalues are are -2δ (with multiplicity 3), 0, $d_0/3R^3 - \hbar\delta$ (multiplicity 2), and $-2d_0/3R^3 - \hbar\delta$. We highlight in particular the eigenvalues 0 and $-2d_0/3R^3 - \hbar\delta$, corresponding to the ground state $|00,00\rangle$ and the state whose dipole moment points in $\hat{R}$, respectively. These two states are pictured in Fig. 6-8(b) (with the centrifugal potential also included there).

Therefore, the eigenstates of the dipole-dipole interaction are more simply described in the body-fixed frame rather than the space-fixed (laboratory) frame.

Formally, the rotated eigenbasis can also be obtained using Wigner matrices. We stress the following discussion produces identical results to what was derived previously. Let $\hat{\mathcal{R}}$ represent the rotation operator that transforms from the body-fixed to the space-fixed frame by angle $\vec{\Omega}$. The rotation acts on the dipole operator of the laboratory frame, in which the microwave polarization σ is defined,

$$\hat{\mathcal{R}}^\dagger \hat{d}_\sigma \hat{\mathcal{R}} = \sum_\kappa D^{(1)*}_{\sigma,\kappa}(\vec{\Omega})\hat{d}_\kappa. \tag{6.25}$$

where $D^{(J)}_{M',M}$ is a Wigner D-matrix of rank J. The matrix subscripts are projection indices denoting components of angular momentum J. For more details on frame

rotations, refer to Appendix F. Then, three of the bi-molecule eigenstates can be written:

$$\hat{\mathcal{R}}\frac{|00,1K\rangle + |1K,00\rangle}{\sqrt{2}}\sqrt{\frac{2J+1}{4\pi}}D^{(J)*}_{M,K}(\vec{\Omega}) \tag{6.26}$$

The good quantum numbers are the total angular momentum J, its space-fixed projection quantum number M, and the body-referred projection K. These eigenstates are convenient to work with, as they are eigenvectors of V_{DDI} with eigenvalues $\frac{1}{3}d_0^2R^{-3}$ for $K = \pm 1$ and $-\frac{2}{3}d_0^2R^{-3}$ for $K = 0$, corresponding to the solutions of Eq. 6.24.

The $K = 0$ case represents the eigenvector described previously whose dipole moment points along the intermolecular axis, and the $K = \pm 1$ eigenvectors are orthogonal to it.

The relevant potential curves are pictured in Fig. 6-9, which is a cartoon representing the situation of Fig. 6-8(b) for the $K = 0$ case. Here, the two-molecule ground state, $|g\rangle = |00,00\rangle|LM_L\rangle$, experiences essentially no dipole-dipole interactions, and its potential is given by the centrifugal term and the background vdW interaction. The excited $K = 0$ state, $|f, JM\rangle = \hat{\mathcal{R}}\frac{|00,10\rangle+|10,00\rangle}{\sqrt{2}}\sqrt{\frac{2J+1}{4\pi}}D^{(J)*}_{M,0}(\vec{\Omega})$, experiences attractive resonant dipole-dipole interactions. It crosses the ground state potential at the Condon point

$$R_{\mathrm{C}} = \left(\frac{2d_0^2}{3\hbar\delta}\right)^{1/3} \tag{6.27}$$

neglecting the contribution of the ground state potential, which does not change significantly in the relevant region. Finally, the ground and excited states are coupled by the microwave field

$$\begin{aligned}\langle f, JM|\hat{H}_{\mathrm{MW}}|g\rangle|LM_L\rangle &= \frac{\hbar\Omega\sqrt{3}}{2d_0}\langle f, JM|\hat{d}_\sigma|g\rangle|LM_L\rangle \\ &= \frac{\hbar\Omega}{\sqrt{2}}\sqrt{\frac{2L+1}{2J+1}}\langle LM_L1\sigma|JM\rangle\langle L010|J0\rangle,\end{aligned} \tag{6.28}$$

where $\sigma = +1$, 0, or -1 for σ^+, π, or σ^- polarized microwaves.

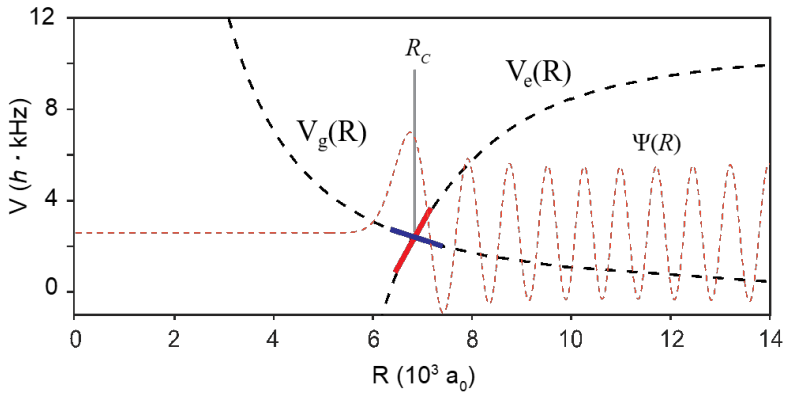

Figure 6-9: Cartoon of the approximation method [130, 40, 27] for the Franck-Condon factor. The dashed red line shows the incoming state wavefunction, $|\Psi_i\rangle$. The ground and excited potentials are depicted as black dashed lines, with their slopes highlighted at the Condon point. Using the slope values and $|\Psi_i(R_C)\rangle$, the Franck-Condon factor can be estimated by Eq. 6.35.

Approximation method for the Franck-Condon factor

With the convenient molecular basis established for our two relevant ground and excited states, we now turn to computing the loss rate using the reflection approximation for the Franck-Condon factor [130, 40, 27].

The Condon approximation was first employed to calculate rate coefficients in binary collisions of cold atoms due to the trapping laser [130]. It assumes losses occur with unit probability on the attractive excited state potential, where the molecules can reach short range, and that non-adiabatic transitions to the excited state occur only at the Condon point. The approximation lies in the ability to estimate the ground-to-excited Franck-Condon factor without knowing the eigenstates of the excited state. All that is required is the ground state wavefunction and the slope difference between the ground and excited wavefunctions at R_C.

The molecular loss rate is given by

$$\beta = \frac{2\pi\hbar}{\mu} \sum_{L,M_L,J,M} \left\langle \frac{1}{k} |S_{f,JM;g,LM_L}|^2 \right\rangle , \tag{6.29}$$

where k is the incoming wavenumber, the angular brackets indicate an ensemble

average, and the squared S-matrix element is given by

$$|S_{i;j}|^2 = 4\pi^2 |\langle \Psi_i | \hat{H}_{\mathrm{MW}} | \Psi_j \rangle|^2, \tag{6.30}$$

where $|\Psi_i\rangle$ denotes an *energy*-normalized scattering state in channel i. The angular part of the matrix element above is given in Eq. (6.28). The square of Eq. (6.28) summed over J, M, and M_L amounts to $\Omega^2/2$, regardless of the polarization of the microwave field, σ. Hence, we obtain for the loss rate coefficient

$$\beta = \frac{4\pi^3 \Omega^2 \hbar}{\mu} \sum_L \left\langle \frac{1}{k} |\langle \psi_e | \psi_g \rangle|^2 \right\rangle. \tag{6.31}$$

The Franck-Condon factor can be computed in the reflection approximation [130, 40, 27]. The full derivation can be found in Appendix B of [130]; here we merely sketch it. For a generic two-state system in the presence of a light field, the ground and excited state wavefunctions can be written $|\psi_{g/e}\rangle = \sqrt{\frac{2\mu}{\pi\hbar^2}}\, \alpha_{g/e}(R, E_{(e)}) \sin(\beta_{g/e}(R, E_{(e)})$. Here, $\beta_{g/e}$ is the phase of the ground/excited wavefunction, $\alpha_{g/e}$ is the amplitude, and the excited state energies are given by the potential differences at the Condon point, $E_e = E + V_e(R_C) - V_g(R_C)$. The ground state phase and amplitude can be exactly solved in the asymptotic limit; the excited state values are obtained through a WKB approximation [130]. The Franck-Condon factor is, by definition, the norm-squared wavefunction overlap:

$$\begin{aligned} |\langle \psi_e | \psi_g \rangle|^2 &= \frac{2\mu}{\pi\hbar^2} \left| \int_0^\infty dR\, \alpha_g \alpha_e \sin\beta_g \sin\beta_e \right|^2 \\ &\approx \frac{2\mu}{\pi\hbar^2} \frac{1}{4} \left| \int_0^\infty dR\, \alpha_g \alpha_e \cos(\beta_g - \beta_e) \right|^2 \end{aligned} \tag{6.32}$$

where the rapidly oscillating phase sum term is neglected in the last line. The phase difference $\beta_g - \beta_e$ is Taylor-expanded about the Condon point R_C to quadratic order in the position R. Then the integral term in the first line of Eq. 6.32 becomes

$$\sqrt{\frac{\pi\hbar^2}{2\mu D_C}}\, \alpha_g(R_C, E) \sin(\beta_g(R_C, E)) \tag{6.33}$$

where D_C is the difference in potential slope at the Condon point,

$$D_{\mathrm{C}} = \left| \frac{\mathrm{d}\left(V_g - V_e\right)}{\mathrm{dR}} \right|_{R_{\mathrm{C}}} \tag{6.34}$$

Upon rewriting in terms of the ground state wavefunction, the simple formula for the reflection approximation is attained:

$$|\langle \psi_e | \psi_g \rangle|^2 = \frac{|\psi_g(R_{\mathrm{C}})|^2}{D_{\mathrm{C}}} \tag{6.35}$$

Analytic result for loss rate from the Franck-Condon factor

At long range, the energy-normalized ground state radial wavefunction is given by

$$\psi_g(R) = R\, j_l(kR) \sqrt{\frac{2\mu k}{\pi}} \tag{6.36}$$

where j_l is the spherical Bessel function of the first kind. For our excited potential and incoming potential, the slope difference at R_C is $D_C = 2d_0^2 R_{\mathrm{C}}^{-4}$, where we have neglected the background vdW interaction and the difference in centrifugal kinetic energy. Combining the result with the reflection approximation, we obtain the analytic loss rate

$$\begin{aligned} \beta &= 4\pi^2 \hbar \Omega_{\mathrm{R}}^2 R_{\mathrm{C}}^6 \langle j_l(kR_{\mathrm{C}})^2 \rangle / d_0^2 \\ &= \frac{16\pi^2}{9\hbar} \frac{\Omega_{\mathrm{R}}^2}{\delta^2} d_0^2 \langle j_l(kR_{\mathrm{C}})^2 \rangle \end{aligned} \tag{6.37}$$

This expression does not include the universal p-wave loss, which has to be added on. The resulting approximation is shown as the solid red line in Fig. 6-6(c). The Condon approximation is also adjusted to take into account the π and σ^- components of the microwave field, resulting in the red dashed line in Fig. 6-6(c). The adjusted Condon approximation matches the experiment at higher detunings.

In summary, the two-state picture at high detunings can produce an accurate analytic estimate for observed loss rates using the Condon approximation. This picture

explains why losses are significantly greater than the background universal p-wave rate even at large detunings, where there is almost no excited state character in the dressed molecular states. This perspective of a resonant microwave transition from the incoming channel to a lossy excited channel is a powerful tool for treating microwave-induced dipolar collisions in general.

6.2.6 Influence of hyperfine structure on collisions

Here we consider how the dressing-induced collisions are affected by hyperfine interactions that shift the "spectator states" relative to the state used for microwave dressing. Recall that the maximum strength of resonant dipolar interactions is given by the full transition dipole matrix element of the dressed transition. This requires reorientation of the molecules along their intermolecular axis and thus inclusion of the relevant $|J, m_J\rangle$ states, typically split by the hyperfine interaction. Hence, resonant interactions take full effect when the dipole-dipole interaction is large compared to the hyperfine splittings.

Though here the microwave dressing was on the lowest $J = 1$ state, the choice to dress on a higher hyperfine state would affect the induced collision rates. Potential curves for dressing on states higher than $|f\rangle$ exhibit many crossings rather than approaching an isolated attractive resonant dipole-dipole potential (see supplement of [248]), leading to slower scattering rates for reaching short range (Fig. 6-10(a)). Additionally, nonadiabatic transitions into lower-lying hyperfine states may increase the inelastic losses of the reflected flux to hyperfine states other than the initial channel, compared to the case of dressing on $|f\rangle$ (Fig. 6-10(b)).

6.3 Summary and outlook

In conclusion, we realized strong dipolar interactions via the technique of microwave dressing, an alternative to using static fields to polarize the molecules. The observed dipolar collision cross-sections were in agreement with calculations from a coupled-channels model and a two-state description using the Condon approximation.

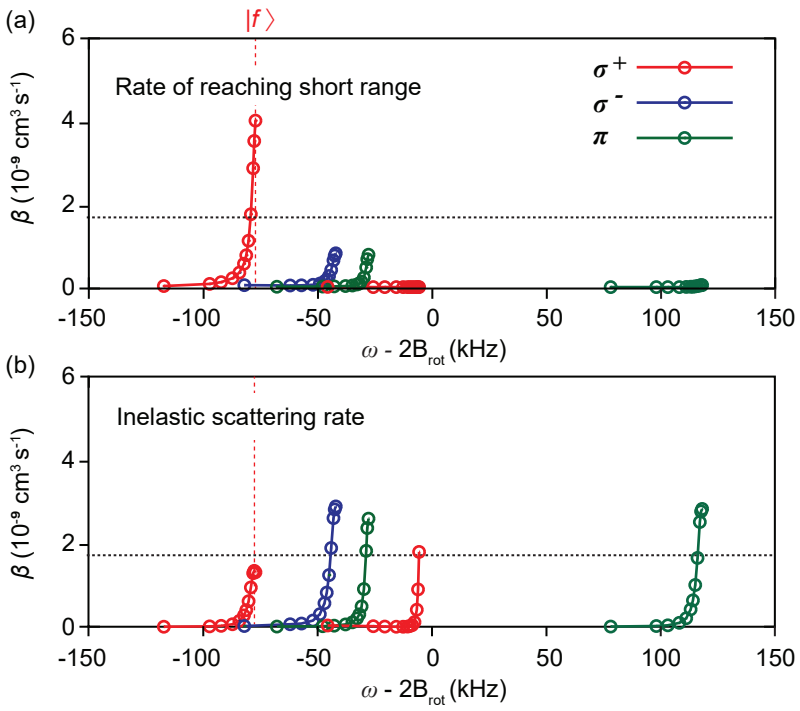

Figure 6-10: Hyperfine-state-dependent interactions, calculated at 129 G. Reproduced from [248]. **(a)** The short-range loss, which occurs when the incoming molecules reach the absorptive boundary condition that models photoinduced loss, is strongest for the lowest hyperfine state $|f\rangle$, whereas excited hyperfine states have larger inelastic loss (shown in **(b)**) due to transitions to different field-dressed levels and hyperfine states. The single-channel unitarity limit is shown as the dotted line.

The characteristic range R_C where the resonant dipolar collision occurs is directly controlled by the microwave detuning. This range can easily reach the typical spacing in optical lattices, $\sim 500\,\text{nm}$, enabling dipolar exchange energies to dominate over all other relevant energy scales in the system. Therefore, state-dependent resonant dipolar interactions induced by microwave dressing will enrich applications of polar molecules in quantum computation and simulation of many-body physics.

Here we observed dressing through collisional losses, but under appropriate conditions (*e.g.*, molecules trapped in a repulsive optical "box" potential) the short-range photo-induced losses should not occur. In such situations, microwave and electric field dressing can lead to strong elastic scattering, offering a powerful technique to tune intermolecular interactions. Prospects for such a "box" potential will be discussed in Ch. 7. Understanding and harnessing dipolar interactions in ultracold polar

molecules will be crucial for the creation of novel phases of matter, including topological superfluidity [59].

Chapter 7

Conclusion and outlook

The quantum toolbox of ultracold atoms and molecules continues to grow in scope and versatility as researchers endeavor to bring various degrees of freedom under control. On the atomic end, this thesis has presented our group's work on realizing the Bose polaron quasiparticle using an ultracold Bose-Fermi mixture. We detected a linear dependence of inverse quasiparticle lifetime on temperature at the Planckian scale, a signature of quantum criticality. This result is one example of ultracold mixtures elucidating the physics of correlated systems through quantum simulation. Additionally, we have probed the collective modes of the fermionic impurities immersed in a BEC and studied the onset of hydrodynamic flow induced in fermions by coupling to the bosonic excitations. The transition from ballistic to hydrodynamic flow is an important but poorly understood phenomenon in novel electronic systems.

For molecules, which are increasingly considered a frontier of the field, control over the numerous degrees of freedom has not yet reached the extent to which cold atoms can be manipulated. This thesis has summarized our work with ultracold dipolar NaK molecules, focusing on tuning their dipole-dipole interactions via microwave dressing. We demonstrated strong, resonant dipolar coupling between molecules, a prerequisite for creating exotic superfluid phases or for fast gates between polar molecule qubits for quantum information. Bit by bit, we and other groups around the world hope to sufficiently tame molecules for studies in quantum simulation, chemistry, and precision measurement, to the degree that our field already enjoys for cold atoms. Now I discuss

some promising directions for near-term research on both fronts.

In this outlook chapter, I discuss a problem that bridges two seemingly disparate topics: Bose polarons and ground state molecules. There are prospects of direct conversion to ground state NaK molecules from fermionic K impurities immersed in a Na BEC with attractive interactions, presented in Sec. 7.1. Additionally, the feasibility of confining molecules in a repulsive "box" potential will be discussed in Section 7.2. Such a trap avoids the fast light-assisted two-body loss that currently limits our molecule lifetimes in an attractive optical potential [57]. Therefore, repulsive trapping could pave the way toward realizing degenerate, long-lived dipolar gases of NaK in our system.

7.1 From Bose polarons to ground state molecules

At first glance, the many-body physics of the Bose polaron is distinct from the two-body physics of a molecule. However, there is a rich interplay between the two frameworks in the vicinity of a Feshbach resonance. Prospects for future work include studying the relationship between a Bose polaron quasiparticle and a molecular dimer formed by mixtures of bosonic ^{23}Na and ^{40}K atoms. Our motivation is twofold. First of all, the phase diagram of the Bose-Fermi mixture is not well understood, and in particular, understanding the Bose polaron impurity problem is an ongoing effort for theory [227, 198, 56, 108, 233, 7, 8, 109, 214, 150, 111, 254, 80, 87] and experiment [200, 50, 123, 128, 247]. Secondly, we would like to explore whether molecule formation of ground state ^{23}Na^{40}K can be made more efficient.

We consider the phase diagram of an impurity immersed in a bosonic bath with strong interactions. As discussed in Ch. 3, the character of the ground state of this system depends on the sign and strength of the interactions, parameterized by ka, where k is the boson wave-vector and a is the s-wave scattering length. For $1/ka<0$, the attractive polaron is the ground state. Far on the repulsive side $1/ka\gg0$, the ground state comprises the impurity pairing with a single boson to form a molecule. There also exists a metastable repulsive polaron branch. Fig. 7-1 shows the energy across

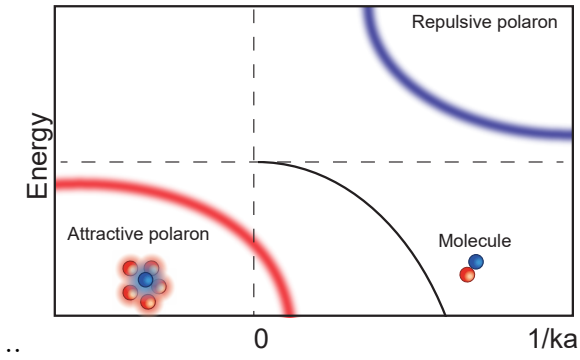

Figure 7-1: **Cartoon of Bose polaron and molecule energies** as a function of interaction strength. The attractive polaron has been predicted to smoothly cross over into the molecular dimer state [198, 152].

interaction strengths. Open questions include the nature of the evolution between the polaron and molecule, the similarity between the attractive polaron and molecule wavefunctions, and the continuity of parameters such as quasiparticle residue Z and contact C as interactions are tuned across the regions. In short, we would like to understand the crossover or transition between the attractive polaron and molecule. This question has been studied theoretically for the Fermi polaron, an impurity interacting with a Fermi sea. There is a predicted first-order transition between the attractive Fermi polaron and a bosonic molecule formed by a majority and minority fermion [192, 193, 36]. But unlike the case of the Fermi polaron to molecule transition, the Bose polaron quasiparticle does not change its quantum statistics (the polaron and the molecule both inherit the quantum statistics of the impurity, which is fermionic in the case of ^{40}K). The evolution from polaron to molecule has been predicted to be a smooth crossover [198, 152]. To our knowledge, these predictions have not been verified experimentally by measurements of spectral functions or derived quantities. Such a verification would benchmark theory and elucidate the connection between many-body and few-body physics in Bose-Fermi mixtures.

Additionally, probing the evolution between polarons and molecules can pave the way for a novel method to create ground state molecules. Currently, ground state molecules are reached by first forming a loosely bound Feshbach molecule in an excited vibrational state. Formation of Feshbach molecules from free atoms is limited by poor overlap in phase space between the two constituents; two atoms need to be roughly a distance a apart or closer, the typical size of a Feshbach dimer. However, attractive polarons may provide a better starting condition for molecule creation.

Our measurements of short-range correlations [247] suggest that at strong-coupling, the attractive Bose polaron is an impurity with an enhanced local density of bosons around itself. Of course, the attractive polaron is not a two-body bound state. However, there could be a high Franck-Condon factor between an attractive polaron and a Feshbach molecule, enough such that direct photoassociation to a much "smaller" molecule is possible. In certain cases, a direct two-photon transfer to the absolute ground state (via STIRAP, see Ch. 5) may be possible.

7.2 Dipolar gases in a homogeneous potential

It could be beneficial to trap molecules in a homogeneous "box" potential for both pragmatic and physics reasons, which I will now explore.

First of all, a homogeneous potential may increase the molecular conversion efficiency, bringing the samples into quantum degeneracy. Thus far, most bulk molecular experiments have been performed in inhomogeneous traps (often generated by optical Gaussian potentials). When atoms of different species are magneto-associated into Feshbach molecules, a bottleneck arises from the spatial overlap between the two samples. Particularly for a Bose-Fermi mixture in a harmonic trap, the Fermi gas extends much further than the condensed bosons, which populate only the center of the trap up to the Thomas-Fermi radius. Therefore, only 10-30% of Na and K atoms transfer into molecules, the single least efficient step in the molecule formation, and this problem is quite general for other bialkali molecule experiments in the bulk. Previous studies have shown that the conversion efficiency in the bulk increases as a function of increasing phase-space density [121]. A pair of atoms must be sufficiently close in phase space for the association process (B-field sweep or rf injection) to transfer it to a molecule– their relative momentum must be small compared to $\hbar/\Delta r$, where Δr is the atoms' separation. For a condensate (every atom in the same phase) and a Fermi gas (all occupying different phase space states) in a box potential, relative distance and relative momentum between the species are constant, on average, over the entire sample. Therefore, optimizing for best conversion locally is identical to a

global optimization, and theoretically an ultracold mixture of equal densities should approach 100% conversion into dimers. Furthermore, densities should be lower than peak densities in harmonic traps, causing a reduction of three-body inelastic collision rates that limit Feshbach molecule formation and lifetime. For these reasons we believe a box potential will enhance our molecular signal.

A second reason to pursue a homogeneous potential is for ease of interpreting thermodynamic quantities of interest. In a harmonic trap, the varying density leads to spatially varying energy and length scales. Local density approximations in harmonic traps can help extract quantities of interest, but this sometimes breaks down, *i.e.,* at the edges of the BEC where density changes drastically over a small spatial region. This poses a problem for studies of critical phenomena in which the correlation length diverges. Furthermore, in a gas with changing density, a large region of the phase diagram is occupied simultaneously, potentially obscuring interesting phases that arise in a narrow parameter regime. Additionally, in a box potential, global probes such as radiofrequency pulses address all molecules instead of a subset, and responses are recorded with a higher signal-to-noise ratio. Thus, a box potential presents advantages beyond molecular formation efficiency.

Given the advantages of a homogeneous potential, how does one construct such a "box"? In cold atoms, a recent advance has been the realization of uniform box potentials for bosonic [94] and fermionic [169] species. Confinement in three dimensions is provided by blue-detuned laser light shaped into sharp barriers. Care must be taken in choosing a wavelength that does not stimulate molecular transitions to higher-lying electronic and vibrational states. However, it must be noted that photon-induced losses on single molecules will be a surface effect in blue-detuned box traps, not a bulk effect as in red-detuned bulk traps, potentially mitigating overall loss rates.

To prevent atoms from "falling down" to the bottom of the box, a magnetic gradient potential levitates atoms against gravity. Fortunately for our experiment, simultaneous levitation of ^{23}Na and ^{40}K should be possible due to the coincidence that the gravitational force $-mg$ can be almost canceled by a single gradient value for the two lowest-energy spin states, Na $|F = 1, m_F = 1\rangle$ and K $|9/2, -9/2\rangle$, which

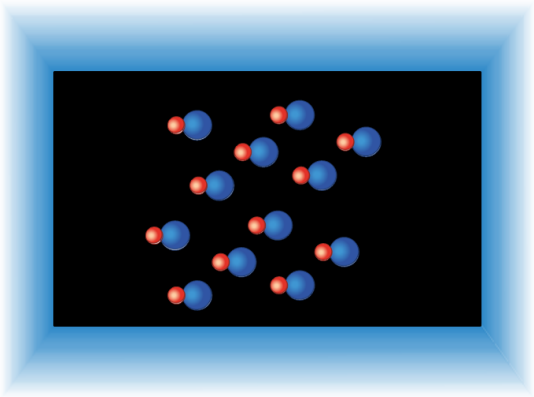

Figure 7-2: **A homogeneous sample of molecules trapped in a repulsive blue-detuned box potential**, avoiding the two-body photo-assisted losses experienced in red-detuned bulk traps.

..

are stable against two-body collisions at working magnetic fields. This simultaneous levitation is, in general, not possible for two arbitrary species. An illustration of NaK molecules trapped in the box is shown in Fig. 7-2.

In conclusion, work in the near term will involve novel ways of creating and trapping molecules. Rich prospects lie ahead for experiments with ultracold quantum mixtures and dipolar molecules.

Appendix A

Feshbach resonance landscape between ^{40}K and ^{23}Na

To tune interactions between the species, we make use of the Feshbach resonances between ^{23}Na and ^{40}K, shown in Fig. A-1. Our group's previous measurement of the interspecies resonances using Feshbach loss spectroscopy was reported in Ref. [184]. Another study on NaK was done by [255]. For this study we refined the location of the resonances and zero-crossing of the scattering length using a technique based on interspecies thermalization (similar to the method in Ref. [178]). We focus exclusively on Na in the $|F, m_F\rangle \equiv |1, 1\rangle$ state's interaction with one of the two lowest K hyperfine states, $|9/2, -7/2\rangle$ and $|9/2, -9/2\rangle$.

We start with a near-balanced thermal mixture of bosons and fermions prepared in their lowest hyperfine states. They are trapped in a 1064 nm optical dipole trap (crossed beams in the x-y plane). The magnetic field is adiabatically ramped to 80.3 G in 20-40 ms. We knew this field to be near a zero-crossing of the scattering length, $a \approx 0$. Then, depending on which K state to be studied, we could perform a Landau-Zener rotation to the $|9/2, -7/2\rangle$ state. We quickly change the field (in < 1 ms) to a varied final value, where we study thermalization. A x-directional beam at 790 nm is applied at an intensity high enough to dominate the trapping in the y- and z-directions. Then, the system thermalizes for a fixed amount of time. All dipole traps are suddenly turned off, and the atoms are allowed to freely expand for

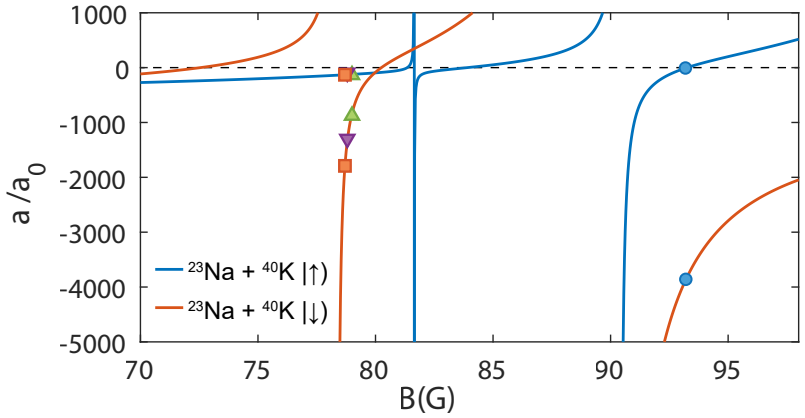

Figure A-1: **Feshbach resonance landscape between ^{23}Na and ^{40}K.** The s-wave scattering lengths versus magnetic field for two K spin states $|F, m_F\rangle = |9/2, -9/2\rangle \equiv |\downarrow\rangle$ and $|9/2, -7/2\rangle \equiv |\uparrow\rangle$ and Na in the $|1, 1\rangle$ *state*. Markers denote the magnetic fields where we perform rf spectrsocopy for various a for the Bose polaron study described in Ch. 3

$\sim$3-10 ms. If the K was in the $|9/2, -7/2\rangle$ state, a second Landau-Zener brings it back to the lowest hyperfine state for imaging. The spatial profile of the K cloud is analyzed, giving the ratio σ_y/σ_x, where σ_i is the Gaussian width of the column density in the ith direction.

The thermalization reveals the scattering length's local minima and maxima as a function of magnetic field. In the absence of interactions, the K width scales in time-of-flight as

$$\sigma_i^2(t) = \sigma_i^2(t)(1 + \omega_i^2 t^2) \tag{A.1}$$

where t is the flight time and ω_i is the trap frequency. As $\omega_x \ll \omega_y$, the ratio σ_y/σ_x is larger than unity for times much greater than the inverse trap frequency. However, when there are Na-K two-body collisions, momentum can be redistributed among all three directions (with total kinetic energy and momentum conserved). The two-body scattering rate is $n\sigma_{\rm el}v_{\rm rel}$, where n is the density overlap, $\sigma_{\rm el}$=$4\pi a^2/(1 + k^2a^2)$ is the elastic scattering cross section, and $v_{\rm rel}$ is the mean relative velocity. The thermalization rate is the elastic two-body scattering rate up to a factor of order unity. Typically it takes three scattering events to rethermalize, so the thermalization rate $\sim n\langle\sigma_{\rm el}v_{\rm rel}\rangle/3$, where brackets indicate a thermal average. Thus, at a Feshbach resonance where $|a|$ is maximized, cross-dimensional rethermalization occurs most

B_0 **(G)**	ΔB **(G)**
K $\|9/2, -7/2\rangle$	
81.65	0.30
90.40	6.50
110.30	17.05
K $\|9/2, -9/2\rangle$	
78.35	5.80
89.80	9.55

Table A.1: NaK Feshbach resonances and widths from [229] involving Na in the $|F, m_F\rangle = |1, 1\rangle$ state and the specified K state.

quickly, and the spatial anisotropy is minimized. In contrast, this rethermalization does not occur when $a = 0$, and the anisotropy is maximized. The positions of the local maxima and minima of σ_y/σ_x therefore correspond to experimentally determined zero-crossings and Feshbach resonances, respectively.

The results of the cross-dimensional thermalization study are shown in Fig. A-2. We have fit a phenomenological model as the solid line,

$$a = a_{bg} \prod_i \left(1 + \frac{\Delta B_i}{B - B_i}\right) \tag{A.2}$$

We compared our empirical data with theoretical calculations from Eberhard Tiemann [229], based on numerically solving a coupled-channels Schrodinger equation with singlet and triplet potential energy curves given by previous experimental measurements. Details on the theory calculation can be found in [255]. Our empirical resonances and zero-crossings are consistent with the calculated measurements given in Tab. A.1. These calculated measurements were used in all reported scattering lengths of this thesis, along with $a_{bg} = -730\, a_0$.

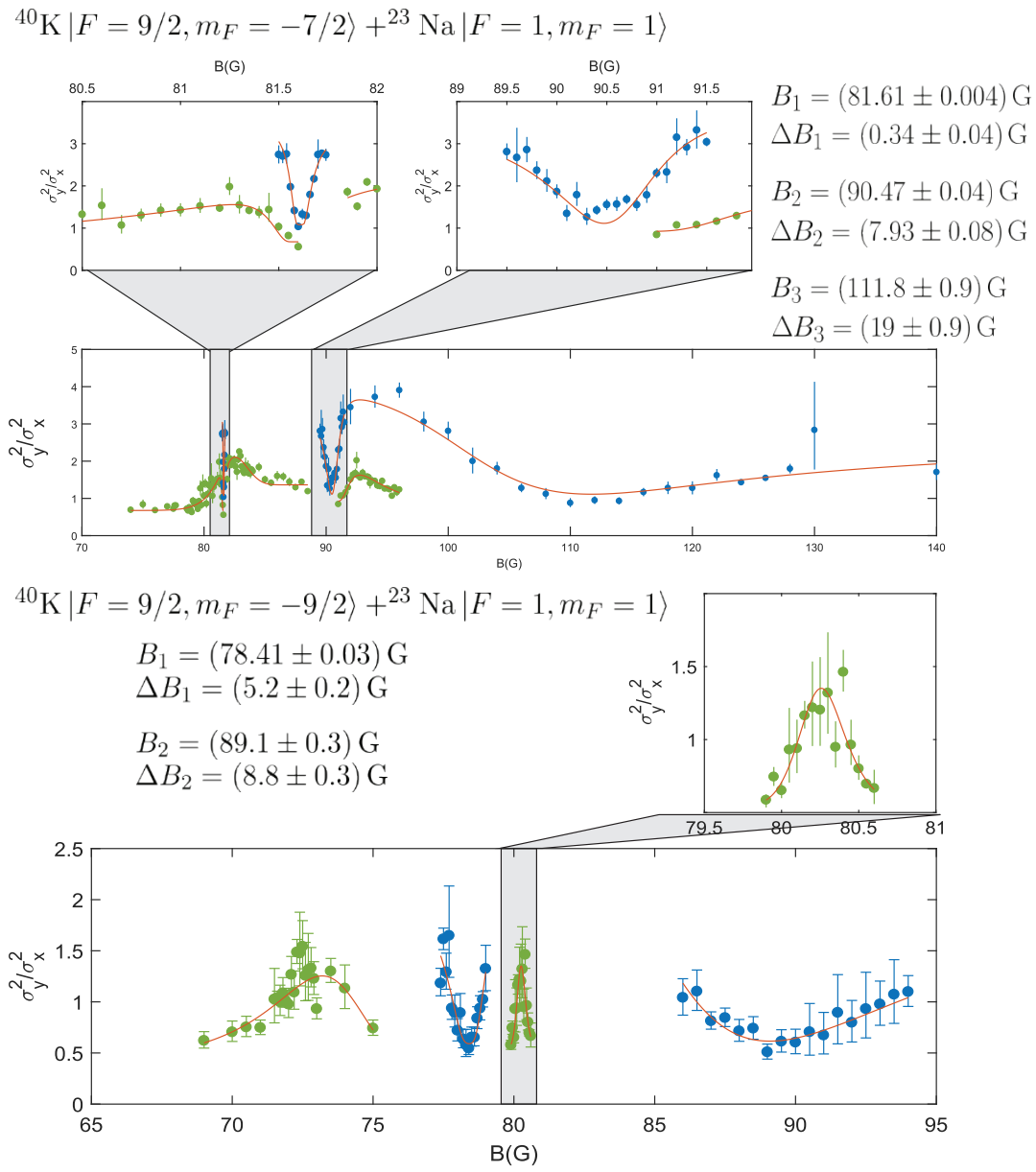

Figure A-2: **Feshbach resonance and zero-crossing positions extracted from cross-dimensional thermalization measurements.** Blue circles show measurements tailored for finding resonance positions, and green show the equivalent for zero-crossings. Reported error bounds are fit errors from a phenomenological model, not estimates of uncertainty.

Appendix B

^{40}K laser system and flux diagnostics

This appendix includes the detailed schematics of the potassium laser system and the absorption characterization of the potassium flux. Details on the source diode laser (DL PRO), frequency locking, slowing light, imaging, and optical pumping setup can be found in Cheng Hsun Wu's thesis [241]. Compared to the setup shown therein, we now directly increase the source diode laser's power via a tapered amplifier (TA) with optical isolation (ISO), and split the source into two separate frequency components, the main MOT light and the repumper (shown in Fig. B-1). These two components seed the MOT and repumper TA's directly (not pictured). A portion of those TA outputs go into the slowing, optical pumping, and imaging paths, as shown in [241]. The remainder is used for magneto-optical trapping via a home-built 2 x 6 fiber manifold, shown in Fig. B-2.

Flux diagnostics

When the atom number in the ^{40}K MOT is unsatisfactory, a characterization of atom flux at the slower may be beneficial. We utilize the more common isotope ^{39}K, the same isotope used for the frequency locking, to characterize flux via spectroscopy. Sending in a 1 mm diameter beam into the chamber, directly after the atom shutter [241], we are able to measure the following absorption feature in Fig. B-3. Care must be taken so the power is below saturation. Moreover, stabilization of light by a

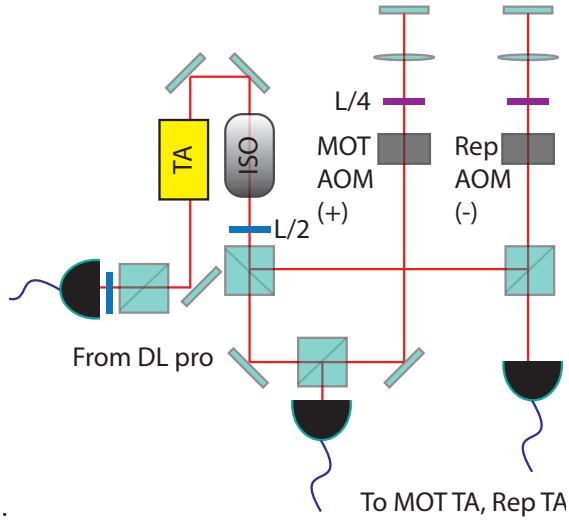

Figure B-1: Schematic of the frequency shifters for the MOT and repumper components for ^{40}K laser cooling.

..

servo is desirable to increase signal-to-noise.

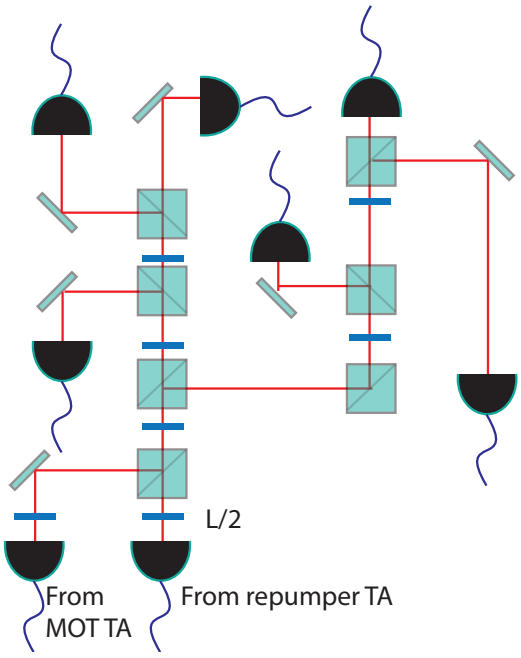

Figure B-2: Schematic of fiber manifold for ^{40}K light, taking inputs from the MOT and repumper tapered amplifiers and outputs into each of the six laser cooling beams on the experiment. Each fiber incoupler has a half- and quarter-waveplate (not pictured) for matching to the polarization-maintaining fiber's slow axis.

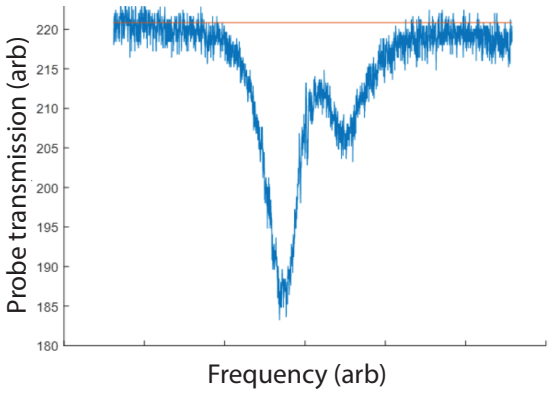

Figure B-3: Absorption signal of ^{39}K at 15% maximum. The two features are dominated by the $F = 1 \rightarrow F' = 0, 1, 2$ and $F = 2 \rightarrow F' = 1, 2, 3$ optical transitions.

Appendix C

Magnetic field gradient control

This appendix describes the magnetic field gradient control system we installed in the apparatus. Many applications require the use of a z-directional B-field gradient to levitate atoms against gravity. For a dual-species experiment, this requirement is even more important as the two species have different masses and different responses to optical potentials (absent the usage of a magic-wavelength trap). To increase the density overlap between ^{23}Na and ^{40}K, we desired this degree of freedom.

The gradient coils are an anti-Helmholtz pair described in Cheng Hsun Wu's thesis [241] and are distinct from the main coils that generate a high gradient for magnetic evaporation (the "magnetic trap coils," which are utilized later to also generate a Feshbach field with the current in the Helmholtz configuration). Since the original construction of the machine, one of the main coils had become clogged, preventing water cooling, necessitating a cannibalization of one of the original gradient coil pairs into the magnetic trap coils. For years we were without a secondary gradient coil that could be applied simultaneously with our Feshbach field, until we decided to recover the gradient by using one of the clogged coils.

The schematic is shown in Fig. C-1. For power, we use a current-controlled Delta SM100-15. The IGBT gates the power, and a flyback diode in parallel protects the power supply. Later, a 0.25-Ohm 1000W resistor was added in parallel to the coil, in series to the flyback diode, for faster current switch-off. However, empirically we did not find a huge difference for the B-field decay time on the atoms, suggesting that

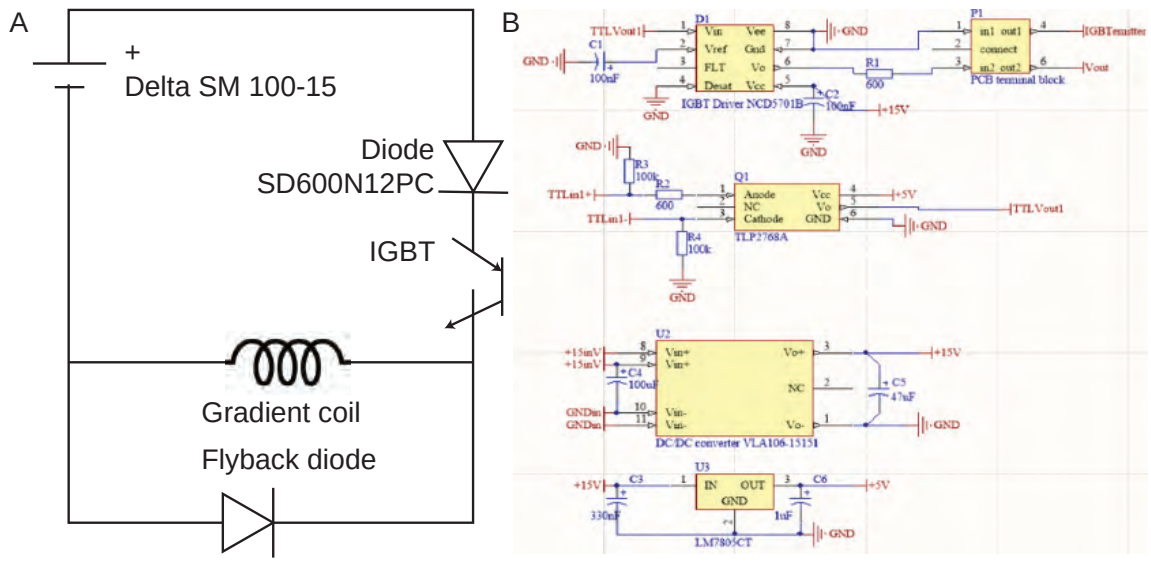

Figure C-1: **Schematic of magnetic gradient coil** (A) Circuit diagram. (B) IGBT control electronics circuit diagram, based on a design from Airlia Shaffer-Moag and Cedric Wilson.

eddy currents (perhaps within the chamber or the gaskets) dominate the decay time.

We calibrated the gradient by levitating Na $|1,1\rangle$ against gravity in the absence of any other trapping potentials, but with a background Feshbach field. The atoms levitated when the gradient satisfied the condition $mg/(0.5\mu_B)$, and we determined the gradient value per current to be $0.22\,\mathrm{G/cm/A}$. A similar study in the absence of any other external fields showed that the "zero" of the coil pair is unfortunately displaced from the magnetic trap center. Because of this, our Feshbach field calibrations slightly shift depending on what value we use for the gradient coils. To maximize the overlap between our two most commonly used states, Na $|F=1,m_F=1\rangle$ and K$|9/2,-9/2\rangle$, requires $\frac{dB}{dz} = 12\,\mathrm{G/cm}$ in a 1064 nm trap with a z-trapping frequency of $\sim 2\pi(100)\,\mathrm{Hz}$. We confirmed this empirically by minimizing the lifetime of the K atoms at strong interactions with the Na atoms as a function of gradient value. At the best overlap gradient value, the K atoms underwent the fastest inelastic 3-body losses with Na atoms.

Appendix D

Bose polaron properties within the variational approach

In the following section, we calculate the Bose polaron's energy, residue, and contact at $T = 0$ from a simple variational ansatz, the results of which were compared to experiment in Ch. 3. We find a negative-energy attractive polaron branch that evolves across the Feshbach resonance into a diatomic molecule on the repulsive scattering side. A more concise version of this appendix can be found in the supplement of Ref. [247].

The variational ansatz was originally introduced by Chevy for the description of the Fermi polaron [53]. An equivalent ansatz was first employed for Bose polarons in Ref. [152]. This turns out to be identical to what is obtained from the lowest-order T-matrix calculation in the same limit [198].

Here, we consider a single impurity immersed in a BEC. The impurity-boson coupling is modeled by a contact interaction, characterized by the s-wave scattering length a. We write a trial wavefunction and minimize the system's energy, obtaining the Bose polaron's dispersion. The impurity-boson interaction is treated beyond the mean-field approximation by the variational method, which is therefore applicable to the strong-coupling regime. We work in the limit of zero boson-boson interaction, justified *a posteriori* as we find that the boson chemical potential is much smaller than the polaron energy E_{p}. In this limit, the linear portion of the Bogoliubov spectrum

for the bosons at low momenta is not relevant for the energy of the polaron, and we can simply work with a free-particle dispersion. (The variational case generalized to weakly repulsive BEC's was considered in [152].)

The Hamiltonian describing the impurity interacting with the Bose gas is

$$H = \sum_{\mathbf{k}} \left(\epsilon_{\mathrm{B},\mathbf{k}} a_{\mathbf{k}}^\dagger a_{\mathbf{k}} + \epsilon_{\mathrm{I},\mathbf{k}} c_{\mathbf{k}}^\dagger c_{\mathbf{k}} \right) + \frac{g_0}{V} \sum_{\mathbf{k}\mathbf{k}'\mathbf{q}} a_{\mathbf{k}+\mathbf{q}}^\dagger c_{\mathbf{k}'-\mathbf{q}}^\dagger c_{\mathbf{k}'} a_{\mathbf{k}}. \tag{D.1}$$

Here, $\epsilon_{\mathrm{B},\mathbf{k}} = \hbar^2 k^2 / 2m_{\mathrm{B}}$ and $\epsilon_{\mathrm{I},\mathbf{k}} = \hbar^2 k^2 / 2m_{\mathrm{I}}$ are the boson and impurity free dispersions, m_{B} and m_{I} the boson and impurity mass, respectively, $a_{\mathbf{k}}^\dagger$ and $c_{\mathbf{k}}^\dagger$ are the boson and impurity creation operators, and V the quantization volume. g_0 is the bare impurity-boson coupling constant, related to the impurity-boson scattering length a via the Lippmann-Schwinger equation

$$\begin{aligned} \frac{1}{g_0} &= \frac{m_r}{2\pi\hbar^2 a} - \frac{1}{V} \sum_{\mathbf{k}} \frac{1}{\epsilon_{\mathrm{B},\mathbf{k}} + \epsilon_{\mathrm{I},\mathbf{k}}} \\ &= \frac{m_r}{2\pi\hbar^2 a} - \frac{1}{V} \sum_{\mathbf{k}} \frac{2m_r}{k^2} \end{aligned} \tag{D.2}$$

where m_r is the reduced mass.

The variational wavefunction is a superposition of the unscattered impurity at rest $|\mathbf{0}\rangle_I$, immersed in the Bose condensate, and the impurity scattered into momentum state $-\mathbf{k}$, having ejected one boson out of the condensate into momentum $\mathbf{k}$:

$$|\Psi\rangle = \phi_0 \, |\mathbf{0}\rangle_{\mathrm{I}} \otimes |\alpha\rangle_{\mathrm{B}} + \sqrt{N_{\mathrm{B}}} \sum_{\mathbf{k}\neq\mathbf{0}} \phi_{\mathbf{k}} a_{\mathbf{k}}^\dagger \, |-\mathbf{k}\rangle_{\mathrm{I}} \otimes |\alpha\rangle_{\mathrm{B}} \, . \tag{D.3}$$

Here, the wavefunction has total momentum $q = 0$, though this ansatz can be generalized to have finite total momentum. The condensate is taken to be in a coherent state $|\alpha\rangle_{\mathrm{B}}$. The factor $\sqrt{N_{\mathrm{B}}}$, where N_{B} is the average boson number, originates from the destruction operator $a_{\mathbf{0}}$ acting on the condensate, giving $\alpha = \sqrt{N_{\mathrm{B}}}$. The expectation

values of the kinetic and potential energies are

$$\langle H_0 \rangle = N_{\rm B} \sum_{\mathbf{k}} |\phi_{\mathbf{k}}|^2 \left(\epsilon_{{\rm B},\mathbf{k}} + \epsilon_{{\rm I},\mathbf{k}}\right) \tag{D.4}$$

$$\langle V \rangle = g_0\, n_{\rm B} \left(|\phi_0|^2 + \sum_{\mathbf{k}\neq\mathbf{0}} \left(\phi_0 \phi_{\mathbf{k}}^* + \phi_0^* \phi_{\mathbf{k}}\right) + \sum_{\mathbf{k},\mathbf{k}'\neq\mathbf{0}} \phi_{\mathbf{k}} \phi_{\mathbf{k}'}^* \right) \tag{D.5}$$

with $n_{\rm B} = N_{\rm B}/V$ the boson density. To find the local minimum of total expected energy $\langle H_0 + V \rangle$, we minimize $\langle H_0 + V \rangle - E_{\rm p}$ with respect to all components of ϕ (*i.e.,* $\phi_0^*, \phi_{\mathbf{k}}^*$), where the Lagrange multiplier $E_{\rm p}$ is associated with the polaron's energy. Under the normalization constraint $\langle \Psi | \Psi \rangle = 1$, this yields the following set of equations:

$$g_0 n_{\rm B} \chi = E_{\rm p} \phi_0 \tag{D.6}$$

$$g_0 \frac{1}{V} \chi = (E_{\rm p} - \epsilon_{{\rm B},\mathbf{k}} - \epsilon_{{\rm I},\mathbf{k}}) \phi_{\mathbf{k}} \tag{D.7}$$

with $\chi = \phi_0 + \sum_{\mathbf{k}} \phi_{\mathbf{k}}$. One obtains for the coefficients $\phi_{\mathbf{k}}$:

$$\phi_{\mathbf{k}} = \frac{1}{N_{\rm B}} \frac{E_{\rm p}}{E_{\rm p} - \epsilon_{{\rm B},\mathbf{k}} - \epsilon_{{\rm I},\mathbf{k}}} \phi_0, \tag{D.8}$$

and for the polaron energy $E_{\rm p}$, after eliminating g_0 in favor of the scattering length a:

$$E_{\rm p} = \frac{n_{\rm B}}{\frac{m_r}{2\pi\hbar^2 a} - \frac{1}{V} \sum_{\mathbf{k}} \left(\frac{1}{E_{\rm p} - \epsilon_{{\rm B},\mathbf{k}} - \epsilon_{{\rm I},\mathbf{k}}} + \frac{1}{\epsilon_{{\rm B},\mathbf{k}} + \epsilon_{{\rm I},\mathbf{k}}} \right)} \tag{D.9}$$

Noting that $\frac{1}{V} \sum_{\mathbf{k}} \left(\frac{1}{E_{\rm p} - \epsilon_{{\rm B},\mathbf{k}} - \epsilon_{{\rm I},\mathbf{k}}} + \frac{1}{\epsilon_{{\rm B},\mathbf{k}} + \epsilon_{{\rm I},\mathbf{k}}} \right) = \frac{m_r \kappa}{2\pi\hbar^2}$, where we have set $E_{\rm p} \equiv -\frac{\hbar^2 \kappa^2}{2m_r}$, one obtains a cubic equation for the polaron energy (given in Ch. 3):

$$E_{\rm p} \equiv -\frac{\hbar^2 \kappa^2}{2m_r} = -\frac{2\pi\hbar^2 n_{\rm B}}{m_r} f(i\kappa) \tag{D.10}$$

where $f(i\kappa) = -\frac{a}{1-\kappa a}$ is the two-body scattering amplitude at imaginary momentum $i\kappa$. The solution on the attractive side ($a<0$) is purely real and negative – the attractive polaron branch. This branch smoothly continues onto the repulsive side. On that

side, another, higher-energy solution is complex with a positive real part, suggesting a limited lifetime for a positive-energy polaron. The metastable repulsive branch has been detected with two injection spectroscopy experiments [123, 128] and will not be discussed further here.

For nonzero total momentum, the polaron dispersion relation can be written as [152]

$$E_{\mathrm{p}}(q) = E_{\mathrm{p}}(0) + \frac{\hbar^2 q^2}{2m_{\mathrm{eff}}} + \mathcal{O}(q^4) \tag{D.11}$$

for small q, where $E_{\mathrm{p}}(0)$ is the binding energy, sometimes called the self-energy, and the prefactor of the quadratic term given by the effective mass m_{eff}. For the rest of this section, we will use E_{p} to exclusively denote the binding energy.

Fig. D-1 compares the variational binding energy of the Bose polaron with that of the Fermi polaron [53] – an impurity immersed in a Fermi sea of the same density. Energies are plotted as a function of the dimensionless interaction parameter $1/k_n a$, where k_n is the wavevector of the majority component. The difference in energies is generally less than $\sim 0.2E_n$ for all interaction strengths, where $E_n = \hbar^2 k_n^2/4m_{\mathrm{r}}$ is the degeneracy energy scale. The Fermi polaron is less strongly bound due to the spread of relative momenta in the initial state and Pauli blocking of final scattering states.

Also shown are comparisons of the attractive Bose polaron branch to two limiting cases: the mean-field limit and the molecular dimer. Deep on the attractive side $1/k_n a \to -\infty$, perturbation theory gives the analytic mean-field result of $E_{\mathrm{mf}} \equiv \frac{2\pi\hbar^2 n_{\mathrm{B}} a}{m_r}$ (see black dashed line of Fig. D-1), which agrees with the variational energy for weak attractions. In the opposite repulsive limit, a single impurity and a single boson pair to form a molecule with energy $-\hbar^2/2m_r a^2$ (see orange dashed line of Fig. D-1). This also agrees with the variational energy for $1/k_n a \to \infty$. At least within the variational approximation, the attractive polaron's energy smoothly crosses over into the molecular branch.

Not only does the variational calculation yield the polaron energy, but it also produces other quasiparticle properties: the residue and contact. The normalization condition $|\phi_0|^2 + N_{\mathrm{B}} \sum_{\mathbf{k}\neq\mathbf{0}} |\phi_{\mathbf{k}}|^2 = 1$ yields the quasiparticle weight (residue) in this

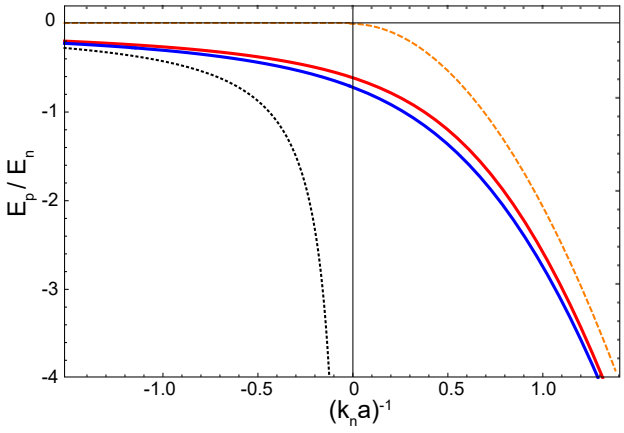

Figure D-1: Binding energy of the Bose and Fermi polaron from the variational ansatz (solid blue and red line, respectively). For comparison, the bare molecular energy is shown (dashed, yellow) as well as the mean-field result (black, dotted). Figure reproduced from the supplement of [247].

approximation:

$$Z \equiv |\phi_0|^2 = \frac{1}{1+\frac{1}{8\pi}\frac{\kappa^3}{n_\mathrm{B}}} = \frac{1}{1+\frac{1}{2}\left(1-\frac{E_\mathrm{p}}{E_\mathrm{mf}}\right)} \tag{D.12}$$

Z is thus simply related to the ratio of E_p and the mean-field result. On resonance with $1/k_n a = 0$, where $1/E_\mathrm{mf} = 0$, this approach yields a quasiparticle weight of $Z = 2/3$, as seen in Fig. D-2.

The contact $C \equiv \frac{8\pi m_r}{\hbar^2}\frac{\partial E_\mathrm{p}}{\partial(-a^{-1})}$ directly follows from the a-dependence of E_p as

$$\frac{C}{k_n} = \pi^2 \frac{\frac{E_\mathrm{p}}{E_n}}{\frac{E_n}{E_\mathrm{p}} - \frac{\pi}{4}\frac{1}{k_n a}} \tag{D.13}$$

The momentum distribution of the polaron is given by a delta-function centered at $\mathbf{k} = 0$, of weight Z, plus a contribution $n_k = N_\mathrm{B}\,|\phi_k|^2$ from impurity-boson scattering:

$$\begin{aligned} n_k &= \frac{Z}{N_\mathrm{B}}\frac{E_\mathrm{p}^2}{\left(E_\mathrm{p} - \epsilon_{\mathrm{B},\mathbf{k}} - \epsilon_{\mathrm{I},\mathbf{k}}\right)^2} \\ &= \frac{Z}{N_\mathrm{B}}\frac{1}{\left(1+\frac{k^2}{\kappa^2}\right)^2} \end{aligned} \tag{D.14}$$

This component of the momentum distribution has the same dependence on momentum as that of a Feshbach molecule of spatial size $1/\kappa$, with the length scale set by the

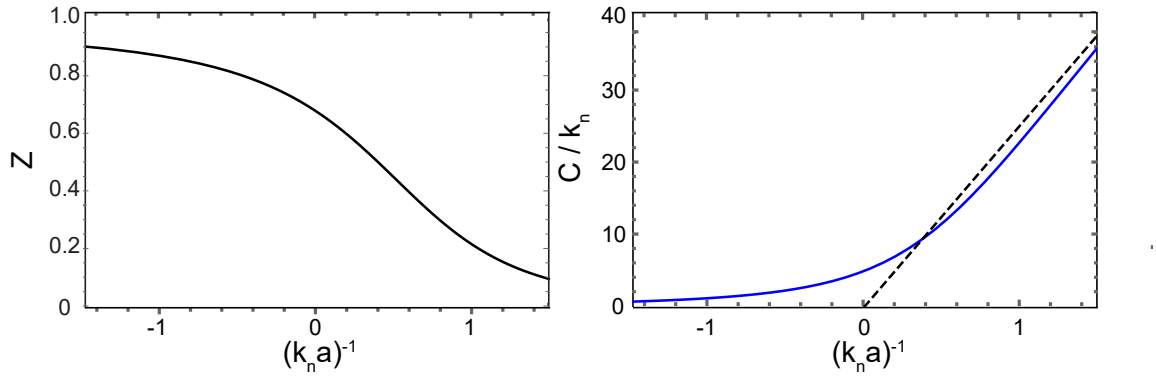

Figure D-2: The residue (left) and contact (right, blue curve) of the Bose polaron, within the variational ansatz. The contact for a bare molecule is shown as the dashed black line. Figure reproduced from the supplement of [247].

polaron energy. In real space, the wavefunction of the polaron thus is a superposition of a delocalized wave of weight Z and a part that is localized, of the form $\frac{1}{r}\exp(-\kappa r)$.

The contact C governs the high-momentum tails of the momentum distribution according to $n_k \to \frac{C/V}{k^4}$ (see Ch. 3.6.1). From this limiting behavior, we obtain a relation between the contact, the quasiparticle weight and the polaron energy (see Fig. D-2), valid within this variational approach:

$$\frac{C}{k_n} = \frac{3\pi^2}{2} Z \left(\frac{E_\mathrm{p}}{E_n}\right)^2 \tag{D.15}$$

Appendix E

Electric field control

Here we include the schematic for an updated electrode to provide static electric fields to the molecules. For the studies of Stark shifts presented in Ch. 5, we used two identical indium-tin-oxide (ITO)-coated plates positioned outside the ultrahigh vacuum chamber, separated by 9.5 cm. However, gradients over our molecule sample limited our trap lifetimes at fields above $\sim$ 0.7 kV/cm. Furthermore, STIRAP resonances were observed to be shifted ($\sim$ 100 kHz) after extended application of voltage to the electrodes, a possible side effect of polarizing the viewports. A UV lamp was installed above the top electrode to deionize the glass.

We replaced the top electrode with the following design, shown in Fig. E-1. Each segment is controlled by a high-voltage operational amplifier Matsusada AMS-10B2-LCN1, connected by CN-40-AHVP high voltage cable. Extensions for the leads were created with high voltage wire from Accuglass. Kapton tape covered any exposed wires to prevent arcing.

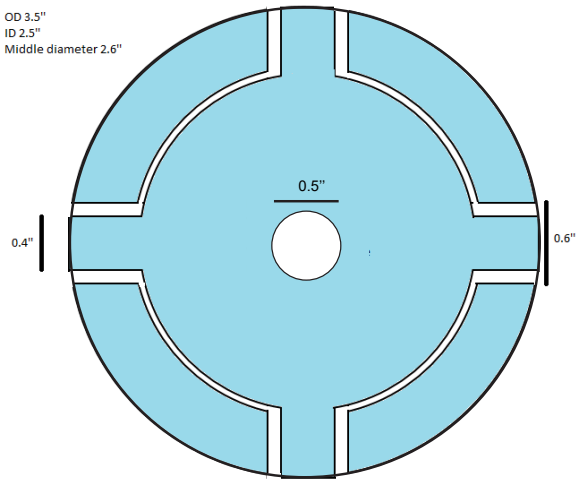

Figure E-1: Design for top electrode placed above the bucket window. The disk was provided by Delta Technologies (unpolished float glass, 0.036 inch ITO-coating on one surface.) White portions were stripped away of their coating by Potomac Photonics. I drilled a 0.5 inch diameter in the center with a diamond-coated hole saw to allow for optical access. Five leads (not pictured) were attached with copper busbars and silver epoxy to the five segments for independent voltage control.

Appendix F

Rotations and Euler Angles

It is often convenient to consider rotation from one set of axes to another, as in Ch. 6. Consider a coordinate transformation that takes the axes (x, y, z) into another set of axes (X, Y, Z), which share the same origin. This change can be obtained by three successive rotations about the Euler angles α, β, γ, and the rotation operator can be written,

$$\mathcal{R}(\alpha, \beta, \gamma) = \mathcal{R}_Z(\gamma)\mathcal{R}_N(\beta)\mathcal{R}_z(\alpha) \tag{F.1}$$

where N denotes the nodal line – the intersection between the two planes xy and XY, shown in Fig. F-1. Equivalently, this rotation operator can be written $\mathcal{R}(\alpha, \beta, \gamma) = \mathcal{R}_z(\alpha)\mathcal{R}_y(\beta)\mathcal{R}_z(\gamma)$. (See, for example, [33] for a more complete description of Euler angles).

For example, our original frame might represent the laboratory frame, and the final

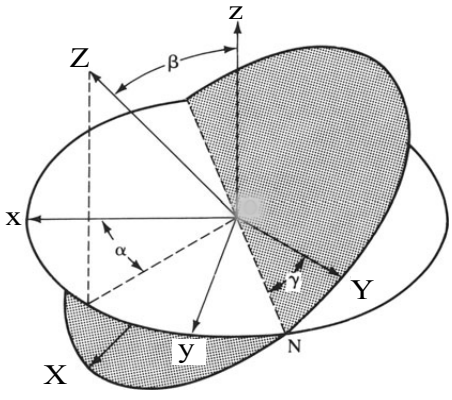

Figure F-1: Rotating between two frames (x, y, z) and (X, Y, Z) using Euler angles α, β, γ.

..

X, Y, Z axes can represent the principal axes of an interaction tensor. In its principal axis system, let $\rho_{J,M}$ denote an irreducible spherical tensor. Upon a rotation given by $\mathcal{R}$, the irreducible spherical tensor component $T_{J,M}$ transforms into $\rho_{J,M}$, which is a linear combination of the $(2J+1)$ components $T_{J,M'}$:

$$\rho_{J,M} = \mathcal{R}(\alpha,\beta,\gamma)T_{J,M}\mathcal{R}^{-1}(\alpha,\beta,\gamma) = \sum_{M'} D^{(J)}_{M',M}(\alpha,\beta,\gamma)T_{J,M'} \tag{F.2}$$

Here, $D^{(J)}_{M',M}$ is a Wigner D-matrix of rank J. Its subscripts are projection indices denoting components of angular momentum J.

The rotational part of a diatomic molecule's wavefunction can be written (see Ch. 5 of Ref. [33])

$$|J,K,M\rangle = \sqrt{\frac{2J+1}{8\pi^2}} D^{(J)*}_{M,K}(\vec{\Omega}) \tag{F.3}$$

where K is the projection of the angular momentum J on the internuclear axis.

Bibliography

[1] Alexandre S. Alexandrov and Jozef T. Devreese. *Advances in Polaron Physics*, volume 159. Springer-Verlag, Berlin, 2010.

[2] A. Altmeyer, S. Riedl, C. Kohstall, M. J. Wright, R. Geursen, M. Bartenstein, C. Chin, J. Hecker Denschlag, and R. Grimm. Precision Measurements of Collective Oscillations in the BEC-BCS Crossover. *Phys. Rev. Lett.*, 98:040401, Jan 2007.

[3] M. H. Anderson, J. R. Ensher, M. R. Matthews, C. E. Wieman, and E. A. Cornell. Observation of Bose-Einstein Condensation in a Dilute Atomic Vapor. *Science*, 269(5221):198–201, 1995.

[4] Rhys Anderson, Fudong Wang, Peihang Xu, Vijin Venu, Stefan Trotzky, Frédéric Chevy, and Joseph H. Thywissen. Conductivity spectrum of ultracold atoms in an optical lattice. *Phys. Rev. Lett.*, 122:153602, Apr 2019.

[5] A. V. Andreev, Steven A. Kivelson, and B. Spivak. Hydrodynamic description of transport in strongly correlated electron systems. *Phys. Rev. Lett.*, 106(25):1–4, 2011.

[6] V. Andreev *et al.* Improved limit on the electric dipole moment of the electron. *Nature*, 562:355, 2018.

[7] L. A. Peña Ardila and S. Giorgini. Impurity in a Bose-Einstein condensate: Study of the attractive and repulsive branch using quantum Monte Carlo methods. *Phys. Rev. A*, 92(3):033612, 2015.

[8] L. A. Peña Ardila and S. Giorgini. Bose polaron problem: Effect of mass imbalance on binding energy. *Phys. Rev. A*, 94(6):063640, 2016.

[9] L. A. Peña Ardila, N. B. Jørgensen, T. Pohl, S. Giorgini, G. M. Bruun, and J. J. Arlt. Analyzing the Bose Polaron Across Resonant Interactions. *Phys. Rev. A*, 99:063607, 2019.

[10] Yoji Asano, Masato Narushima, Shohei Watabe, and Tetsuro Nikuni. Collective Excitations in Bose–Fermi Mixtures. *J. Low Temp. Phys.*, 196(1-2):133–139, 2019.

[11] Yoji Asano, Shohei Watabe, and Tetsuro Nikuni. Dipole oscillation of a trapped Bose-Fermi-mixture gas in collisionless and hydrodynamic regimes. *Phys. Rev. A*, 101(1):013611, 2020.

[12] N. Balakrishnan. Perspective: Ultracold molecules and the dawn of cold controlled chemistry. *J. Chem. Phys.*, 145(15):150901, 2016.

[13] N. Balakrishnan and A. Dalgarno. Chemistry at ultracold temperatures. *Chemical Physics Letters*, 341:652, 2001.

[14] D. A. Bandurin, I. Torre, R. Krishna Kumar, M. Ben Shalom, A. Tomadin, A. Principi, G. H. Auton, E. Khestanova, K. S. Novoselov, I. V. Grigorieva, L. A. Ponomarenko, A. K. Geim, and M. Polini. Negative local resistance caused by viscous electron backflow in graphene. *Science*, 351(6277):1055–1058, 2016.

[15] Denis A. Bandurin, Andrey V. Shytov, Leonid S. Levitov, Roshan Krishna Kumar, Alexey I. Berdyugin, Moshe Ben Shalom, Irina V. Grigorieva, Andre K. Geim, and Gregory Falkovich. Fluidity onset in graphene. *Nat. Commun.*, 9:4533, 2018.

[16] Arup Banerjee. Collective oscillations of a Bose-Fermi mixture: Effect of unequal masses of Bose and Fermi particles. *Phys. Rev. A*, 76(2):023611, 2007.

[17] M. A. Baranov, M. Dalmonte, G. Pupillo, and P. Zoller. Condensed matter theory of dipolar quantum gases. *Chem. Rev.*, 112(9):5012–5061, 2012.

[18] M. A. Baranov, M. S. Mar'enko, Val. S. Rychkov, and G. V. Shlyapnikov. Superfluid pairing in a polarized dipolar Fermi gas. *Phys. Rev. A*, 66:013606, Jul 2002.

[19] Ryan Barnett, Dmitry Petrov, Mikhail Lukin, and Eugene Demler. Quantum magnetism with multicomponent dipolar molecules in an optical lattice. *Phys. Rev. Lett.*, 96(19):190401, 2006.

[20] G. Baym and C. Pethick. *Landau Fermi-Liquid Theory: Concepts and Applications*. Wiley-VCH, Weinheim, 2004.

[21] Gordon Baym, C. J. Pethick, Zhenhua Yu, and Martin W. Zwierlein. Coherence and clock shifts in ultracold Fermi gases with resonant interactions. *Phys. Rev. Lett.*, 99(19):190407, 2007.

[22] A. I. Berdyugin, S. G. Xu, F. M.D. Pellegrino, R. Krishna Kumar, A. Principi, I. Torre, M. Ben Shalom, T. Taniguchi, K. Watanabe, I. V. Grigorieva, M. Polini, A. K. Geim, and D. A. Bandurin. Measuring Hall viscosity of graphene's electron fluid. *Science*, 364(6436):162–165, 2019.

[23] G. Bertaina, E. Fratini, S. Giorgini, and P. Pieri. Quantum Monte Carlo Study of a Resonant Bose-Fermi Mixture. *Phys. Rev. Lett.*, 110:115303, Mar 2013.

[24] Jacob A. Blackmore, Luke Caldwell, Philip D. Gregory, Elizabeth M. Bridge, Rahul Sawant, Jesús Aldegunde, Jordi Mur-Petit, Dieter Jaksch, Jeremy M. Hutson, B. E. Sauer, M. R. Tarbutt, and Simon L. Cornish. Ultracold molecules for quantum simulation: Rotational coherences in CaF and RbCs. *Quantum Sci. Technol.*, 4(1):014010, 2019.

[25] Immanuel Bloch, Jean Dalibard, and Wilhelm Zwerger. Many-body physics with ultracold gases. *Rev. Mod. Phys.*, 80(3):885–964, 2008.

[26] John L. Bohn, Ana Maria Rey, and Jun Ye. Cold molecules: Progress in quantum engineering of chemistry and quantum matter. *Science*, 357(6355):1002–1010, 2017.

[27] C. Boisseau, E. Audouard, J. Vigué, and P. S. Julienne. Reflection approximation in photoassociation spectroscopy. *Phys. Rev. A*, 62:052705, Oct 2000.

[28] T. Bourdel, J. Cubizolles, L. Khaykovich, K. M. F. Magalhães, S. J. J. M. F. Kokkelmans, G. V. Shlyapnikov, and C. Salomon. Measurement of the Interaction Energy near a Feshbach Resonance in a ^{6}Li Fermi Gas. *Phys. Rev. Lett.*, 91:020402, Jul 2003.

[29] Eric Braaten. Universal relations for fermions with large scattering length. *Lect. Notes Phys.*, 836:193–231, 2012.

[30] Eric Braaten, Daekyoung Kang, and Lucas Platter. Short-time operator product expansion for rf spectroscopy of a strongly interacting Fermi gas. *Phys. Rev. Lett.*, 104(22):223004, 2010.

[31] Eric Braaten and Lucas Platter. Exact relations for a strongly interacting Fermi gas from the operator product expansion. *Phys. Rev. Lett.*, 100(20):205301, 2008.

[32] B. A. Braem, F. M.D. Pellegrino, A. Principi, M. Röösli, C. Gold, S. Hennel, J. V. Koski, M. Berl, W. Dietsche, W. Wegscheider, M. Polini, T. Ihn, and K. Ensslin. Scanning gate microscopy in a viscous electron fluid. *Phys. Rev. B*, 98(24):1–5, 2018.

[33] John M. Brown and Alan Carrington. *Rotational Spectroscopy of Diatomic Molecules*. Cambridge Molecular Science. Cambridge University Press, Cambridge, 2003.

[34] Peter T. Brown, Debayan Mitra, Elmer Guardado-Sanchez, Reza Nourafkan, Alexis Reymbaut, Charles David Hébert, Simon Bergeron, A. M.S. Tremblay, Jure Kokalj, David A. Huse, Peter Schauß, and Waseem S. Bakr. Bad metallic transport in a cold atom Fermi-Hubbard system. *Science*, 363(6425):379–382, 2019.

[35] M. Bruderer, W. Bao, and D. Jaksch. Self-trapping of impurities in Bose-Einstein condensates: Strong attractive and repulsive coupling. *Europhysics Letters*, 82(3):30004, Apr 2008.

[36] G. M. Bruun and P. Massignan. Decay of polarons and molecules in a strongly polarized Fermi gas. *Phys. Rev. Lett.*, 105(2):020403, 2010.

[37] G. M. Bruun and E. Taylor. Quantum phases of a two-dimensional dipolar Fermi gas. *Phys. Rev. Lett.*, 101(24):245301, 2008.

[38] Georg M. Bruun and Charles W. Clark. Ideal gases in time-dependent traps. *Phys. Rev. A*, 61:061601, May 2000.

[39] H. P. Büchler, E. Demler, M. Lukin, A. Micheli, N. Prokof'ev, G. Pupillo, and P. Zoller. Strongly correlated 2D quantum phases with cold polar molecules: Controlling the shape of the interaction potential. *Phys. Rev. Lett.*, 98(6):060404, 2007.

[40] K Burnett, Paul S Julienne, and K-A Suominen. Laser-driven collisions between atoms in a Bose-Einstein condensed gas. *Phys. Rev. Lett.*, 77(8):1416, 1996.

[41] L. Caldwell, H. J. Williams, N. J. Fitch, J. Aldegunde, Jeremy M. Hutson, B. E. Sauer, and M. R. Tarbutt. Long rotational coherence times of molecules in a magnetic trap. *Phys. Rev. Lett.*, 124:063001, Feb 2020.

[42] A. Camacho-Guardian, L. A. Peña Ardila, T. Pohl, and G. M. Bruun. Bipolarons in a Bose-Einstein Condensate. *Phys. Rev. Lett.*, 121(1):013401, 2018.

[43] C. Cao, E. Elliott, J. Joseph, H. Wu, J. Petricka, T. Schäfer, and J. E. Thomas. Universal quantum viscosity in a unitary fermi gas. *Science*, 331(6013):58–61, 2010.

[44] P. Capuzzi and E. S. Hernández. Zero-sound density oscillations in Fermi-Bose mixtures. *Phys. Rev. A*, 64(4):043607, 2001.

[45] P. Capuzzi, A. Minguzzi, and M. P. Tosi. Collisional oscillations of trapped boson-fermion mixtures in the approach to the collapse instability. *Phys. Rev. A*, 69:053615, 2004.

[46] C. Carcy, S. Hoinka, M. G. Lingham, P. Dyke, C. C. N. Kuhn, H. Hu, and C. J. Vale. Contact and Sum Rules in a Near-Uniform Fermi Gas at Unitarity. *Phys. Rev. Lett.*, 122:203401, May 2019.

[47] Lincoln D. Carr, David DeMille, Roman V. Krems, and Jun Ye. Cold and ultracold molecules: Science, technology and applications. *New J. Phys.*, 11(0):055049, 2009.

[48] W. Casteels, J. Tempere, and J. T. Devreese. Bipolarons and multipolarons consisting of impurity atoms in a Bose-Einstein condensate. *Phys. Rev. A*, 88(1):013613, 2013.

[49] Y. Castin and R. Dum. Bose-Einstein condensates in time dependent traps. *Phys. Rev. Lett.*, 1996.

[50] J. Catani, G. Lamporesi, D. Naik, M. Gring, M. Inguscio, F. Minardi, A. Kantian, and T. Giamarchi. Quantum dynamics of impurities in a one-dimensional Bose gas. *Phys. Rev. A*, 85:023623, Feb 2012.

[51] Marko Cetina, Michael Jag, Rianne S. Lous, Isabella Fritsche, Jook T.M. Walraven, Rudolf Grimm, Jesper Levinsen, Meera M. Parish, Richard Schmidt, Michael Knap, and Eugene Demler. Ultrafast many-body interferometry of impurities coupled to a Fermi sea. *Science*, 354(6308):96–99, 2016.

[52] Lawrence W Cheuk, Loïc Anderegg, Yicheng Bao, Sean Burchesky, Scarlett Yu, Wolfgang Ketterle, Kang-kuen Ni, and John M Doyle. Observation of Collisions between Two Ultracold Ground-State CaF Molecules. *arXiv:2002.00048*, 2020.

[53] F. Chevy. Universal phase diagram of a strongly interacting Fermi gas with unbalanced spin populations. *Phys. Rev. A*, 74(6):063628, 2006.

[54] Cheng Chin, Rudolf Grimm, Paul Julienne, and Eite Tiesinga. Feshbach resonances in ultracold gases. *Reviews of Modern Physics*, 82(2):1225–1286, 2010.

[55] Ching-Kai Chiu, Jeffrey C. Y. Teo, Andreas P. Schnyder, and Shinsei Ryu. Classification of topological quantum matter with symmetries. *Rev. Mod. Phys.*, 88:035005, Aug 2016.

[56] Rasmus Søgaard Christensen, Jesper Levinsen, and Georg M. Bruun. Quasiparticle Properties of a Mobile Impurity in a Bose-Einstein Condensate. *Phys. Rev. Lett.*, 115:160401, Oct 2015.

[57] Arthur Christianen, Martin W. Zwierlein, Gerrit C. Groenenboom, and Tijs Karman. Photoinduced two-body loss of ultracold molecules. *Phys. Rev. Lett.*, 123:123402, 2019.

[58] R. Combescot, A. Recati, C. Lobo, and F. Chevy. Normal State of Highly Polarized Fermi Gases: Simple Many-Body Approaches. *Phys. Rev. Lett.*, 98(18):180402, 2007.

[59] N R Cooper and G V Shlyapnikov. Stable topological superfluid phase of ultracold polar fermionic molecules. *Phys. Rev. Lett.*, 103(15):155302, 2009.

[60] Jesse Crossno, Jing K. Shi, Ke Wang, Xiaomeng Liu, Achim Harzheim, Andrew Lucas, Subir Sachdev, Philip Kim, Takashi Taniguchi, Kenji Watanabe, Thomas A. Ohki, and Kin Chung Fong. Observation of the Dirac fluid and the breakdown of the Wiedemann-Franz law in graphene. *Science*, 351(6277):1058–1061, 2016.

[61] F. M. Cucchietti and E. Timmermans. Strong-coupling polarons in dilute gas Bose-Einstein condensates. *Phys. Rev. Lett.*, 96(21):210401, 2006.

[62] F. Dalfovo, S. Giorgini, L. P. Pitaevskii, and S. Stringari. Theory of Bose-Einstein condensation in trapped gases. *Rev. Mod. Phys.*, 71(3):463, 1998.

[63] Kedar Damle and Subir Sachdev. Nonzero-temperature transport near quantum critical points. *Phys. Rev. B*, 56(14):8714–8733, 1997.

[64] Johann G. Danzl, Elmar Haller, Mattias Gustavsson, Manfred J. Mark, Russell Hart, Nadia Bouloufa, Olivier Dulieu, Helmut Ritsch, and Hanns-Christoph Nägerl. Quantum gas of deeply bound ground state molecules. *Science*, 321(5892):1062–1066, 2008.

[65] Johann G. Danzl, Manfred J. Mark, Elmar Haller, Mattias Gustavsson, Russell Hart, Jesus Aldegunde, Jeremy M. Hutson, and Hanns Christoph Nägerl. An ultracold high-density sample of rovibronic ground-state molecules in an optical lattice. *Nat. Phys.*, 6(4):265–270, 2010.

[66] R. Daou, Nicolas Doiron-Leyraud, David Leboeuf, S. Y. Li, Francis Laliberté, Olivier Cyr-Choinière, Y. J. Jo, L. Balicas, J. Q. Yan, J. S. Zhou, J. B. Goodenough, and Louis Taillefer. Linear temperature dependence of resistivity and change in the Fermi surface at the pseudogap critical point of a high-Tc superconductor. *Nat. Phys.*, 5(1):31–34, 2009.

[67] K. B. Davis, M. O. Mewes, M. R. Andrews, N. J. van Druten, D. S. Durfee, D. M. Kurn, and W. Ketterle. Bose-Einstein Condensation in a Gas of Sodium Atoms. *Phys. Rev. Lett.*, 75:3969–3973, Nov 1995.

[68] Richard A. Davison, Koenraad Schalm, and Jan Zaanen. Holographic duality and the resistivity of strange metals. *Phys. Rev. B.*, 89(24):245116, 2014.

[69] M. J. M. de Jong and L. W. Molenkamp. Hydrodynamic electron flow in high-mobility wires. *Phys. Rev. B*, 51:13389–13402, May 1995.

[70] Marion Delehaye, Sébastien Laurent, Igor Ferrier-Barbut, Shuwei Jin, Frédéric Chevy, and Christophe Salomon. Critical Velocity and Dissipation of an Ultracold Bose-Fermi Counterflow. *Phys. Rev. Lett.*, 115(26), 2015.

[71] B. DeMarco, J. L. Bohn, J. P. Burke, M. Holland, and D. S. Jin. Measurement of p-wave threshold law using evaporatively cooled fermionic atoms. *Phys. Rev. Lett.*, 82:4208–4211, May 1999.

[72] Luigi DeMarco, Giacomo Valtolina, Kyle Matsuda, William G. Tobias, Jacob P. Covey, and Jun Ye. A degenerate Fermi gas of polar molecules. *Science*, 363:853–856, 2019.

[73] D. DeMille. Quantum Computation with Trapped Polar Molecules. *Phys. Rev. Lett.*, 88(6):067901, 2002.

[74] D. DeMille, D. R. Glenn, and J. Petricka. Microwave traps for cold polar molecules. *Eur. Phys. J. D*, 31(2):375–384, 2004.

[75] B. J. DeSalvo, Krutik Patel, Geyue Cai, and Cheng Chin. Observation of fermion-mediated interactions between bosonic atoms. *Nature*, 568(7750):61–64, 2019.

[76] B. J. DeSalvo, Krutik Patel, Jacob Johansen, and Cheng Chin. Observation of a Degenerate Fermi Gas Trapped by a Bose-Einstein Condensate. *Phys. Rev. Lett.*, 119:233401, 2017.

[77] John F. Dobson. Harmonic-Potential Theorem: Implications for Approximate Many-Body Theories. *Phys. Rev. Lett.*, 73(16):2244–2247, 1994.

[78] Björn Drews, Markus Deiß, Krzysztof Jachymski, Zbigniew Idziaszek, and Johannes Hecker Denschlag. Inelastic collisions of ultracold triplet Rb2 molecules in the rovibrational ground state. *Nat. Commun.*, 8:14854, 2017.

[79] D. P. Dunseith, S. Truppe, R. J. Hendricks, B. E. Sauer, E. A. Hinds, and M. R. Tarbutt. A high quality, efficiently coupled microwave cavity for trapping cold molecules. *J. Phys. B*, 48(4):045001, 2015.

[80] David Dzsotjan, Richard Schmidt, and Michael Fleischhauer. Dynamical variational approach to Bose polarons at finite temperatures. *arXiv:1909.12856*, 2019.

[81] D. V. Efremov and L. Viverit. p-wave Cooper pairing of fermions in mixtures of dilute Fermi and Bose gases. *Phys. Rev. B*, 65(13):134519, 2002.

[82] P. Engels, C. Atherton, and M. A. Hoefer. Observation of Faraday waves in a Bose-Einstein condensate. *Physical Review Letters*, 98(9):2–5, 2007.

[83] F. Ferlaino, R. J. Brecha, P. Hannaford, F. Riboli, G. Roati, G. Modugno, and M. Inguscio. Dipolar oscillations in a quantum degenerate Fermi-Bose atomic mixture. *J. Opt. B Quantum Semiclassical Opt.*, 5(2):S3–S8, 2003.

[84] G. Ferrari, M. Inguscio, W. Jastrzebski, G. Modugno, G. Roati, and A. Simoni. Collisional properties of ultracold K-Rb mixtures. *Phys. Rev. Lett.*, 89(5):053202, 2002.

[85] I. Ferrier-Barbut, M. Delehaye, S. Laurent, A. T. Grier, M. Pierce, B. S. Rem, F. Chevy, and C. Salomon. A mixture of Bose and Fermi superfluids. *Science*, 345(6200):1035–1038, 2014.

[86] R. P. Feynman. Slow electrons in a polar crystal. *Phys. Rev.*, 97(3):660–665, 1955.

[87] Bernard Field, Jesper Levinsen, and Meera M. Parish. Fate of the Bose polaron at finite temperature. *Phys. Rev. A*, 101(1):013623, 2020.

[88] Richard J. Fletcher, Raphael Lopes, Jay Man, Nir Navon, Robert P. Smith, Martin W. Zwierlein, and Zoran Hadzibabic. Two- and three-body contacts in the unitary bose gas. *Science*, 355(6323):377–380, 2017.

[89] Richard J. Fletcher, Jay Man, Raphael Lopes, Panagiotis Christodoulou, Julian Schmitt, Maximilian Sohmen, Nir Navon, Robert P. Smith, and Zoran Hadzibabic. Elliptic flow in a strongly interacting normal Bose gas. *Physical Review A*, 98(1):011601, 2018.

[90] H. Fröhlich. Electrons in lattice fields. *Adv. Phys.*, 3(11):325–361, Jul 1954.

[91] Chenguang Fu, Thomas Scaffidi, Jonah Waissman, Yan Sun, Rana Saha, Sarah J. Watzman, Abhay K. Srivastava, Guowei Li, Walter Schnelle, Peter Werner, Machteld E. Kamminga, Subir Sachdev, Stuart S. P. Parkin, Sean A. Hartnoll, Claudia Felser, and Johannes Gooth. Thermoelectric signatures of the electron-phonon fluid in $PtSn_4$. *arXiv:1802.09468*, 2018.

[92] T. Fukuhara, T. Tsujimoto, and Y. Takahashi. Quadrupole oscillations in a quantum degenerate Bose-Fermi mixture. *Appl. Phys. B Lasers Opt.*, 96(2-3):271–274, 2009.

[93] Bryce Gadway and Bo Yan. Strongly interacting ultracold polar molecules. *J. Phys. B*, 49(15):152002, 2016.

[94] Alexander L. Gaunt, Tobias F. Schmidutz, Igor Gotlibovych, Robert P. Smith, and Zoran Hadzibabic. Bose-Einstein Condensation of Atoms in a Uniform Potential. *Phys. Rev. Lett.*, 110:200406, May 2013.

[95] G.D. Mahan. *Many-particle physics*. Springer Science+Business Media New York, New York, 2000.

[96] S. D. Gensemer and D. S. Jin. Transition from collisionless to hydrodynamic behavior in an ultracold Fermi gas. *Phys. Rev. Lett.*, 87(17):15–18, 2001.

[97] I. M. Georgescu, S. Ashhab, and Franco Nori. Quantum simulation. *Rev. Mod. Phys.*, 86:153–185, Mar 2014.

[98] Maykel L. González-Martínez, John L. Bohn, and Goulven Quéméner. Adimensional theory of shielding in ultracold collisions of dipolar rotors. *Phys. Rev. A*, 96:032718, 2017.

[99] J. Gooth, F. Menges, N. Kumar, V. Süβ, C. Shekhar, Y. Sun, U. Drechsler, R. Zierold, C. Felser, and B. Gotsmann. Thermal and electrical signatures of a hydrodynamic electron fluid in tungsten diphosphide. *Nat. Commun.*, 9(1):1–8, 2018.

[100] A. V. Gorshkov, P. Rabl, G. Pupillo, A. Micheli, P. Zoller, M. D. Lukin, and H. P. Büchler. Suppression of inelastic collisions between polar molecules with a repulsive shield. *Phys. Rev. Lett.*, 101(7):073201, 2008.

[101] Alexey V Gorshkov, Salvatore R Manmana, Gang Chen, Jun Ye, Eugene Demler, Mikhail D Lukin, and Ana Maria Rey. Tunable superfluidity and quantum magnetism with ultracold polar molecules. *Phys. Rev. Lett.*, 107(11):115301, 2011.

[102] P. D. Gregory, J. A. Blackmore, S. L. Bromley, and S. L Cornish. Loss of ultracold $^{87}Rb^{133}Cs$ molecules via optical excitation of long-lived two-body collision complexes. *arXiv:2002.04431*, 2020.

[103] Philip D. Gregory, Matthew D. Frye, Jacob A. Blackmore, Elizabeth M. Bridge, Rahul Sawant, Jeremy M. Hutson, and Simon L. Cornish. Sticky collisions of ultracold RbCs molecules. *Nat. Commun.*, 10(1):3104, 2019.

[104] Markus Greiner, Olaf Mandel, Tilman Esslinger, Theodor W. Haensch, and Immanuel Bloch. Quantum phase transition from a superfluid to a Mott insulator in a gas of ultracold atoms. *Nature*, 415:39, 2002.

[105] Alexander Groot. *Excitations in Hydrodynamic Ultra-Cold Bose Gases*. PhD thesis, Utrecht University, 2015.

[106] F. Grusdt, R. Schmidt, Y. E. Shchadilova, and E. Demler. Strong-coupling Bose polarons in a Bose-Einstein condensate. *Phys. Rev. A*, 96(1):013607, Jul 2017.

[107] F. Grusdt, Y. E. Shchadilova, A. N. Rubtsov, and E. Demler. Renormalization group approach to the Fröhlich polaron model: Application to impurity-BEC problem. *Sci. Rep.*, 5:12124, 2015.

[108] Fabian Grusdt and Eugene Demler. New theoretical approaches to Bose polarons. *Proc. Int. Sch. Phys. "Enrico Fermi"*, 191:325–411, 2016.

[109] Fabian Grusdt and Michael Fleischhauer. Tunable Polarons of Slow-Light Polaritons in a Two-Dimensional Bose-Einstein Condensate. *Phys. Rev. Lett.*, 116:053602, Feb 2016.

[110] Fabian Grusdt, Kushal Seetharam, Yulia Shchadilova, and Eugene Demler. Strong-coupling Bose polarons out of equilibrium: Dynamical renormalization-group approach. *Phys. Rev. A*, 97(3):033612, 2018.

[111] Nils Eric Guenther, Pietro Massignan, Maciej Lewenstein, and Georg M. Bruun. Bose Polarons at Finite Temperature and Strong Coupling. *Phys. Rev. Lett.*, 120(5):050405, 2018.

[112] Mingyang Guo, Xin Ye, Junyu He, Maykel L. González-Martínez, Romain Vexiau, Goulven Quéméner, and Dajun Wang. Dipolar Collisions of Ultracold Ground-State Bosonic Molecules. *Phys. Rev. X*, 8(4):041044, 2018.

[113] Mingyang Guo, Bing Zhu, Bo Lu, Xin Ye, Fudong Wang, Romain Vexiau, Nadia Bouloufa-Maafa, Goulven Quéméner, Olivier Dulieu, and Dajun Wang. Creation of an Ultracold Gas of Ground-State Dipolar $^{23}Na^{87}Rb$ Molecules. *Phys. Rev. Lett.*, 116(20):205303, 2016.

[114] S. Gupta, Z. Hadzibabic, M. W. Zwierlein, C. A. Stan, K. Dieckmann, C. H. Schunck, E. G.M. Van Kempen, B. J. Verhaar, and W. Ketterle. Radio-frequency spectroscopy of ultracold fermions. *Science*, 300(5626):1723–1726, 2003.

[115] G. M. Gusev, A. D. Levin, E. V. Levinson, and A. K. Bakarov. Viscous transport and Hall viscosity in a two-dimensional electron system. *Phys. Rev. B*, 98(16):2–6, 2018.

[116] Sean A. Hartnoll, Pavel K. Kovtun, Markus Müller, and Subir Sachdev. Theory of the Nernst effect near quantum phase transitions in condensed matter and in dyonic black holes. *Phys. Rev. B*, 76(14):1–23, 2007.

[117] Sean A. Hartnoll, Andrew Lucas, and Subir Sachdev. *Holographic quantum matter*. MIT Press, Cambridge, 2018.

[118] Kaden R.A. Hazzard, Bryce Gadway, Michael Foss-Feig, Bo Yan, Steven A Moses, Jacob P Covey, Norman Y Yao, Mikhail D Lukin, Jun Ye, Deborah S Jin, and Ana Maria Rey. Many-body dynamics of dipolar molecules in an optical lattice. *Phys. Rev. Lett.*, 113(19):195302, 2014.

[119] G. Herzberg. *Molecular Spectra and Molecular Structure*. Reitell Press, Redditch, UK, 2008.

[120] Tin-lun Ho and Erich J. Mueller. High Temperature Expansion Applied to Fermions near Feshbach Resonance. *Phys. Rev. Lett.*, 92(16):160404, 2004.

[121] E. Hodby, S. T. Thompson, C. A. Regal, M. Greiner, A. C. Wilson, D. S. Jin, E. A. Cornell, and C. E. Wieman. Production efficiency of ultracold Feshbach molecules in bosonic and fermionic systems. *Phys. Rev. Lett.*, 94(12):120402, 2005.

[122] M. G. Hu, Y. Liu, D. D. Grimes, Y. W. Lin, A. H. Gheorghe, R. Vexiau, N. Bouloufa-Maafa, O. Dulieu, T. Rosenband, and K. K. Ni. Direct observation of bimolecular reactions of ultracold KRb molecules. *Science*, 366(6469):1111–1115, 2019.

[123] Ming-Guang Hu, Michael J. Van de Graaff, Dhruv Kedar, John P. Corson, Eric A. Cornell, and Deborah S. Jin. Bose polarons in the strongly interacting regime. *Phys. Rev. Lett.*, 117:055301, Jul 2016.

[124] Bo Huang, Isabella Fritsche, Rianne S. Lous, Cosetta Baroni, Jook T.M. Walraven, Emil Kirilov, and Rudolf Grimm. Breathing mode of a Bose-Einstein condensate repulsively interacting with a fermionic reservoir. *Phys. Rev. A*, 99(4):041602, 2019.

[125] Zbigniew Idziaszek and Paul S. Julienne. Universal rate constants for reactive collisions of ultracold molecules. *Phys. Rev. Lett.*, 104(11):113202, 2010.

[126] Adilet Imambekov and Eugene Demler. Exactly solvable case of a one-dimensional Bose-Fermi mixture. *Phys. Rev. A*, 73(2):021602, 2006.

[127] D. S. Jin, J. R. Ensher, M. R. Matthews, C. E. Wieman, and E. A. Cornell. Collective excitations of a Bose-Einstein condensate in a dilute gas. *Phys. Rev. Lett.*, 77(3):420–423, 1996.

[128] Nils B. Jørgensen, Lars Wacker, Kristoffer T. Skalmstang, Meera M. Parish, Jesper Levinsen, Rasmus S. Christensen, Georg M. Bruun, and Jan J. Arlt. Observation of Attractive and Repulsive Polarons in a Bose-Einstein Condensate. *Phys. Rev. Lett.*, 117(5):055302, 2016.

[129] J. A. Joseph, E. Elliott, and J. E. Thomas. Shear Viscosity of a Unitary Fermi Gas Near the Superfluid Phase Transition. *Phys. Rev. Lett.*, 115:020401, Jul 2015.

[130] Paul S. Julienne. Cold binary atomic collisions in a light field. *Journal of Research of the National Institute of Standards and Technology*, 101:487, 1996.

[131] Ryan M. Kalas and D. Blume. Interaction-induced localization of an impurity in a trapped Bose-Einstein condensate. *Phys. Rev. A*, 73:043608, Apr 2006.

[132] Tijs Karman and Jeremy M. Hutson. Microwave Shielding of Ultracold Polar Molecules. *Phys. Rev. Lett.*, 121(16):163401, 2018.

[133] W. Ketterle and M. W. Zwierlein. Making, probing, and understanding ultracold Fermi gases. *Rivista del Nuovo Cimento*, 31:247, 2008.

[134] Jami J. Kinnunen, Zhigang Wu, and Georg M. Bruun. Induced p-Wave Pairing in Bose-Fermi Mixtures. *Phys. Rev. Lett.*, 121(25):253402, 2018.

[135] Christiane P. Koch, Mikhail Lemeshko, and Dominique Sugny. Quantum control of molecular rotation. *Rev. Mod. Phys.*, 91(3):35005, 2019.

[136] Joannis Koepsell, Jayadev Vijayan, Pimonpan Sompet, Fabian Grusdt, Timon A. Hilker, Eugene Demler, Guillaume Salomon, Immanuel Bloch, and Christian Gross. Imaging magnetic polarons in the doped Fermi–Hubbard model. *Nature*, 572:358, 2019.

[137] C. Kohstall, M. Zaccanti, M. Jag, A. Trenkwalder, P. Massignan, G. M. Bruun, F. Schreck, and R. Grimm. Metastability and coherence of repulsive polarons in a strongly interacting Fermi mixture. *Nature*, 485(7400):615–618, 2012.

[138] Marco Koschorreck, Daniel Pertot, Enrico Vogt, Bernd Fröhlich, Michael Feld, and Michael Köhl. Attractive and repulsive Fermi polarons in two dimensions. *Nature*, 485(7400):619–622, 2012.

[139] R. V. Krems. Cold Controlled Chemistry. *Phys. Chem. Chem. Phys.*, 10(28):4079–4092, 2008.

[140] R. V. Krems, W. C. Stwalley, and Bretislav Friedrich. *Cold Molecules: Theory, Experiment, Applications*. CRC Press, Boca Raton, 2009.

[141] R. Krishna Kumar, D. A. Bandurin, F. M.D. Pellegrino, Y. Cao, A. Principi, H. Guo, G. H. Auton, M. Ben Shalom, L. A. Ponomarenko, G. Falkovich, K. Watanabe, T. Taniguchi, I. V. Grigorieva, L. S. Levitov, M. Polini, and A. K. Geim. Superballistic flow of viscous electron fluid through graphene constrictions. *Nat. Phys.*, 13(12):1182–1185, 2017.

[142] C. C. N. Kuhn, S. Hoinka, I. Herrera, P. Dyke, J. J. Kinnunen, G. M. Bruun, and C. J. Vale. High-Frequency Sound in a Unitary Fermi Gas. *Phys. Rev. Lett.*, 124:150401, Apr 2020.

[143] L. D. Landau. Uber die bewegung der elektronen in kristallgitter. *Phys. Z. Sowjetunion*, 3:644, 1933.

[144] Lucas Lassablière and Goulven Quéméner. Controlling the scattering length of ultracold dipolar molecules. *Phys. Rev. Lett.*, 121:163402, Oct 2018.

[145] Chaohong Lee and Elena A. Ostrovskaya. Quantum computation with diatomic bits in optical lattices. *Phys. Rev. A*, 72:062321, Dec 2005.

[146] Patrick A. Lee, Naoto Nagaosa, and Xiao-Gang Wen. Doping a Mott insulator: Physics of high-temperature superconductivity. *Rev. Mod. Phys.*, 78:17–85, Jan 2006.

[147] D. Pines Lee, T. D., F. E. Low. The Motion of Slow Electrons in a Polar Crystal. *Phys. Rev.*, 90(2):297, 1953.

[148] J Levinsen, N R Cooper, and G V Shlyapnikov. Topological $p_x + ip_y$ superfluid phase of fermionic polar molecules. *Phys. Rev. A*, 84(1):013603, 2011.

[149] Jesper Levinsen, Meera M. Parish, and Georg M. Bruun. Impurity in a Bose-Einstein Condensate and the Efimov Effect. *Phys. Rev. Lett.*, 115(12):125302, 2015.

[150] Jesper Levinsen, Meera M. Parish, Rasmus S. Christensen, Jan J. Arlt, and Georg M. Bruun. Finite-temperature behavior of the Bose polaron. *Phys. Rev. A*, 96(6):063622, 2017.

[151] Ming Li, Alexander Petrov, Constantinos Makrides, Eite Tiesinga, and Svetlana Kotochigova. Pendular trapping conditions for ultracold polar molecules enforced by external electric fields. *Phys. Rev. A*, 95(6):063422, 2017.

[152] Weiran Li and S Das Sarma. Variational study of polarons in Bose-Einstein condensates. *Phys. Rev. A*, 90(1):013618, Jul 2014.

[153] M. G. Lingham, K. Fenech, T. Peppler, S. Hoinka, P. Dyke, P. Hannaford, and C. J. Vale. Bragg spectroscopy of strongly interacting Fermi gases. *J. Mod. Opt.*, 63(18):1783–1794, 2016.

[154] Xia Ji Liu and Hui Hu. Collisionless and hydrodynamic excitations of trapped boson-fermion mixtures. *Phys. Rev. A*, 67(2):023613, 2003.

[155] Y. Liu, M.-G. Hu, M.A. Nichols, D.D. Grimes, T. Karman, H. Guo, and K.-K. Ni. Steering ultracold reactions through long-lived transient intermediates. *arXiv:2002.05140*, 2020.

[156] Andrew Lucas, Jesse Crossno, Kin Chung Fong, Philip Kim, and Subir Sachdev. Transport in inhomogeneous quantum critical fluids and in the Dirac fluid in graphene. *Phys. Rev. B*, 93(7):075426, 2016.

[157] D. Ludwig, S. Floerchinger, S. Moroz, and C. Wetterich. Quantum phase transition in Bose-Fermi mixtures. *Phys. Rev. A*, 84:033629, Sep 2011.

[158] M.-O. Mewes, M. R. Andrews, N. J. van Druten, D. M. Kurn, D. S. Durfee, C. G. Townsend and W. Ketterle. Collective excitations of a Bose-Einstein condensate in a magnetic trap. *Phys. Rev. Lett.*, 77(6):988, 1996.

[159] Salvatore R. Manmana, E. M. Stoudenmire, Kaden R.A. Hazzard, Ana Maria Rey, and Alexey V. Gorshkov. Topological phases in ultracold polar-molecule quantum magnets. *Phys. Rev. B*, 87(8):081106, 2013.

[160] Tomoyuki Maruyama, Tike'S Yamamoto, Takushi Nishimura, and Hiroyuki Yabu. Deformation dependence of breathing oscillations in Bose-Fermi mixtures at zero temperature. *J. Phys. B At. Mol. Opt. Phys.*, 47(22):25–34, 2014.

[161] Pietro Massignan, Matteo Zaccanti, and Georg M. Bruun. Polarons, dressed molecules and itinerant ferromagnetism in ultracold Fermi gases. *Reports Prog. Phys.*, 77(3):034401, 2014.

[162] C. Menotti, P. Pedri, and S. Stringari. Expansion of an Interacting Fermi Gas. *Phys. Rev. Lett.*, 89:250402, Dec 2002.

[163] A. Micheli, G. K. Brennen, and P. Zoller. A toolbox for lattice spin models with polar molecules. *Nat. Phys.*, 2(May):341–347, 2006.

[164] A. Micheli, G. Pupillo, H. P. Büchler, and P. Zoller. Cold polar molecules in two-dimensional traps: Tailoring interactions with external fields for novel quantum phases. *Phys. Rev. A*, 76(4):043604, 2007.

[165] T. Miyakawa, T. Suzuki, and H. Yabu. Sum-rule approach to collective oscillations of a boson-fermion mixed condensate of alkali-metal atoms. *Phys. Rev. A*, 62(6):063613, 2000.

[166] Philip J.W. Moll, Pallavi Kushwaha, Nabhanila Nandi, Burkhard Schmidt, and Andrew P. Mackenzie. Evidence for hydrodynamic electron flow in $PdCoO_2$. *Science*, 351(6277):1061–1064, 2016.

[167] Peter K. Molony, Philip D. Gregory, Zhonghua Ji, Bo Lu, Michael P. Köppinger, C. Ruth Le Sueur, Caroline L. Blackley, Jeremy M. Hutson, and Simon L. Cornish. Creation of ultracold ^{87}Rb^{133}Cs molecules in the rovibrational ground state. *Phys. Rev. Lett.*, 113(25):255301, 2014.

[168] Biswaroop Mukherjee, Parth B. Patel, Zhenjie Yan, Richard J. Fletcher, Julian Struck, and Martin W. Zwierlein. Spectral Response and Contact of the Unitary Fermi Gas. *Phys. Rev. Lett.*, 122(20), 2019.

[169] Biswaroop Mukherjee, Zhenjie Yan, Parth B. Patel, Zoran Hadzibabic, Tarik Yefsah, Julian Struck, and Martin W. Zwierlein. Homogeneous Atomic Fermi Gases. *Phys. Rev. Lett.*, 118:123401, Mar 2017.

[170] M. Naraschewski and D. M. Stamper-Kurn. Analytical description of a trapped semi-ideal Bose gas at finite temperature. *Phys. Rev. A*, 58:2423–2426, Sep 1998.

[171] S. Nascimbène, N. Navon, K. J. Jiang, L. Tarruell, M. Teichmann, J. McKeever, F. Chevy, and C. Salomon. Collective oscillations of an imbalanced Fermi gas: Axial compression modes and polaron effective mass. *Phys. Rev. Lett.*, 103(17):170402, 2009.

[172] B. Neyenhuis, B. Yan, S. A. Moses, J. P. Covey, A. Chotia, A. Petrov, S. Kotochigova, J. Ye, and D. S. Jin. Anisotropic polarizability of ultracold polar ^{40}K^{87}Rb molecules. *Phys. Rev. Lett.*, 109(23):230403, 2012.

[173] J. H.V. Nguyen, M. C. Tsatsos, D. Luo, A. U.J. Lode, G. D. Telles, V. S. Bagnato, and R. G. Hulet. Parametric Excitation of a Bose-Einstein Condensate: From Faraday Waves to Granulation. *Physical Review X*, 9(2):11052, 2019.

[174] K. K. Ni, S. Ospelkaus, M. H.G. De Miranda, A. Pe'er, B. Neyenhuis, J. J. Zirbel, S. Kotochigova, P. S. Julienne, D. S. Jin, and J. Ye. A high phase-space-density gas of polar molecules. *Science*, 322(5899):231–235, 2008.

[175] K. K. Ni, S. Ospelkaus, D. Wang, G. Quéméner, B. Neyenhuis, M. H.G. De Miranda, J. L. Bohn, J. Ye, and D. S. Jin. Dipolar collisions of polar molecules in the quantum regime. *Nature*, 464(7293):1324–1328, 2010.

[176] Matthew A. Nichols, Lawrence W. Cheuk, Melih Okan, Thomas R. Hartke, Enrique Mendez, T. Senthil, Ehsan Khatami, Hao Zhang, and Martin W. Zwierlein. Spin transport in a mott insulator of ultracold fermions. *Science*, 363(6425):383–387, 2019.

[177] Predrag Nikolić and Subir Sachdev. Renormalization-group fixed points, universal phase diagram, and 1/N expansion for quantum liquids with interactions near the unitarity limit. *Phys. Rev. A*, 75(3):033608, 2007.

[178] K. M. O'Hara, S. L. Hemmer, M. E. Gehm, S. R. Granade, and J. E. Thomas. Observation of a strongly interacting degenerate Fermi gas of atoms. *Science*, 298(5601):2179–2182, 2002.

[179] S. Ospelkaus, K.-K. Ni, D. Wang, M. H. G. de Miranda, B. Neyenhuis, G. Quéméner, P. S. Julienne, J. L. Bohn, D. S. Jin, and J. Ye. Quantum-state controlled chemical reactions of ultracold potassium-rubidium molecules. *Science*, 327(5967):853–857, 2010.

[180] P. Nozieres and D. Pines. *The Theory of Quantum Liquids*. Perseus Books, Cambridge, 1999.

[181] Jee Woo Park. *An Ultracold Gas of Dipolar Fermionic $^{23}Na^{40}K$ Molecules*. PhD thesis, Massachusetts Institute of Technology, 2016.

[182] Jee Woo Park, Sebastian A Will, and Martin W Zwierlein. Two-photon pathway to ultracold ground state molecules of ^{23}Na^{40}K. *New Journal of Physics*, 17(7):075016, 2015.

[183] Jee Woo Park, Sebastian A. Will, and Martin W. Zwierlein. Ultracold Dipolar Gas of Fermionic ^{23}Na^{40}K Molecules in Their Absolute Ground State. *Phys. Rev. Lett.*, 114(20):205302, 2015.

[184] Jee Woo Park, Cheng-Hsun Wu, Ibon Santiago, Tobias G. Tiecke, Sebastian Will, Peyman Ahmadi, and Martin W. Zwierlein. Quantum degenerate bose-fermi mixture of chemically different atomic species with widely tunable interactions. *Phys. Rev. A*, 85:051602, May 2012.

[185] Jee Woo Park, Zoe Z. Yan, Huanqian Loh, Sebastian A. Will, and Martin W. Zwierlein. Second-scale nuclear spin coherence time of ultracold ^{23}Na^{40}K molecules. *Science*, 357(6349):372, 2017.

[186] Parth B. Patel, Zhenjie Yan, Biswaroop Mukherjee, Richard J. Fletcher, Julian Struck, and Martin W. Zwierlein. Universal Sound Diffusion in a Strongly Interacting Fermi Gas. *arXiv:1909.02555*, 2019.

[187] S. I. Pekar. Zh. Eksp. Teor. Fiz. **16**, 335 (1946). *English translation in* Journal of Physics USSR, **10**, 341 (1946).

[188] S. I. Pekar. Zh. Eksp. Teor. Fiz. **16**, 341 (1946). *English translation in* Journal of Physics USSR, **10**, 347 (1946).

[189] C. Pethick and H. Smith. *Bose-Einstein Condensation in Dilute Gases*. Cambridge University Press, Cambridge, 2008.

[190] David Pines, P. Nozieres, and Noel Corngold. The Theory of Quantum Liquids. *Am. J. Phys.*, 36(3):279–280, Mar 1968.

[191] Andrew C. Potter, Erez Berg, Daw-Wei Wang, Bertrand I. Halperin, and Eugene Demler. Superfluidity and Dimerization in a Multilayered System of Fermionic Polar Molecules. *Phys. Rev. Lett.*, 105:220406, Nov 2010.

[192] Nikolay Prokof'ev and Boris Svistunov. Fermi-polaron problem: Diagrammatic Monte Carlo method for divergent sign-alternating series. *Phys. Rev. B*, 77(2):020408, 2008.

[193] M. Punk, P. T. Dumitrescu, and W. Zwerger. Polaron-to-molecule transition in a strongly imbalanced Fermi gas. *Phys. Rev. A*, 80(5):053605, 2009.

[194] M. Punk and W. Zwerger. Theory of rf-spectroscopy of strongly interacting fermions. *Phys. Rev. Lett.*, 99(17):170404, 2007.

[195] G. Pupillo, A. Griessner, A. Micheli, M. Ortner, D. W. Wang, and P. Zoller. Cold atoms and molecules in self-assembled dipolar lattices. *Phys. Rev. Lett.*, 100(5):050402, 2008.

[196] Goulven Quéméner and John L. Bohn. Strong dependence of ultracold chemical rates on electric dipole moments. *Phys. Rev. A*, 81(2):022702, 2010.

[197] Goulven Quéméner and Paul S. Julienne. Ultracold Molecules under Control! *Chem. Rev.*, 112(9):4949–5011, 2012.

[198] Steffen Patrick Rath and Richard Schmidt. Field-theoretical study of the Bose polaron. *Phys. Rev. A*, 88(5):053632, 2013.

[199] C. A. Regal and D. S. Jin. Measurement of Positive and Negative Scattering Lengths in a Fermi Gas of Atoms. *Physical Review Letters*, 90(23):4, 2003.

[200] T. Rentrop, A. Trautmann, F. A. Olivares, F. Jendrzejewski, A. Komnik, and M. K. Oberthaler. Observation of the Phononic Lamb Shift with a Synthetic Vacuum. *Phys. Rev. X*, 6:041041, Nov 2016.

[201] Richard Roy, Alaina Green, Ryan Bowler, and Subhadeep Gupta. Two-Element Mixture of Bose and Fermi Superfluids. *Phys. Rev. Lett.*, 118(5):055301, Feb 2017.

[202] Timur M. Rvachov, Hyungmok Son, Ariel T. Sommer, Sepehr Ebadi, Juliana J. Park, Martin W. Zwierlein, Wolfgang Ketterle, and Alan O. Jamison. Long-Lived Ultracold Molecules with Electric and Magnetic Dipole Moments. *Phys. Rev. Lett.*, 119(14):143001, 2017.

[203] Subir Sachdev. *Quantum Phase Transitions*. Cambridge University Press, Cambridge, 2nd edition, 2011.

[204] M. S. Safronova, D. Budker, D. Demille, Derek F.Jackson Kimball, A. Derevianko, and Charles W. Clark. Search for new physics with atoms and molecules. *Rev. Mod. Phys.*, 90(2):25008, 2018.

[205] Jun John Sakurai. *Modern Quantum Mechanics*. Addison-Wesley, Reading, MA, 1994.

[206] F. Scazza, G. Valtolina, P. Massignan, A. Recati, A. Amico, A. Burchianti, C. Fort, M. Inguscio, M. Zaccanti, and G. Roati. Repulsive Fermi Polarons in a Resonant Mixture of Ultracold ^{6}Li Atoms. *Phys. Rev. Lett.*, 118(8):083602, 2017.

[207] André Schirotzek, Cheng Hsun Wu, Ariel Sommer, and Martin W. Zwierlein. Observation of Fermi polarons in a tunable Fermi liquid of ultracold atoms. *Phys. Rev. Lett.*, 102(23):230402, 2009.

[208] Richard Schmidt, Michael Knap, Dmitri A. Ivanov, Jhih-Shih You, Marko Cetina, and Eugene Demler. Universal many-body response of heavy impurities coupled to a Fermi sea: A review of recent progress. *Reports Prog. Phys.*, 81(2):024401, 2018.

[209] William Schneider, Vijay B. Shenoy, and Mohit Randeria. Theory of Radio Frequency Spectroscopy of Polarized Fermi Gases. *arXiv:0903.3006*, 2009.

[210] Frauke Seeßelberg, Nikolaus Buchheim, Zhen-Kai Lu, Tobias Schneider, Xin-Yu Luo, Eberhard Tiemann, Immanuel Bloch, and Christoph Gohle. Modeling the adiabatic creation of ultracold polar ^{23}Na^{40}K molecules. *Phys. Rev. A*, 97:013405, Jan 2018.

[211] Frauke Seeßelberg, Xin-Yu Luo, Ming Li, Roman Bause, Svetlana Kotochigova, Immanuel Bloch, and Christoph Gohle. Extending rotational coherence of interacting polar molecules in a spin-decoupled magic trap. *Phys. Rev. Lett.*, 121:253401, Dec 2018.

[212] Aditya Shashi, Fabian Grusdt, Dmitry A. Abanin, and Eugene Demler. Radio-frequency spectroscopy of polarons in ultracold Bose gases. *Phys. Rev. A*, 89(5):053617, 2014.

[213] Yulia E. Shchadilova, Fabian Grusdt, Alexey N. Rubtsov, and Eugene Demler. Polaronic mass renormalization of impurities in Bose-Einstein condensates: Correlated Gaussian-wave-function approach. *Phys. Rev. A*, 93(4):043606, 2016.

[214] Yulia E. Shchadilova, Richard Schmidt, Fabian Grusdt, and Eugene Demler. Quantum dynamics of ultracold Bose polarons. *Phys. Rev. Lett.*, 117(11):113002, Apr 2016.

[215] Zhe Yu Shi, Shuhei M. Yoshida, Meera M. Parish, and Jesper Levinsen. Impurity-Induced Multibody Resonances in a Bose Gas. *Phys. Rev. Lett.*, 121(24):243401, 2018.

[216] L. Sidorenkov, M. Tey, R. Grimm, Y.-H Hou, L. Pitaevskii, and S. Stringari. Second sound and the superfluid fraction in a Fermi gas with resonant interactions. *Nature*, 498:78, 2013.

[217] T. Sogo, T. Miyakawa, T. Suzuki, and H. Yabu. Random-phase approximation study of collective excitations in the Bose-Fermi mixed condensate of alkali-metal gases. *Phys. Rev. A*, 66(1):136181–1361812, 2002.

[218] A. Sommer, M. Ku, G. Roati, and M. W. Zwierlein. Universal spin transport in a strongly interacting Fermi gas. *Nature*, 472:201, 2011.

[219] Boris Spivak and Steven A. Kivelson. Transport in two dimensional electronic micro-emulsions. *Ann. Phys.*, 321(9):2071–2115, 2006.

[220] D. M. Stamper-Kurn, H. J. Miesner, S. Inouye, M. R. Andrews, and W. Ketterle. Collisionless and hydrodynamic excitations of a Bose-Einstein condensate. *Phys. Rev. Lett.*, 81(3):500–503, 1998.

[221] S. Stringari. Collective Excitations of a Trapped Bose-Condensed Gas. *Phys. Rev. Lett.*, 77(12):2360–2363, 1996.

[222] Joseph A. Sulpizio, Lior Ella, Asaf Rozen, John Birkbeck, David J. Perello, Debarghya Dutta, Moshe Ben-Shalom, Takashi Taniguchi, Kenji Watanabe, Tobias Holder, Raquel Queiroz, Alessandro Principi, Ady Stern, Thomas Scaffidi, Andre K. Geim, and Shahal Ilani. Visualizing Poiseuille flow of hydrodynamic electrons. *Nature*, 576(7785):75–79, 2019.

[223] Sergey V. Syzranov, Michael L. Wall, Victor Gurarie, and Ana Maria Rey. Spin-orbital dynamics in a system of polar molecules. *Nat. Commun.*, 5:5391, 2014.

[224] Tetsu Takekoshi, Lukas Reichsöllner, Andreas Schindewolf, Jeremy M. Hutson, C. Ruth Le Sueur, Olivier Dulieu, Francesca Ferlaino, Rudolf Grimm, and Hanns Christoph Nägerl. Ultracold dense samples of dipolar RbCs molecules in the rovibrational and hyperfine ground state. *Phys. Rev. Lett.*, 113(20):205301, 2014.

[225] Shina Tan. Energetics of a strongly correlated Fermi gas. *Ann. Phys.*, 323(12):2952–2970, 2008.

[226] Shina Tan. Large momentum part of a strongly correlated Fermi gas. *Ann. Phys.*, 323(12):2971–2986, 2008.

[227] J. Tempere, W. Casteels, M. K. Oberthaler, S. Knoop, E. Timmermans, and J. T. Devreese. Feynman path-integral treatment of the BEC-impurity polaron. *Phys. Rev. B*, 80(18):184504, 2009.

[228] Meng Khoon Tey, Leonid A. Sidorenkov, Edmundo R. Sánchez Guajardo, Rudolf Grimm, Mark J. H. Ku, Martin W. Zwierlein, Yan-Hua Hou, Lev Pitaevskii, and Sandro Stringari. Collective Modes in a Unitary Fermi Gas across the Superfluid Phase Transition. *Phys. Rev. Lett.*, 110:055303, Jan 2013.

[229] E. Tiemann. Private communication, 2018.

[230] Eite Tiesinga, Carl J Williams, Paul S Julienne, Kevin M Jones, Paul D Lett, and William D Phillips. A Spectroscopic Determination of Scattering Lengths for Sodium Atom Collisions. *J. Res. Natl. Inst. Stand. Technol.*, 101(101):505, 1996.

[231] C. Trefzger, M. Alloing, C. Menotti, F. Dubin, and M. Lewenstein. Quantum magnetism and counterflow supersolidity of up-down bosonic dipoles. *New J. Phys.*, 12:093008, 2010.

[232] Senne Van Loon, Wim Casteels, and Jacques Tempere. Ground-state properties of interacting Bose polarons. *Phys. Rev. A*, 98(6):063631, 2018.

[233] Jonas Vlietinck, Wim Casteels, Kris Van Houcke, Jacques Tempere, Jan Ryckebusch, and Jozef T Devreese. Diagrammatic Monte Carlo study of the acoustic and the Bose–Einstein condensate polaron. *New Journal of Physics*, 17(3):033023, 2015.

[234] Matthias Vojta. Impurity quantum phase transitions. *Philos. Mag.*, 86(13-14):1807–1846, 2006.

[235] M. L. Wall and L. D. Carr. Emergent timescales in entangled quantum dynamics of ultracold molecules in optical lattices. *New J. Phys.*, 11:055027, 2009.

[236] M L Wall and L D Carr. Hyperfine molecular Hubbard Hamiltonian. *Phys. Rev. A*, 82(1):013611, 2010.

[237] Takayuki Watanabe. Effect of dipole-dipole interaction on unpolarized ultracold fermionic gases in a two-dimensional optical lattice. *Phys. Rev. A*, 80(5):053621, 2009.

[238] R. J. Wild, P. Makotyn, J. M. Pino, E. A. Cornell, and D. S. Jin. Measurements of Tan's contact in an atomic Bose-Einstein condensate. *Phys. Rev. Lett.*, 108(14):145305, 2012.

[239] Sebastian A. Will, Jee Woo Park, Zoe Z. Yan, Huanqian Loh, and Martin W. Zwierlein. Coherent microwave control of ultracold $^{23}Na^{40}K$ molecules. *Phys. Rev. Lett.*, 116:225306, Jun 2016.

[240] S. C. Wright, T. E. Wall, and M. R. Tarbutt. Microwave trap for atoms and molecules. *Phys. Rev. Research*, 1:033035, Oct 2019.

[241] Cheng-Hsun Wu. *Strongly Interacting Quantum Mixtures of Ultracold Atoms*. PhD thesis, Massachusetts Institute of Technology, 2013.

[242] Cheng Hsun Wu, Jee Woo Park, Peyman Ahmadi, Sebastian Will, and Martin W. Zwierlein. Ultracold fermionic Feshbach molecules of $^{23}Na^{40}K$. *Phys. Rev. Lett.*, 109(8):085301, 2012.

[243] Yu Ping Wu, Xing Can Yao, Xiang Pei Liu, Xiao Qiong Wang, Yu Xuan Wang, Hao Ze Chen, Youjin Deng, Yu Ao Chen, and Jian Wei Pan. Coupled dipole oscillations of a mass-imbalanced Bose-Fermi superfluid mixture. *Phys. Rev. B*, 97(2):020506, 2018.

[244] Bo Yan, Steven A. Moses, Bryce Gadway, Jacob P. Covey, Kaden R.A. Hazzard, Ana Maria Rey, Deborah S. Jin, and Jun Ye. Observation of dipolar spin-exchange interactions with lattice-confined polar molecules. *Nature*, 501(7468):521–525, 2013.

[245] Zhenjie Yan, Parth B. Patel, Biswaroop Mukherjee, Richard J. Fletcher, Julian Struck, and Martin W. Zwierlein. Boiling a Unitary Fermi Liquid. *Phys. Rev. Lett.*, 122(9):093401, 2019.

[246] Zoe Z. Yan. A heavy impurity immersed in a Bose-Einstein Condensate, 2018. 49th Annual Meeting of the APS Division of Atomic, Molecular and Optical Physics APS Meeting.

[247] Zoe Z. Yan, Yiqi Ni, Carsten Robens, and Martin W. Zwierlein. Bose polarons near quantum criticality. *Science*, 368(6487):190–194, 2020.

[248] Zoe Z Yan, Jee Woo Park, Yiqi Ni, Huanqian Loh, Sebastian Will, Tijs Karman, and Martin Zwierlein. Resonant dipolar collisions of ultracold molecules induced by microwave dressing. *arXiv:2003.02830*, 2020.

[249] Huan Yang, De-Chao Zhang, Lan Liu, Ya-Xiong Liu, Jue Nan, Bo Zhao, and Jian-Wei Pan. Observation of magnetically tunable Feshbach resonances in ultracold ^{23}Na^{40}K + ^{40}K collisions. *Science*, 363(6424):261–264, 2019.

[250] N. Y. Yao, M. P. Zaletel, D. M. Stamper-Kurn, and A. Vishwanath. A quantum dipolar spin liquid. *Nat. Phys.*, 14(4):405–410, 2018.

[251] Xin Ye, Mingyang Guo, Maykel L González-Martínez, Goulven Quéméner, and Dajun Wang. Collisions of ultracold ^{23}Na^{87}Rb molecules with controlled chemical reactivities. *Sci. Adv.*, 4(1):eaaq0083, 2018.

[252] S. F. Yelin, K. Kirby, and Robin Côté. Schemes for robust quantum computation with polar molecules. *Phys. Rev. A*, 74(5):050301, 2006.

[253] S. K. Yip. Collective modes in a dilute Bose-Fermi mixture. *Phys. Rev. A*, 64(2):023609, 2001.

[254] Shuhei M. Yoshida, Shimpei Endo, Jesper Levinsen, and Meera M. Parish. Universality of an Impurity in a Bose-Einstein Condensate. *Phys. Rev. X*, 8:011024, Feb 2018.

[255] Min Jie Zhu, Huan Yang, Lan Liu, De Chao Zhang, Ya Xiong Liu, Jue Nan, Jun Rui, Bo Zhao, Jian Wei Pan, and Eberhard Tiemann. Feshbach loss spectroscopy in an ultracold ^{23}Na^{40}K mixture. *Phys. Rev. A*, 96(6):062705, 2017.

[256] W. Zwerger. Strongly Interacting Fermi Gases. In M. Inguscio, W. Ketterle, S. Stringari, and G. Roati, editors, *Proceedings of the International School of Physics "Enrico Fermi"*, volume 191, chapter 2. IOP Press Books, Amsterdam, 2016.

[257] M. W. Zwierlein. Thermodynamics of strongly interacting Fermi gases. In M. Inguscio, W. Ketterle, S. Stringari, and G. Roati, editors, *Proceedings of the International School of Physics "Enrico Fermi"*, volume 191, chapter 3. IOP Press Books, Amsterdam, 2016.